MEMORY SWITCHING AND OPTICAL PROPERTIES OF GLASS-METAL MICROCOMPOSITES

A Thesis Submitted
in Partial Fulfilment of the Requirements
for the Degree of

DOCTOR OF PHILOSOPHY

by

GOPES CHANDRA DAS

to the

INTERDISCIPLINARY PROGRAMME IN MATERIALS SCIENCE

INDIAN INSTITUTE OF TECHNOLOGY KANPUR

JANUARY, 1982

Dedicated

to   my

Parents

CERTIFICATE - I

This is to certify that Mr. Gopes Chandra Das has satisfactorily completed all the course requirements for the Ph.D. degree programme. The courses include :

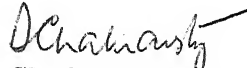|		
MS	607	Amorphous Solids
MS	620	Materials Engineering
Met	668	Structure and Properties of Glass
MS	602	Materials Science II

Mr. Gopes Chandra Das successfully completed his Ph.D. degree qualifying examination in January, 1978.

(K.N. Rai)
Convenor
Departmental Post Graduate
Committee

(D. Chakravorty)
Head
Interdisciplinary Programme in
Materials Science
I.I.T. Kanpur.

1S-1982-D-DAS-MEM

CERTIFICATE - II

Certified that the work described in this thesis entitled 'Memory Switching and Optical Properties of Glass-Metal Microcomposites' is the original work of Mr. Gopes Chandra Das performed under my supervision and has not been submitted elsewhere for a degree.

(D. Chakravorty)
Professor
Department of Metallurgical Engg.
and
Interdisciplinary Programme in Materials Scien
I.I.T. Kanpur.

ACKNOWLEDGEMENTS

I take the pleasure in expressing my heartfelt gratitude to Professor D. Chakravorty for his excellent and lively guidance throughout the course of this research work.

I am very much thankful to Mr. V. Saxena, Dr. S. Datta and Mr. P. Sarkar for their valuable help.

I am grateful to Dr. S. Bandopadhyay, Mr. P.K. Nandi for their co-operation and unassuming help.

I thank all my friends particularly, Messrs. D. Roy, A.K. Ghosh, L. Shil, A. Srivastava, A. Sen, S. Mukhopadhyay, S. Das, R. Bhatnagar and Dr. D. Kumar for giving me nice company and timely help.

The help rendered by Messrs. B. Sharma, Nar Singh and I. Sharma is gratefully acknowledged.

My sincere thanks go to Messrs. C.M. Abraham for his excellent typing and to V.P. Gupta for beautiful drawing.

Last but not the least, I thank Messrs. Vishwanath Singh, Triveni Tiwari and Gangaram for their help in cyclostyling.

G.C. Das

CONTENTS

        2.2 Theoretical Model   24

            2.2.1 Determination of electrostatic
                  stretching force, F_{el} 25
            2.2.2 Determination of excess surface
                  tension force, F_s 28
            2.2.3 Determination of critical electric
                  field   29
            2.2.4 Solution of one dimensional heat
                  equation   31
            2.2.5 Numerical solution   32
            2.2.6 Dependence of melting point on
                  particle size   34
            2.2.7 Relation of computed fields to
                  bulk field   38

        2.3 Results and Discussions   39

3   CURRENT-VOLTAGE CHARACTERISTICS OF VANADIUM
        PHOSPHATE GLASSES CONTAINING BISMUTH GRANULES   50

        3.1 Introduction   50

        3.2 Theoretical Consideration   50

            3.2.1 Calculation of I-V characteristics
                  in the negative resistance region   50
            3.2.2 Numerical scheme for I-V computation   56
            3.2.3 Relaxation of temperature   57
            3.2.4 Numerical solution   59

        3.3 Experimental   63

            3.3.1 Preparation of glass   63
            3.3.2 Sample preparation   63
            3.3.3 Differential thermal analysis(DTA)   64
            3.3.4 X-ray analysis   64
            3.3.5 Electron microscopic analysis   65
            3.3.6 Electrical measurement   66

        3.4 Results and Discussions   70

            3.4.1 Switching characteristics of thin
                  samples   70
            3.4.2 Switching characteristics of thick
                  samples   77
            3.4.3 Temperature dependent memory state
                  resistance variation   90

LIST OF TABLES

LIST OF FIGURES

Figure No.   Page

SYNOPSIS

1. Name of Student   : GOPES CHANDRA DAS

2. Programme   : Ph.D.

3. Department   : Materials Science Programme
                            Indian Institute of Technology
                            Kanpur, India

4. Title of Thesis   : MEMORY SWITCHING AND OPTICAL
                            PROPERTIES OF GLASS-METAL
                            MICROCOMPOSITES

5. Thesis Supervisor   : Professor D. Chakravorty

Glass-metal microcomposites consist of a glass phase containing a distribution of metallic particles having dimensions of the order of a few hundred angstroms. These materials are extensively used in photosensitive glasses, photosensitively nucleated glass-ceramics, photochromic glasses, photothermal conversion, solar coatings etc. Recently memory switching properties have been found in certain oxide glasses containing bismuth particles of a few hundred angstroms dimension. In this thesis a detailed theoretical model has been developed to explain the various features of this switching. Also the optical absorption characteristics of these materials have been delineated over a range of frequency spectrum and the results are explained on the basis of various theoretical models.

Chapter 1 gives a brief literature survey on research in glass-metal microcomposites.

Chapter 2 deals with the theoretical model. According to this, a two-stage process sets in when an electric field is applied to the specimen. Firstly, Joule heating raises the sample temperature sufficiently to cause the metallic granules to melt. Subsequently, the electric field stretches the molten granules against the surface tension force and at the threshold field, the granules touch each other thereby causing the material to switch to the "on" state. A one dimensional heat equation has been solved numerically to find the electrical field necessary to raise the temperature to the effective melting point of bismuth particles. However, the critical field necessary to stretch the molten granules so that they touch each other is found to be larger than the previous one and hence determines the overall switching field. The values of the latter for different particle diameters and separation to diameter ratios have been calculated. These compare reasonably well with experimental data obtained in the cases of silicate and vanadium phosphate glasses containing bismuth particles.

In Chapter 3, the voltage-current characteristics of vanadium phosphate glasses containing bismuth granules especially in the negative resistance region have been computed using the model developed in Chapter 2. It is shown that according to the mechanism proposed first a conducting region is formed at the specimen centre due to the metal spheres touching each other. A regenerative process then sets in as a result of increase in the current flow through the specimen ultimately leading to the "on"

state when the percolation of the metal phase in the glass matrix is attained. One dimensional time dependent heat equation has been solved numerically at different instants of time to delineate the corresponding temperature profile within the sample and the concommitant changes in its resistance and the current flow through it. Experimental measurements on well-characterized specimens in the $V_2O_5-P_2O_5-Bi_2O_3$ system have been carried out and the results are compared with the theoretical values. Satisfactory agreement between the two has been obtained It is observed that increase in sample thickness leads to a threshold switching. For a memory switched sample measurement of its resistance in the "on" state as a function of temperature shows that in the range 75°C - 110°C it reverts back to the off state through a voltage controlled negative resistance in the range 0.2 to 0.5 volt. All these have been explained on the basis of the present theory.

In Chapter 4, the kinetics of switching has been investigated by solving numerically fluid flow equations corresponding to the movement of boundaries of the molten granules during the stretching process. Switching time has been measured experimentally by applying electrical pulses on samples in $V_2O_5-P_2O_5-Bi_2O_3$ system at room temperature and monitoring changes in their resistance. Experimental values (in the range 50 - 80 microseconds) are found to be orders of magnitude higher than the theoretical prediction ($\sim 10^{-9}$ second). However, the

switching time computed from the solution of time dependent heat equation is in reasonable agreement with experimental data. It is concluded, therefore, that the kinetics is controlled primarily by the Joule heating step.

In Chapter 5, the optical properties of vanadium phosphate as well as sodium borosilicate glasses containing bismuth granules of dimensions of the order of a few hundred angstroms have been investigated. The microstructures of samples having different compositions and subjected to various reduction treatments have been characterized by transmission electron microscopy. Optical absorption in the visible range has been measured using Carry 17D Spectrophotometer. Vanadium phosphate glasses containing bismuth show an absorption peak around (450 ± 10 nm) while the silicate glasses containing bismuth show two peaks in the ranges 500 nm - 530 nm and 420 nm - 430 nm respectively. The peak position in V_2O_5-P_2O_5-Bi_2O_3 glasses is predicted in fair agreement with experiment by Maxwell-Garnett (MG), Maxwell-Garnett as extended by Polder and Van Santen (MG-PVS) and Bruggeman (BR) effective medium theories with MG theory giving the best fit. In the case of silicate glasses containing bismuth the predicted positions do not agree so well with experimental results. The possibility of a fraction of the metal spheres being present in the form of interconnected metallic chains and/or f.c.c. clusters in the present microcomposites has also been explored. A typical computation has been carried out by using a constrained optimisation technique with some

assumed fractions of spheres, f.c.c. clusters and single strand chains as the optimising parameters. It is observed that in a vanadium phosphate glass containing bismuth quantitative agreement between the computed and experimental α values within an error of 4% over the entire spectral range can be achieved if the metallic phase is assumed to consist of 26% spheres 0.6% single strand chain and 73.6% f.c.c. clusters.

In Chapter 6, the main conclusions drawn on the basis of the entire investigation are summarised.

CHAPTER   1

INTRODUCTION

1.1   Applications of Glass-Metal Microcomposites

Glass-metal microcomposites consist of a glass matrix
with a distribution of metallic particles in the range of a few
hundred angstroms in size. The metallic particles may be preci-
pitated either during melting, controlled cooling of the melt
or during subsequent heattreatment depending on the glass com-
positions and melting conditions. The applications of glass-
metal microcomposites may be broadly classified as follows[1].

1.   Photosensitive glasses

2.   Photosensitively nucleated glass-ceramics

3.   Photochromic glasses

4.   Polychromatic glasses

5.   Photothermal conversion (cermet)

6.   Solar control coatings (electro float process)

Some of the other possible applications will be :

1.   Electro-conducting glasses and fibres

2.   Memory switching

3.   High strength glasses and fibres

A brief review of the present state of research of the glass-
metal microcomposites is presented in the following sections.

1.2 Photosensitive Glasses

In photosensitive glasses, metallic granules of colloidal dimensions are precipitated by subjecting the glass to certain heattreatment schedules. The precipitation is greatly enhanced if the glasses are exposed to UV radiation prior to heattreatment[2].

Weyl[3] considers that copper, silver and gold may be present in glass in true solution and they get precipitated either by controlled cooling of the molten glass or by subsequent heating of the same. The relative proportions of ions (Cu^+, Ag^+ and Au^{3+}) and the corresponding metallic atoms depend on the melting condition and the composition of the glass. When the molten glass is quickly cooled the high temperature state is retained and the glass remains colourless. The glass strikes the colour when it is subjected to a heattreatment. The mechanisms involved are as follows. During heattreatment the reducing agents, e.g., SnO, As_2O_3, Sb_2O_3 etc. get oxidised after reducing suitable ions in the melt to their metallic counterparts. These metal atoms along with those which are already present in the matrix nucleate and grow to colloidal dimensions. These metallic granules are responsible for the selective absorption of light and so colour is developed. In this connection, it should be mentioned that platinum in the form of colloidal dispersion has not been used as colourant, because this leads to greyish tint. However, the importance of

colloidal platinum is that it can be used as a nucleation catalyst to prepare glass-ceramics. In contrast to copper, silver and gold no heattreatment is necessary to form colloidal platinum[4]. The platinic chloride which is usually added as the source of platinum breaks during melting to form platinum colloids in the melt.

The earliest photosensitive glasses contain copper as the photosensitive element. In later development it has been shown that silver and gold can also act as photosensitive elements. A range of photosensitive glass compositions containing these elements have been worked out by Stookey[5]. The fundamental mechanism of the photosensitive process involves two steps. The glass is first irradiated selectively by placing a photographic negative to form the latent image. This is achieved by reducing the ions to their atomic states as follows :

$$Cu^+ + e \rightarrow Cu^o \tag{1.1}$$

The electron necessary for this reduction reaction is obtained by photo-assisted oxidation of Cu^+ to Cu^{2+} ions, according to the following reaction,

$$Cu^+ + h\nu \rightarrow Cu^{2+} + e \tag{1.2}$$

The irradiated glass is then subjected to a heattreatment in the temperature range of 500°C-600°C for a suitable period of time. Since the irradiated portion of glass contains more metallic atoms the metallic phase nucleates and grows to give

colour and thus the latent image is developed.

It has been shown by Stookey[6] that inclusion of cerium oxide in the glass batch greatly improves the photosensitivity. This is essentially due to the ease with which electrons are made available by the reaction,

$$Ce^{3+} + h\nu \rightarrow Ce^{4+} + e \qquad (1.3)$$
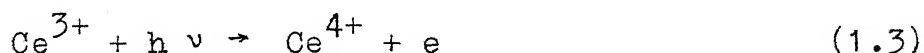
Gold and silver are introduced in the photosensitive glass batches as their chlorides. The glass batches are melted in oxidising condition. The amount of silver present is equivalent to 0.05% of 0.3% AgCl, while the concentration of gold varies in the range of 0.01% to 0.1%. On the other hand glasses containing 0.05 to 1.0% of copper (calculated as Cu_2O) as photosensitive element are melted in reducing atmosphere. The glasses contain small amount of Sb_2O_3 (about 0.1%) along with cerium oxide. The beneficial effects of Sb_2O_3 lie in the fact that it provides electrons by being oxidised to Sb^{5+} ionic state.

1.3 Photosensitively Nucleated Glass-Ceramics

The process of photosensitively nucleated glass-ceramics involves three steps. Firstly, the chilled glass is exposed to UV radiation so that the formation of metal atoms takes place. Secondly, the glass is heattreated to a temperature which depends on the system used, for a certain period of time so that submicroscopic metallic particles get precipitated by a process of

nucleation and growth. Lastly, the glass is further heated to higher temperatures when the metallic granules act as heterogeneous sites for controlled crystallisation of glass. This is one of the early methods of producing glass-ceramics.

Stookey[7] has studied many glasses of the $Li_2O-Al_2O_3-SiO_2$ system. These glasses contain either gold in the range of 0.001% to 0.003% or copper in the range of 0.001% to 1.0% (computed as Cu_2O) or 0.001% to 0.3% of silver (calculated as AgCl). The glasses are exposed to UV radiation followed by heattreatment at 500°-540°C and subsequently heattreated at temperatures around 950°C to produce the glass-ceramics. These materials have good mechanical strength and electrical properties. In a later development it has been shown by Stookey et al.[8] that there is a minimum size of metal namely 80 Å below which they cannot act as nucleation catalysts to crystallise lithium metasilicate. Rindone[4] has studied the use of metallic platinum as heterogeneous nucleation catalyst to crystallise lithium silicate glasses. It has been demonstrated that an optimum amount of platinum (0.004% to 0.007% at 600°C) is needed to get maximum crystallisation. It has been shown that there is an optimum radiation dose necessary for the photosensitively nucleated gold containing lithium aluminosilicate glass-ceramics to attain the maximum mechanical strength[2].

1.4 Photochromic Glasses

When photochromic glasses are exposed to sunlight they

darken and fade when the light is removed. This is a reversible process. A similar process called solarisation has been known for many years. In contrast to photochromic glasses the latter are sensitive to high energy electromagnetic radiation. Recently, Araujo[9] has reviewed different aspects of photochromic glasses.

Armistead et al.[10] have developed alkali aluminoborosilicate system which has perhaps been .. most thoroughly studied. The other systems investigated are alkali and alkali earth borates[11], heavy metal aluminoborates[12] to name a few. The silver halide crystal which gets precipitated, induces photochromic properties. The mechanism involved is believed to be quite analogous to that operative in photographic films. When the photochromic glass is irradiated with light silver halide is decomposed into silver and halogen. Unlike the photographic film, the liberated halogen is trapped into close proximity of silver due to the rigidity and impermeability of glass. When light is removed the silver and the halogen atoms recombine and revert to transparent colourless silver halide crystals. The reversible reaction, which causes darkening and fading of photochromic glasses can be represented as follows[13] :

$$AgX \underset{h\nu_2}{\overset{h\nu_1}{\rightleftarrows}} Ag^0 + X^0 \qquad\qquad (1.4)$$
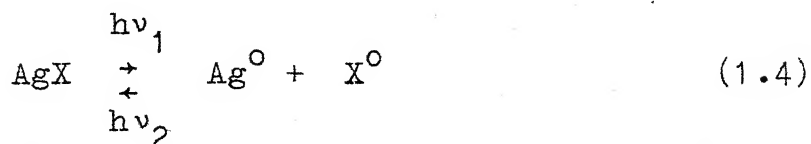
In many photochromic glasses, the absorption band is found near 500 nm and this is attributed to colloidal silver by Moriya[14].

Seward[15] suggests that ellipsoidal silver particles are res-
ponsible for optical absorption in the visible range. The
theoretical model explaining the behaviour of photochromic
glasses can be found in a review article by Araujo[9].

If the glass is cooled very rapidly from molten state,
photochromic property is not developed because no silver halide
particles are precipitated. To develop photochromism a sub-
sequent heattreatment is necessary. There is an optimum range
of silver halide particle size, namely 80-150 $\mathring{A}$. If the
particles are smaller than the lower limit the glasses do not
darken at all. On the other hand if the particles are larger
than the upper limit the glasses become hazy. Since the
increase of subsequent heattreatment temperature increases the
particle size usually silver halide containing photochromic
glasses are heattreated in the temperature range of 400°-800°C
for 15 minutes to 4 hours[9]. After the precipitation of silver
halide particles, further low temperature heattreatments have
profound influence on photochromic properties[16,17]. The combined
influence of compositions and different heattreatment tempera-
ture for different periods of time of some glasses in the alkali
aluminoborosilicate system has been studied by Hares et al.[18].
It indicates the importance of base glass compositions and
thermal history on the darkening and fading characteristics of
the photochromic glasses. Gliemeroth[19] has discussed the

properties of photochromic glasses as a function of temperature and radiation dose. This is important from the point of view of applications in different weather conditions. The presence of copper in small amount ($\sim$ 0.02%) increases the darkening sensitivity very effectively[13] as it augments the production of neutral silver atoms according to the reaction,

$$Ag^+ + Cu^+ \underset{h\nu_2}{\overset{h\nu_1}{\rightleftarrows}} Ag^O + Cu^{2+} \qquad (1.5)$$
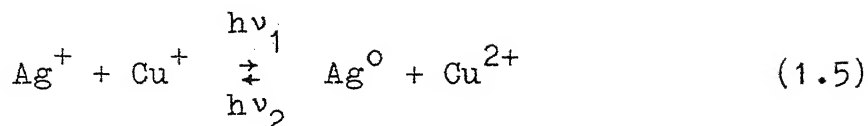
Similarly the presence of cadmium only in presence of copper[20] enhances the darkening sensitivity. Along with the composition as mentioned earlier, the melting conditions can affect the photochromic properties as they strongly influence the retention of halide and oxidation states of copper and silver in the glass melt.

We have, so far, discussed the photochromic glasses containing the silver halide particles. However, highly reduced homogeneous alkali silicate glasses[21], $CdO-B_2O_3-SiO_2$ glasses[22], $Na_2O.Al_2O_3.2SiO_2.1/2NaX$[23] (X being chloride or sulfide) glasses show photochromic behaviour also. Glasses containing suspension of crystallites-hackmanite, silver molybdate[24], thallium chloride[25] and copper cadmium halides[20] show photochromism.

The thermally darkenable photochromic glass (TDPC) is quite different from the usual photochromic glasses. Unlike the latter the TDPC glasses are dark at room temperature and become darker with further heating. When exposed to visible

light the glasses bleach to colourless state at a rate dependent on the intensity of light. On removing the source of light the TDPC glasses returns to darkened state at a temperature dependent rate. Seward III[26] has described the TDPC properties of lanthanum borate based glasses containing copper doped silver halide crystals. The composition ranges of these lanthanum borate glasses can be found in the patent literature[27].

Seward III[26] has observed high temperature bistable optical states of TDPC glasses. When the glasses are heated in the temperature range of 400°-450°C, they are bleached to a colourless state. When the temperature is lowered to the range of 300°-350°C, they spontaneously go to a darkened state and do not bleach despite the presence of intense light. These two bistable states are believed to arise due to melting and precipitation of silver halide crystals[28].

The proposed mechanism of TDPC glasses is the precipitation of colloidal silver from the molten silver halide droplet of nonstoichiometric composition during the crystallisation of the latter. Copper may act as either Cu^+ hole trap or Cu^{2+} electron trap and may take part in the optical bleaching or the thermal darkening. On the other hand its only role may be the controlling of oxidation states and hence producing more neutral silver atoms required for the precipitation of colloidal silver from molten halide droplets.

1.5 Polychromatic Glasses

The polychromatic glasses are a special kind of photo-sensitive glasses. A variety of colours can be generated by the application of controlled thermo-optical treatments.

The sequence of steps involved to form the polychromatic glass is as follows[29]. Firstly, the glass is exposed to UV radiation to precipitate the small silver particles and this is assisted by the presence of Ce^{3+} photosensitisers. In the second step the glass is subjected to a heattreatment such that the silver particles act as heterogeneous sites for the nucleation and growth of sodium halide microcrystals. It has been shown by Stookey[30] that the sodium halide crystals have cubic base with different degrees of pyramidal protrusion. A second UV exposure followed by heattreatment serves to produce silver at the tips of the sodium halide crystals. The amount of silver is related to the type of colour generation[30,31].

The colour which is obtained is primarily a function of the first UV exposure. A strong UV exposure produces a large number of silver particles and hence a large number of sodium halide crystals is precipitated as a result. The second UV exposure produces a relatively fixed amount of silver. This amount of silver is then distributed over the tips of the crystals. So, if the number of sodium halide crystals is less it produces longer and larger specks (higher aspect ratio) compared to the case when the number of crystals is large. This aspect ratio

controls the generation of colour in polychromatic glasses.

1.6 Photothermal Conversion

The efficiency of photothermal conversion of selective black absorbers can be increased by increasing the absorptivity over the solar radiation spectrum and by decreasing the infrared emissivity. In principle this can be obtained in a single material. However most of the selective black absorbers now available is produced by depositing a thin film of metal-dielectric composite which is transparent in the infrared range but highly absorbing in the visible range, on a metal substrate which has low infrared emissivity. The commonly used photothermal conversion materials are electroplated Ni-black, Cu-black on metal sheets. The operating temperature required for photothermal conversion may vary from 400°C - 1000°C. However, the Ni-black and Cu-black are not stable above 200°C while Cr-black is not much stable above 200°C. The MgO/Au[32] cermet film has been produced by rf sputtering on metallic sheet. It has excellent solar absorptivity viz., over 0.9 and its infrared emissivity is less than 0.1. With Mo metal sheet the selective black absorber is stable upto 400°C. The Cr_2O_3/Cr[33] rf sputtered film on metal has solar absorptivity and infrared emissivity similar to MgO/Au cermet film. Its behaviour remains essentially unchanged even after heating at 300°C for 60 hours. The co-sputtered Ni/Al_2O_3[34] cermet film on metal has also similar absorptivity and emissivity but it is thermally more

stable (stable upto 500°C) as compared to other films. Recently, Niklasson et al.[35] have shown by detailed optical study on evaporated nickel particles that these are stable upto 600°C in air without lossing their selectivity. This makes the use of nickel grains very useful for photothermal conversion of solar energy.

1.7 Electrofloat Glasses

Electrofloat process involves the electric field induced ion-exchange of alkali containing glasses, one of the ion-exchange species being copper. The ion-exchanged glass is then subjected to a reduction treatment to precipitate the metallic particles. This process has been developed by Pilkingtons to produce the solar control coating.

1.8 Electro-conducting Glasses

1.8.1 Metallic regime

A number of methods has been developed to obtain a highly conducting layer on or within the surface of the glass. These can be divided under two broad catagories. In the first, the layer is simply applied on to the surface of the glass. Platinum, gold[36] or copper salts are heated to reduction on the surface, metals are vaporised on to the surface[37], silver oxides and metal powders are fired on with the help of auxiliary fluxes and lacquers containing suspensions of flaky metals[38] are applied. The second catagory involves techniques

whereby various glasses containing lead oxide and other metal oxides are reduced in hydrogen gas to induce a conducting layer within the glass surface[39,40].

Some alkali containing silicate glasses develop high surface conductivity[41,42] when they are subjected to an ion-exchange treatment followed by reduction. The process involves the dipping of the glass in molten silver nitrate at about 300°C for certain period of time so that alkali silver ion-exchange takes place. Then the glass is reduced in hydrogen gas in the temperature range of 250°C to 400°C so that silver metal atoms nucleate and grow to form the interconnected chains of metal and hence a highly conducting layer is induced within the surface of the glass. This is confirmed by electron micro-structural analysis. The surface resistance is typically in the range of 0.15 $\Omega/\square$ to 4.1 $\Omega/\square$ depending on temperature and duration of the reduction treatment. It is found that prior to the thermo-chemical treatment it is necessary to make the glass surface sufficiently rough by grinding with 120 mesh silicon carbide powder to induce highly conducting layer. It is believed that the rough surface provides the potential sites for silver metal to nucleate and grow during the reduction treatment. It has been shown recently[43] that the ceramised CaO-SiO_2-Na_2O-Bi_2O_3 systems develop high surface conductivity when they are ion-exchanged in molten silver nitrate followed by reduction in hydrogen gas. The typical surface resistance varies in the range

of 0.08 $\Omega/\square$ to 14.76 $\Omega/\square$ depending on the compositions and reduction temperature and time. The glass-crystal interface of the partially crystallised glass provides the potential sites for the silver metals to nucleate and grow during reduction treatment. Hence, surface roughness is not necessary in this process of generating highly conducting layer.

1.8.2 Dielectric regime

When oxide glass systems containing metals are melted under ordinary or reducing conditions, they develop a micro-structure very similar to that of cermet films produced by sputtering or evaporation. Mixtures of oxides in the $V_2O_5-P_2O_5$ system containing Ag_2O or Bi_2O_3[44], $Na_2O-B_2O_3-SiO_2$ system containing Bi_2O_3 or pure selenium[45] and $PbO-B_2O_3$ system[46] containing Bi_2O_3 when melted and cooled rapidly induce preci-pitation of metallic granules of silver, bismuth or selenium in the corresponding glass matrix. The precipitated phases have been confirmed by selected area electron diffraction. The particle size found by electron microstructural analysis is of the order of a few hundred angstroms. Compared to base glasses the metal containing glasses show a decrease in resistivity. These glasses containing a distribution of metallic particles show semiconducting behaviour. From the temperature dependent conductivity measurements it has been concluded that the mechanism involved is the tunnelling of electrons between conducting metallic islands[45,47].

The borosilicate system[48] containing Bi_2O_3 and/or Ag_2O have been melted in a reducing condition. Fibres have been drawn from single hole bushing made of pure Al_2O_3[49], at a fiberising temperature of around 1100°C. The fibres are found to have a microstructure consisting of bismuth and/or silver metallic particles of sizes ranging from 100 to 500 Å, dispersed in the glass phase. The conductivity is electronic in nature and the mechanism is found to be electron tunnelling between the conducting metallic species similar to what has been observed in the case of bulk glass-metal microcomposites.

1.9 Memory Switching

In certain amorphous systems, when an applied electric field to the sample crosses a certain critical value the sample goes from a high resistance state to a low resistance state. This phenomenon is known as switching. There are two types of switching - threshold and memory. When the applied electric field is removed the threshold switch reverts back to the off-state. On the other hand the memory switch remains in the on-state even after the removal of the electric field. Alkali borosilicate glasses containing bismuth oxide when subjected to ion-exchange in molten silver nitrate followed by a reduction in hydrogen are found to have microstructures consisting of metallic particles distributed in a glassy matrix. This system[50] is found to exhibit memory switching with a reduction of resistance of six orders of magnitude when the applied electric field

crosses the critical value of 30 V/cm. When a 5-volt pulse of 10 msec. duration is applied to the sample it goes from the off to the on-state. However, on application of a 50-volt pulse of 10 μ sec. duration the sample switches back to the off-state. These glasses have been evaporated in a vacuum of 10^{-5} torr on to alumina substrates to form thin films of a few micron thickness. Such films[51] also show memory switching. When the sample in the on-state is heated above a temperature (around the melting point of bismuth metal) it reverts from the on to the off-state. Recently, V_2O_5-P_2O_5 glasses[44] containing metallic bismuth or silver have been reported to show memory switching. The memory switching action has been explained on the basis of a particle stretching model.

1.10 High Strength Glasses and Fibres

Alkali borosilicate glass fibres[48] containing bismuth and/or silver are found to have higher strength compared to those drawn from the base glass composition. However, the improvement is small. This increase in strength is believed to arise due to the deflection of cracks along the glass-metal interface during the course of crack propagation[52]. All fibres containing metallic silver particles are found to have higher Young's modulii compared to the base glass fibres. This arises due to a higher modulus of silver. SiO_2-B_2O_3-K_2O-Al_2O_3-As_2O_3[53] glasses containing silver are found to have higher rupture modulii as obtained from the three point bending measurement compared to base glasses.

Similarly alkali aluminoborosilicate glasses[54] containing bismuth have higher rupture modulii and Young's modulii compared to base glasses.

1.11 Present Work

Memory switching observed in silicate and vanadium phosphate glasses containing metallic granules of bismuth has been qualitatively explained as due to the stretching of these particles under the action of an electric field. The objectives of the present thesis are the following :

1. To develop a detailed model to explain quantitatively the memory action in oxide glasses containing microgranules of metallic bismuth, specifically to calculate the threshold field as a function of different microstructural parameters.

2. To compute the current-voltage characteristics of these systems using this model especially in the negative resistance region.

3. To estimate the switching time for different microstructural configurations.

4. To carry out suitable experimental measurements to test the validity of the model.

5(a) To undertake detailed optical characterization of these glass-metal composites.

(b) To apply the different models of inhomogeneous media to explain the optical absorption data.

CHAPTER 2[*]

PARTICLE STRETCHING MODEL AND THRESHOLD FIELD IN
VANADIUM PHOSPHATE AND SILICATE GLASSES
CONTAINING BISMUTH GRANULES

2.1 Introduction

Preliminary reports on switching in chalcogenide glasses first appeared in the literature nearly two decades ago[55,56]. Ovshinsky's paper[57] in 1968 described the prototype of a reliable potential device and subsequently extensive theoretical and experimental investigation have been undertaken in various laboratories to understand the phenomenon. The switch described by Ovshinsky is a sputtered film of a typical thickness of about 1 μm sandwitched between two metal or graphite electrodes. The material used is an amorphous semiconductor with an activation energy ~ 0.5 eV and optical band gap ~ 1.0 eV[58]. The physical properties of these materials have since been widely discussed in literature[59-66].

Switching can be of two types - threshold and memory. Figures 2.1(a) and 2.1(b) show the schematic representations of I-V characteristics of a threshold and a memory switch respectively. Both of these switches go from a high resistance state (off-state) to a low resistance state (on-state) via

---

[*] A paper based on this work has been published in J.Appl.Phys. <u>51</u>, 3896 (1980).
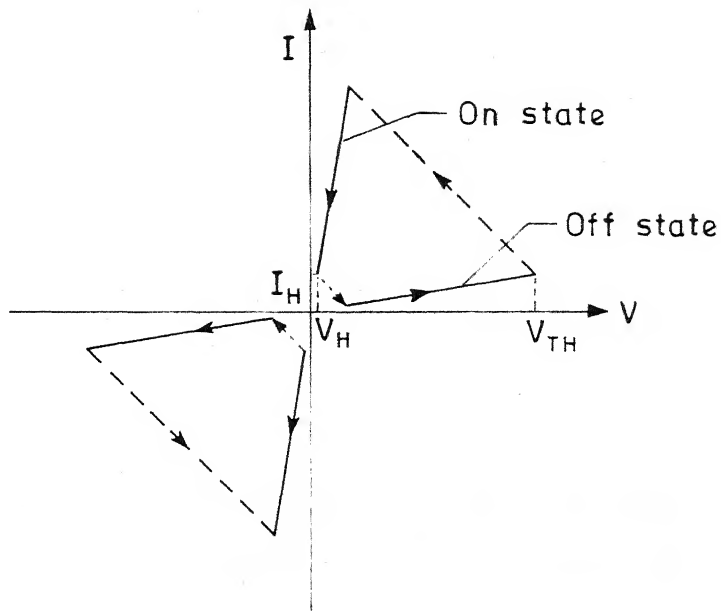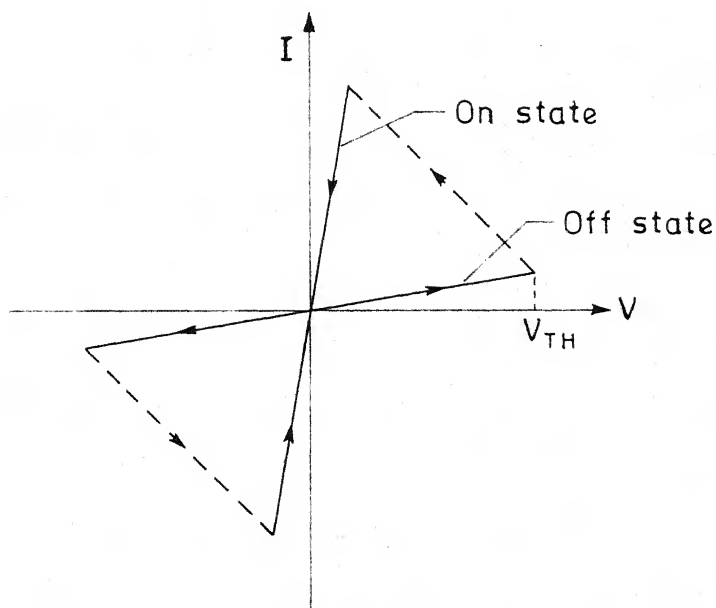
Fig. 2.1 Schematic representations of I-V characteristics of (a) threshold (b) memory switch.

negative resistance when the applied electric field crosses a critical value. This is denoted as V_{TH} in figure 2.1. In contrast to the threshold switch, a memory switch remains in the on-state even after the removal of the applied field. However, a minimum holding current I_H is required to retain the on-state of the threshold switch. When the applied field is removed, the threshold switch returns to the off-state. A strong electrical pulse with short duration is required to bring the memory switch from the on-state to the off-state.

Whether a chalcogenide glass exhibits threshold or memory switching is primarily determined by its composition[67]. A typical threshold composition is $As_{30}Te_{48}Si_{12}Ge_{10}$ (the so-called STAG glass)[57]. Usually most of the memory compositions are close to $Ge_{15}Te_{81}X_4$ (X being As,S,Sb etc. or a combination[68,69]). The composition dependent switching characteristics of chalcogenide glasses can be understood qualitatively from their glass forming ability. The glass forming regions in the two ternary systems Ge-Te-As and Si-Te-As have been experimentally determined[70,71]. From these Owen et al.[67] have delineated the glass forming region of four component system, Ge-As-Te-Si by interpolation. It is reported that the so-called STAG glass falls at the centre of the glass forming region and hence the STAG glasses are resistant to crystallisation. On the otherhand the memory glass composition $Ge_{15}Te_{81}As_4$ falls near the edge of the glass forming boundary. So they easily get crystallised

above the glass transformation temperature (T_g) but at the
same time can be quenched quickly from molten state to form
glass. Thus the choice of memory composition should be a
balance between the ease of crystallisation above T_g and
tendency to glass formation. The threshold composition
should be such that it makes the glassy state as stable as
possible.

Two types of theories - thermal and electronic have
been proposed to explain the switching behaviour. The classi-
fication depends on whether the on-state is achieved by heating
(thermal model) or by non-equilibrium enhancement of carriers
(electronic model). In the thermal model, the application of
voltage across the sample causes the temperature to rise to a
critical value due to Joule heating. After a certain time when
the critical temperature is exceeded no stable temperature
distribution is possible and any fluctuation causes the tem-
perature to rise very fast until an upper limit, set by the
external circuit resistance, is reached[72]. The result is the
formation of the hot conducting channel in the on-state and the
associated negative resistance state prior to switching.
Earlier investigations on thermal instability have been reported
by Lueder et al.[73] and Ridley[74]. Recently, many
authors[67,72,75-80] have applied the thermal model to explain
the threshold switching characteristics. Some authors[67,79,80]
have also incorporated the field dependent conductivity along

with the temperature dependence to explain the switching characteristics in chalcogenide glasses.

According to the thermal model, the system returns to the off-state when the slope of I-V characteristics of the sample is equal to that determined by the load line of the circuit. Therefore, depending on the value of the external resistance the cut-off points should vary. Indeed this is observed by Hughes et al.[81]. The sample studied is a thick film. On the other hand Esquda et al.[82] have observed no matching of slopes for thin samples. A system where switching is possibly caused by the thermal mechanism is the vanadate glass system studied by Higgins et al.[83]. The switching in these glasses is attributed to a metal-insulator transition at $68^{o}C$.

The electronic model was first proposed by Mott[84] and Henisch[85]. The theory states that in the on-state sufficient double injection of carriers takes place to ensure the presence of degenerate electron and hole gas. The carrier density is $\sim 10^{18}$/c.c. and the Fermi energy of both carriers lies on the extended side of the respective mobility edge[86]. Thus the potential drop across the sample is small and obviously the holding voltage is slightly greater than the mobility gap. A number of authors[87-92,58] have used the electronic model to explain the chalcogenide switching characteristics.

To maintain the high density of electron and hole gas in the on-state, the supply of carriers should be there to

balance the loss of carriers by recombination and by diffusion out of the glass sample. Thus the minimum holding current represents the condition when the replacement of carriers fails to balance the loss and so the switch changes from the on-state to the off-state[58].

In memory switching the on-state is induced by the precipitation of the conducting crystals in the glass system. Ovshinsky et al.[93] have shown that strong illumination can induce a similar behaviour. Fritzsche et al.[94] have observed by calorimetric measurement that there exists an exothermic peak between 200°-300°C and an endothermic peak at higher temperature for chalcogenide glasses showing memory switching. Therefore it is not entirely clear whether the crystallisation is induced by heating or by a high density of carrier injections[86]. To bring the memory switch from the on-state to the off-state a high amplitude pulse with short duration is applied such that the crystals get melted and quenched to the glassy state.

As described in Section 1.9 of Chapter 1, alkali borosilicate glasses containing bismuth show memory switching after ion-exchange[50] and reduction. It has recently been reported that V_2O_5-P_2O_5 glasses containing bismuth and silver[44] and the evaporated thin films of alkali borosilicate glass containing bismuth[51] show memory switching. The typical switching field is of the order of 10^4 V/cm. Unlike the chalcogenide glasses

where memory switching is explained by crystallisation of glassy phase, the memory switching in glass-metal composite systems[44] has been explained qualitatively on the basis of particle stretching model. The model essentially states that if the metallic particles are in molten condition, the application of an electric field causes the particles to stretch which is being opposed by a surface tension force. Thus a critical electrical field causes the particles to stretch and form interconnected chains thereby forming a low-resistance on-state. So, in this chapter we shall develop this model to predict quantitatively the critical field for switching in the glass-metal micro-particulate system mentioned above.

2.2 Theoretical Model

When an electric field $\vec{E}$ is applied to a dielectric matrix containing uniformly distributed metallic particles, the field induces opposite charges on the surface of the conducting species. If these metallic particles are in a molten state, two forces acting opposite to each other are operative. One is the coulombic attraction arising between two oppositely charged neighbouring metallic grains. This attraction force tends to stretch the molten metallic granules. The other is the surface tension force which opposes the stretching force[95]. Therefore, depending on the magnitude of the applied field an equilibrium will be reached when the two forces balance each other. The threshold field then corresponds to the situation when two

neighbouring grains touch each other. We assume that the
metallic particles are spherical in shape in accordance with
the experimental observation. Further we make the following
assumptions for the simplicity of calculation :

1) The electric field is uniform throughout the matrix and
   is normal to the electrodes.

2) When the molten sphere is stretched it becomes ellipsoidal
   with major axis forming the axis of revolution.

2.2.1 Determination of electrostatic stretching force, F_{el}

To find the expression for the electrostatic force (F_{el})
between the two polarised ellipsoids due to the presence of an
electric field $\vec{E}$, the left hand ellipsoid is displaced by δx
in the negative direction of x-axis as shown in figure 2.2.
The work done against F_{el} is given by

$$\delta w = F_{el} \, \delta x . \tag{2.1}$$

This work is equal to the electrostatic energy stored in the
volume (δv) swept by the ellipsoid. Since electrostatic energy
density is given by $\frac{1}{2}\varepsilon\varepsilon_o E^2$,

$$F_{el}\delta x = \frac{1}{2}\varepsilon\varepsilon_o E^2 \delta v \tag{2.2}$$

where ε and ε_o are the relative dielectric permittivity of the
glass-metal composite and the dielectric permittivity of free-
space respectively.
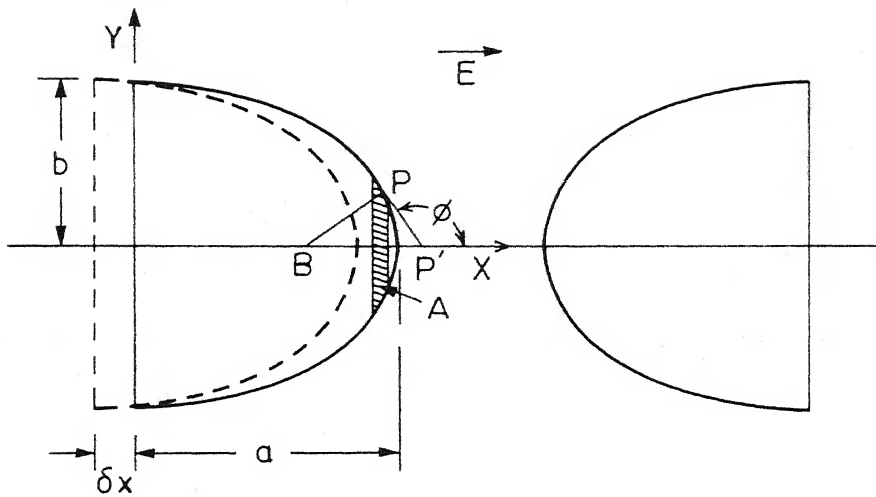
Fig. 2.2   Two metallic ellipsoids in an electric field.

2.2.1.1 Determination of volume δv

Let us consider an elemental circular strip of area dA at the point A in figure 2.2. The area dA is given by

$$dA = 2\pi y \sqrt{1 + y'^2} \, dx .$$ (2.3)

Due to the movement of strip by δx the volume (dv) is given by

$$dv = dA \, \vec{n} \cdot \vec{i} \, \delta x$$ (2.4)

where $\vec{n}$ and $\vec{i}$ are the unit normal vector and unit vector along the x axis respectively.

For an ellipsoid with major axis as the axis of revolution $\vec{n}$ is given by

$$\vec{n} = (\vec{i} \, \frac{x}{a^2} + \vec{j} \, \frac{y}{b^2} + \vec{k} \, \frac{z}{b^2}) / \sqrt{\frac{x^2}{a^4} + \frac{1}{b^2}(1 - \frac{x^2}{a^2})}$$ (2.5)

where, a and b are respectively the semi-major and semi-minor axes of the ellipse respectively.

Substituting dA and $\vec{n}$ respectively from equations (2.3) and (2.5) in equation (2.4) and then integrating the resulting expression from x = o to x = a, we get δv as follows :

$$\delta v = \pi b^2 \delta x$$ (2.6)

Substituting equation (2.6) in equation (2.2) and simplifying, we get,

$$F_{el} = \tfrac{1}{2}\pi\varepsilon\varepsilon_0 E^2 b^2 \qquad (2.7)$$

2.2.2 Determination of excess surface tension force F_s

A curved surface is characterised by two radii of curvature R_1 and R_2 which are given by the expressions,

$$1/R_1 = -y'' / (1+y'^2)^{3/2} \qquad (2.8)$$

$$1/R_2 = 1/[y(1+y'^2)^{\tfrac{1}{2}}] . \qquad (2.9)$$

The excess pressure (ΔP) at point P on the ellipsoid (Fig. 2.2) is given by[96],

$$\Delta P = \gamma(\frac{1}{R_1} + \frac{1}{R_2}) \qquad (2.10)$$

where γ is the surface tension of molten metallic particle.

The component of force along the x-axis acting on a circular strip passing through P is therefore given by

$$dF = \Delta P \ dA \ \vec{n}.\vec{i} . \qquad (2.11)$$

After substituting R_1 and R_2 from equations (2.8) and (2.9) respectively in equation (2.10), the resulting ΔP and dA and $\vec{n}$ respectively from equations (2.3) and (2.5) are substituted in the equation (2.11). Then integrating the resulting expression from $x = o$ to $x = a$, we get the excess force F_s along the x-axis given by

$$F_s = 2\pi\gamma b . \qquad (2.12)$$

2.2.3 Determination of critical electric field

Figure 2.3 represents the situation when two grains of identical radius r are stretched into ellipsoidal shapes under the application of an electric field. The net surface tension force acting in a direction opposite to electrostatic force is given by

$$F_{ns} = 2\pi\gamma(r-b) \; . \tag{2.13}$$

At equilibrium the electrostatic force F_{el} and the net surface tension force (F_{ns}) must balance. Hence,

$$\tfrac{1}{2}\pi\varepsilon\varepsilon_o E^2 b^2 = 2\pi\gamma(r-b) \tag{2.14}$$

Assuming that the volume of the particle remains unchanged after stretching, it can be shown that

$$b^2 = r^3/a \tag{2.15}$$

From figure 2.3 it can be shown that

$$a = r + (s_o - s)/2 \tag{2.16}$$

Using equations (2.15) and (2.16) we get from equation (2.14) after simplification,

$$E^2 = \frac{4\gamma}{\varepsilon\varepsilon_o} \left[r - \left(\frac{r^3}{r+(s_o-s)/2} \right)^{\frac{1}{2}} \right] \cdot \left[\frac{r^3}{r+(s_o-s)/2} \right]^{-1} \tag{2.17}$$

The critical field (or switching field) E_m is defined as the field for which the two ellipsoidal particles touch each other in equilibrium. So by putting s = o in expression (2.17), we get the critical field E_m, given by
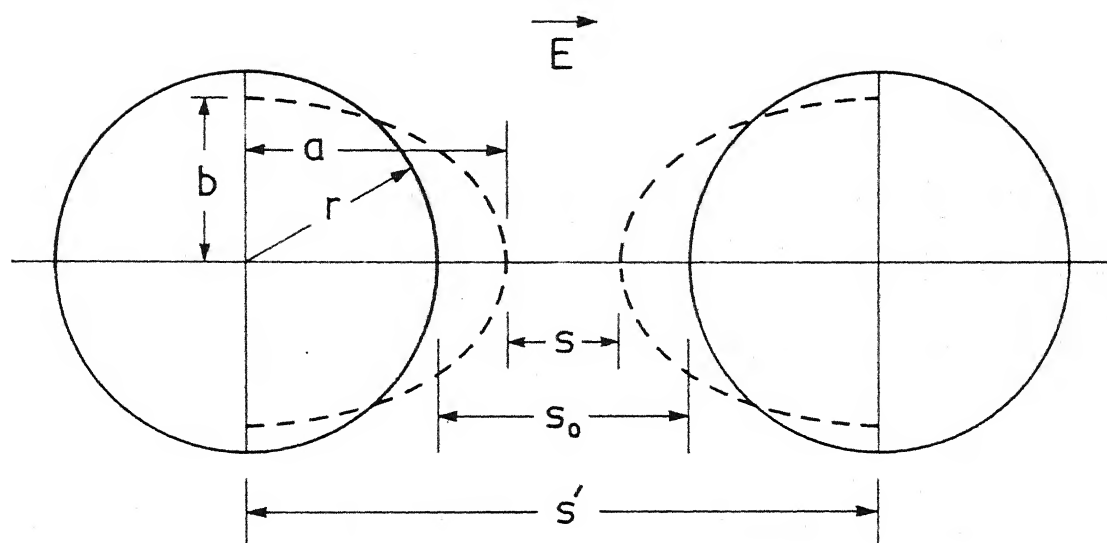
Fig. 2.3 Two metallic grains stretched into ellipsoidal shapes by an electric field.

$$E_m = \{\frac{4\gamma}{\varepsilon\varepsilon_0 r}[(1+\frac{s_0}{2r}) - (1+\frac{s_0}{2r})^{\frac{1}{2}}]\}^{\frac{1}{2}} \qquad (2.18)$$

2.2.4 Solution of one dimensional heat equation

E_m has been derived on the assumption that the metallic particles are in the molten state. In our model the temperature rise of the metallic species is brought about by Joule heating. For delineating the corresponding temperature profile, within the sample we consider the following one dimensional heat equation :

$$\frac{d^2T}{dx^2} = -\frac{\sigma}{\kappa} E^2 \qquad (2.19)$$

where σ be the electrical conductivity and κ is the thermal conductivity and T is the temperature in degree Kelvin.

The boundary conditions are :

$$T = T_{exp} \qquad at \quad x = o,$$

and

$$T = T_{exp} \qquad at \quad x = l$$

where l is the thickness of the sample and T_{exp} is the temperature at which the experiment is carried out[97]. It has been established[45] for the silicate system under consideration that the electrical conduction takes place due to electron tunnelling between the metallic particles. So, we have taken the expression, for high field conductivity[47] as given by

$$\sigma_H = \{\sigma_\infty(T) \exp(-E_0/E) \int_{-E_0/E}^{\infty} dz\, z\} \cdot$$

$$\cdot \{\exp(-z)/[1-\exp(-\frac{z}{z+E_0/E} \cdot \frac{Ec_0}{E_0 kT})]\} \qquad (2.20)$$

where σ_H is the high field conductivity and k is the Boltzmann constant. σ_∞ and E_0 and c_0 are given by,

$$\sigma_\infty = e^2 l' \gamma'/[(s_0'+d_0')^2 (2 \times s_0' + 1)^2 h] \qquad (2.21)$$

$$E_0 = c_0/e(s_0' + d_0') \qquad (2.22)$$

$$c_0 = x s E_c^0 (1 + \frac{1}{2 \times s_0}) \qquad (2.23)$$

where l' be the recombination length, γ' be the geometric factor, s_0' be the most probable separation between the two metallic grains of diameter d_0', e be the electric charge, x is a constant, h is the Planck's constant, s be the separation between the two metallic granules and E_c^0 is the energy required to generate a pair of fully dissociated positively and negatively charged metallic grains.

For V_2O_5-P_2O_5 glass system the temperature dependent conductivity has been taken as[44],

$$\sigma = \sigma_0 \exp(-\varphi/kT) \qquad (2.24)$$

where φ is the activation energy.

The heat equation (2.19) is nonlinear and no analytical solution is available. Therefore, it has been solved numerically.

2.2.5 Numerical solution

Equation (2.19) has been normalised, by putting $y = x/l$ as follows :

$$\frac{d^2 T}{dy^2} = - \frac{l^2}{\kappa} \sigma E^2 \qquad (2.25)$$

The boundary conditions in this case become

$$T = T_{exp} \quad \text{at} \quad y = o$$

and

$$T = T_{exp} \quad \text{at} \quad y = 1 \; .$$

Fourth order Runge-Kutta-Nyström[98] method has been used to solve equation (2.25). The normalised length has been divided into 10 equal parts with a step length h' = 0.1. To use the Runge-Kutta-Nyström method for second order differential equation, it is necessary to know the functional value and the first derivative at the same point. Since, in our case, we know only the functional values but not the first derivative, so to start with a trial value of slope at the boundary has been assumed. In the case of silicate system, the conductivity expression (2.20) involves the integration and this has been evaluated by using Simpson 1/3 rule[99]. After computing the temperature distribution, we have compared the computed temperature at h' = 1 with the boundary value at h' = o. Depending on whether the computed temperature at h' = 1 is greater or less than the temperature at h = o, the trial value of slope is reduced or increased respectively. This process is continued until we get two slopes in subsequent iterations such that in one case the computed temperature at h' = 1 is greater than the

boundary value and in the other case the temperature at h' = 1 is less than the same. By using Regula-Falsi method, we have computed the temperature distribution, within an error of $\pm 0.1^{\circ}$K. The same technique has been used for a particular value of electric field to find the thickness within ± 0.1 µm error such that the centre of the sample reaches the melting temperature of bismuth. The above scheme has been used to compute the temperature distribution for different combination of particle sizes, particle diameter to separation ratios, electric fields etc. In the computation the appropriate values of κ and ε have been taken from references ([100], [44] and [45]). In the numerical computation of the temperature profile, the effect of particle size on the melting point of bismuth to be described in the following section, has been incorporated. The computer programme written in fortran language is given in Appendix 1.

2.2.6 Dependence of melting point on particle size

It has been observed experimentally[101] that the melting te perature of bismuth particle decreases as the particle size decreases. The implication of this in our model is that the applied electric field necessary to bring the metallic bismuth in the molten condition will be small for smaller particles. So the functional relation between the melting temperature and the particle size has been derived thermodynamically in the following section.

2.2.6.1 Derivation of particle size dependent melting point expression

Let α and β in figure 2.4 denote the solid and the liquid phases respectively under equilibrium at the melting temperature T of the solid phase. In such a case, it can be shown that under constant pressure,

$$(S_\beta - S_\alpha)dT = -(d\mu_\beta - d\mu_\alpha), \qquad (2.26)$$

where S denotes entropy, μ the chemical photential, and the subscripts indicate the phases.

For a transfer of dn_α moles from α to β phase, the Gibbs free energy change at constant temperature and pressure is given by

$$dG\,|_{T,P} = (\mu_\alpha - \mu_\beta)dn_\alpha + \gamma(dA_\alpha + dA_\beta) , \qquad (2.27)$$

where dA_α and dA_β represent the change of surface area in the two phases and γ is the surface energy (we assume that solid-liquid and liquid-matrix interfacial energies have the same value).

For the geometry assumed we can write

$$dA_\alpha = (2/r)\overline{V}_\alpha \, dn_\alpha \qquad (2.28)$$

and

$$dA_\beta = 2\left(\frac{RdR}{R^2dR - r^2dr}\right)\overline{V}_\beta dn_\beta, \qquad (2.29)$$
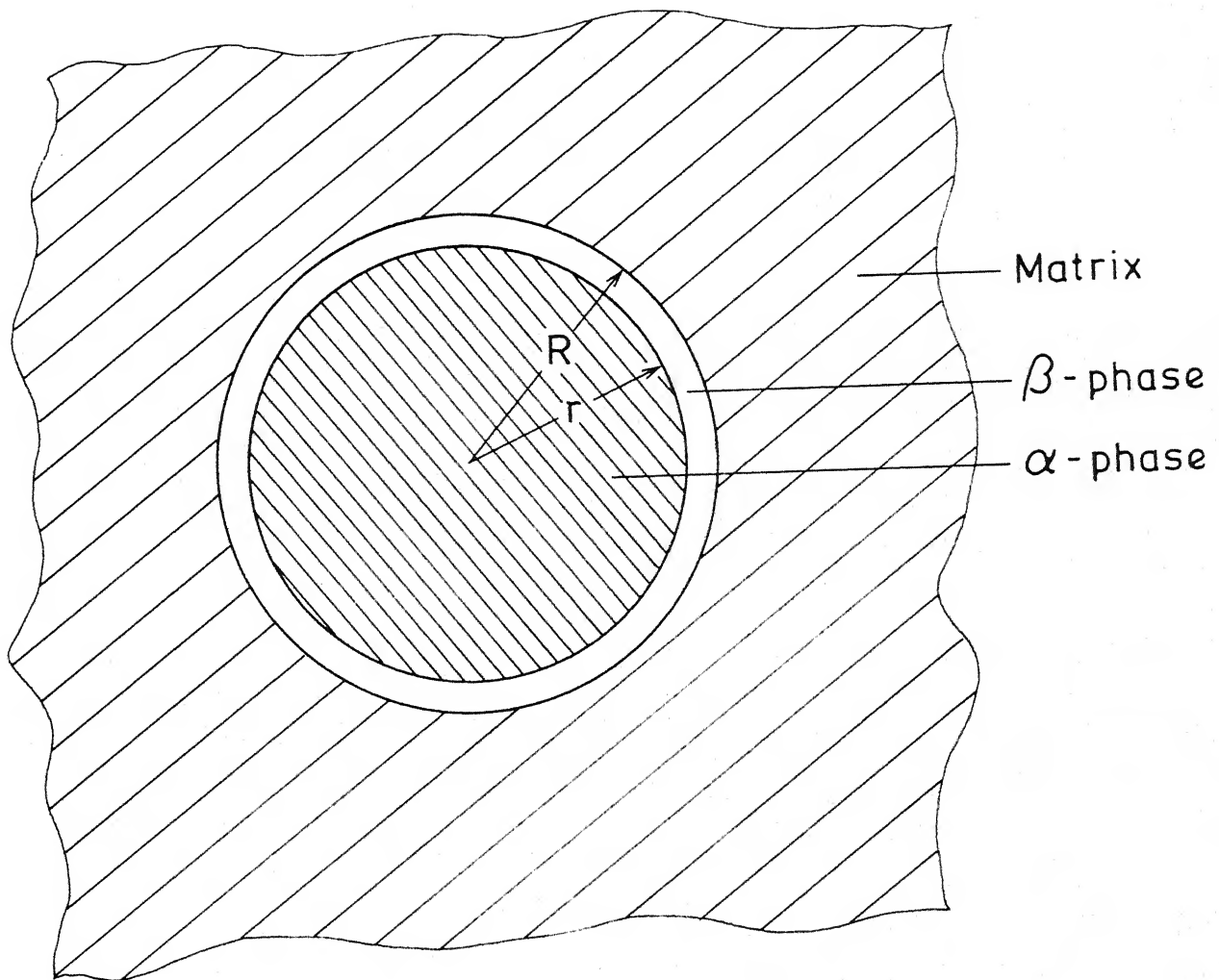
Fig. 2.4 α and β phases in equilibrium within a matrix.

where $\overline{V}_\alpha, \overline{V}_\beta$ are the molar volumes of α and β phases respectively. At the start of melting, we can assume $R \simeq r$ and equation (2.29) then becomes

$$dA_\beta = \frac{2}{r} \left(\frac{dR/dr}{(dR/dr)-1} \right) \overline{V}_\beta dn_\beta. \tag{2.30}$$

We can also write

$$4\pi r^2 dr \overline{V}_\beta / \overline{V}_\alpha = 4\pi R^2 dR, \tag{2.31}$$

where terms on both sides represent the change of volume of the β phase as a result of the transfer of dn_α moles from the solid to the liquid phase. Assuming $R \simeq r$, equation (2.31) simplifies to

$$dR/dr = \overline{V}_\beta / \overline{V}_\alpha. \tag{2.32}$$

Combining equation (2.30) and (2.32) we get

$$dA_\beta = \frac{2}{r} \left(\frac{\overline{V}_\beta^2}{\overline{V}_\beta - \overline{V}_\alpha} \right) dn_\beta. \tag{2.33}$$

Substituting equations (2.28) and (2.33) in equation (2.27) and using the relation $dn_\alpha = -dn_\beta$, we get

$$dG|_{T,P} = (\mu_\alpha - \mu_\beta) dn_\alpha + \frac{2\gamma}{r} \left(\overline{V}_\alpha - \frac{\overline{V}_\beta^2}{\overline{V}_\beta - \overline{V}_\alpha} \right) dn_\alpha. \tag{2.34}$$

At equilibrium, $dG|_{T,P} = 0$. Therefore from equation (2.34) we can write

$$d\mu_\beta - d\mu_\alpha = -\frac{2\gamma}{r^2} \left(\overline{V}_\alpha - \frac{\overline{V}_\beta^2}{\overline{V}_\beta - \overline{V}_\alpha} \right) dr. \tag{2.35}$$

For the transition from α to β phase, we can write

$$\Delta H - T(S_\beta - S_\alpha) = 0 , \qquad (2.36)$$

i.e.,

$$S_\beta - S_\alpha = \Delta H/T ,$$

where ΔH is the molar heat of fusion. From equations (2.26), (2.35) and (2.36) we get,

$$\frac{\Delta H}{T} \, dT = \frac{2\gamma}{r^2} \left(\bar{V}_\alpha - \frac{\bar{V}_\beta^2}{\bar{V}_\beta - \bar{V}_\alpha} \right) dr. \qquad (2.37)$$

Integrating between the limits from T_m (bulk melting point) to T and from $r = \infty$ to r the following expression is obtained :

$$\ln \frac{T}{T_m} = -\frac{2\gamma}{\Delta H} \left(\bar{V}_\alpha - \frac{\bar{V}_\beta^2}{\bar{V}_\beta - \bar{V}_\alpha} \right) \frac{1}{r} . \qquad (2.38)$$

The values for different parameters appearing in equation (2.38) have been taken from references ([102] and [103]).

2.2.7 <u>Relation of computed fields to bulk field</u>

The computed critical fields E_m and E_c are assumed to be related to the fields E_m^b and E_c^b respectively calculated on the basis of thickness by the following expressions,

$$E_m = (1 + d/s_o)E_m^b \qquad (2.39a)$$

$$E_c = (1 + d/s_o)E_c^b \qquad (2.39b)$$

where d and s_o are average particle diameter and inter-particle separation. This is justified because of the large value of $\rho_{glass}/\rho_{metal}$ ratio[47], ρ being resistivity.

2.3 Results and Discussions

Figure 2.5 is the plot of equation (2.38) showing the variation of the melting temperature of bismuth as a function of particle size. It is evident from the figure that the melting temperature decreases with the decrease in the radius of metallic particles. The implication is that for smaller particle sizes, the electric field necessary to reach the melting temperature of bismuth will be reduced.

Figure 2.6 shows a typical temperature profile as obtained by solving one dimensional heat equation (2.19). Open circles in the figure represent the bismuth in silicate system with the radius of bismuth particle 250 $\overset{o}{A}$, $E_c^b = 1.4 \times 10^3$ V/cm and $s_o/d = 0.01$. Closed circles represent bismuth in V_2O_5-P_2O_5 system with radius of bismuth particle 400 $\overset{o}{A}$, $E_c^b = 0.4 \times 10^3$ V/cm and $s_o/d = 0.01$. The calculation is carried out at a temperature around 160^oC so that the theoretically computed critical fields can be compared with the experimental results.

Figures 2.7 and 2.8 represent the bulk critical memory switching field E_m^b (equation 2.39a) as a function of different particle radii and separation to particle diameter ratios for bismuth in the silicate system and V_2O_5-P_2O_5 system respectively.
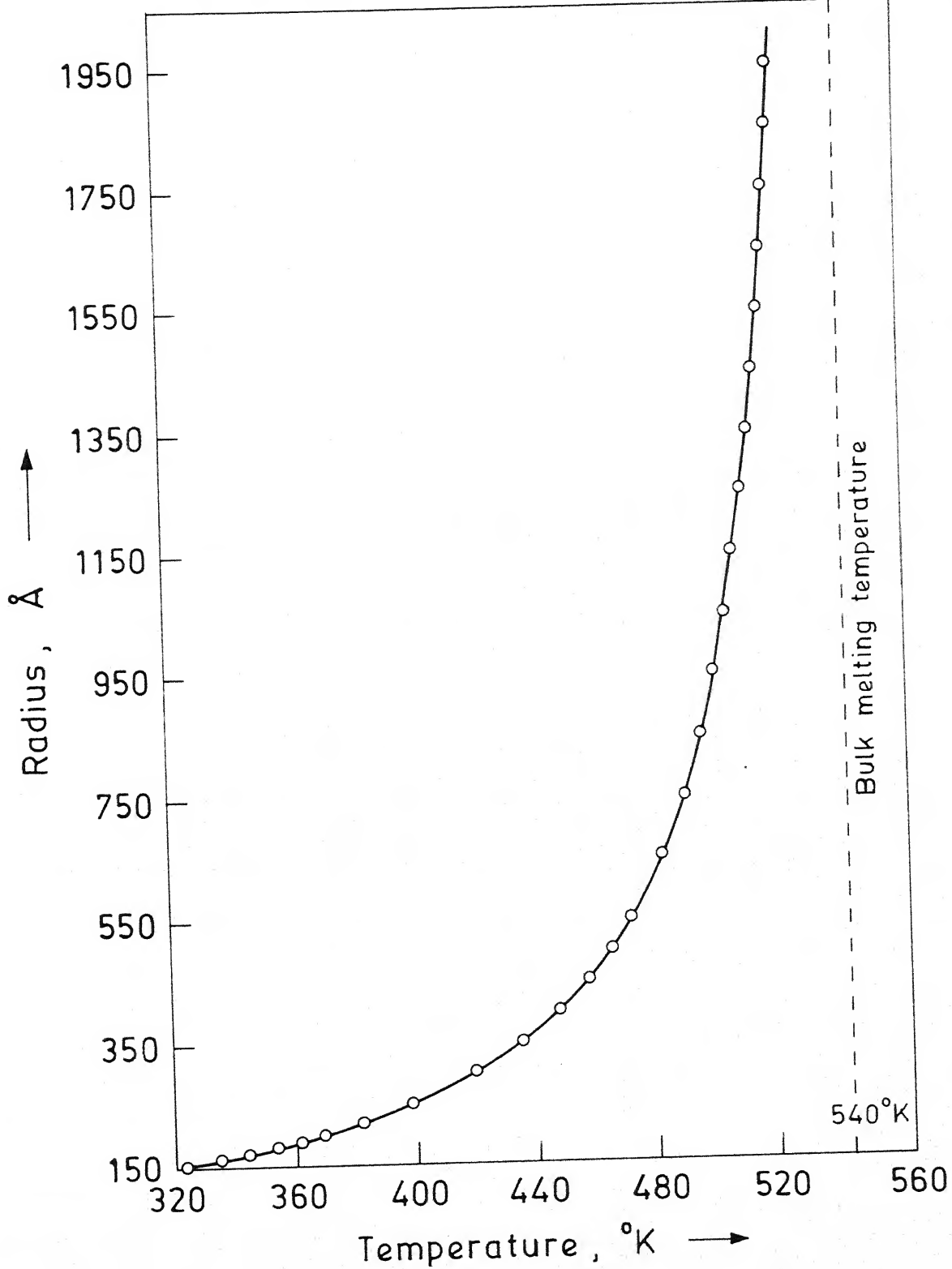
Fig. 2.5 Variation of melting temperature of bismuth metal as a function of particle radius.
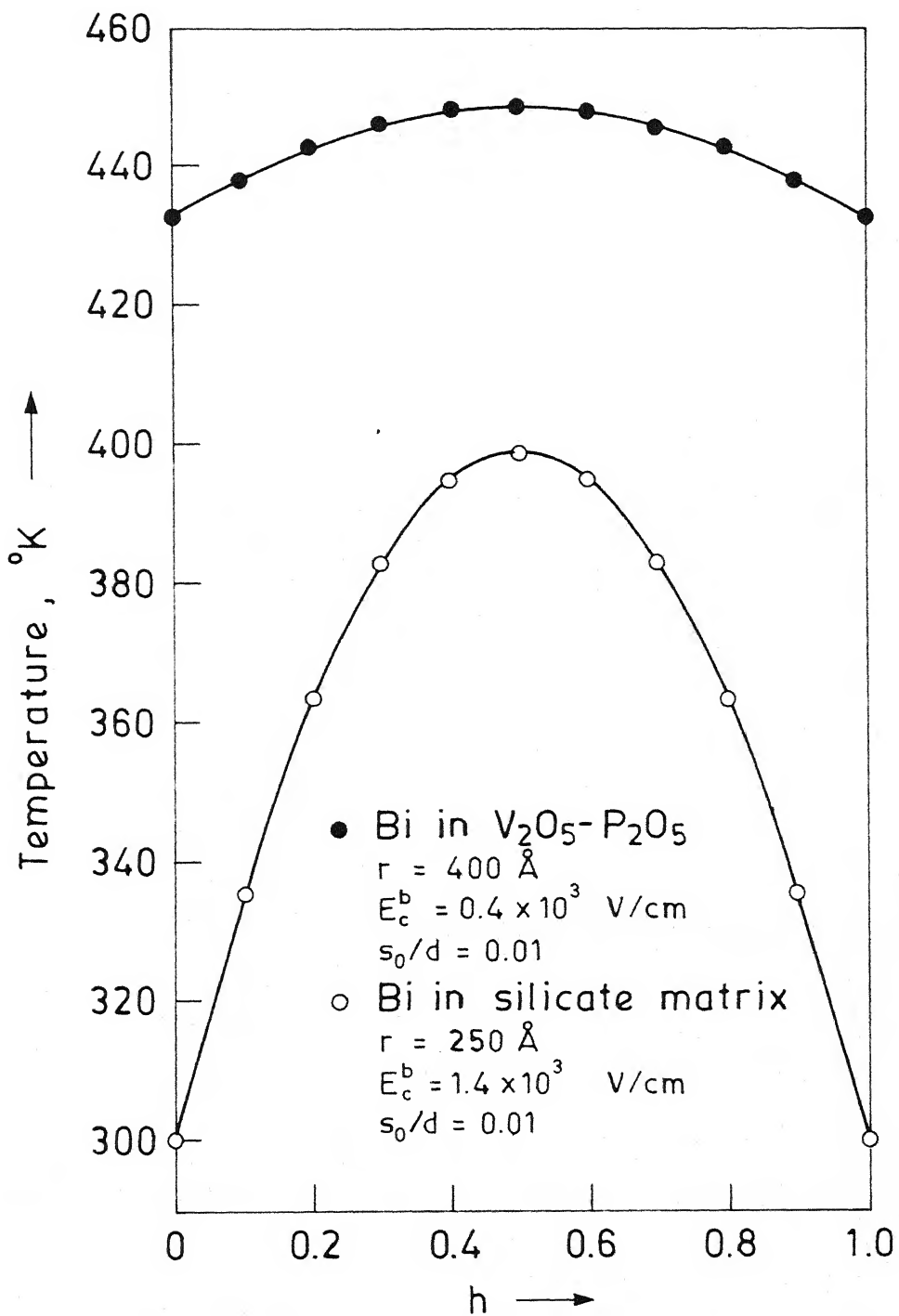
Fig. 2.6 Temperature profile from solution of one
dimensional heat equation in a sample of
thickness 10 μm.
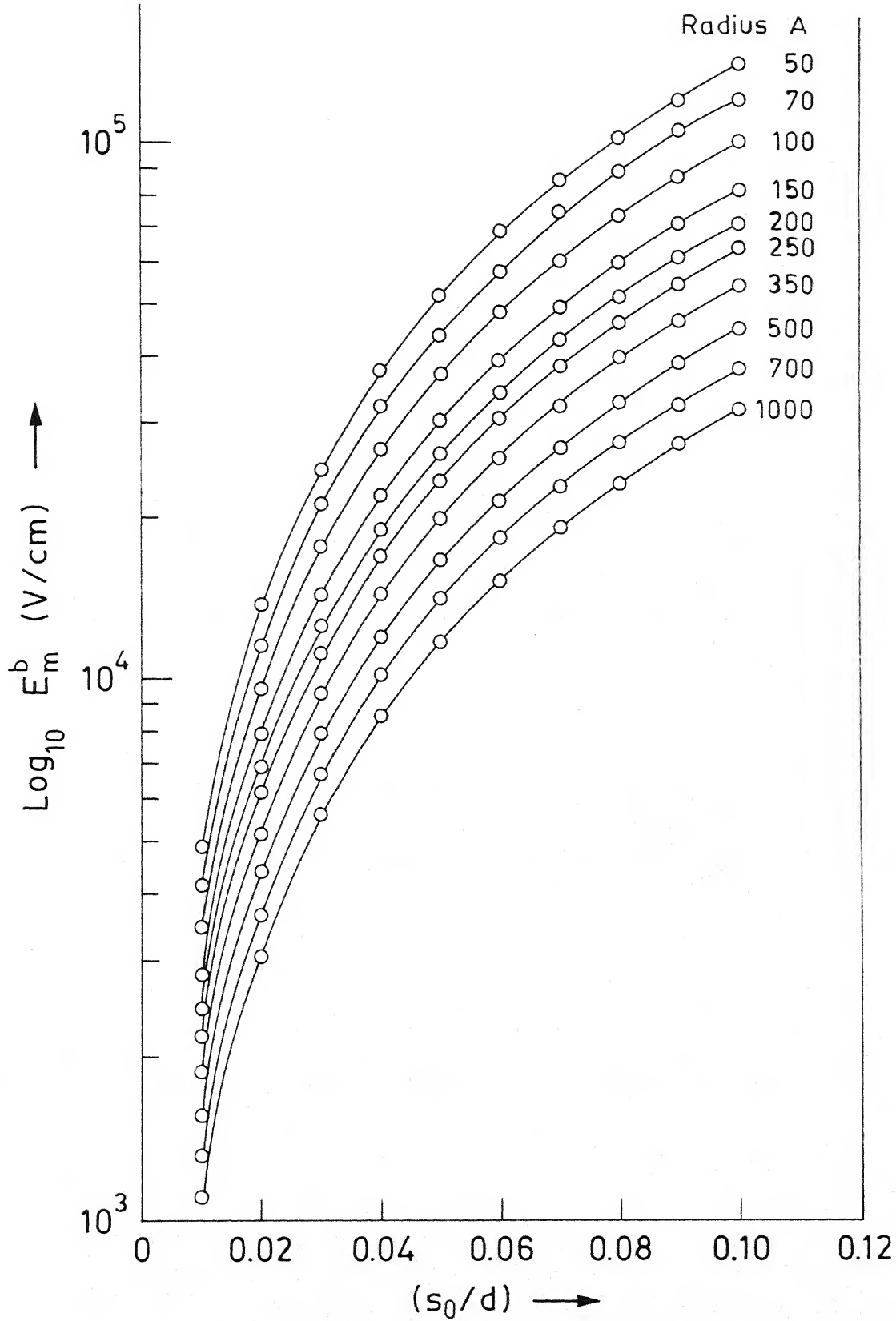
Fig. 2.7 Variation of critical field E_m^b as a function of (s_0/d) for different values of particle radius in silicate glass matrix.
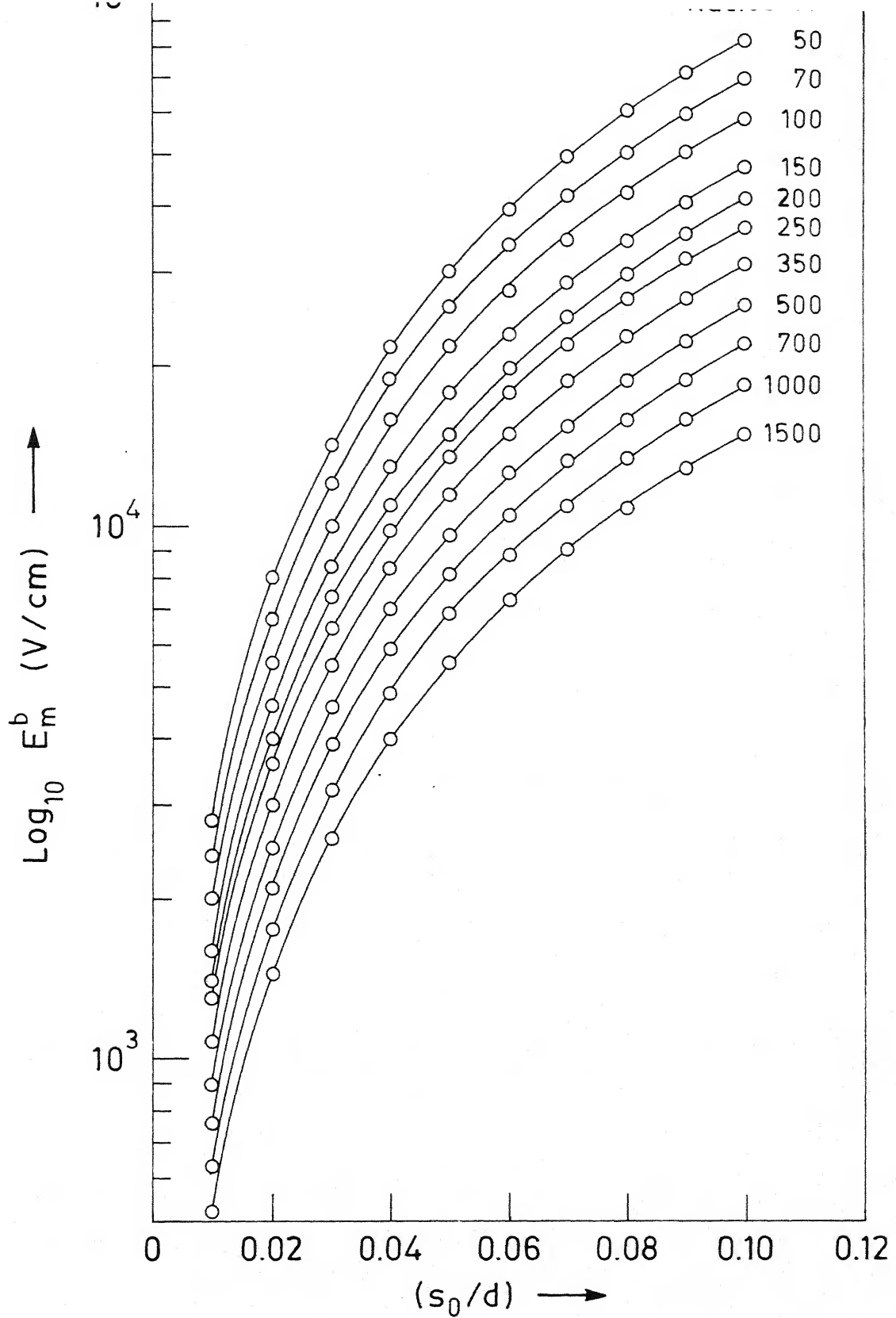
Fig. 2.8 Variation of critical field E_m^b as a function of (s_0/d) for different values of particle radius in $V_2O_5-P_2O_5$ glass matrix.

It is evident from figure 2.7 that the threshold field in silicate system varies over two orders of magnitude (10^3 - 10^5 V/cm) for a particular value of particle radius as the s_o/d varies from 0.01 to 0.1. Similarly for vanadium phosphate glass (figure 2.8) the threshold field varies over two orders of magnitude (10^2 - 10^4 V/cm) as s_o/d varies from 0.01 to 0.1. In table 2.1 values of critical field E_c^b for melting the metallic bismuth and field E_m^b needed for memory action are compared for different values of particle radii and separation to diameter (s_o/d) ratios for a sample of thickness 10 μm. It is observed that for parameters which can be realised in practice, the E_m^b is in general greater than E_c^b. It is, therefore, concluded that the threshold field for the systems under investigation will essentially be controlled by E_m^b.

In table 2.2 the threshold field values predicted by the present model are compared with the experimental results reported to-date for some silicate and vanadium phosphate glasses containing metallic bismuth. It is seen that the computed critical electric fields are of the same order of magnitude as observed experimentally. The agreement between these values are reasonable considering that we have made a number of simplifying assumptions in our analysis.

Table 2.1 Critical fields for melting (E_c^b) and memory action (E_m^b) in glass matrix containing bismuth granules

| Particle Radius in Å | s_o/d | Specimen thickness = 10 μm | | | |
| | | E_c^b(V/cm)×10⁻³ | | E_m^b(V/cm)×10⁻³ | |
		SiO_2-B_2O_3 Matrix	V_2O_5-P_2O_5 Matrix	SiO_2-B_2O_3 Matrix	V_2O_5-P_2O_5 Matrix
150	0.01	0.7		2.8	1.6
	0.03	2.1		14.5	8.4
	0.05	3.4		30.7	17.7
	0.07	4.5		50.0	28.8
	0.09	6.4		71.7	41.4
200	0.01	1.2		2.5	1.4
	0.03	3.4		12.6	7.2
	0.05	5.7		26.6	15.3
	0.07	8.0		43.3	25.0
	0.09	10.4		62.1	35.8
250	0.01	1.4		2.2	1.3
	0.03	4.1		11.2	6.5
	0.05	7.3		23.8	13.7
	0.07	9.5		38.7	22.3
	0.09	12.2		55.5	32.0

300	0.01	1.5		2.0	1.2
	0.03	4.5		10.3	5.9
	0.05	7.4		21.7	12.5
	0.07	10.4		35.3	20.4
	0.09	13.4		50.7	28.3
350	0.01	1.6	0.2	1.9	1.1
	0.03	4.8	0.6	9.5	5.5
	0.05	7.9	1.0	20.1	11.6
	0.07	11.0	1.3	32.7	18.9
	0.09	15.0	1.7	46.9	27.1
400	0.01	1.7	0.4	1.7	1.0
	0.03	5.0	1.2	8.9	5.1
	0.05	8.2	2.0	18.8	10.8
	0.07	11.5	2.7	30.6	17.7
	0.09	15.2	3.4	43.9	25.3
450	0.01	1.7	0.5	1.6	1.0
	0.03	5.1	1.4	8.4	4.8
	0.05	8.4	2.4	17.7	10.2
	0.07	11.9	3.3	28.8	16.7
	0.09	15.8	4.2	41.4	23.9

500	0.01	1.8	0.6	1.6	0.9
	0.03	5.3	1.6	7.9	4.6
	0.05	8.6	2.6	16.8	9.7
	0.07	12.3	3.6	27.4	15.8
	0.09	16.2	4.6	39.3	22.7
550	0.01	1.8	0.6	1.5	0.9
	0.03	5.4	1.7	7.6	4.4
	0.05	8.8	2.8	46.0	9.2
	0.07	12.6	3.8	26.1	15.1
	0.09	16.5	4.8	37.4	21.6
600	0.01	1.8	0.6	1.4	0.8
	0.03	5.5	1.8	7.3	4.2
	0.05	9.0	2.9	15.3	8.9
	0.07	12.8	4.0	25.0	14.4
	0.09	16.8	5.0	35.8	20.7
650	0.01	1.9	0.6	1.4	0.8
	0.03	5.5	1.8	7.0	4.0
	0.05	9.1	2.9	14.7	8.5
	0.07	13.0	4.0	24.0	13.9
	0.09	17.0	5.1	34.4	19.9

700	0.01	1.9	0.6	1.3	0.8
	0.03	5.6	1.8	6.7	3.9
	0.05	9.3	3.0	14.2	8.2
	0.07	13.1	4.1	23.1	13.4
	0.09	17.2	5.2	33.2	19.2
750	0.01	1.9	0.6	1.3	0.7
	0.03	5.6	1.9	6.5	3.7
	0.05	9.4	3.0	13.7	7.9
	0.07	13.2	4.2	22.3	12.9
	0.09	17.3	5.3	32.1	18.5

Table 2.2   Comparison of theoretical and experimental switching fields

Glass Composition (mole %)	Maximum Diameter Å	E_m^b/Exp (V/cm)	E_m^b/Calc (V/cm)
$64SiO_2, 18\ B_2O_3$	500	1.2×10^4	$1.1 \times 10^4 (s_o/d = 0.03)$
$8\ Bi_2O_3, 10\ Na_2O$			$2.4 \times 10^4 (s_o/d = 0.05)$
			$3.9 \times 10^4 (s_o/d = 0.07)$
			$5.6 \times 10^4 (s_o/d = 0.09)$
$80V_2O_5, 15P_2O_5$	800	4.0×10^3	$1.0 \times 10^3 (s_o/d = 0.01)$
$5\ Bi_2O_3$			$2.8 \times 10^3 (s_o/d = 0.02)$
			$5.1 \times 10^3 (s_o/d = 0.03)$
			$7.8 \times 10^3 (s_o/d = 0.04)$

CHAPTER 3

CURRENT-VOLTAGE CHARACTERISTICS OF VANADIUM PHOSPHATE
GLASSES CONTAINING BISMUTH GRANULES

3.1 Introduction

In Chapter 2, the threshold field for memory switching has been calculated in the case of glasses containing microgranules of bismuth dispersed in them. The I-V characteristics of the present systems of glass-metal composites show negative resistance region[44,51]. In the present chapter, the particle stretching model which has been developed in Chapter 2 has been used to compute the I-V characteristics of vanadium phosphate glasses containing bismuth, especially in the negative resistance region prior to the on-state as a function of particle diameters and particle separation to diameter ratios. The effect of specimen thickness on switching behaviour has been delineated both theoretically and experimentally. Also, the effect of temperature on the resistance of the samples in the memory state has been studied.

3.2 Theoretical Consideration

3.2.1 Calculation of I-V characteristics in the negative resistance region

The threshold field as calculated in Chapter 2 for memory action corresponds to the beginning of the negative resistance

region in the I-V plot of the glass-metal composite. According
to the present model, initially within a portion of the sample
at the centre where the temperature attains the value corres-
ponding to the melting point of bismuth, elongated metal grains
touch each other and thereby form a highly conducting region.
Due to higher current flow more heat is generated and the
conductive region grows from centre outwards. Such a regenera-
tive process results in negative resistance characteristics and
ultimately the system attains the highly conducting on-state.

For calculating the current-voltage (I-V) values in the
negative resistance region we consider in figure 3.1 the
situation within the specimen at some instant of time after
the application of the critical switching field. In this
figure l_m indicates the width of the conducting region
(referred to as metallic **region in subsequent discussion**) where
molten granular metal particles are interconnected and l_d
represents the overall width of the remaining portion (referred
to as dielectric region in subsequent discussion) of the sample.
The resistance R_m of the metallic region **is given by,**

$$R_m = \rho_m \frac{l_m}{A} \tag{3.1}$$

where ρ_m is the resistivity of the specimen in the on-state.
Experimentally observed ρ_m in the on-state has been used in the
present analysis. A is the electrode area of the specimen.
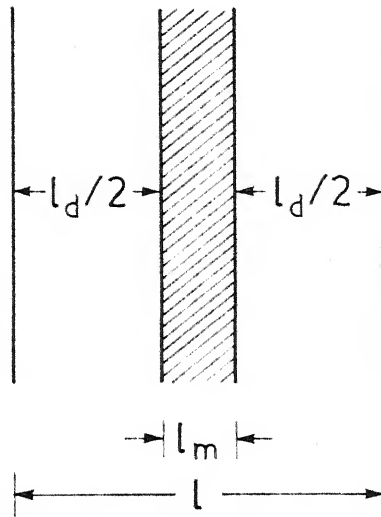
Fig. 3.1　Schematic representation of a glass-
metal composite after the application
of a critical field .
l_m : width of metallic region
l_d : width of dielectric region

Since resistivity of the glass-metal particulate system is dependent on temperature, to find the resistance of the dielectric region one has to take into account the temperature profile within the sample after the application of the critical electric field. The dielectric region has been divided into n equal parts each of width w so that the resistance R_d of this region is given by

$$R_d = \frac{w}{A} \sum_{i=1}^{n} \rho_{T_i} \qquad (3.2)$$

where ρ_{T_i} denotes the resistivity of ith strip having a mean temperature T_i and

$$w = l_d/n \qquad (3.3)$$

In our calculation we have chosen n suitably such that at every step of metallic region formation, the value of w is kept constant. The temperature distribution in the sample has been obtained by solving the time-dependent heat equation to be described in the following section. The resistivity has been evaluated from the equation (2.24) in Chapter 2. The pre-exponential factor and the activation energy have been obtained from experimental data of the present vanadium phosphate system containing bismuth[44].

If the current passing through the circuit consisting of the sample and the series resistance R_s ohms be denoted by I_s amperes, we can write,

$$I_s = \frac{V_{app}}{R_m + R_d + R_s} \qquad (3.4)$$

and

$$V_s = I_s(R_m + R_d) \qquad (3.5)$$

where V_{app} is the applied voltage across the circuit.

For delineating the temperature profile within the sample, the rate of heat generation per unit volume needs to be evaluated. The latter is given by $\sigma_d E^2$, where σ_d is the conductivity of the specimen and E the electric field. However, after the onset of switching, in the present model, the sample consists of two regions viz. metallic and dielectric. The average values of field and conductivity to be used for computing the rate of heat generation per unit volume are therefore obtained as follows :

We can assume that after the coalescence of neighbouring metal granules near the specimen centre, the potential drop in the dielectric region occurs only in the glass matrix intervening the particles[47]. With this assumption, the effective field E_{eff}^d is then given by

$$E_{eff}^d = \frac{I_s R_d(s_o + d)}{l_d s_o} \qquad (3.6)$$

where, s_o is the average interparticle separation and d the average diameter of metal particles.

Substituting I_s and R_d respectively from equations (3.4) and (3.2) in equation (3.6) we get,

$$E^d_{eff} = \frac{V_{app}(1 + (d/s_o)) \frac{W}{A} \sum\limits_{i=1}^{n} \rho_{T_i}}{(R_m + R_s + \frac{W}{A} \sum\limits_{i=1}^{n} \rho_{T_i}) l_d} \qquad (3.7)$$

Similarly, the effective field, E^m_{eff} in the metallic region is given by,

$$E^m_{eff} = \frac{I_s R_m}{l_m} \qquad (3.8)$$

From equations (3.1), (3.4) and (3.8) we can write,

$$E^m_{eff} = \frac{V_{app} \rho_m}{(R_s + R_s + \frac{W}{A} \sum\limits_{i=1}^{n} \rho_{T_i}) A} \qquad (3.9)$$

The average electric field E_{av} in the glass-metal particulate system at any time after the onset of switching is then given by,

$$E_{av} = (l_d E^d_{eff} + l_m E^m_{eff})/l \qquad (3.10)$$

The average conductivity σ_{av} is given by,

$$\frac{1}{\sigma_{av}} = (\frac{l_d}{\sigma_d} + \frac{l_m}{\sigma_m}) \frac{1}{l} \qquad (3.11)$$

where σ_d and σ_m refer to the conductivities of the dielectric and the metallic region respectively.

The present analysis has been carried out with the applied field which corresponds to the critical field for memory action E_m given by the expression (2.18) in Chapter 2. E_m is related to the bulk field E_b, calculated on the basis of sample thickness by,

$$E_m = (1 + d/s_o)E_b \qquad (3.12)$$

where

$$E_b = V_{app}/l \qquad (3.13)$$

From equations (3.12), (3.13) and equation (2.18) of Chapter (2). We get

$$V_{app} = (\frac{1}{1+d/s_o}) \{ \frac{4\gamma}{\varepsilon\varepsilon_o r} [(1+ \frac{s_o}{2r}) - (1+ \frac{s_o}{2r})^{\frac{1}{2}}] \}^{\frac{1}{2}} \qquad (3.14)$$

In the above expression, $\varepsilon, \varepsilon_o, \gamma, r$ have the same meaning as given in Chapter 2. To find the expression for V_{app}, the voltage applied to the circuit, we have neglected the potential drop across the resistance in series with the sample. This is because of the fact that the magnitude of series resistance is orders of magnitude less than that of the sample in the off-state.

3.2.2 Numerical scheme for I-V computation

The normalised thickness is divided into ten equal parts and the grid points are denoted by 1,2, ..., 11 respectively. First of all the resistance of the sample is calculated from equation (3.2) corresponding to ambient temperature. From equations (3.4), (3.5) and (3.14) the potential drop and the current passing through the sample are then evaluated. These correspond to the starting point of the negative resistance region. In our calculation, we have neglected the temperature rise, due to Joule heating in the pre-switching region. The

time-dependent heat equation is then solved numerically to find

a temperature distribution such that the sample centre (grid

point 6) has attained the melting temperature of bismuth

corresponding to the average particle size (equation (2.38),

Chapter 2). Solution is then carried out corresponding to the

time when the grid points 5 and 7 reach the melting temperature

of bismuth. The molten particles in the region lying between

the grid points 7 and 5 will be stretched forming the metallic

region, because the electric field has the critical value.

Values of R_m and R_d are then calculated corresponding to this

state from equations (3.1) and (3.2) respectively. Substituting

these in equations (3.4) and (3.5) the I_s and V_s values are

calculated. The values of E_{av} and σ_{av} are then estimated from

equations (3.10) and (3.11) respectively, which are then used

in the next step of the computation. This procedure is

repeated and I_s, V_s values are found at every step till we

come to the one which involves the pair of grid points 2 and

10 respectively. The latter give the last but one point in

the negative resistance region. The final point corresponds

to the situation when the entire sample forms the metallic

region thereby attaining the on-state.

3.2.3 Relaxation of temperature

To explain the threshold switching behaviour of the thick

sample, as we shall see later, it is necessary to calculate the

time required for the temperature at the centre of the sample

to go below the melting point of bismuth after the applied
electric field is reduced to zero. The relaxation time (τ)
is defined as the time which elapses after the removal of the
electric field for the on-state temperature at the centre of
the sample to attain the melting temperature of bismuth. The
decay of temperature distribution in a rectangular slab after
normalisation with respect to thickness is given by,

$$\frac{\partial T}{\partial t} = \frac{\kappa}{\rho' cl^2} \frac{\partial^2 T}{\partial x^2} \qquad (3.15)$$

where κ, ρ' and c respectively denote thermal conductivity,
density and specific heat respectively.

The boundary conditions are :

$$T(o,t) = T(1,t) = 0$$

$$\qquad (3.16)$$

$$T(x,o) = f(x) \text{ for } o \le x \le 1$$

where $f(x)$ is the temperature distribution within the
sample when it attains the on-state.

Solution of equation (3.15) is given by[98]

$$T(x,t) = \sum_{n=1}^{\infty} [B_n e^{-\lambda_n^2 t} \sin(n\pi x)] \qquad (3.17)$$

where, $\quad \lambda_n = \frac{n\pi}{l} (\frac{\kappa}{\rho' c})^{\frac{1}{2}} \qquad (3.18)$

and

$$B_n = 2 \int_0^1 f(x) \sin(n\pi x) dx \qquad (3.19)$$

The solution of equation (3.17) has been worked out numerically, since only numerical values of temperature distribution function f(x) are known in the on-state.

3.2.4 Numerical solution

3.2.4.1 Numerical solution of time dependent heat equation

The time dependent heat equation which is solved to find the temperature distribution within the sample for computing the I-V characteristics in the negative resistance region is given by

$$\rho' c \ \frac{\partial T}{\partial t^*} = \kappa \frac{\partial^2 T}{\partial y^2} + \sigma(T)E^2 \qquad (3.20)$$

The boundary conditions are :

$$T(y) = T_{exp} \text{ for } o \leq y \leq 1 \quad \text{at } t^* = o$$

$$T(o) = T(1) = T_{exp} \qquad \text{at } t^* > o$$

For ease of numerical computation, the equation (3.20) has been normalised with respect to thickness and for some time t_1 by setting $x = y/1$ and $t = t^*/t_1$ and the normalised equation becomes,

$$\frac{\rho' c}{t_1} \frac{\partial T}{\partial t} = \frac{\kappa}{1^2} \frac{\partial^2 T}{\partial x^2} + \sigma(T)E^2 \qquad (3.21)$$

The boundary conditions become ,

$$T(x) = T_{exp} \text{ for } o \leq x \leq 1 \quad \text{at } t = o$$

$$T(o) = T(1) = T_{exp} \qquad \text{at } t > o$$

For solving equation (3.21) we have used Crank-Nicolson implicit finite difference formula[104]. The advantage of implicit finite difference scheme is that it gives unrestricted stability for p/h^2 ratio[105], where p and h are respectively the step lengths in time and x direction. So we have chosen a step length p = 0.1 and h = 0.1 in our computation.

In Crank-Nicolson implicit formula the time derivative is replaced by forward difference and the second order derivative in the x direction is replaced by a weighted sum of second order central difference at t and t+p. Applying these to equation (3.21), we get after simplification the following finite difference formula at a particular time t,

$$-\frac{\kappa}{2h^2} T_{x-h,t+p} + \left(\frac{l^2 \rho' c}{t_1 p} + \frac{\kappa}{h^2}\right) T_{x,t+p} - \frac{\kappa}{2h^2} T_{x+h,t+p}$$

$$= \frac{\kappa}{2h^2} T_{x-h,t} + \left(\frac{l^2 \rho' c}{t_1 p} - \frac{\kappa}{h^2}\right) T_{x,t} + \frac{\kappa}{2h^2} T_{x+h,t}$$

$$+ l^2 \sigma \left(\frac{T_{x,t+p} + T_{x,t}}{2}\right) E^2 \qquad (3.22)$$

In equation (3.22) the conductivity has been evaluated at a mean temperature of $T_{x,t+p}$ and $T_{x,t}$[104]. Writing equation (3.22) for all the grid points along the x-direction we obtain a (9x9) tridiagonal matrix. For finding the temperature distribution from the above equations the Gauss matrix iteration[99] has been used. It can be shown from the above (9x9) tridiagonal matrix that each diagonal element is greater than the absolute sum of

the corresponding off-diagonal elements. This satisfies the condition for convergence of Gauss iteration scheme.

The following steps are involved to calculate the temperature distribution at different time intervals and to compute the time necessary to reach the melting temperature of bismuth.

Step 1 : A temperature distribution is assumed to start the Gauss iteration. $t = o$ and $p = 0.1$ are set, and a value of t_1 is assumed.

Step 2 : σ is evaluated corresponding to time t.

Step 3 : Temperature distribution is computed using σ as evaluated in step 2.

Step 4 : σ is evaluated at the mean value of temperatures evaluated at time t and the temperatures evaluated in the last iteration.

Step 5 : Temperature distribution is obtained using σ as evaluated in step 4.

Step 6 : Steps 4 and 5 are repeated until the difference of temperature distributions between two successive iterations is less than $0.1^{o}K$. This gives the temperature distribution at time t+p.

Step 7 : $t = t+p$ is set and steps 2 to 6 are repeated till $t = 0.9$.

Step 8 : The difference between the temperature at the centre of the sample and the melting point of bismuth is computed.

Step 9 :   Depending on whether the difference is positive or negative t_1 is decreased or increased.

Step 10:   The value of t_1 in step 1 is replaced by the new value of t_1 of step 9.

Step 11:   Steps 1 to 10 are repeated until we get two values of t_1 such that in one case the difference as evaluated in step 8 is positive and in the other case it is negative.

Step 12:   Using method of bisection new value of t_1 is evaluated and t_1 in step 1 is replaced by this new value of t_1.

Step 13:   Steps 1 to 8 and then step 12 are repeated until the difference as computed in step 8 is within $\pm\ 1^{\circ}K$ and the time which is evaluated in step 12 is the required time.

The programme for the above numerical computation is given in Appendix 2.

3.2.4.2   Numerical solution of temperature relaxation

The coefficient B_n (equation (3.19))has been evaluated by using Simpson 1/3 rule using the numerical values of $f(x)$, the temperature distribution as obtained from the solution of time dependent heat equation for different particle diameters and separation to diameter ratios. Using the method of bisection, the relaxation time as defined in Section 3.2.3 has been evaluated numerically for thin as well as thick samples.

3.3 Experimental

3.3.1 Preparation of glass

A glass batch of composition $80V_2O_5, 15P_2O_5, 5Bi_2O_3$ (mole %) has been prepared from reagent grade chemicals. P_2O_5 is added as $(NH_4)_2 HPO_4$ and V_2O_5 and Bi_2O_3 are introduced as their oxides. The mixture is melted in a pure Al_2O_3 crucible at temperature of $700^O C$ for half an hour. Then the molten glass is cast in an aluminium mold and annealed at $100^O C$ for half an hour and left for furnace cooling.

3.3.2 Sample preparation

3.3.2.1 Preparation of thin film

The thin film of glass has been prepared as follows[44] : The liquid droplet of molten glass is collected by dipping a stainless steel tube in the crucible containing the molten glass. The droplet has been blown into a large bubble by passing an inert gas e.g. nitrogen/argon through the tube from the other end. The thin film samples are collected from the resulting glass bubble.

3.3.2.2 Preparation of thick film

The bulk glass has been thinned by successively grinding and polishing in SiC powder. Since vanadium phosphate glasses are readily attacked by water, the grinding and polishing are carried out in the presence of acetone. Samples of thickness

a few hundred microns are prepared by this method and are termed thick films.

3.3.3 Differential thermal analysis (DTA)

The bulk sample is ground and then sieved out in the range of -14 mesh to 20 mesh. This particle size is large enough so that the effect of surface crystallisation can be neglected in DTA[106]. To the ground sample is added around 30% of calcined Al_2O_3 to avoid sintering of the glass particles. The DTA has been carried out in a MOM Derivatograph Hungary, at a heating rate of $7^{\circ}C$/minute.

3.3.4 X-ray analysis

Both heattreated and virgin glasses have been used for X-ray studies. The heattreatment of sample has been carried out in a wire wound furnace at $359^{\circ}C$ for a period of one hour. The glass sample is ground and sieved to get powder of size below 400 mesh. The X-ray diffraction pattern of the powdered sample has been taken using General Electric XRD 5 Diffractometer. The monochromatic radiation used is Cu K_{α}. The interplanar spacings have then been calculated from the intensity vs 2θ plot of the diffraction pattern by using the relation,

$$2d_{hkl} \sin\theta = n\lambda \qquad (3.23)$$

where d_{hkl}, λ and θ are the interplanar spacing, X-ray wavelength and the diffraction angle respectively.

3.3.5 Electron microscopic analysis

Electron microscopic analysis has been carried out for both heattreated and virgin glass samples. The electron microscopic sample has been prepared as follows : First, the sample is thoroughly ground in an agate mortar and then dispersed in acetone, so that the very fine particles, needed for transmission electron microscope remain in suspension. A few drops of acetone containing finely suspended glass particles is poured on the carbon coated electron microscope (EM) grid. One drop of collodion is then poured on deionised distilled water to form a very thin film of collodion. The EM grid containing the powdered glass sample is then put on the film so that the sample particles face the collodion film. Lastly, the EM grids are fished out by clean glass slides. The sample is, therefore, sandwitched between the carbon and callodion thin films. The electron microstructure and the selected area diffraction of the samples at 100 kV have been taken in a Phillips EM 301 Electron Microscope.

The diameters of the diffraction rings have been measured from the negative by using a graduated eye-piece with an accuracy of 0.1 mm. The interplanar spacings are calculated from the relation given below :

$$\text{Camera constant} = r \, d_{hkl} \qquad (3.24)$$

where r is the radius of the diffraction ring and d_{hkl} the corresponding interplanar spacing. The camera constant has been determined from the standard gold diffraction pattern obtained at 100 kV.

3.3.6 Electrical measurement

The I-V characteristics of both thick and thin samples have been measured. The resistance of the thin film sample in the memory state has been measured as a function of temperature. To carry out the electrical measurement, the samples have been coated with gold to form electrodes. This has been done by evaporating pure gold in vacuum.

3.3.6.1 Electrical circuit

Figure 3.2 represents schematically the electrical circuit used for measurements of I-V characteristics of different samples. The sample and the standard resistance are in series with a 30 Volts 2 amperes DC regulated power supply (Aplab, Model 7152). The potential drops across the sample and the standard resistance are fed to the X-axis and Y-axis of the X-Y recorder respectively (No. 2000 made by Digital Electronics Ltd., India). Hence, the plot on the X-Y recorder corresponds to the I-V characteristics of the sample. The same circuit has been used to measure the resistance of thin samples in the memory state as a function of temperature from $23^{o}C$ to about $100^{o}C$.
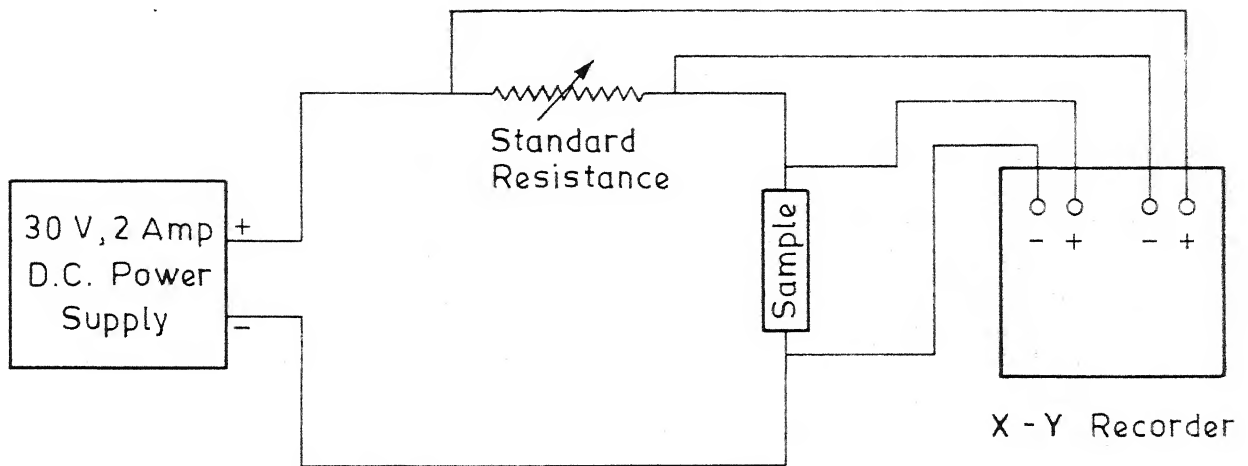
Fig. 3.2   Schematic representation of electrical circuit.

3.3.6.2 <u>Measuring cell</u>[107]

Figure 3.3 shows the schematic view of the cell used
for electrical measurements. This consists of a double
walled pyrex glass Jacket J, 300 mm long and having a diameter
of 50 mm. E_1 and E_2 are two gold plated copper electrodes
being placed co-axially with the metallic hollow cylinder S.
They are separated from the metallic hollow cylinder S by two
teflon discs T. The lower electrode E_1 is fixed while the
upper electrode E_2 can move up and down. The electrodes are
connected to the BNC connectors B with shielded wires. The
sample can be placed between the two electrodes by inserting it
through a rectangular hole O in S. On the other side, a copper
constantant thermocouple is inserted through a small hole H.
The sample holder assembly is suspended with the help of three
brass rods R brazed to the upper copper flange W, with a
rubber gasket G in between, H.C. is a heating coil wound on a
porcelain tube. This is connected to a 30 volts 2 amperes
regulated DC power supply through a proportional temperature
controller. The copper constantant thermocouple TC serves
the purpose of measuring temperature as well as sensing ele-
ment for temperature control. By this set up the temperature
can be varied from room temperature to about $150^{o}C$ with an
accuracy of temperature control $\pm 1^{o}C$. The inside of the
assembly can be flushed with dry inert gas. To make the inside
of the assembly moisture free silica gel dessicant D is used.
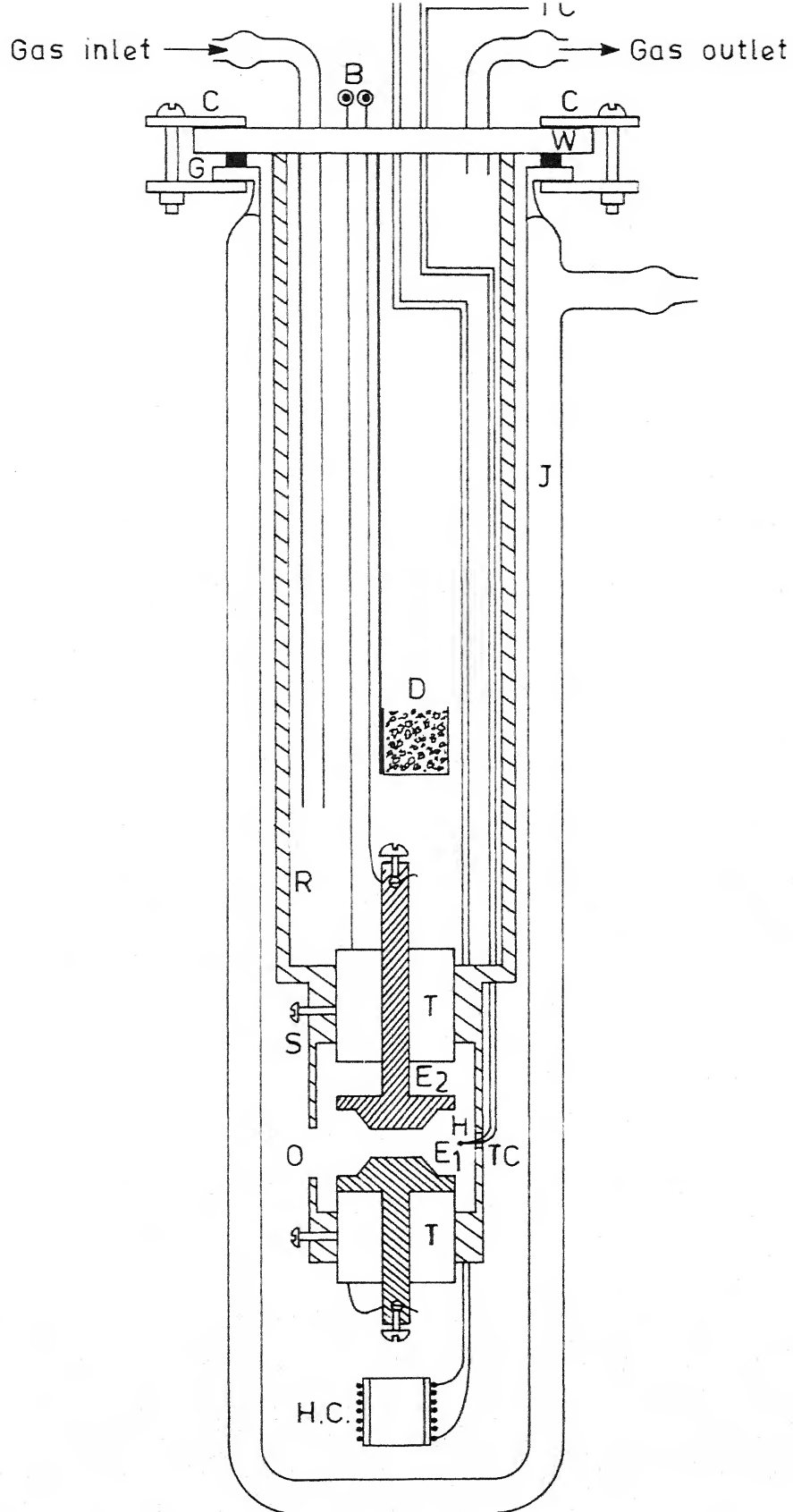
Fig. 3.3   Schematic diagram of the resistivity
measuring cell .

3.4   Results and Discussion

3.4.1   Switching characteristics of thin samples

Figures 3.4(a) and (b) show the theoretical I-V characteristics obtained for a film of thickness 10 μm and electrode area 6.3×10^{-6} m^2 for different particle diameters and particle separation to diameter ratios. In figure 3.5 are shown the theoretical temperature distribution in a sample at different instants of time after the application of the critical field. It is seen that the time taken for the sample centre to attain the melting temperature of bismuth corresponding to a particle diameter 700 Å and separation to diameter ratio 0.03 is 1.7×10^{-4} second . In column 3 of table 3.1 we give the calculated time t_h for the entire sample to reach the melting temperature of bismuth for different values of d and s_o/d ratios. The kinetics of switching at room temperature is controlled by the heating step. However, we will show in Chapter 4 that the stretching kinetics is much faster.

In figure 3.6 the I-V characteristics obtained experimentally on a sample of identical geometry to that considered above are shown. It is noted that the sample switched to the memory state when potential drop across the sample is around 6.3 Volts. Also plotted in the figure are some theoretical I-V curves taken from figure 3.4(a) for particle diameter values of 300 Å and 400 Å and s_o/d ratios equal to 0.02 and 0.03. The agreement
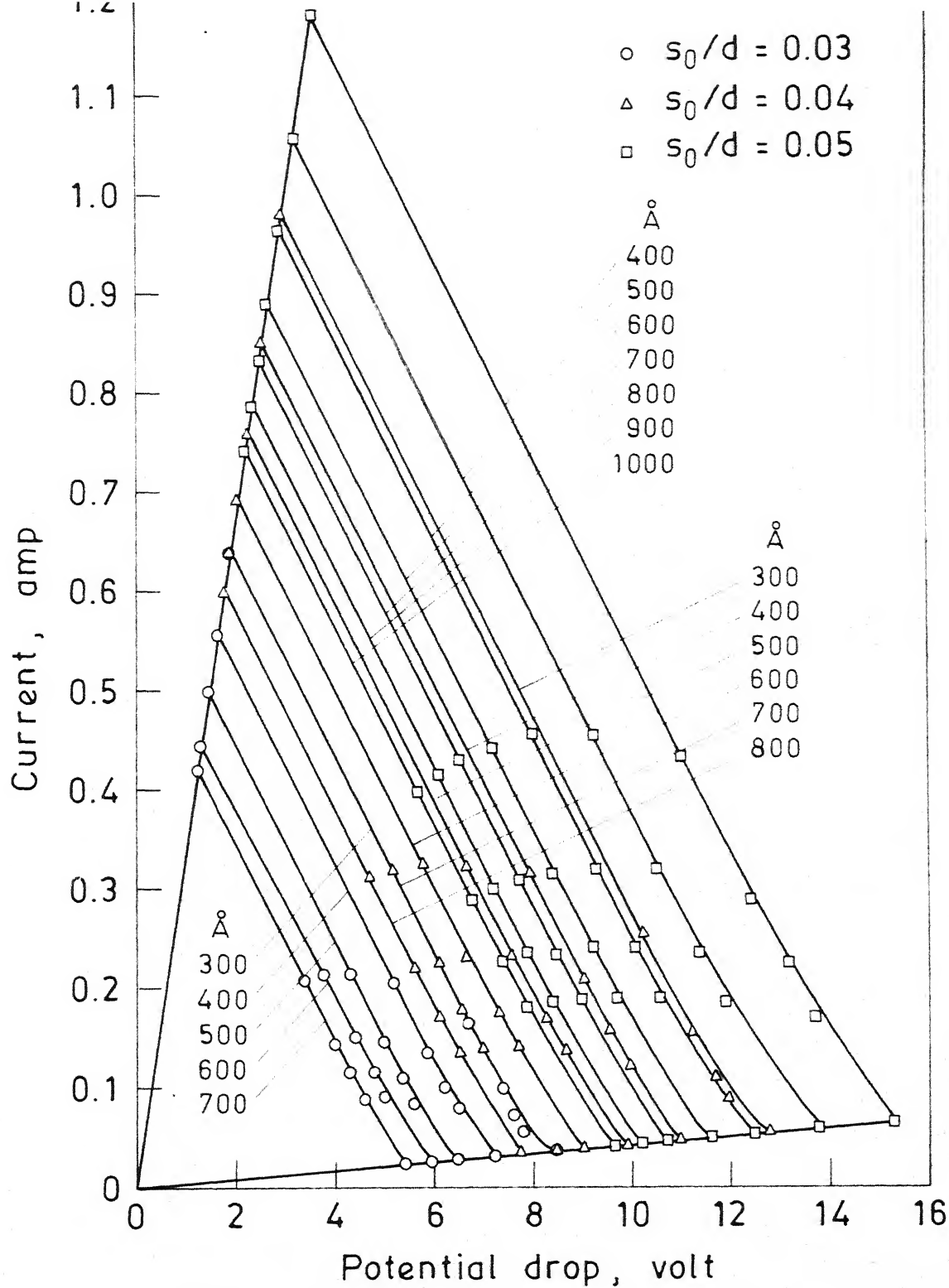
Fig. 3.4(a)   Theoretical I-V characteristics for a glass-metal system of composition $80\,V_2O_5\,15\,P_2O_5\,5\,Bi_2O_3$ (mole %) for various particle diameters
Sample thickness = 10 μm
Electrode area = $6.3 \times 10^{-6} m^2$
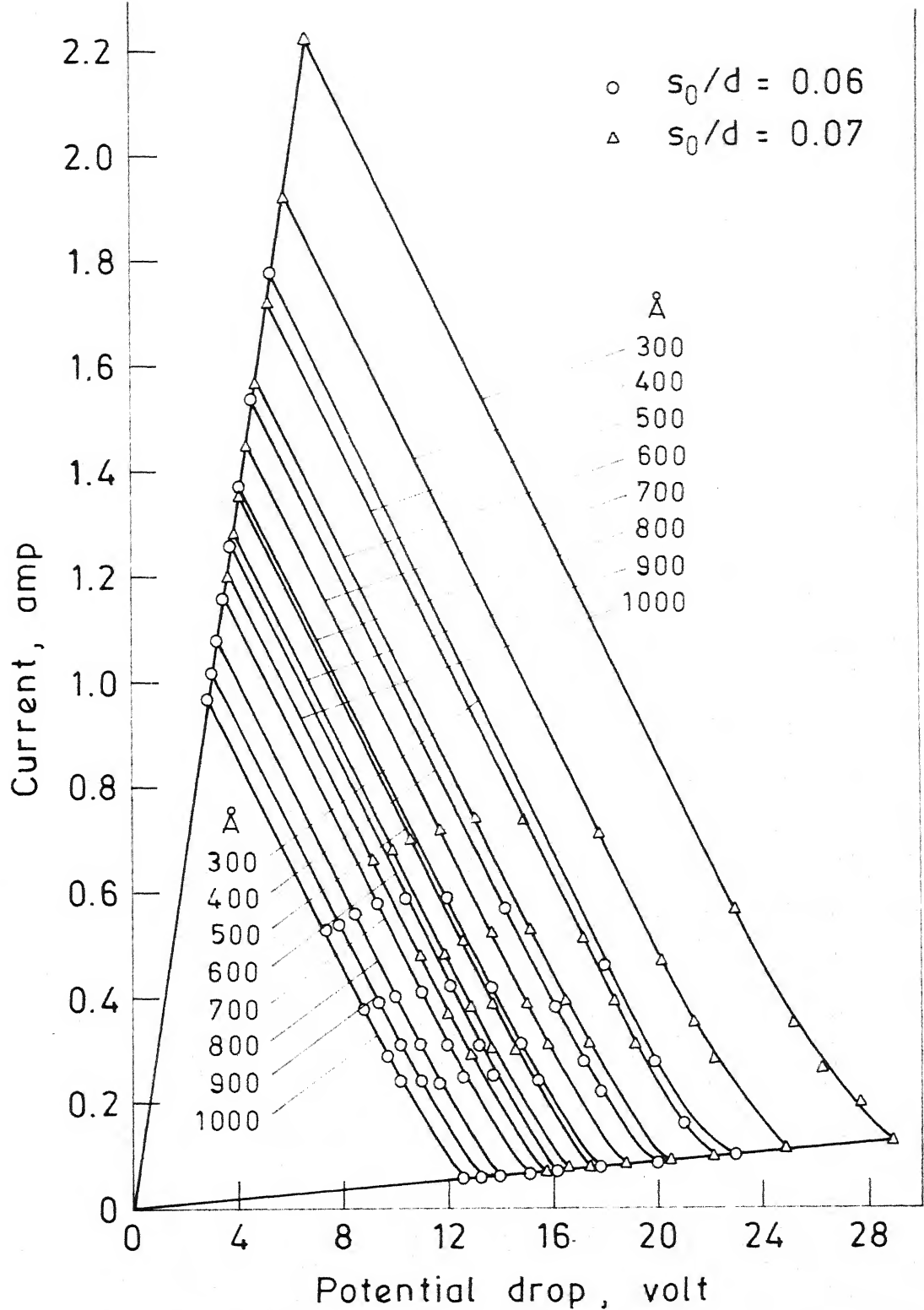
Fig. 3.4 (b)   Theoretical I-V characteristics of glass - metal system of composition $80V_2O_5 \, 15P_2O_5 \, 5Bi_2O_3$ (mole %) for various particle diameters.
Sample thickness = 10 μm
Electrode area = 6.3 x 10^{-6} m^2
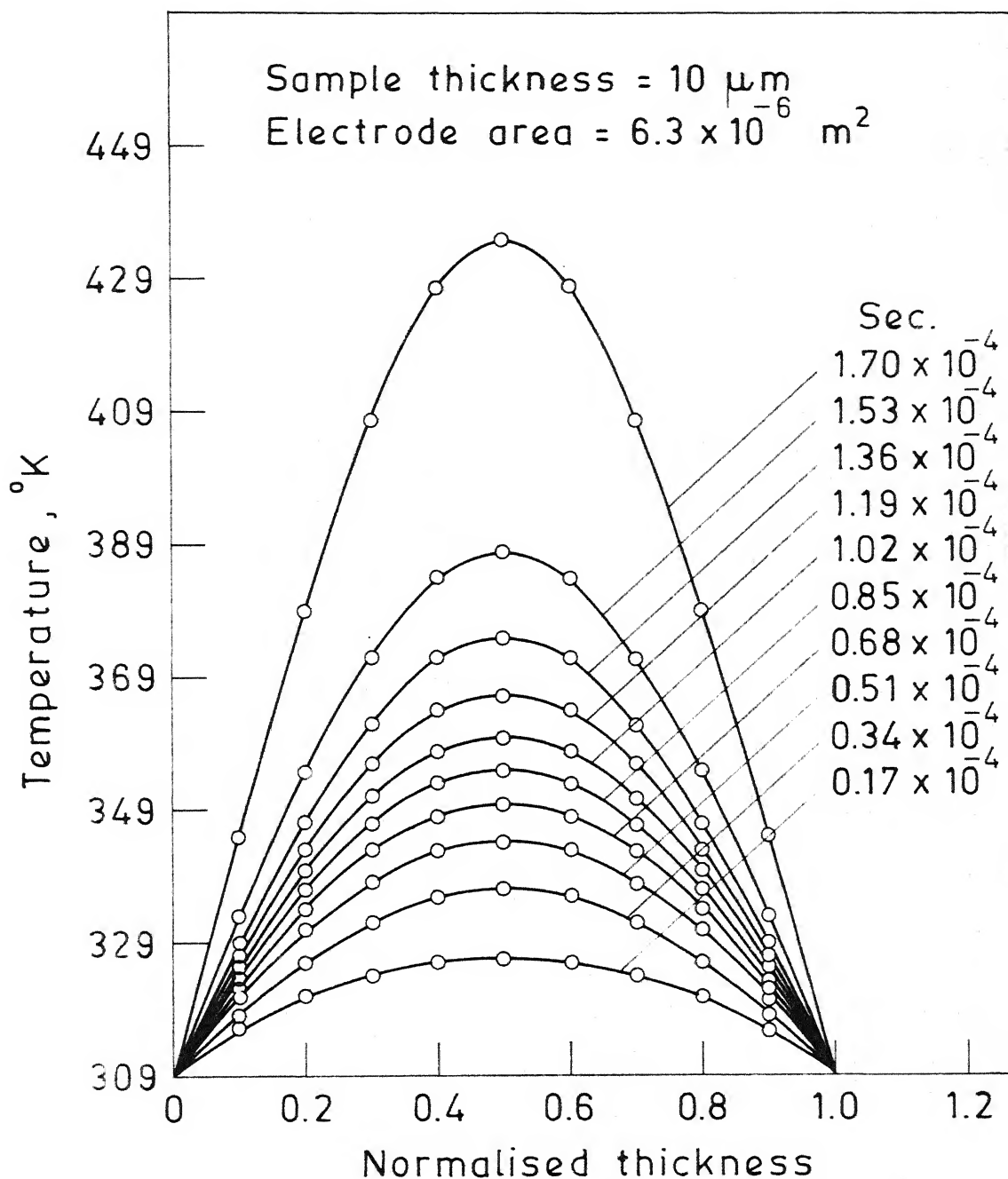
Fig. 3.5 Theoretical temperature profile within the glass-metal system of composition $80V_2O_5$ $15P_2O_5$ $5Bi_2O_3$ (mole %) with d= 700 Å and s_0/d = 0.03 .

Table 3.1 Calculated parameters for switching in a glass of composition $80V_2O_5, 15P_2O_5, 5Bi_2O_3$ (mole %) for different d and s_o/d values

Separation to diameter ratio s_o/d	Switching time t_h controlled by heating step $\times 10^5$ sec.		Relaxation time τ for temperature profile $\times 10^4$ sec.	
	$l=10\mu m$	$l=45\mu m$	$l=10\mu m$	$l=45\mu m$
0.02	1.32	0.69	0.11	0.42
0.03	0.72	0.45	0.10	0.10
0.04	0.50	0.34	0.10	0.10
0.05	0.36	0.27	0.09	0.10
0.06	0.28	0.22	0.09	0.10
0.07	0.23	0.20	0.08	0.10
0.02	7.39	5.73	0.15	2.27
0.03	3.88	3.09	0.15	1.83
0.04	1.82	2.00	0.15	1.51
0.05	1.36	1.40	0.17	1.32
0.06	1.07	1.06	0.16	1.14
0.07	0.89	0.85	0.16	1.03
0.02	–	11.88	–	2.50
0.03	5.01	6.90	0.15	2.32
0.04	2.88	4.73	0.16	2.11
0.05	2.05	3.45	0.16	1.97
0.06	1.59	2.65	0.16	1.79
0.07	1.29	2.05	0.16	1.59

	0.02	–	21.72	–	2.55
	0.03	8.49	11.77	0.14	2.44
	0.04	4.15	8.20	0.14	2.35
600	0.05	3.41	6.08	0.14	2.22
	0.06	2.12	4.76	0.15	2.11
	0.07	1.72	3.80	0.16	2.02
	0.02	–	56.67	–	2.55
	0.03	18.46	19.50	0.14	2.50
	0.04	5.86	12.55	0.14	2.41
700	0.05	3.69	9.20	0.14	2.32
	0.06	2.72	7.33	0.15	2.27
	0.07	2.16	5.91	0.16	2.19
	0.02	–	–	–	–
	0.03	–	–	–	–
	0.04	8.60	19.10	–	2.47
800	0.05	4.82	13.27	0.14	2.41
	0.06	3.42	10.25	0.14	2.35
	0.07	2.65	8.28	0.14	2.11
	0.02	–	–	–	–
	0.03	–	–	–	–
	0.04	–	30.10	–	2.50
900	0.05	6.36	18.88	0.14	2.44
	0.06	4.27	13.95	0.14	2.38
	0.07	3.23	11.10	0.14	2.35
	0.02	–	–	–	–
	0.03	–	–	–	–
	0.04	–	67.95	–	2.53
1000	0.05	8.63	29.11	0.14	2.50
	0.06	5.31	19.58	0.14	2.44
	0.07	3.90	14.90	0.14	2.41
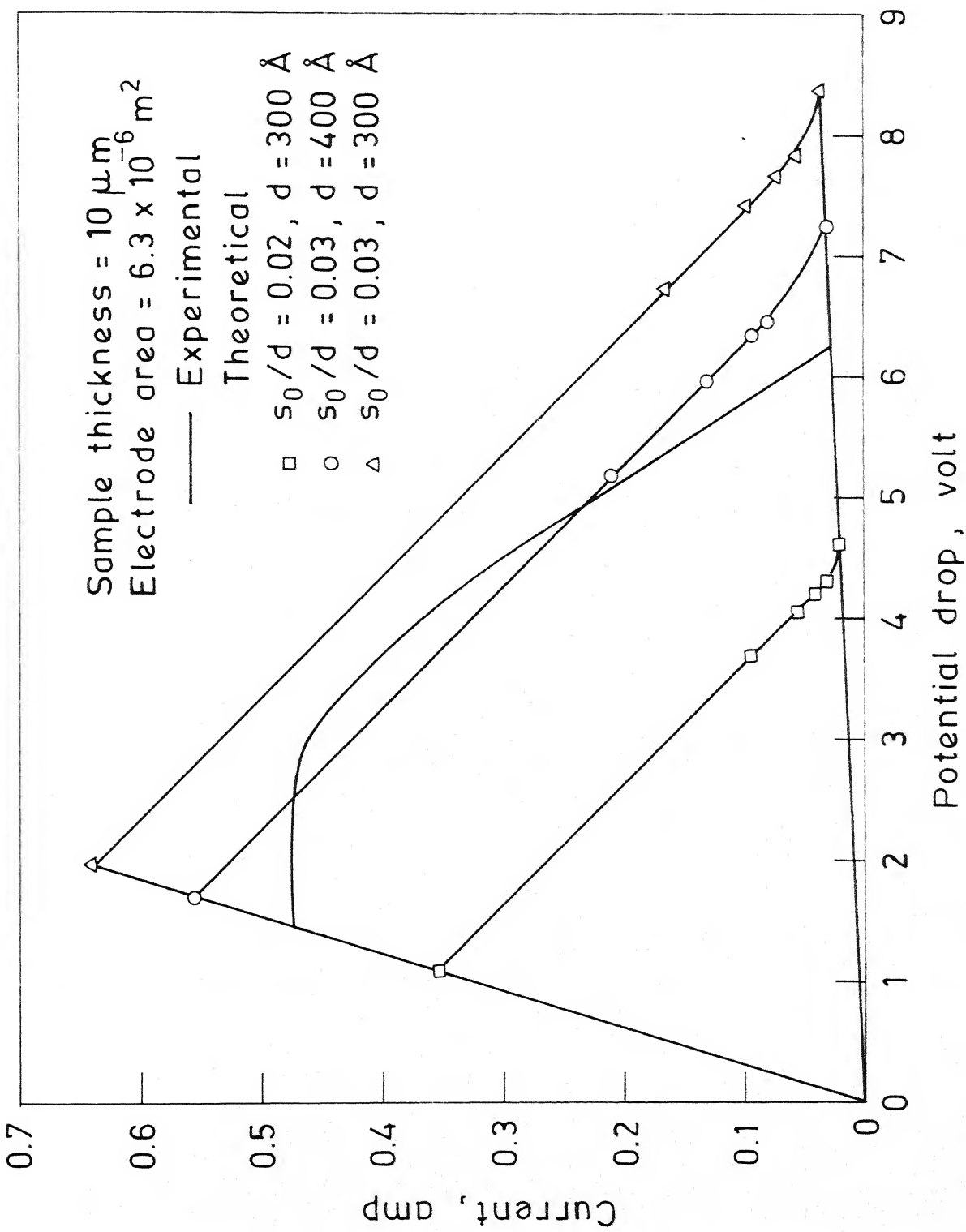
Fig. 3.6 Comparison of theoretical and experimental I-V curves.

between the two is found to be reasonable. Figures 3.7(a) and (b) give the electron micrograph and the selected area electron diffraction pattern of the sample respectively. The particles are observed to have diameters varying from 50 Å to 450 Å. In table 3.2 the interplanar spacings (d_{hkl}) calculated from the diffraction pattern are compared with the standard values for bismuth[108] metal. The agreement between the two sets of values indicates that the particles comprise of metallic bismuth.

3.4.2 Switching characteristics of thick samples

The effect of specimen thickness on the switching behaviour has been investigated by measuring the I-V characteristics of a sample of thickness 356 μm. No switching has been observed at room temperature and upto an applied voltage of 60 Volts. When the sample is however heattreated at $360^{\circ}C$ for an hour it shows threshold switching with a threshold voltage of around 26 Volts. Also the resistance of the heattreated sample is about an order of magnitude lower than that of the untreated one. The heattreatment is believed to cause further precipitation of metallic bismuth in the glass matrix thereby bringing about coalescence of larger particles which effectively gives rise to the formation of metallic region in a major portion of the glass-metal particulate system. This is substantiated as follows :
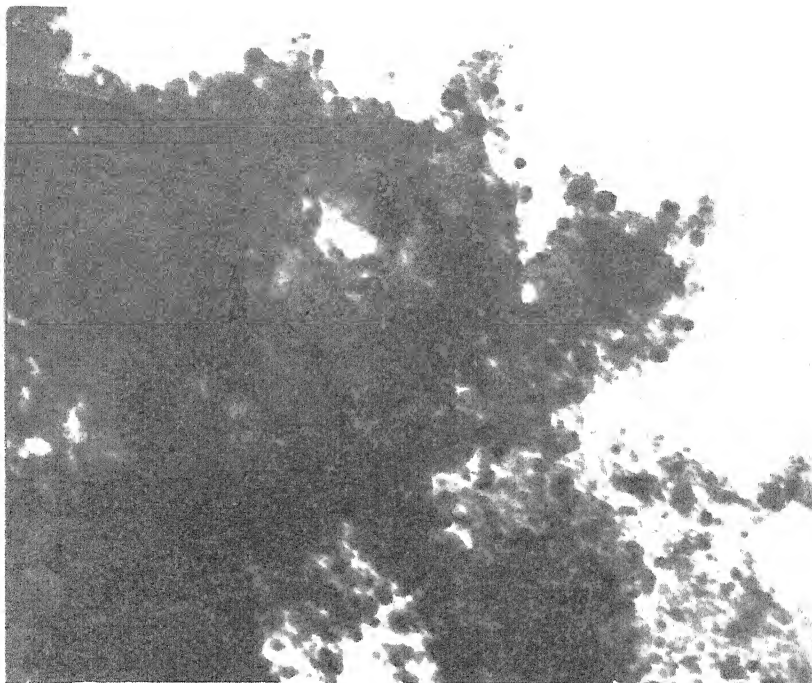
Fig.3.7(a) Electron micrograph of a sample
of composition $80V_2O_5, 15P_2O_5,$
$5Bi_2O_3$(mole %)
X 84,000
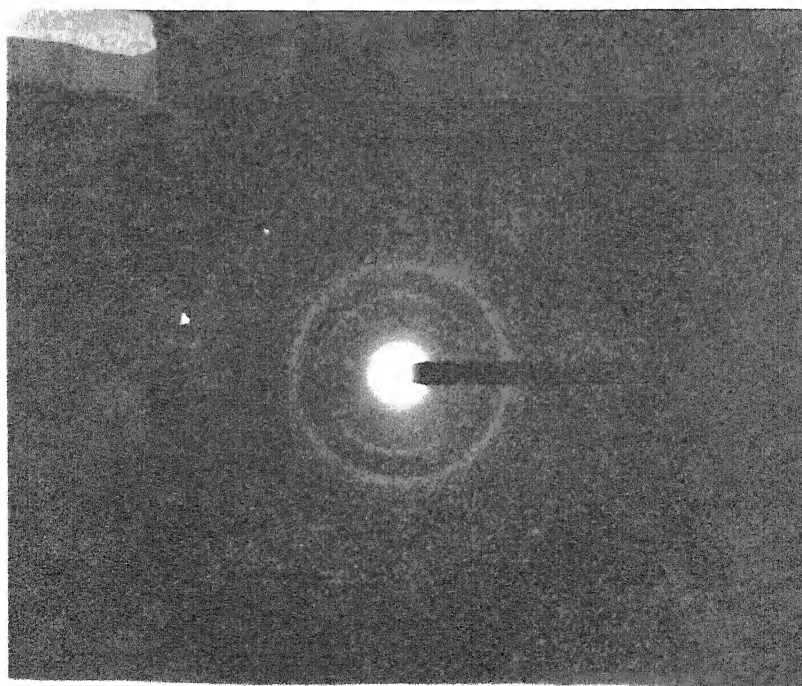
Fig.3.7(b) Electron diffraction pattern from
the above microstructure
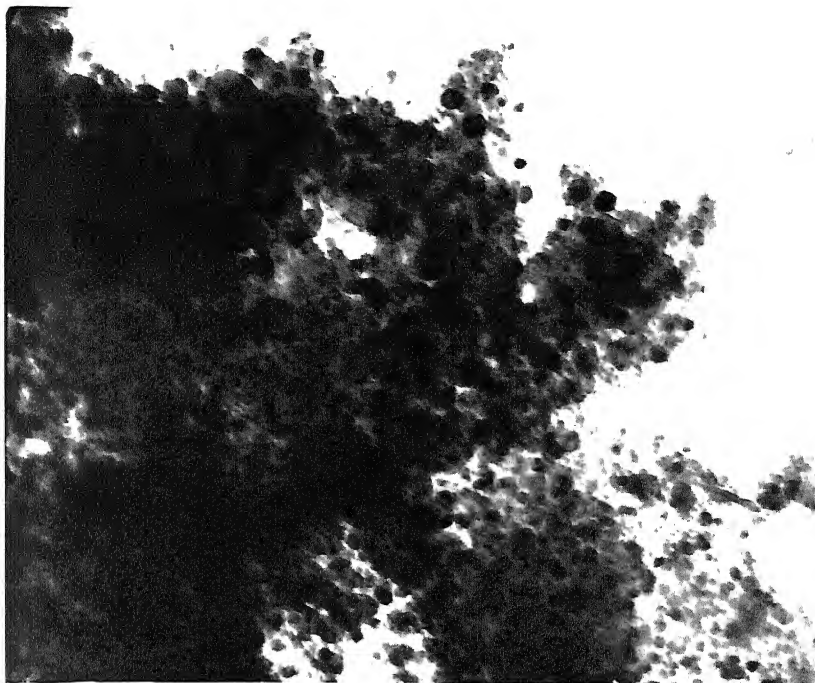
Fig.3.7(a) Electron micrograph of a sample
            of composition $80V_2O_5, 15P_2O_5,$
            $5Bi_2O_3$(mole %)
            X 84,000
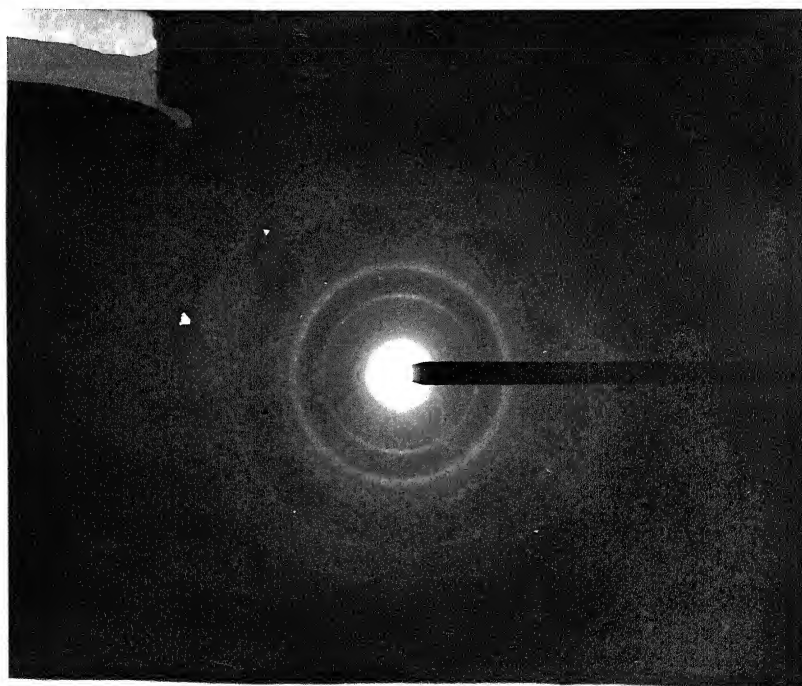
Fig.3.7(b) Electron diffraction pattern from
           the above microstructure

Table 3.2 Electron diffraction data for a
glass-metal composite

d_{hkl} values calculated from experimental data $\overset{o}{A}$	Standard d_{hkl} values of bismuth metal[108] $\overset{o}{A}$
3.30	3.28
2.89	-
2.18	2.27
2.07	2.03
1.86	1.87
1.64	1.64
1.30	1.31
1.11	1.12

Figure 3.8 shows the DTA curve obtained for the as-cast glass. The exothermic peak at $360^\circ C$ indicates that some crystalline phase is precipitated within the glass matrix at this temperature. In figure 3.9 are shown the X-ray diffraction patterns of the as-cast glass and of the sample heated at $359^\circ C$ for an hour respectively in the range of 2θ values where the most intense peak of the heattreated sample occurs. Figures 3.10(a) and (b) give the electron micrograph and the selected area diffraction pattern respectively of a heattreated sample. Table 3.3 summarises the X-ray and electron diffraction data of the same. It is evident from this table that the precipitated phase consists of metallic bismuth. Also from figure 3.9, it is obvious that the amount of metallic bismuth present in the heattreated sample is higher than that in the untreated sample. From figure 3.10(a) we conclude that the bismuth particles in this sample have diameters in the range 50Å to 700 Å.

Figure 3.11 gives the theoretical I-V curves obtained for a sample of thickness 45 μm and electrode area 16×10^{-6} m^2 for different particle diameters and separation to diameter ratios. The above thickness value has been chosen such that the experimental data match closely the theoretical results, for particle diameter values 400 Å and 500 Å and s_o/d value equals to 0.03, as shown in figure 3.12. From the discussion given above the effective thickness should be an order of magnitude smaller than
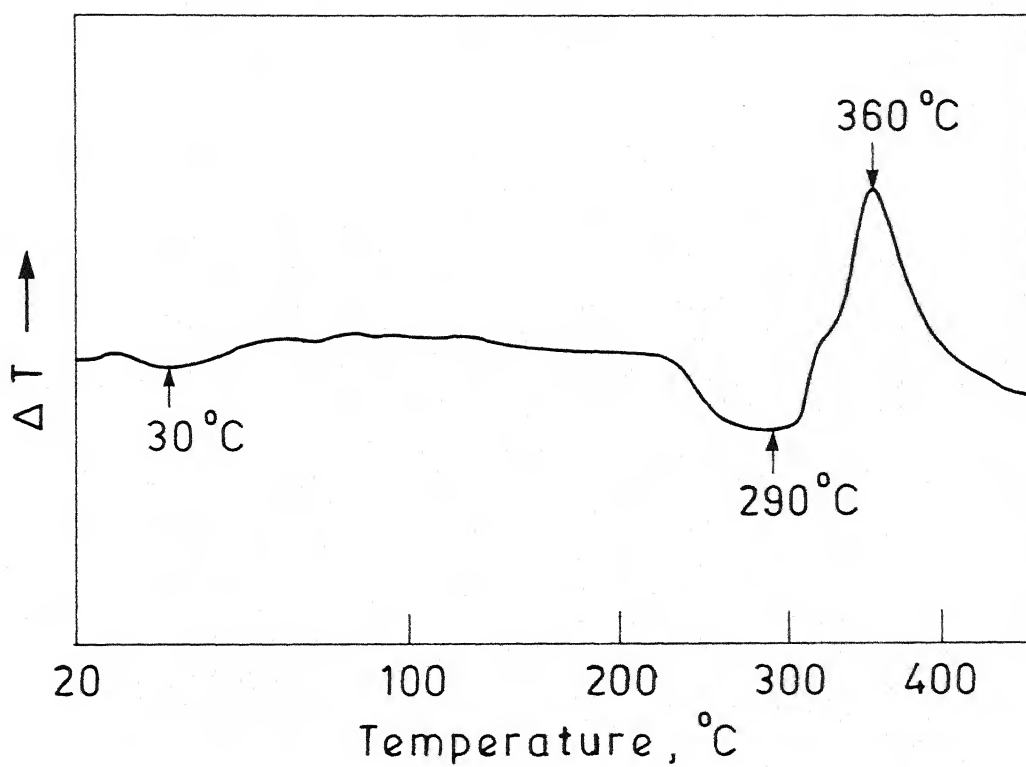
Fig. 3.8   DTA curve for a sample of composition
80V_2O_5 15P_2O_5 5Bi_2O_3 (mole %)
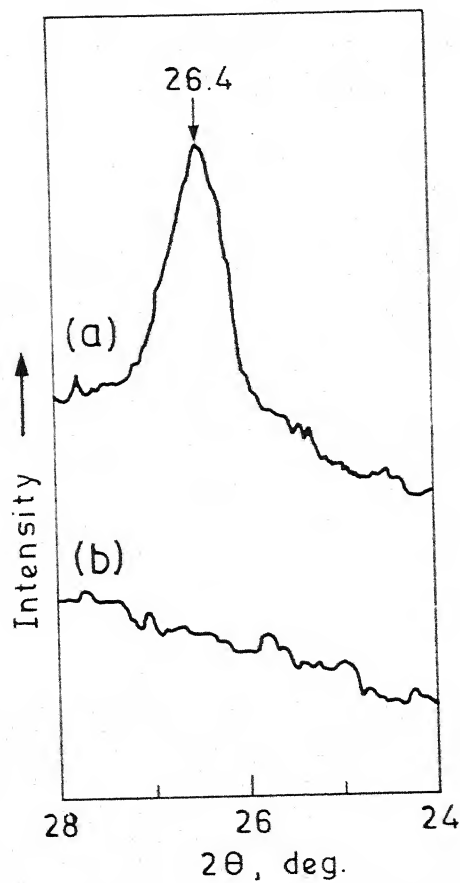
Fig. 3.9   X-ray diffraction pattern for a sample of composition $80 V_2O_5 \ 15P_2O_5 \ 5Bi_2O_3$ (mole %)
(a) Heat-treated at $359°C$ for 1 hour
(b) As-cast.
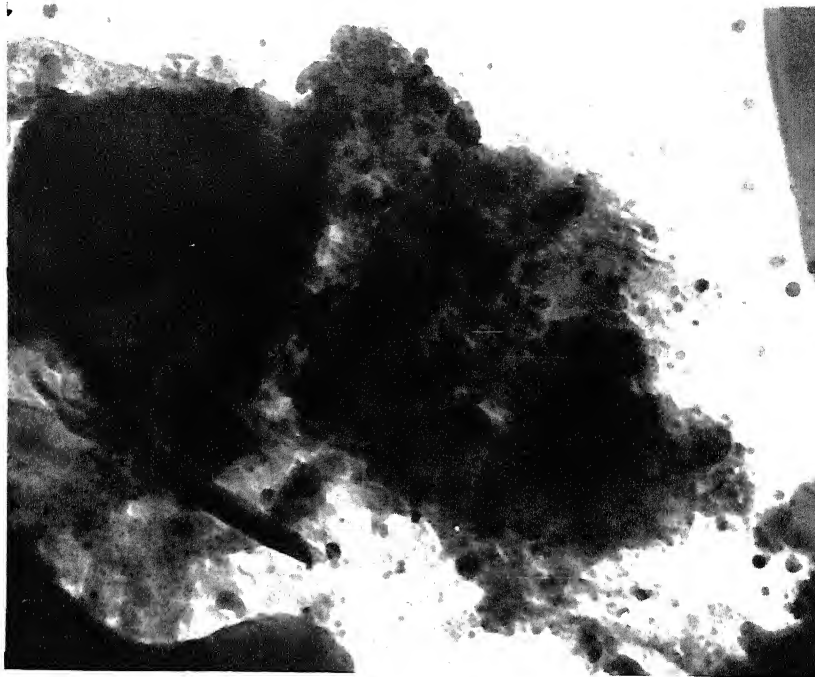
Fig.3.10(a) Electron micrograph of a sample of composition $80V_2O_5, 15P_2O_5, 5Bi_2O_3$ (mole %) after being heat-treated at 359°C for 1 hour
X 84,000
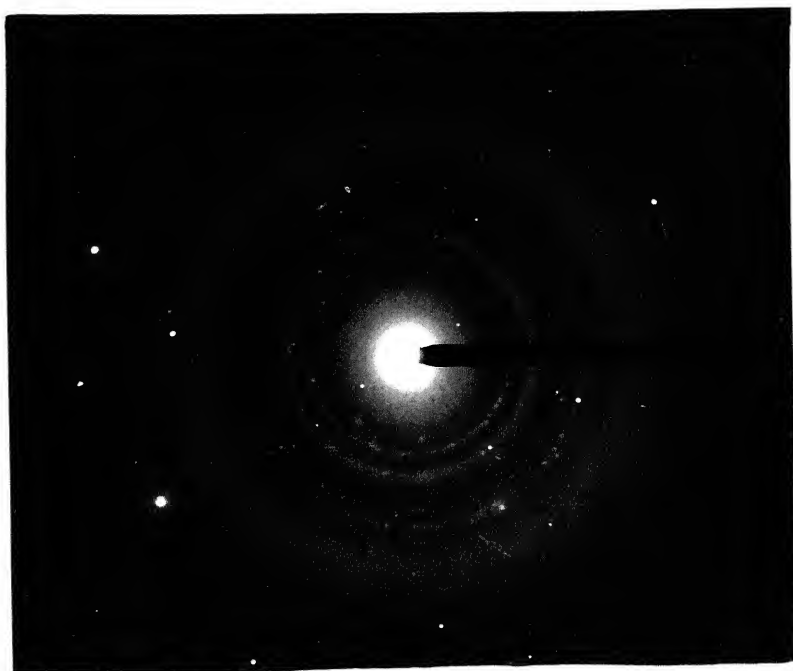
Fig.3.10(b) Electron diffraction pattern from the above microstructure

Table 3.3   X-ray and electron diffraction data for
a glass-metal composite heated at 359°C
for 1 hour

d_{khl} values calculated from electron diffraction Å	d_{hkl} values calculated from X-ray diffraction Å	Standard d_{hkl} values of bismuth metal[108] Å
-	4.39	-
-	3.37	3.28
-	2.90	-
2.56	-	2.39
2.23	2.18	2.27
1.84	-	1.87
-	1.50	1.49
1.42	-	1.44
1.29	-	1.28

Fig. 3.11(a)   Theoretical I-V characteristics for a sample of composition $80V_2O_5$ $15P_2O_5$ $5Bi_2O_3$ (mole %) for various particle diameters.
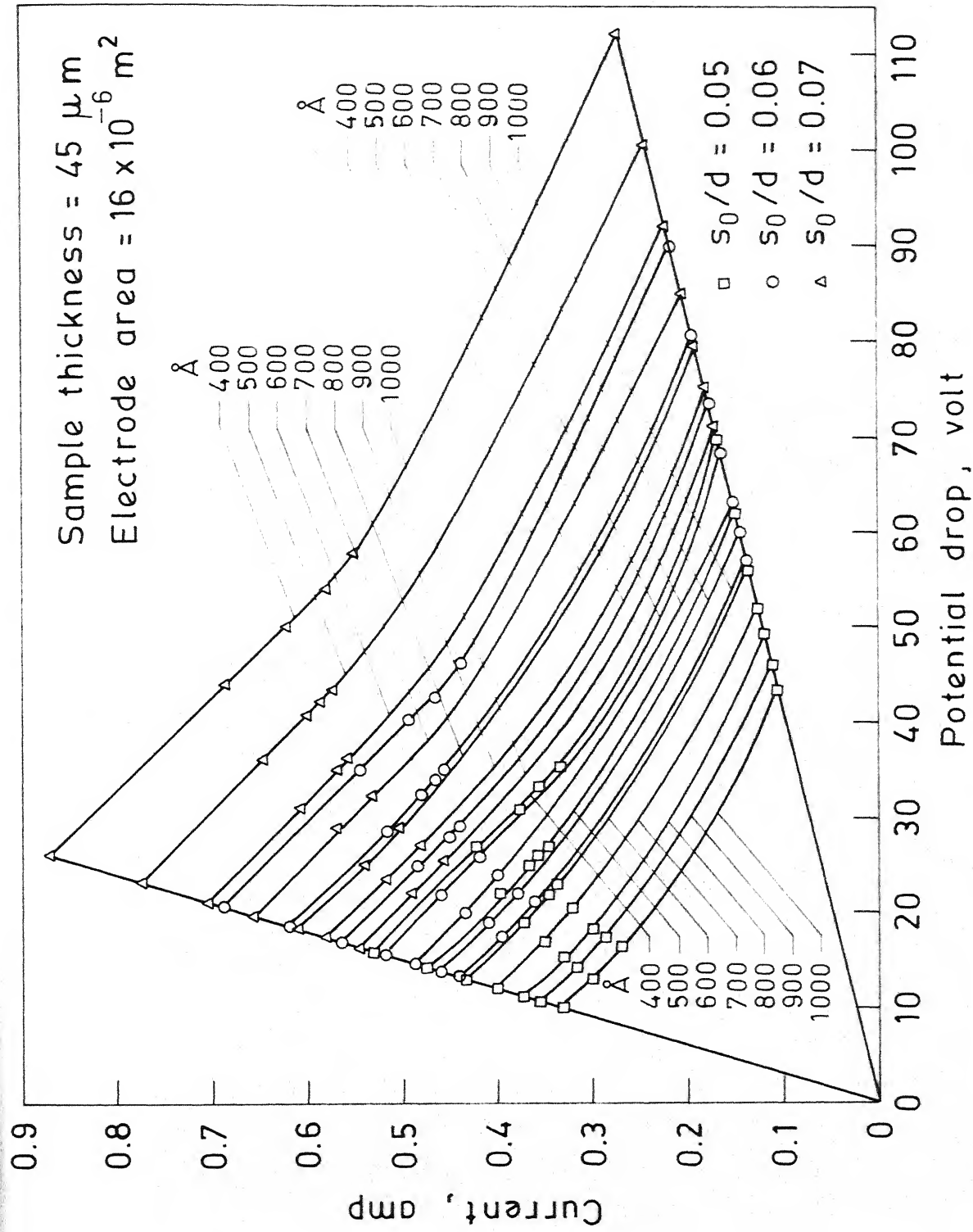
Fig. 3.11(b) Theoretical I-V characteristics for a sample of composition $80V_2O_5 \; 15P_2O_5 \; 5Bi_2O_3$ (mole %) for various particle diameters.
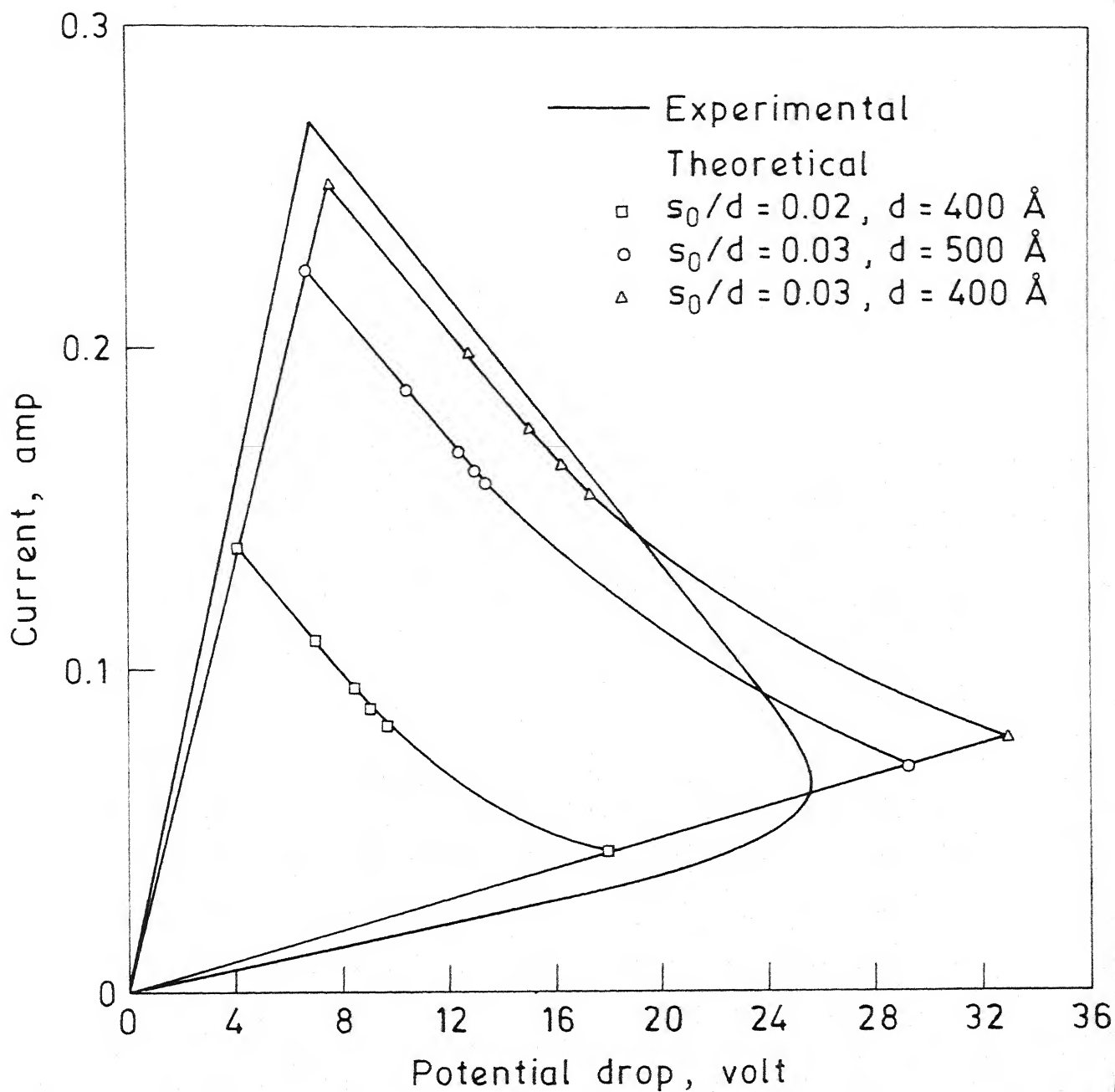
Fig. 3.12 Comparison of theoretical and experimental I-V curves.
Sample thickness = 45 μm
Electrode area = 16 x 10^{-6} m^2

the actual thickness (356 μm in our case). Our estimated value (45 μm) therefore seems reasonable. In column 4 of table 3.1 we give the calculated time required for the entire sample to reach the melting temperature of bismuth for various d and s_o/d values. The time t_h for the thick   sample is found to be in general greater than that for the thin sample which is expected from physical reasons.

In contrast to thin sample the threshold switching behaviour of thick sample can be explained from the calculated values of relaxation time τ which has been defined earlier (Section 3.2.3) as the time required for the temperature at the centre of the sample to go below the melting temperature of bismuth after the applied electric field is reduced to zero. The relaxation time has been computed by the procedure outlined in Section 3.2.3 and Section 3.2.4.2 for different d and s_o/d values and for both the sample thicknesses under investigation. Figure 3.13 shows a typical calculated temperature profile as a function of time for a sample of thickness 10 μm with d and s_o/d values of 400 Å and 0.03 respectively. The results are summarised in the last two columns of table 3.1. It is evident from these data that τ values obtained for the sample with a thickness of 45 μm are an order of magnitude higher than those of the thinner one (10 μm). If the rate of removal of the electric field is faster as compared to the relaxation time τ, it is likely that the stretched particles
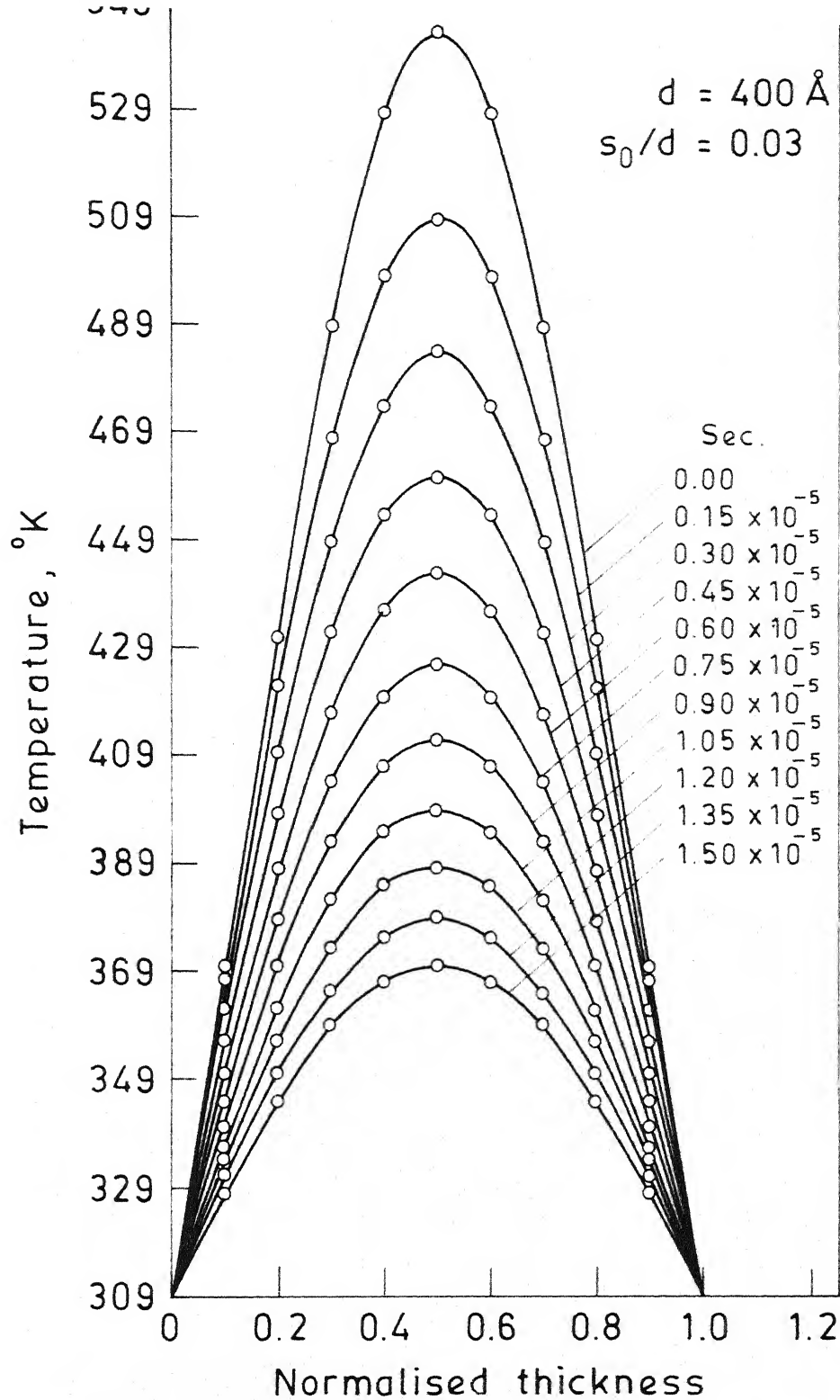
Fig. 3.13　Theoretical relaxation of temperature profile within a sample of composition $80\,V_2O_5\,15\,P_2O_5\,5\,Bi_2O_3$ (mole %) after the removal of the electric field. Sample thickness = 10 μm.

will regain their original shape due to the surface tension forces still effective in the molten state of metal granules. This will break the interconnections between the conducting particles and the sample will go back to the off-state. The occurrence of threshold switching in the case of the thick sample investigated here is therefore believed to arise due to a higher value of τ pertaining to the specimen.

3.4.3 Temperature dependent memory state resistance variation

Figure 3.14 shows a typical variation of resistance in the memory state of the blown thin film as a function of temperature over the range $20^{\circ}C$ to $110^{\circ}C$. Before switching the off-state resistance of the sample is 1070 Ohms. It goes to the memory state via a negative resistance region at an applied voltage of 9.5V at $23^{\circ}C$. The resistance in the memory state is 8.0 Ohms at the same temperature. It is found from figure 3.14 that the on-state resistance remains constant with temperature. At $107^{\circ}C$ the sample goes to the off-state of resistance about 8000 Ohms with an application of 0.5 volt . This behaviour can be explained as follows. According to particle stretching model, if the particles are in molten condition in the on-state, the removal of electric field causes the stretched particles to go back to their original shapes due to surface tension. Thus, the interconnections of the metallic chains are broken and a high resistance off-state is achieved. This condition is

realised by heating the sample in the memory state to $107^{\circ}C$ along with an applied voltage of 0.5 Volt. It is believed that the role of the applied voltage is to help achieving the melting temperature of bismuth.

A similar behaviour has been reported in the case of silicate glass system containing bismuth at high temperature alone[51].

When the interconnected chains in the memory state between the molten bismuth particles are broken due to the effect of surface tension force, the resistance of the sample increases and at the same time the increased resistance of the sample causes the current to decrease. Thus more the breaking of the interconnected chains the greater is the resistance of the sample and therefore the potential drop across the sample increases along with a reduction of current giving rise to a voltage controlled negative resistance region in the I-V characteristics. Figure 3.15 is the I-V plot of another sample in the on-state at $78^{\circ}C$. The sample goes to off-state at 0.18 Volt through a voltage controlled negative resistance region. Similar voltage controlled negative resistance region has been observed in the insulating thin film sandwitched between two metallic electrodes due to thermal rupture of conducting filaments[109,110].

A number of samples has been studied which show qualitatively same behaviour as described above.
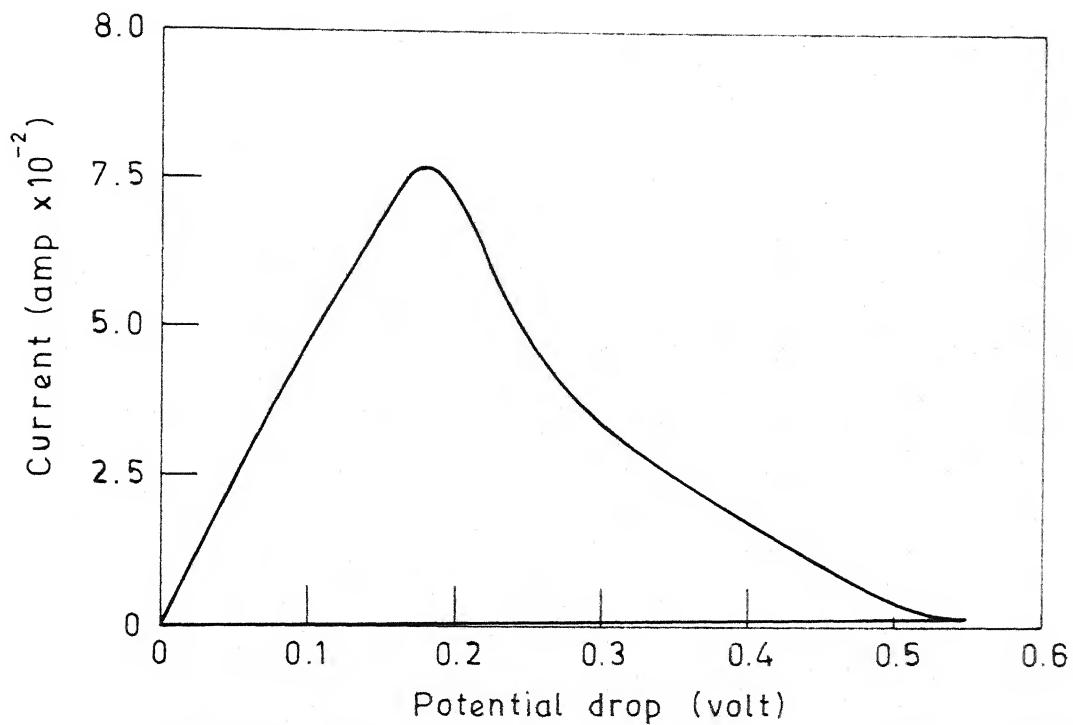
Fig. 3.15 I - V plot of $80V_2O_5$-$15P_2O_5$-$5Bi_2O_3$ (mole %) glass switching from on to the off-state at 78°C.

KINETICS OF SWITCHING IN VANADIUM PHOSPHATE GLASSES
CONTAINING BISMUTH GRANULES

4.1   Introduction

In Chapter 2, we have developed a model. This predicts
the critical switching fields which are of the same order as
those obtained experimentally. In Chapter 3 with the help
of the model developed in Chapter 2, the I-V characteristics
especially in the negative resistance region have been computed.
There it has been assumed that once the temperature reaches the
size dependent melting point of bismuth interconnected chains
are formed because of the presence of critical electric field.
This implies that the time required for two physically proxi-
mate grains to touch each other in molten condition is much
less compared to the time required for the temperature profile
to reach the melting temperature of bismuth. In this chapter,
we present the solution for the dynamics of stretching and
compute the time required for two physically proximate grains
to touch each other in molten condition after the application
of critical switching field.

4.2   Theoretical Consideration

When an electric field is applied to a glass-metal
composite, the metallic particles in the molten state will be

stretched as described in Chapter 2. Figure 2.3 of Chapter 2 shows, at some instant of time, the state of two proximate grains during stretching into ellipsoidal forms from spherical shapes. The problem is to find the time required by each sphere to elongate by a distance $s_o/2$, so that the particles can join up. It is noted that the boundary of the ellipsoid changes during stretching. This moving boundary fluid flow problem has been analysed with the help of well known fluid flow equations.

The following assumptions have been made in our analysis for simplicity of calculations.

1) The molten liquid is inviscid i.e., the viscous drag has been neglected compared to surface tension.

2) The flow is irrotational and the liquid is incompressible.

3) The flow problem has been solved in two dimensions.

4.2.1 Determination of potential φ_f

To determine the force acting on the deformed granule at a distance x from the origin, we use the same method as described in Section 2.2.1 of Chapter 2. By displacing the ellipsoid by δx (figure 4.1) against the force $F_{el}|_x$ in the negative direction of x, we can write,

$$F_{el}|_x \, \delta x = \tfrac{1}{2} \, \varepsilon \varepsilon_o \, E^2 \delta V \qquad (4.1)$$

where δV, is the volume as cross-hatched in figure 4.1.
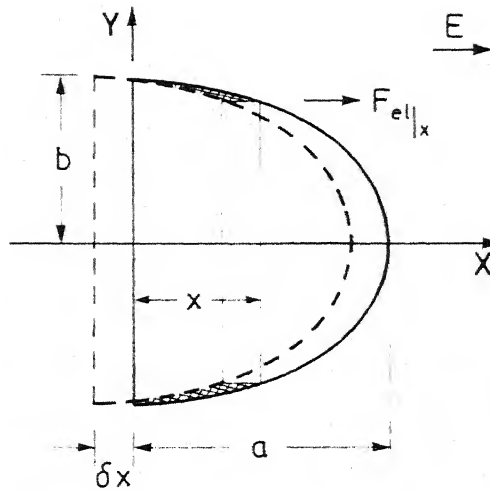
Fig. 4.1   Configuration of a half ellipsoid
stretched under the action of an
electric field .

Its value is obtained by integrating the equation (2.4) of Chapter 2 from x = o to x = x and we get,

$$\delta V = \pi(\frac{b^2}{a^2}) \ x^2 \ \delta x \qquad (4.2)$$

where a and b are semi-major and semi-minor axes of the ellipse respectively.

Substituting equation (4.2) into equation (4.1) and after simplification, we get,

$$F_{el} \mid_x = \frac{1}{2} \ \pi \ \varepsilon\varepsilon_o \ E^2(\frac{b^2}{a^2})x^2 \qquad (4.3)$$

This force will act on the mass of the ellipsoid between x = o and x = x. The volume (V) of ellipsoid between x = o and x = x is given by,

$$V = \int_o^x \pi \ y^2 \ dx \qquad (4.4)$$

Writing y in terms of x from the equation of the ellipse and integrating we get,

$$V = \pi b^2(x - \frac{x^3}{3a^2}) \qquad (4.5)$$

The force per unit mass is therefore given by,

$$F = \frac{3}{2} \ \frac{\varepsilon\varepsilon_o E^2}{\rho} \ (\frac{x}{3a^2-x^2}) \qquad (4.6)$$

where ρ is the density of the liquid.

In a conservative system, force $\vec{F}$ is given by the expression,

$$\vec{F} = - \vec{\nabla}\varphi_f \qquad (4.7)$$

where φ_f is the scalar potential. φ_f is obtained by integrating equation (4.7) and is given by,

$$\varphi_f = - \int_o^x F \, dx \qquad (4.8)$$

Substituting F from equation (4.6) in equation (4.8) and integrating we get,

$$\varphi_f = - \frac{3}{4} \frac{\varepsilon\varepsilon_o E^2}{\rho} \ln \left[\frac{3a^2}{3a^2-x^2}\right] \qquad (4.9)$$

4.2.2 <u>Determination of pressure</u>

The effective pressure $\triangle P$ which is operative in restraining the fluid flow, is given by,

$$\triangle P = \gamma\left(\frac{1}{R_1} + \frac{1}{R_2}\right) - \frac{2\gamma}{r} \qquad (4.10)$$

where R_1, R_2 are the radii of curvature of the ellipsoid and are given by the expressions (2.8) and (2.9) of Chapter 2. γ and r are the surface tension and radius of metallic particle. Substituting y' and y'' ($y' = \frac{dy}{dx}$ and $y'' = \frac{d^2y}{dx^2}$) in equation (4.10) and on simplification we get,

$$\triangle P = \gamma\left[(a/b)(1/b)\left\{\frac{[(a/b)^2(1-(x/a)^2) + 1+(x/a)^2]}{[(a/b)^2(1-(x/a)^2) + (x/a)^2]^{3/2}}\right\} - \frac{2}{r}\right]$$

$$(4.11)$$

4.2.3 Fluid flow equations

For an incompressible liquid the continuity equation is given by,

$$\vec{\nabla} \cdot \vec{q} = 0 \qquad (4.12)$$

where q is the velocity vector and is given by,

$$\vec{q} = \vec{i}\, u + \vec{j}\, v \qquad (4.13)$$

where u and v are the components of velocity in x and y directions respectively.

From the definition of circulation and Stokes theorem[111],

$$\oint_c \vec{q} \cdot d\vec{r} = \iint_A \vec{n} \cdot (\vec{\nabla} \times \vec{q}) \qquad (4.14)$$

where $\oint_c$ indicates the integration over a closed contour c in the liquid and A the area enclosed by this contour. Since the liquid flow is irrotational,

$$\vec{\nabla} \times \vec{q} = 0 \qquad (4.15)$$

Hence from equation (4.14) we get,

$$\oint_c \vec{q} \cdot d\vec{r} = 0 \qquad (4.16)$$

Equation (4.16) implies[98] that,

$$\vec{q} = \vec{\nabla}\varphi \qquad (4.17)$$

where φ is a single valued scalar velocity potential function.
Substituting equation (4.17) in (4.12), the continuity equation becomes,

$$\nabla^2 \varphi = 0 \qquad (4.18)$$

For an inviscid liquid, the Navier-Stokes equation is given by[111],

$$\frac{D\vec{q}}{Dt} = \frac{\partial \vec{q}}{\partial t} + (\vec{q} \cdot \vec{\nabla})\vec{q} = \vec{F} - \frac{\vec{\nabla}P}{\rho} \qquad (4.19)$$

where $\vec{F}$ is the body force per unit mass, $\vec{\nabla}P$ the pressure gradient and ρ the density of liquid.

In a conservative system, the body force is given by equation (4.7). Substituting equation (4.7) in (4.19),

$$\frac{D\vec{q}}{Dt} = -\vec{\nabla}\varphi_f - \frac{\vec{\nabla}P}{\rho} \qquad (4.20)$$

For irrotational flow[111] the $(D\vec{q}/Dt)$ can also be written as,

$$\frac{D\vec{q}}{Dt} = \vec{\nabla}\frac{\partial \varphi}{\partial t} + \frac{1}{2}\vec{\nabla}q^2 \qquad (4.21)$$

The integration in equation (4.16) is evaluated at a fixed time. Hence, the time derivative can be written as,

$$\oint_c \frac{D}{Dt}(\vec{q} \cdot d\vec{r}) = 0 \qquad (4.22)$$

or

$$\oint_c \left(\frac{D\vec{q}}{Dt} \cdot d\vec{r} + \vec{q} \cdot d\vec{q}\right) = 0 \qquad (4.23)$$

Substituting $\frac{D\vec{q}}{Dt}$ from equation (4.20) in equation (4.23) and integrating we get,

$$- \varphi_f - \frac{P}{\rho} + \tfrac{1}{2} q^2 = 0 \tag{4.24}$$

Similarly substituting $\frac{D\vec{q}}{Dt}$ from equation (4.21) in equation (4.23) and integrating we get,

$$\frac{\partial \varphi}{\partial t} + q^2 = 0 \tag{4.25}$$

Equating (4.24) and (4.25) we get,

$$\frac{\partial \varphi}{\partial t} = -(\varphi_f + \frac{P}{\rho} + \tfrac{1}{2}q^2) \tag{4.26}$$

Substituting φ_f and P from equations (4.9) and (4.11) respectively and putting the dot product of $\vec{q}$ (equation 4.13) in equation (4.26) we get,

$$\frac{\partial \varphi}{\partial t} = \frac{3}{4} \frac{\varepsilon \varepsilon_o E^2}{\rho} \ln \frac{3a^2}{3a^2 - x^2} - \tfrac{1}{2}(u^2 + v^2) -$$

$$\frac{\gamma}{\rho}[(\frac{a}{b})(\frac{1}{b})\{\frac{(a/b)^2(1-x^2/a^2)+(1+x^2/a^2)}{[(a/b)^2(1-x^2/a^2)+(x^2/a^2)]^{3/2}}\} - \frac{2}{r}] \tag{4.27}$$

In our analysis the closed contour is the boundary of the liquid droplet. From symmetry of the geometrical shape we consider only the first quadrant in the x-y plane. viz., $o \leq x \leq a$ and $o \leq y \leq b$.

As we have mentioned earlier, the boundary moves with time. Therefore, one has to consider the dynamic boundary condition. This is given by[112],

$$\frac{\partial v}{\partial t}\Big|_{boundary} = \left[v - u\,\frac{\partial v}{\partial x}\right]\Big|_{boundary} \qquad (4.28)$$

Initial conditions, at $t = o$, are

$$u = v = \varphi = \frac{\partial \varphi}{\partial t} = o \qquad (4.29)$$

According to our assumption, the initial shape is spherical.

At $t > o$, from symmetry consideration, along the straight boundaries $(x = o, y = o)$, $\frac{\partial \varphi}{\partial x} = o$ and $\frac{\partial \varphi}{\partial y} = o$ respectively. Along the curved boundary, the functional value of φ is obtained from the solution of the equation (4.27). Thus, the problem is to solve the Laplace equation (4.18) consistent with the above boundary conditions. Since no analytical solution is available, we have solved the equation numerically by using a finite difference scheme.

4.3 Numerical Solution

For ease of computation it is necessary to normalise the equations. The normalisation is carried out by setting,

$$X = x/a \qquad (4.30)$$

$$Y = y/b \qquad (4.31)$$

and

$$t^* = t/t_1 \qquad (4.32)$$

such that

$$o \le X \le 1, \quad o \le Y \le 1 \quad \text{and} \quad o \le t^* \le 1 \qquad (4.33)$$

By using expressions (4.30) and (4.31) the Laplace equation (4.18) becomes,

$$\frac{1}{(a/b)^2} \frac{\partial^2 \varphi}{\partial X^2} + \frac{\partial^2 \varphi}{\partial Y^2} = 0 \tag{4.34}$$

By using expressions (4.30) to (4.32) equation (4.27) becomes,

$$\frac{1}{t_1} \frac{\partial \varphi}{\partial t^*} = \frac{3}{4} \frac{\varepsilon \varepsilon_o E^2}{\rho} \ln\left(\frac{3}{3-X^2}\right) - \frac{1}{2}(u^2+v^2) -$$

$$\frac{\gamma}{\rho} \left[\left(\frac{a}{b}\right)\left(\frac{1}{b}\right)\left\{ \frac{\left[\left(\frac{a}{b}\right)^2(1-X^2)+(1+X^2)\right]}{\left[\left(\frac{a}{b}\right)^2(1-X^2)+X^2\right]^{3/2}} \right\} - \frac{2}{r} \right] \tag{4.35}$$

where, u and v after normalisation become

$$u = \frac{1}{a} \frac{\partial \varphi}{\partial X} \tag{4.36}$$

$$v = \frac{1}{b} \frac{\partial \varphi}{\partial Y} \tag{4.37}$$

Using equations (4.30) and (4.31), the equation (4.28) becomes,

$$b \frac{\partial Y}{\partial t} + \frac{\partial b}{\partial t} Y = v - u \frac{b}{a} \frac{\partial Y}{\partial X} \tag{4.38}$$

Substituting expressions (4.30) and (4.31) in an equation of ellipse,we get,

$$X^2 + Y^2 = 1 \tag{4.39}$$

Under this condition we must have,

$\frac{\partial Y}{\partial t} = 0$ and evaluating $\frac{\partial Y}{\partial X}$ from (4.39), the equation (4.38) becomes,

$$\sqrt{1-X^2} \ \frac{\partial b}{\partial t} = v + u \ \frac{b}{a} \ \frac{X}{\sqrt{1-X^2}} \qquad (4.40)$$

The above equation is valid for any value of $o \leq X \leq 1$. There-fore, at $X = o$ and using equation (4.32) equation (4.40) becomes

$$\frac{1}{t_1} \ \frac{\partial b}{\partial t^*} = v \Big|_{X=o} \qquad (4.41)$$

Since v is a function of time and its functional form is not known it has been evaluated numerically.

4.3.1 Numerical scheme

Figure 4.2 represents the first quadrant in the X-Y plane in which the equations have been solved numerically. The normalised X and Y axes have been divided into 10 equal parts such that the steplengths are h = 0.1 and k = 0.1 respectively. $X_0, X_{0.1}, \ldots, X_{0.9}$ represent the points of intersection of the curve and the lines X = 0, X = 0.1, ..., X = 0.9. Similarly $Y_0, Y_{0.1}, \ldots, Y_{0.9}$ represent the points of intersection of the curve and the lines Y = 0, Y = 0.1, ..., Y = 0.9. These are the boundary points on the curve at which φ's have to be evaluated at a particular time so that the Laplace equation can be solved at that instant of time at the grid points as shown in figure 4.2. It is to be noted that the grid points marked with open circles near the boundary have unequal step-lengths. The following steps are involved in the numerical solution of the problem[112].
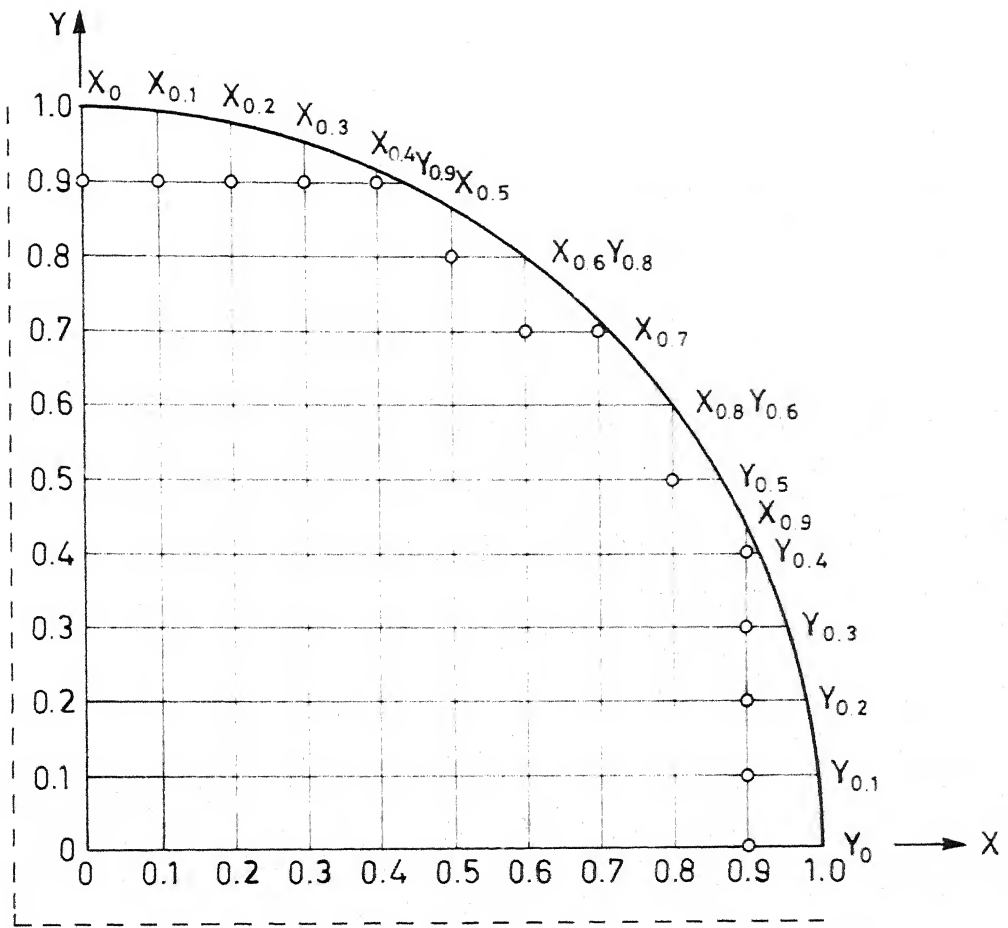
Fig. 4.2   Grid points in the first quadrant of a circle for solution of fluid flow equations.

Step 1 : t_1 is assigned an arbitrary value and the normalised time is divided into 10 parts such that step length $p = 0.1$, $t^* = 0$ is set.

Step 2 : The first order partial derivative (of equation(4.35)) is replaced by backward difference. The finite difference formula becomes

$$\varphi_{t^*+p} = \varphi_{t^*} + t_1 p [\frac{3}{4} \frac{\varepsilon \varepsilon_0 E_{t^*}^2}{\rho} \ln (\frac{3}{3-X^2}) - \tfrac{1}{2}(u_{t^*}^2 + v_{t^*}^2) -$$

$$\frac{\Upsilon}{\rho} [(\frac{a_{t^*}}{b_{t^*}})(\frac{1}{b_{t^*}}) \{ \frac{(a_{t^*}/b_{t^*})^2(1-X^2)+(1+X^2)}{\{(a_{t^*}/b_{t^*})^2(1-X^2)+X^2 \}^{3/2}} \}- \frac{2}{r}]]$$

$$(4.42)$$

φ_{t^*+p} is evaluated from above equation at the boundary points, X_o, $X_{0.1}$, ..., $X_{0.9}$, Y_0, $Y_{0.1}$, ..., $Y_{0.9}$. E_{t^*} is given by the expression (2.18) of Chapter 2.

Step 3 : At every grid point (i,j) the Laplace equation (4.34) is replaced by the following finite difference formula,

$$\frac{\varphi_{i-1,j} - 2\varphi_{i,j} + \varphi_{i+1,j}}{(a_{t^*}/b_{t^*})^2 h^2} + \frac{\varphi_{i,j-1} - 2\varphi_{i,j} + \varphi_{i,j+1}}{k^2} = 0$$

$$(4.43)$$

Two things to be noted in the above formula.

First, for any j, when i = 0, we get $\varphi_{-1,j}$, $\varphi_{0,j}$ and $\varphi_{1,j}$ in the first term of equation (4.43). From the boundary condition at $t^* > 0$ on Y axis $(\frac{\partial \varphi}{\partial X} = 0)$, we get,

$$\frac{\varphi_{+1,0} - \varphi_{-1,0}}{2a_{t^*}h} = 0 \qquad (4.44)$$

From equation (4.44), the unknown $\varphi_{-1,j}$ on the fictitious boundary represented as dotted line in figure 4.2 is eliminated. Similarly, for any i when j = 0, $\varphi_{i,-1}$ is eliminated from the boundary condition at $t^* > 0$, $\frac{\partial \varphi}{\partial Y} = 0$ on X-axis.

Second, for grid points represented by small circles in figure 4.2, the step lengths are unequal and the situation around such a grid point is magnified in figure 4.3. The equation (4.43) is replaced by[112],

$$\frac{2h^{-2}}{(\frac{a_{t^*}}{b_{t^*}})^2} \left[\frac{1}{(\lambda_i + 1)} \varphi_{i-1,j} - \frac{1}{\lambda_i} \varphi_{i,j} + \frac{1}{\lambda_i(\lambda_i + 1)} \varphi_{i+1,j} \right] +$$

$$2k^{-2} \left[\frac{1}{\lambda_j + 1} \varphi_{i,j-1} - \frac{1}{\lambda_j} \varphi_{i,j} + \frac{1}{\lambda_j(\lambda_j + 1)} \varphi_{i,j+1} \right] = 0$$

$$(4.45)$$

$$0 \leq \lambda_i \leq 1$$
$$0 \leq \lambda_j \leq 1$$
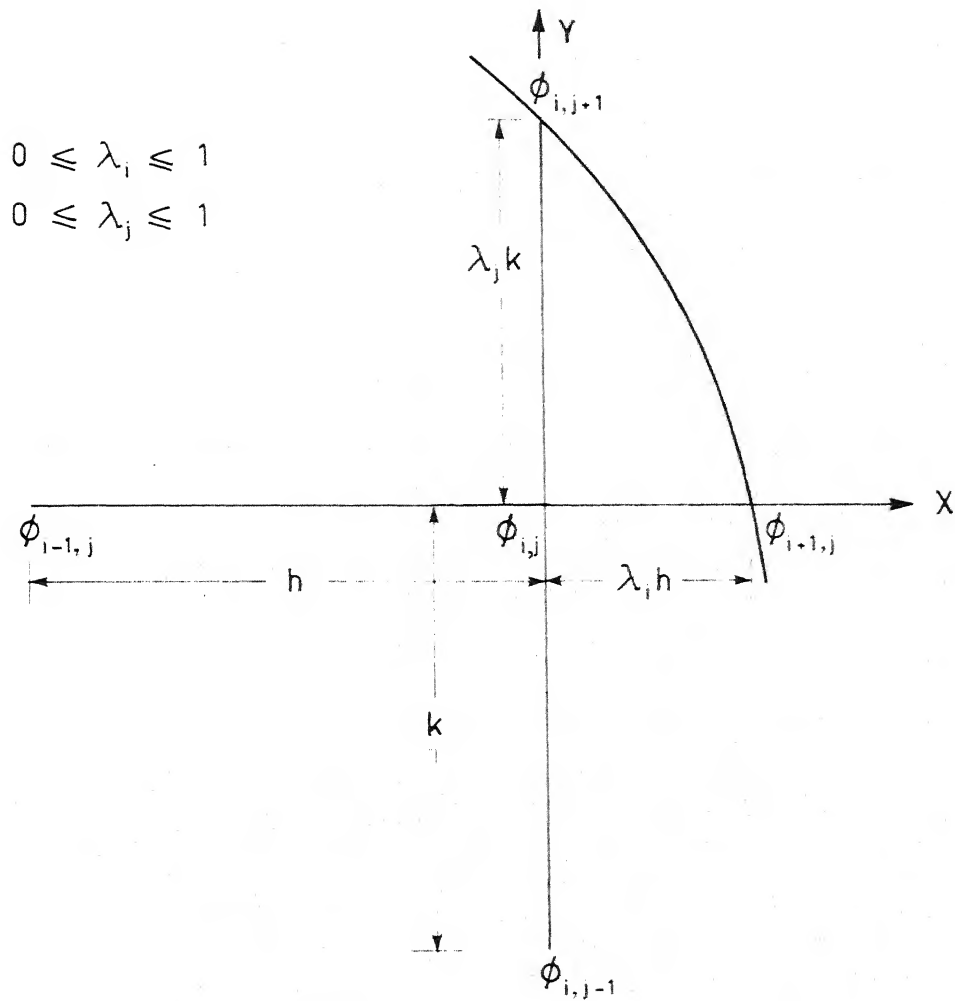
Fig. 4.3   Magnified view of the surroundings of a grid point near the boundary for solution of fluid flow equations.

It is to be noted that for $\lambda_i = \lambda_j = 1$ equations (4.45) and (4.43) become identical. Using equations (4.43) and (4.45) for all i,j's we get a set of algebraic equations which can be put in a matrix form. By using matrix iteration [Gauss iteration][99] the φ values at time (t^*+p) are evaluated, since the boundary values evaluated in step 2 are valid for time t^*+p.

[In the present problem the matrix iteration scheme converges. This can be shown as follows. The absolute value of a diagonal element in any row of the matrix as stated earlier is given by,

$$|\text{Diagonal element}| = \frac{2h^{-2}}{(\frac{a_{t^*}}{b_{t^*}})^2}(\frac{1}{\lambda_i}) + 2k^{-2}(\frac{1}{\lambda_j}) \qquad (4.46)$$

The absolute sum of off-diagonal elements

$$= \frac{2h^{-2}}{(\frac{a_{t^*}}{b_{t^*}})^2}[\frac{1}{\lambda_i + 1} + \{\frac{1}{\lambda_i(\lambda_i+1)}\}^I] +$$

$$2k^{-2}[\frac{1}{\lambda_j+1} + \{\frac{1}{\lambda_j(\lambda_j+1)}\}^{II}]$$

$$= \frac{2h^{-2}}{(\frac{a_{t^*}}{b_{t^*}})^2}(\frac{1}{\lambda_i}) + 2k^{-2}(\frac{1}{\lambda_j}) \qquad (4.47)$$

Near the boundary points either I or II or both terms will be transferred to the known vector side. Therefore, from equations (4.46) and (4.47) we get for the matrix,

Absolute value of diagonal element

$\geq$ Absolute sum of off-diagonal elements (4.48)

This (4.48) satisfies the condition for convergence of matrix iteration (Gauss-iteration)[99]].

Step 4 : Velocity components at time t^*+p are computed from $\varphi_{i,j}$'s as evaluated in Step 3 at time t^*+p. At the interior points $u_{i,j}$ and $v_{i,j}$ are computed by the following finite difference formula,

$$u_{i,j} = (2h\ a_{t^*})^{-1} \left[\varphi_{i+1,j} - \varphi_{i-1,j}\right] \qquad (4.49)$$

$$v_{i,j} = (2k\ b_{t^*})^{-1} \left[\varphi_{i,j+1} - \varphi_{i,j-1}\right] \qquad (4.50)$$

At the interior points as represented by small open circles in figure 4.2, due to unequal step lengths, the equations (4.49) and (4.50) are replaced by[112] (see figure 4.3),

$$u_{i,j}=(a_{t^*}h)^{-1}\left[-\frac{\lambda_i}{\lambda_i(\lambda_i+1)}\,\varphi_{i-1,j} - \frac{1-\lambda_i}{\lambda_i}\,\varphi_{i,j} + \right.$$

$$\left. \frac{1}{\lambda_i(\lambda_i+1)}\,\varphi_{i+1,j}\right] \qquad (4.51)$$

$$v_{i,j} = (b_{t*}k)^{-1}[-\frac{\lambda_j}{\lambda_j(\lambda_j+1)}\varphi_{i,j-1} - \frac{1-\lambda_j}{\lambda_j}\varphi_{i,j} +$$

$$\frac{1}{\lambda_j(\lambda_j+1)}\varphi_{i,j+1}] \tag{4.52}$$

At the boundary backward differences are employed to extrapolate the velocity components at points $X_0, X_{0.1}, \ldots, X_{0.9}$ and $Y_0, Y_{0.1}, \ldots, Y_{0.9}$ at time t^*+p, from $\varphi_{i,j}$ values evaluated in previous steps (2 and 3).

Step 5 : Replacing time derivative of equation (4.41) by backward difference we get,

$$b_{t*+p} = b_{t*} + t_1 p\, v_{t*+p}\,|_{X=0} \tag{4.53}$$

where $v_{t*+p}\,|_{X=0}$ is the velocity component evaluated at time t^*+p at the point X_0 in Step 4. As the volume of the ellipsoid remains constant, using b_{t*+p} as evaluated by equation (4.53), we get,

$$a_{t*+p} = r^3/b_{t*+p}^2 \tag{4.54}$$

Since the potential drop between the two grains remains unchanged even after stretching, the field increases as a function of time. From figure 2.3 of Chapter 2 it can be shown that, at time t^*+p,

$$E_{t*+p} = E_0(s_0/s_{t+p}^*) \tag{4.55}$$

where $\quad s_{t*+p} = s_0 - 2(a_{t*+p} - r) \tag{4.56}$

Step 6 : $t^* = t^*+p$ is set.

Step 7 : Steps 2 to 6 are repeated, till $t = 0.9$.

Step 8 : The difference between $(s_0/2 - a_t*)$ is evaluated.

Step 9 : Depending on whether difference is positive or negative, time t_1 is increased or decreased.

Step 10 : t_1 in Step 1 is replaced by t_1 in Step 9.

Step 11 : Steps 1 to 10 are repeated. This process is continued until we get two values of t_1 such that in one case the difference $(s_0/2 - a_t*)$ is negative and in other case the difference is positive.

Step 12 : Using the method of bisection t_1 is evaluated and time t_1 in Step 1 is replaced by this new value of t_1.

Step 13 : Steps 1 to 8 and then Step 12 are repeated till the difference as evaluated in Step 8 is within $\pm 0.1 \overset{o}{A}$ and the time which is evaluated in Step 12 is the required time.

The programme developed for the solution is given in Appendix 3. The programme is written in Fortran language with some features permitted in DEC System 1090 computer.

4.4 Experimental

4.4.1 Preparation of glass and blowing of thin film

A glass batch of composition $80V_2O_5, 15P_2O_5, 5Bi_2O_3$ (mole %)
has been melted. The melting is described in Section 3.3.1
of Chapter 3. The blowing of thin films used for pulse response
measurement has been described in Section 3.3.2.1 of Chapter 3.

4.4.2 Pulse response measurement at room temperature

4.4.2.1 Pulse circuit

Figure 4.4 shows block diagram of circuit configuration
indicating the principle of pulse circuit operation. A standard
pulse generator (Systronics Dual Channel, Model 1110-D) is used
as a source of stimulus for providing a rectangular pulse of
appropriate height and width to be impressed across the sample.
However, the driving capacity in terms of power and current
demanded by the sample of pulse generator is inadequate and
therefore a buffer circuit combination consisting of Schmitt
trigger interface and a solid state high speed (transistor)
switch are interposed between the stimulus pulse generator and
the sample. The regulated D.C. power supply (Aplab, Model 7152)
is essential for providing the requisite supply voltages for
proper biasing of Schmitt trigger and the power driver switch.
In addition, it performs the essential function of determining
the height or amplitude of final pulse that is applied across
the sample. This is accomplished by varying the front panel DC
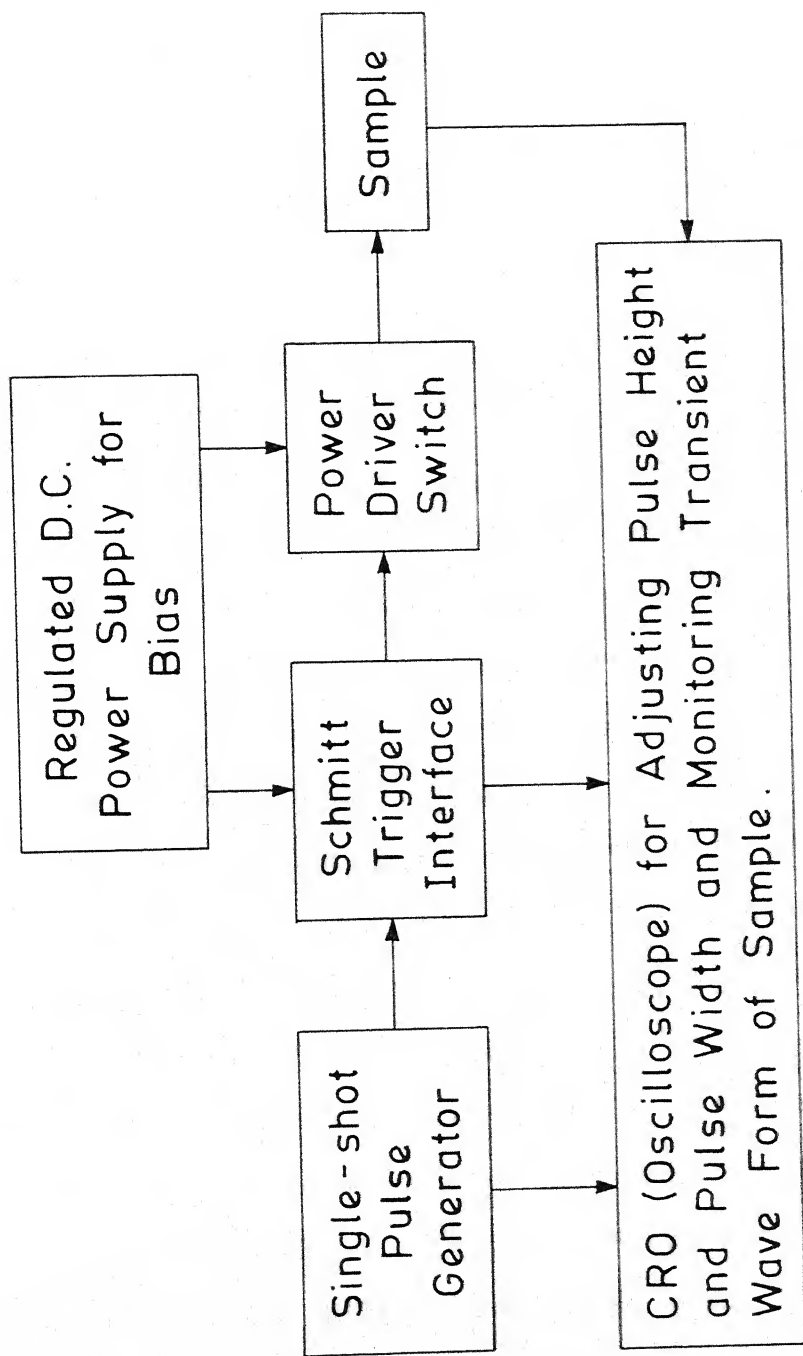
Fig. 4.4 Block diagram of circuit configuration showing principles of pulse circuit operation.

level control, provided on this equipment and monitoring it on
the CRO which is also connected to the circuit at relevant
mode for this purpose. The CRO made by Hewlett Packard
(Model 1725A; 275 MHz) is a dual trace oscilloscope with
delayed time base and digital volt/ohm meter.

Figure 4.5 shows the schematic representation of the
circuit used for pulse response measurement. Transistor Q_4
(ECN 055) is used as a shunt type of electronic switch and the
current limiting resistor R_{11} is in series with the parallel
combination of transistor Q_4 and the sample. The positive DC
supply voltage (V_{cc}) is used for supply the pulsed current.
When the input pulse to the base drive of Q_4 turns it off
from normally on-state, a pulse height of V_{cc} volts and
duration of τ seconds is impressed across the sample, conse-
quently when the pulse height and width are correct the sample
undergoes switching from the off to the on-state thereby
conducting current of significant magnitude limited only by
the series combination of resistor R_{11} and the sample in the
on-state. Finally, on termination of pulse duration τ, the
presently off-transistor Q_4 turns on again but this time shares
the current in parallel with the low impedance of the switched
sample. To apply a pulse which first turns off Q_4 on its
leading edge and then turns it back to the on-state τ seconds
later, the requisite base drive current is supplied by the pre-
driver stage consisting of transistor Q_3 (2N 2904) which in

Fig. 4.5   Schematic representation of pulse circuit.
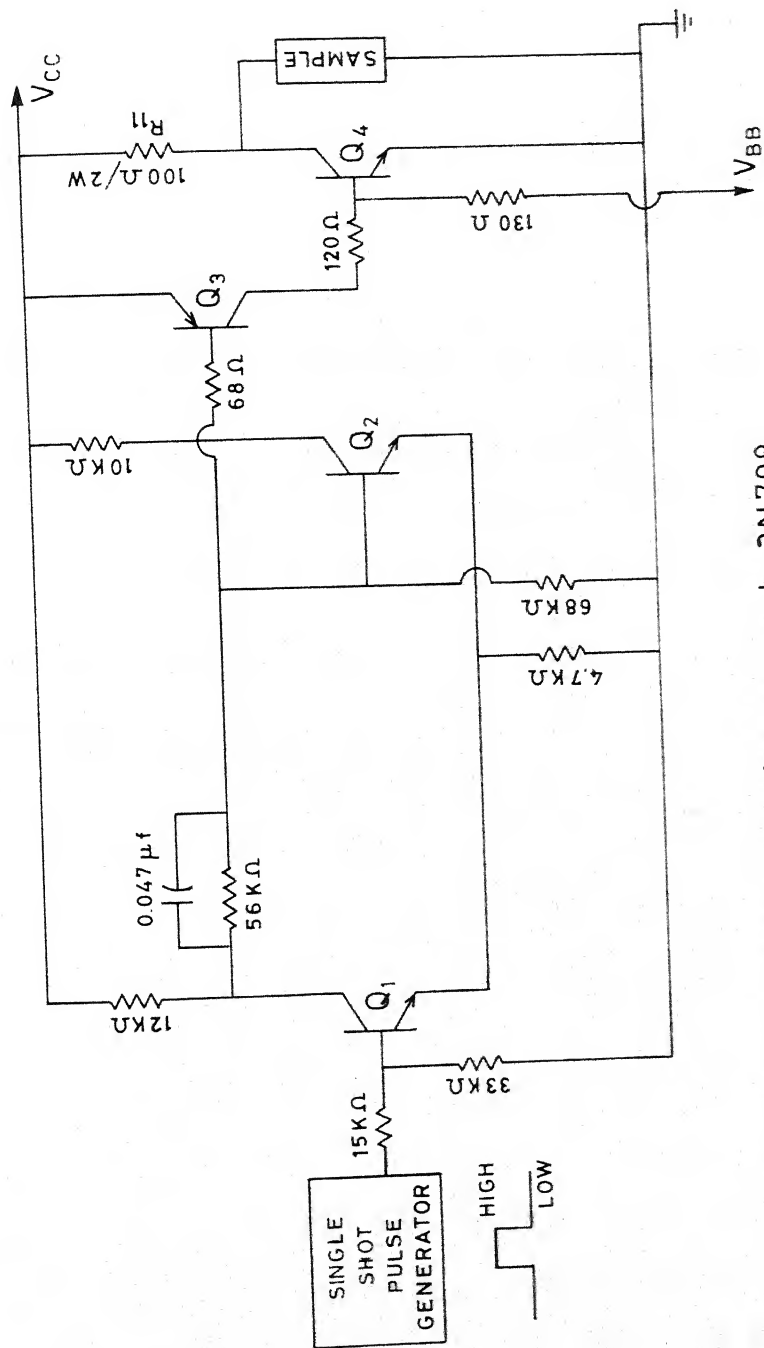
Q_1, Q_2 : Schmitt trigger transistors each 2N708
Q_3, Q_4 : Power driver switches (Q_3: 2N2904, Q_4: ECN055)
V_{CC} : Positive DC regulated supply
V_{BB} : Negative DC regulated supply

turn is driven by the composite combination of transistors Q_1 (2N 708) and Q_2 (2N 708) and associated components connected in Schmitt trigger configuration. The Schmitt trigger circuit $(Q_1 + Q_2)$ is a bistable regenerative switching circuit designed to buffer the pulse generator from the load of pre-driver and driver stages $(Q_3 + Q_4)$ and offers the additional important advantage of high speed switching action with improvement in the time of transitions on the leading and trailing edges.

4.4.2.2 Measurement procedure

For measurement we have placed the thin film sample vacuum deposited with gold on two faces between two metallic electrodes housed in a measuring cell as described in Section 3.3.6.2 of Chapter 3. The rectangular pulse is provided by a standard dual pulse generator. The internal trigger is used to provide a direct output monitored on a high bandwidth delayed time base (275 MHz) dual trace CRO with sample disconnected from the circuit. This is necessary to obtain a recurrent pulse train on the CRO screen which is held stationary thereon enabling to adjust via pulse generator controls the width of the positive pulse position to the requisite magnitude prior to each switching operation. The precision and accuracy of pulse width measurement is enhanced by the availability of the feature of time interval mode capability built into the specific CRO. The height of pulse actually driving the sample is V_{cc}, being determined by the DC regulated supply

voltage. Next, mode of pulse generator is changed over to the manual trigger mode and the sample is connected to the circuit in shunt across the driver Q_4. Now using the push botton microswitch of pulse generator a single shot pulse is injected into the circuit causing the driver to apply a single shot pulse drive across the sample so as to subject it to switching action. Finally the sample is disconnected from the circuit and its resistance is measured on a low voltage ohm meter (1V DC excitation) so as to determine whether the sample has switched from the off-state to the low resistance on-state (memory state). First we fix the pulse height at 5 volts and sequentially increase the pulse duration from 10 micro-seconds to a few hundred microseconds by suitable interval. Each time after passing a single pulse the sample is checked whether it has switched or not.

In the event of no switching taking place the pulse height is increased and the above sequence of experiments are repeated till the memory state is achieved.

4.5 Results and Discussions

Figure 4.6 represents the stretching of semi-major axis of the ellipsoid in molten condition by the critical switching field as a function of time for bismuth metal of radius 150 Å and separation to diameter ratio 0.03. The time required to join up is 9.5×10^{-10} second. It is seen from the figure
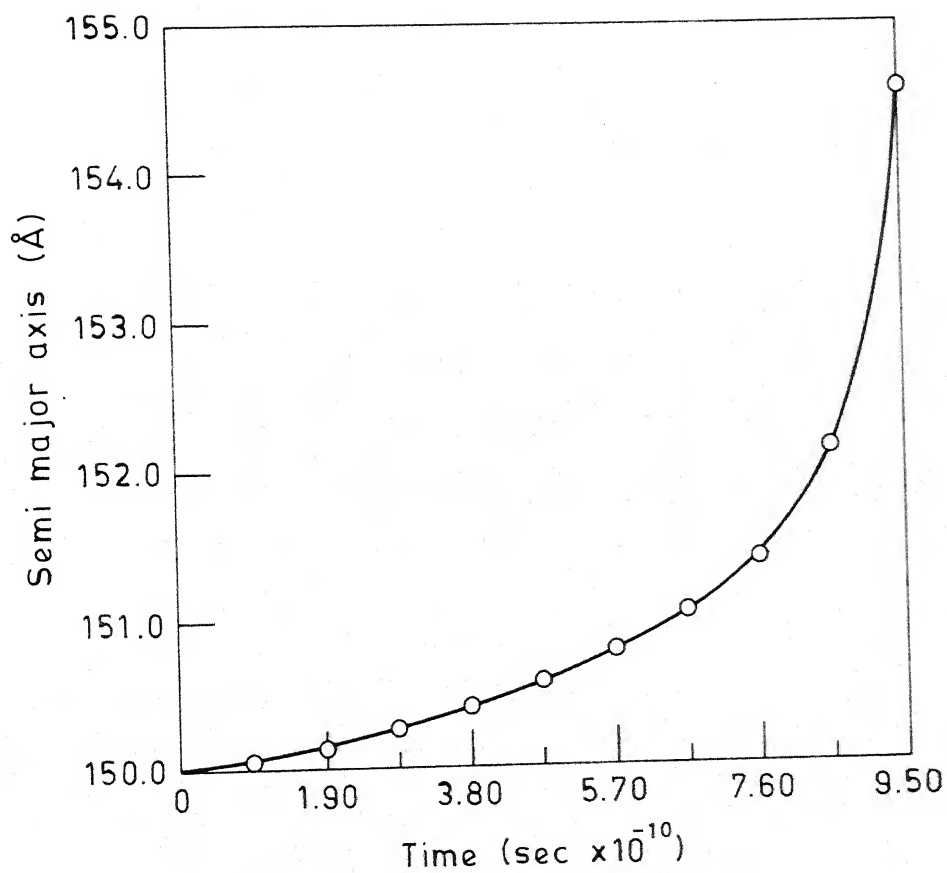
Fig. 4.6 Stretching of two neighbouring ellipsoids as a function of time under the influence of an electric field.

that initially the semi-major axis elongates slowly but later on at a rapid rate. This is because of the fact that as the distance between the two proximate grains decreases, the effective field increases (equation (4.55)) thereby causing a faster rate of deformation.

Table 4.1 gives the switching time (t_h) as calculated from the solution of the time dependent heat equation in Chapter 3 and the time (t_s) required for two proximate grains to coalesce as obtained from the solution of the fluid flow equations which has been described in this chapter for different diameters and separation to diameter ratios.

We observe that t_s remains almost constant for a particular diameter even if the s_o/d ratio increases. This arises due to the fact that a larger electric field is present in the latter case which lowered the time taken by the granules to stretch by the required amount. It is evident from the table 4.1 that t_s is less than t_h by approximately four orders of magnitude. Thus the stretching dynamics is much faster than the kinetics of the heating of the sample due to Joule losses. This, therefore, justifies the assumption made in Chapter 3 for the computation of I-V characteristics that once the required temperature profile is achieved within the sample, coalescence of proximate metallic granules takes place.

Table 4.2 gives a few typical values of switching time obtained by pulse experiments. These are found to have values

Table 4.1 Calculated switching time for a glass of composition $80V_2O_5, 15P_2O_5, 5Bi_2O_3$ (mole%) for different d and (s_o/d) ratios

Particle diameter $\overset{o}{A}$	Separation to diameter ratio (s_o/d)	Switching time for sample of thickness 10 μm $t_h \times 10^5$ sec.	Switching time as calculated from stretching of grains $t_s \times 10^9$ sec.
	0.02	1.32	0.95
	0.03	0.72	0.95
	0.04	0.50	0.94
300	0.05	0.36	0.94
	0.06	0.28	0.93
	0.07	0.23	0.93
	0.02	7.39	1.46
	0.03	3.88	1.45
	0.04	1.82	1.45
400	0.05	1.36	1.44
	0.06	1.07	1.43
	0.07	0.89	1.43
	0.02	–	2.03
	0.03	5.01	2.03
	0.04	2.88	2.02
500	0.05	2.05	2.01
	0.06	1.59	2.01
	0.07	1.29	2.00
	0.02	–	2.69
	0.03	8.49	2.68
	0.04	4.15	2.67
600	0.05	3.41	2.66
	0.06	2.12	2.65
	0.07	1.72	2.64

	0.02	–	3.38
	0.03	18.46	3.36
	0.04	5.86	3.35
700	0.05	3.69	3.33
	0.06	2.72	3.32
	0.07	2.16	3.31
	0.02	–	4.13
	0.03	–	4.10
	0.04	8.60	4.10
800	0.05	4.82	4.08
	0.06	3.42	4.06
	0.07	2.65	4.04
	0.02	–	4.92
	0.03	–	4.90
	0.04	–	4.88
900	0.05	6.36	4.86
	0.06	4.27	4.85
	0.07	3.23	4.83
	0.02	–	5.76
	0.03	–	5.74
	0.04	–	5.72
1000	0.05	8.63	5.69
	0.06	5.31	5.68
	0.07	3.90	5.65

Table 4.2 Comparison of experimentally determined switching time and switching field under pulse measurement with those theoretically calculated for a glass composition $80V_2O_5,15VP_2O_5,5Bi_2O_3$ (mole %)

Experimental switching field V/cm x 10^{-4}		E_m^b/calc. V/cm x 10^{-4}	Experimental switching time x 10^5 sec.	Switching time t_h x 10^5 sec. (calc.)	Switching time t_s x 10^9 sec. (calc.)
DC	Pulse				
0.63		$0.46(d=300\text{Å},s_o/d=0.02)$		$1.32(d=300\text{Å},s_o/d=0.02)$	$0.95(d=300\text{Å})$
	3.8	$0.87(d=300\text{Å},s_o/d=0.03)$	6.0	$0.72(d=300\text{Å},s_o/d=0.03)$	
		$1.30(d=300\text{Å},s_o/d=0.04)$		$7.39(d=400\text{Å},s_o/d=0.02)$	$1.46(d=400\text{Å})$
	2.5	$0.72(d=400\text{Å},s_o/d=0.03)$	5.0		

around 50-60 microseconds. The last two columns include the switching times t_h and t_s respectively taken from columns 3 and 4 of table 4.1. Columns 1 and 2 of table 4.2 give the switching fields as obtained by DC (from figure 3.6 of Chapter 3) and pulse measurements respectively. In column 3 of table 4.2, the theoretically calculated switching fields (taken from column 6 of table 2.1 of Chapter 2) are given.

Comparing columns 4 and 5 of table 4.2 we see that the calculated t_h is in agreement within order of magnitude of the experimental switching time for particles of diameters 300 Å and 400 Å with separation to diameter ratios of 0.02 and 0.03.

However, t_s is much smaller as compared to the experimental value. Hence, switching at room temperature is controlled by the Joule heating step as we have mentioned earlier. However, it is possible in principle to get a switching speed of the order of nano-seconds provided the metallic particles are in the molten state.

Comparing columns 1,2 and 3 of table 4.2 we see that experimental switching fields (DC and pulse) are within order of magnitude of the predicted fields for particles of diameters 300 Å and 400 Å with separation to diameter ratios of 0.02, 0.03 and 0.04. The differences in the switching fields as measured under DC and pulse conditions are attributed to the variation in microstructure depending on the melting and the blowing conditions of glasses. This agreement is reasonable

in view of the fact that a number of simplifying assumptions have been made in developing the model in Chapter 2.

It is necessary to raise the temperature to the melting point of bismuth so that the molten metallic bismuth granules can be stretched under the action of an electric field. It has been shown in Chapter 2 that the critical electric field for heating is less than the critical field for memory switching. Thus the electric field applied will raise the temperature level within the material to a value much higher than what is required for melting of bismuth granules. As the temperature increases the glass structure becomes more open and also due to the fact that $V_2O_5-P_2O_5-Bi_2O_3$ glasses are fairly low melting it is believed that the resistance offered by the matrix to the stretching of molten bismuth particles will be small as compared to the surface tension forces. We have, therefore, neglected any such opposing force by the glass matrix to the granule deformation in our analysis.

CHAPTER 5

OPTICAL PROPERTIES OF VANADIUM PHOSPHATE AND SILICATE GLASSES CONTAINING BISMUTH GRANULES

5.1 Introduction

Colloidal suspensions in glasses scatter light. Colloids of large particle size and sufficient concentration can generate turbidity in the glass which is undesirable. Therefore, to induce interesting optical properties highly absorbing materials are needed to predominate over the scattering. Metals being highly absorbing meet this condition provided the particle sizes are kept below 50 nm. Therefore, a proper choice of glass compositions and control of melting conditions can lead to the formation of ultrafine metal particles in a glassy matrix.

Doremus[113,114] has studied the optical absorption of photosensitive alkali aluminoborosilicate glasses containing gold and silver. The latter are precipitated in the colloidal form by UV radiation followed by a suitable heattreatment. The spectral dependence of optical absorption has been analysed by Mie theory. In the case of glass containing gold the correspondence between theory and experiment is good while in the other case the measured absorption compares reasonably well with that predicted by Mie theory with regard to the shape and position of the absorption peak.

Yellow, amber and red colours can be induced in the glasses by the process of staining. In this process compounds of silver or copper or a mixture of these are applied on the surface of the glass. Then the coated glass is baked to a temperature in the range of annealing so that silver and copper undergo ion-exchange with the alkali metal-ions. The subsequent reduction treatment induces metallic colloids within the surface of the glass by nucleation and growth. The optical absorption of the borosilicate glass (composition similar to 'Pyrex') stained with copper and a mixture of copper and silver has been studied by Rawson[115]. Mie theory has been used to quantitatively account for the spectral transmission curve in the range of 0.4 to 0.8 μm. The quantitative agreement between the calculated and the experimental transmission is good for glasses stained with copper alone, but the agreement is less satisfactory when a mixture of copper and silver is present. This deviation is attributed to the formation of copper-silver alloy particles.

Chakravorty et al.[116] have studied the optical absorption of the float glass which has been subjected to ion-exchange with copper salt followed by reduction. The ion-exchange and reduction produce metallic copper within the surface of the glass. The characteristic absorption bands have been explained by Maxwell-Garnett theory. Recently, optical studies in the visible range have been carried out on alkali containing

C-glasses and borosilicate glasses which have been subjected to ion-exchange in molten $AgNO_3$ followed by a reduction treatment in hydrogen gas at different temperatures and for various time periods[117]. The absorption peak position has been explained on the basis of Maxwell-Garnett effective medium theory.

The optical properties of cermet films produced by co-sputtering or evaporation (see Section 1.6 of Chapter 1) have also been studied extensively. The early measurement of optical properties of evaporated Au/SiO_2 cermet films in the range $0.4 < \lambda < 0.7$ has been reported by Hampe[118]. Cohen et al[119] have investigated in details the optical properties of co-sputtered Ag/SiO_2 and Au/SiO_2 cermet films in the entire range of 0.2 μm to 1.7 μm. Lissberger et al,[120,121] have studied the optical properties of MgF_2/Au and Co/MgF_2 in the range of $0.4 < \lambda < 0.6$ μm.

Granqvist et al.[122] have studied the optical properties of ultrafine gold particles produced by evaporation of pure gold in presence of air at a few torr. The percent transmission shows a characteristics transmittance dip at around 0.6 μm. Extensive computer calculations have been carried out based on the effective medium theories of Maxwell-Garnett as extended by Polder and van Santen (MG-PvS), of Hunderi (HU) and of Bruggeman (BR) to explain the spectral dependence of optical absorption. It has been shown that in the limit of low

concentration of metal all the above effective medium theories predict the same result. By invoking the dipole-dipole interaction between the metallic particles a better quantitative agreement has been achieved. The dipole-dipole interaction has been accounted for approximately by a set of effective depolarisation factors. Further assuming that the microstructure consists of certain fractions of spheres, f.c.c. clusters and single strand chains quantitative agreement within a few percent has been obtained. In the case of ultrafine aluminium produced by evaporation in a gas mixture of helium and oxygen, the optical transmission characteristics have been explained within the MG formalism by suitably incorporating the dipole-dipole interaction and size dependent dielectric permittivity of metal particles coated with oxide.[123] However the transmission dip occurring at 0.85 µ is much less compared to the theoretically predicted one. This has tentatively been ascribed to defect scattering within the metal particles. Similarly, the optical properties of metal-dielectric[35,124-126] composites formed by evaporation of metals - nickel, chromium, silver and gold have been interpreted by using effective medium theories.

Abeles and Gittleman[127] have studied the insulator rich Ag/SiO_2 cermet films and by applying MG theory they conclude that the latter is superior to BR theory to explain the data. However, Granqvist et al.[128] have studied the applicability of MG-PvS, HU and BR theories on the experimental data of

Cohen et al.[119]. It has been found that no single effective medium theory can explain the experimental transmittance dip. However, this feature can atleast be explained qualitatively by incorporating the distribution of depolarisation factors in the MG type of effective medium theory. Optical properties of co-sputtered Cr_2O_3/Cr[33], MgO/Au[32] and co-evaporated Ni/Al_2O_3[34] have been investigated with a view to study the suitability of their application to photothermal conversion. Craighead et al.[34] have found a good correspondence between the prediction of MG theory and the optical absorption data of Ni/Al_2O_3 cermet films. Granqvist[129] has carried out theoretical analysis based on MG and BR effective medium theories on the experimental optical data of MgO/Au[32,130], Al_2O_3/Au[131] and MgF_2/Au[120]. The analysis shows that BR theory is superior to MG formalism in Au/MgO and Au/Al_2O_3 cermet films but no such definite conclusion can be drawn in the case of MgF_2/Au cermet systems. Granqvist et al.[132,133] have carried out extensive computer calculations based on effective medium theories and applied to the case of silver in glassy matrix[134,135] and to the Cr/Cr_2O_3[33] cermet system.

Compared to an extensive investigation on the optical properties of metal-dielectric composite systems produced by sputtering or evaporation, such studies on glasses containing metallic granules are few. In this chapter we report on the characterisation of optical properties of oxide glasses

containing bismuth granules of dimensions of the order of a few hundred angstroms. Analyses of the type used in the case of cermet films have been applied extensively in the present investigation.

5.2 Experimental Procedure

5.2.1 Glass preparation and making of films

The glass compositions which have been investigated for optical studies are given in table 5.1.

The melting and preparations of thin films for first three glasses are similar to those discussed in Section 3.3.1 and 3.3.2.1 of chapter 3. Glasses 4,5 and 6 have been prepared from reagent grade chemicals. B_2O_3 has been added as H_3BO_3 Na_2O as Na_2CO_3, and SiO_2 and Bi_2O_3 have been introduced as their oxides. The glass batch is accurately weighed, thoroughly mixed in acetone and melted in a hard fired alumina crucible in an electrically heated furnace in the temperature range of $1300^\circ C$ to $1400^\circ C$. After homogenisation, the films of glasses are prepared by blowing as discussed in Section 3.3.2.1 of Chapter 3.

5.2.2 Reduction of thin films

Figure 5.1 shows the reduction furnace schematically. A pyrex tube closed at both ends is inserted through the mullite muffle of an electrically heated furnace. R represents

132

Table 5.1   Compositions of glasses

Glass No.	Composition in mole percent					
	V_2O_5	P_2O_5	SiO_2	B_2O_3	Na_2O	Bi_2O_3
1	80	20	–	–	–	–
2	80	15	–	–	–	5
3	70	20	–	–	–	10
4	–	–	64	26	10	–
5	–	–	64	18	10	8
6	–	–	64	14	10	12
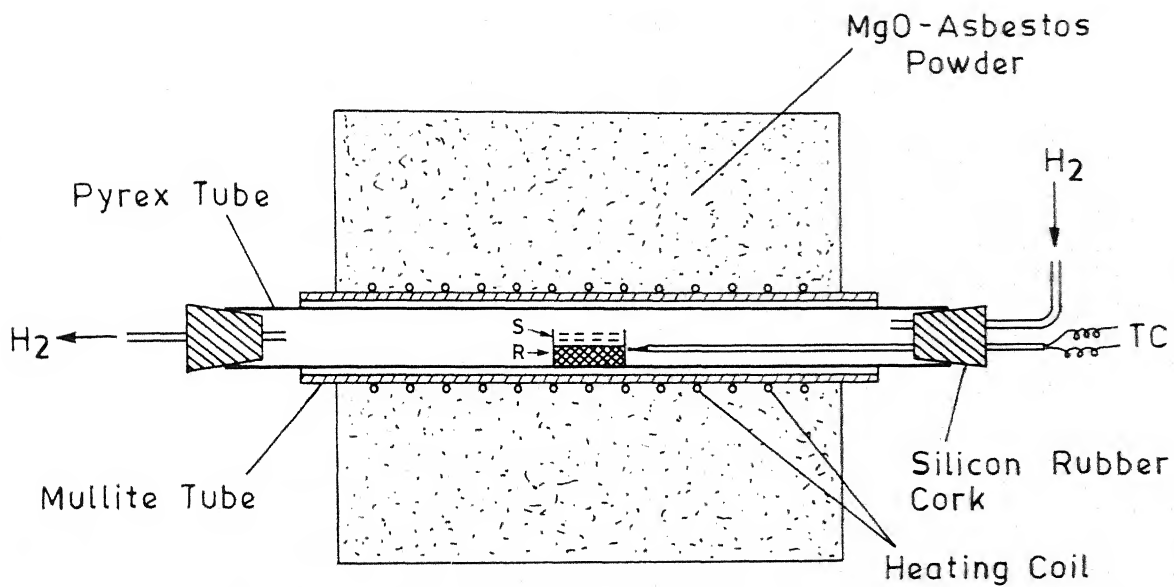
Fig. 5.1 Reduction furnace.

a refractory block on which the thin glass films S sandwitched between perforated metallic sheets are placed. A thermocouple TC is placed near the sample and is connected to an Aplab temperature controller. The reduction treatment has been carried out by passing hydrogen at a rate of 100 c.c./minute. Glasse no. 2 and 3 of the V_2O_5-P_2O_5-Bi_2O_3 system have been reduced at $200^{\circ}C$ for 1.0 hour and 2.0 hours respectively whereas the glass no. 5 and 6 of the Na_2O-B_2O_3-SiO_2-Bi_2O_3 system have been reduced at $300^{\circ}C$ for the duration of 1.0 hour and 1.5 hours respectively.

5.2.3 Transmission electron microscopic studies

The technique for electron microscopic sample preparation has been described in Section 3.3.5 of Chapter 3. The microstructure and selected area diffraction (SAD) patterns of all virgin and reduced glasses containing bismuth have been taken by using Phillips EM 301 Electron Microscope. The SAD patterns have been analysed in a manner similar to that discussed in Section 3.3.5.

5.2.3.1 Average particle size determination

For each sample a number of electron micrographs have been taken. A few hundred particles are measured. Then using the following formulae the average particle size and standard deviation have been calculated.

$$\bar{x} = \sum_{j=1}^{n} x_j n_j / N \qquad (5.1)$$

$$s = [\sum_{j=1}^{N} (x_j - \bar{x})^2 / (N-1)]^{\frac{1}{2}} \qquad (5.2)$$

where x_j and n_j are respectively the mean particle size and frequency of the ith interval, n and N are the number of intervals and the total number of particles respectively. s is the standard deviation.

5.2.3.2 Calculation of volume fraction

Assuming the precipitation of particles to be homogeneous throughout the glass matrix, we have used the point counting method to estimate the volume fraction (f_c) by the following expression[136],

$$f_c = \frac{n'}{N'} \qquad (5.3)$$

where n' and N' are respectively the number of cross points coinciding with the particles and the total number of points present in the selected area of the transparent graph paper. However, the volume fraction calculated by this method is greater than the actual one because of the superimposition of all the particles across the thickness on the two dimensional electron microphotograph. Assuming the particles to be spherical the actual volume fraction f of the particles can be related to f_c by the following expression ,

$$f = \frac{2}{3} f_c (\frac{\bar{x}}{t_{em}}) \qquad (5.4)$$

where t_{em} is the thickness of electron microscopic sample.

5.2.4 Optical absorption studies

For studying the optical absorption the thin glass films have been sandwitched between two hard papers each having a square hole of about 5 mm x 5 mm punched in it. The optical spectra of virgin as well as reduced V_2O_5-P_2O_5-Bi_2O_3 glasses (glass no. 2 and 3) have been taken in the visible range using base glass no.1 as the reference, while for Na_2O-B_2O_3-SiO_2-Bi_2O_3 glasses (glass no. 5 and 6), base glass no.4 has been used as reference. The spectra for the base glasses (glass no. 1 and 4) have been taken using air as the reference. All the spectra have been measured using Carry 17D Spectrophotometer.

5.2.4.1 Calculation of optical absorption coefficient, α

Carry 17D plots the optical density (O.D.) as a function of wavelength λ. From this curve at any wavelength we get,

$$(O.D.)_{sample} = (O.D.)_{observed} + (O.D.)_{reference} \qquad (5.5)$$

From Beer-Lambert's law which relates optical density to absorption coefficient α, we get,

$$\alpha = \frac{2.303\left[(O.D.)_{observed} + (O.D.)_{reference}\right]}{t_{sample}} \qquad (5.6)$$

where t_{sample} represents the thickness of the sample.

5.3 Results

Figures 5.2(a) and (b) show the plots of optical density as a function of wavelength in the visible range for vanadium
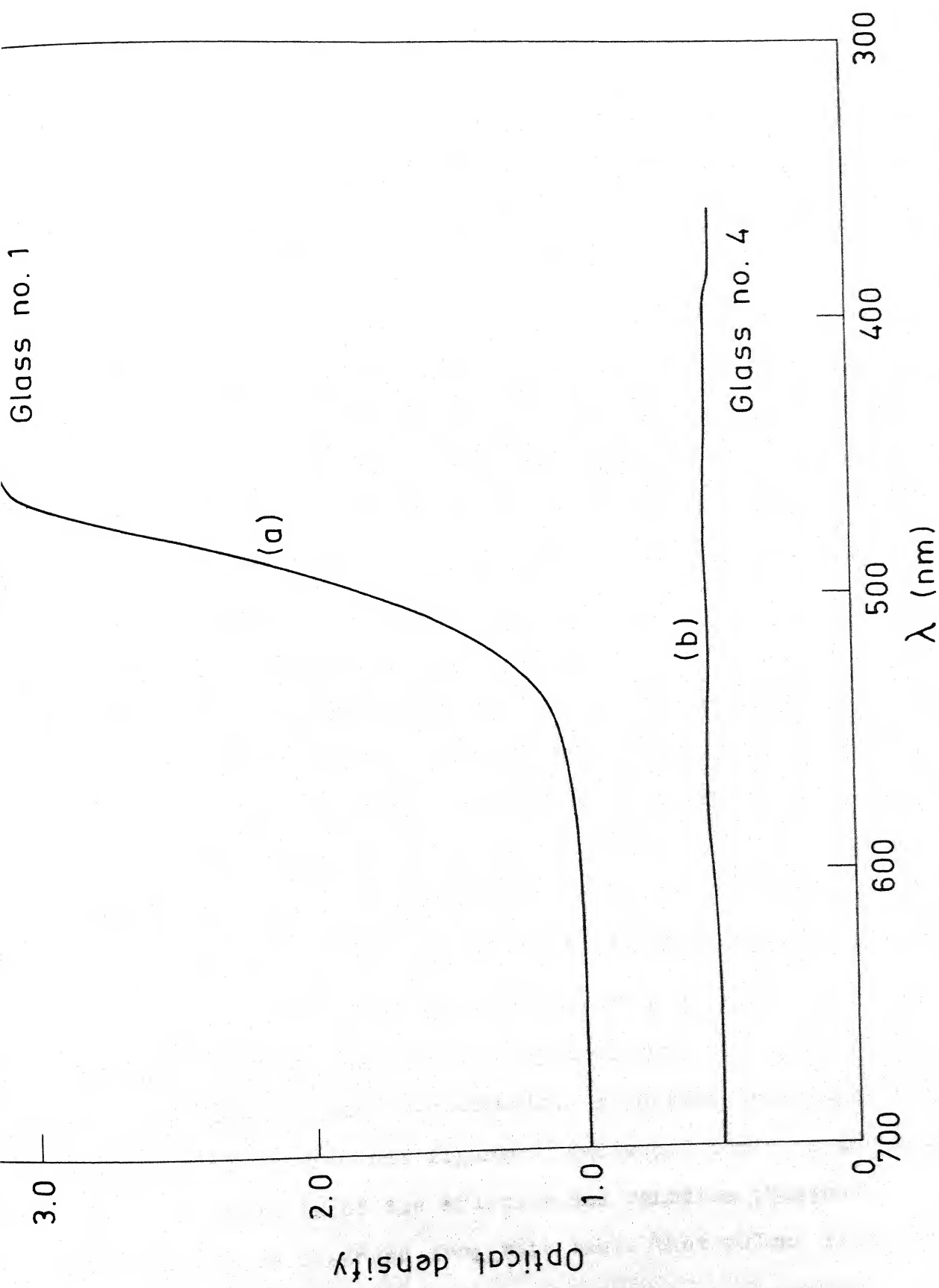
Fig. 5.2 Optical density as a function of wavelength for base glasses

phosphate base glass no.1 and silicate base glass no.4 respectively. While glass no.1 shows an absorption edge, the glass no.4 is featureless. Figure 5.3 represents the plots of optical absorption coefficients as a function of wavelength for glass no.2 and 3. Different reduction treatments applied to these glasses are indicated on the curves. It is observed that as the reduction time is increased for the same amount of bismuth in the glass compositions the absorption coefficients increase . The absorption peaks for glass no.3 subjected to different heattreatments occur at the same wavelength 440 nm, while for glass no.2 they occur in the range of 450-460 nm. Figure 5.4 represents the plots of α values as a function of wavelength for glass no.5 and 6 for different reduction treatments. The arrow head attached to the curve indicates the scale of α to the right. Like the vanadium phosphate system, it is observed that as the reduction time increases α values for both glass no.6 and glass no.5 increase. Unlike vanadium phosphate system, each absorption curve showstwo broad peaks in the range 500-530 nm and 420 nm to 430 nm respectively.

Figures 5.5 to 5.16 show the electron micrographs of the vanadium phosphate and silicate systems under investigation for different reduction treatments. Reduction treatments are indicated along with the figures. Table 5.2 contains the micro-structural details of the silicate and vanadium phosphate glasses. It is observed from this table that volume fraction f
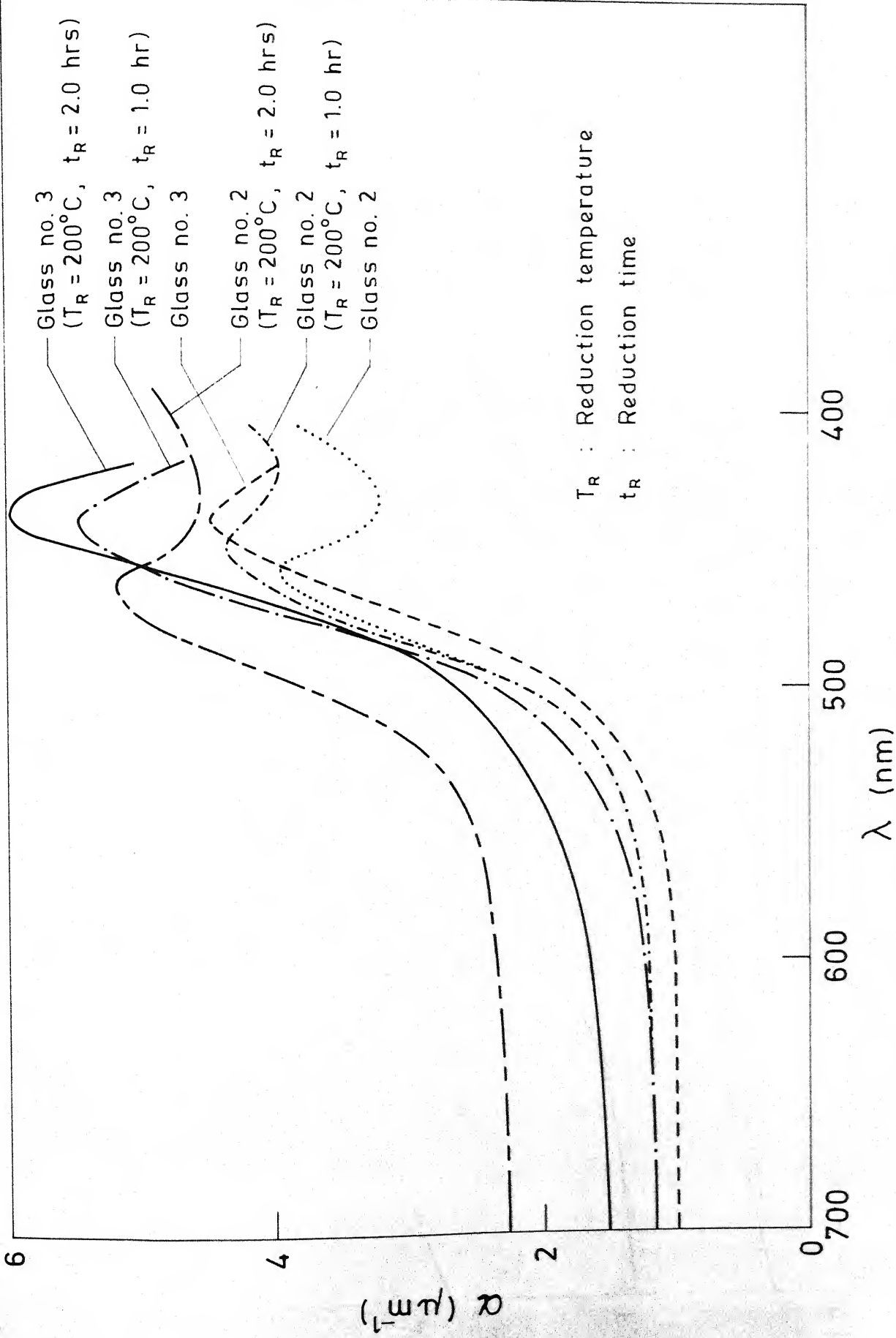
Fig. 5.3 Absorption coefficient α as a function of wavelength λ for $V_2O_5 \cdot P_2O_5$ glasses containing bismuth.

Legend:

Glass no. 3 ($T_R = 200°C$, $t_R = 2.0$ hrs)
Glass no. 3 ($T_R = 200°C$, $t_R = 1.0$ hr)
Glass no. 3
Glass no. 2 ($T_R = 200°C$, $t_R = 2.0$ hrs)
Glass no. 2 ($T_R = 200°C$, $t_R = 1.0$ hr)
Glass no. 2

T_R : Reduction temperature
t_R : Reduction time
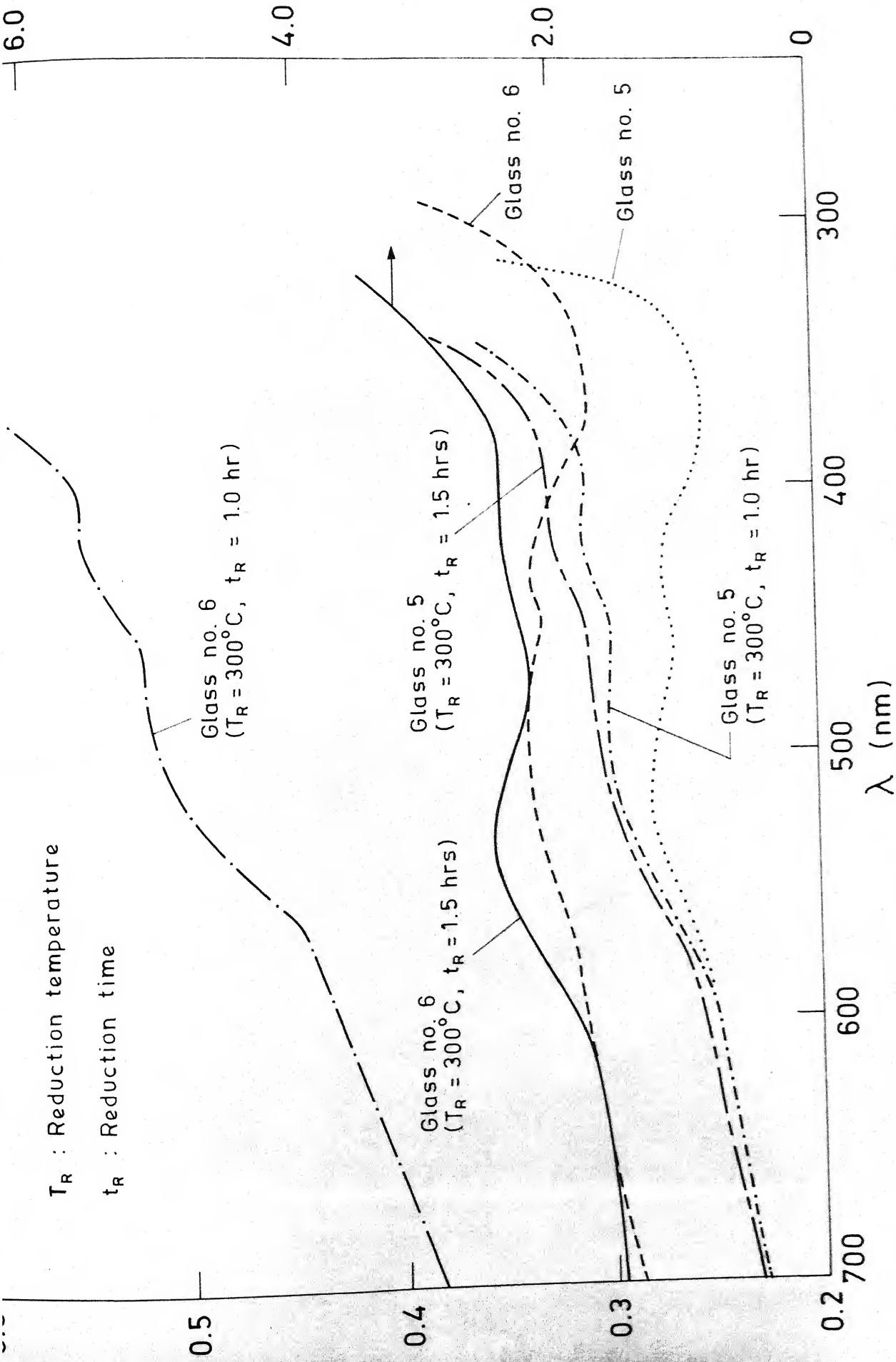
Fig. 5.4 Absorption coefficient α as a function of wavelength λ for silicate
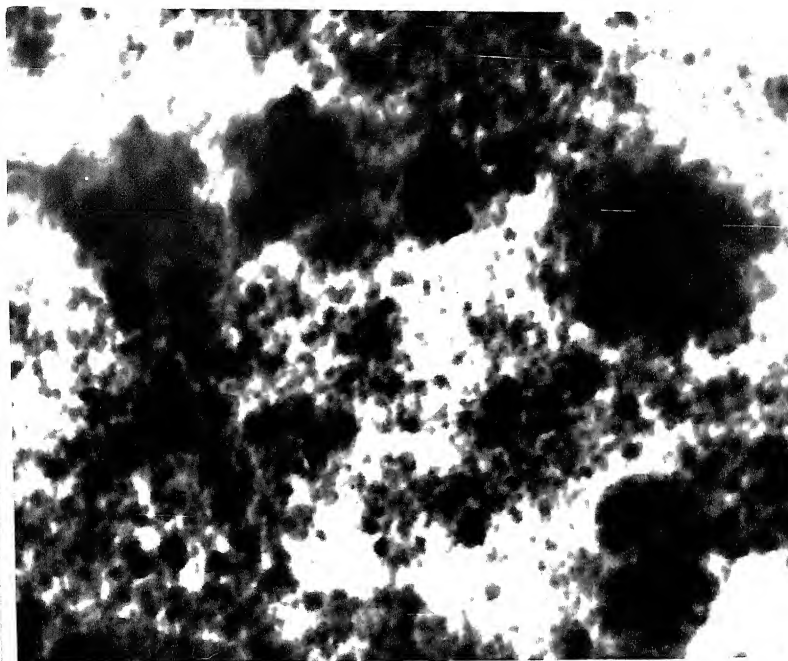
Fig.5.5 Electron micrograph of a sample of
        glass no.2
        X 117,000
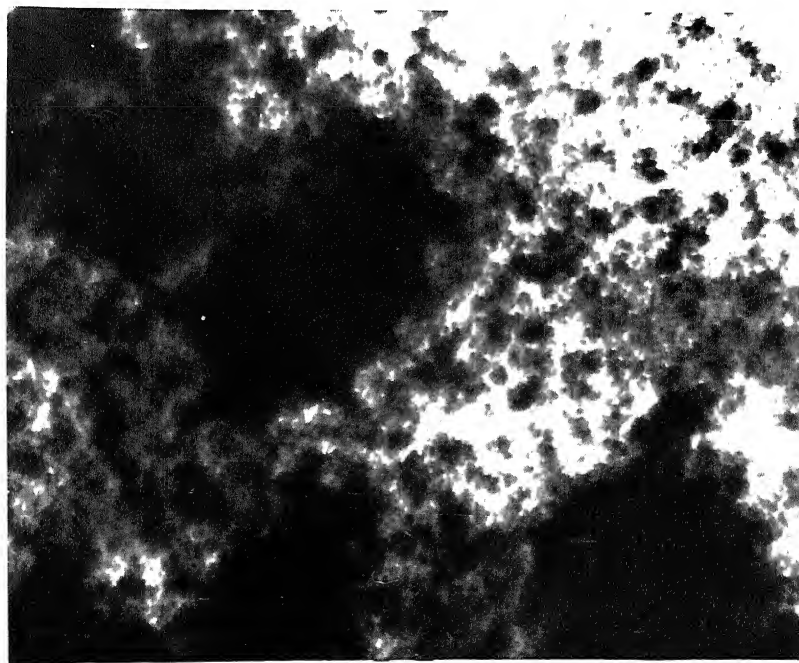
Fig.5.6 Electron micrograph of a sample of
        glass no.2 reduced at 200°C for
        1.0 hour
        X 84,000
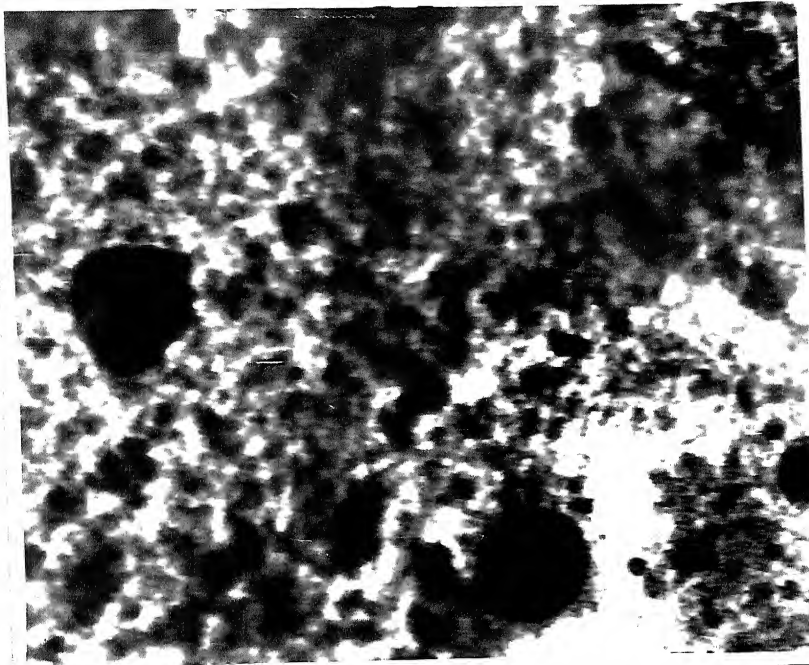
Fig.5.7 Electron micrograph of a sample of
glass no.2 reduced at 200°C for
2.0 hours
X 84,000

Fig.5.8 Electron micrograph of a sample of
glass no.3
X 84,000
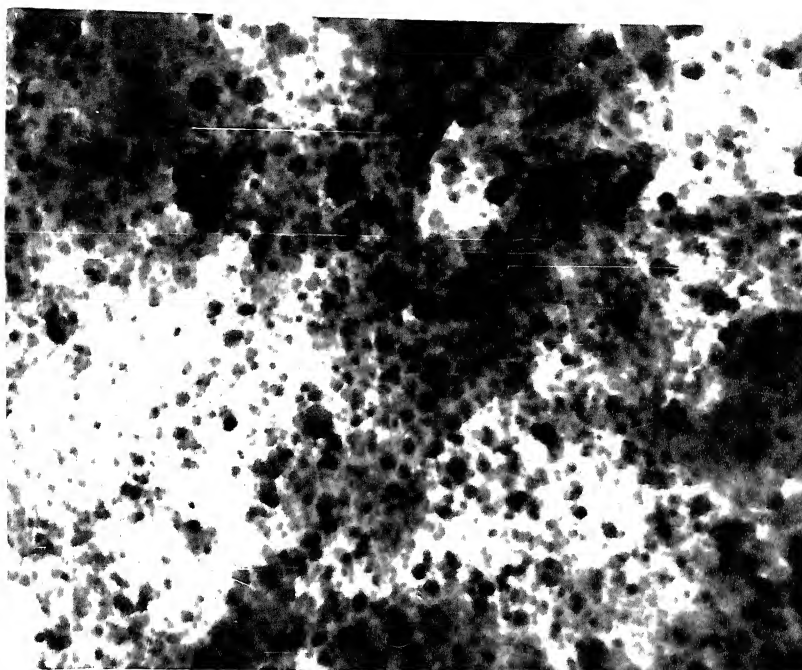
Fig.5.9 Electron micrograph of a sample of
glass no.3 reduced at 200°C for
1 hour
X 84,000
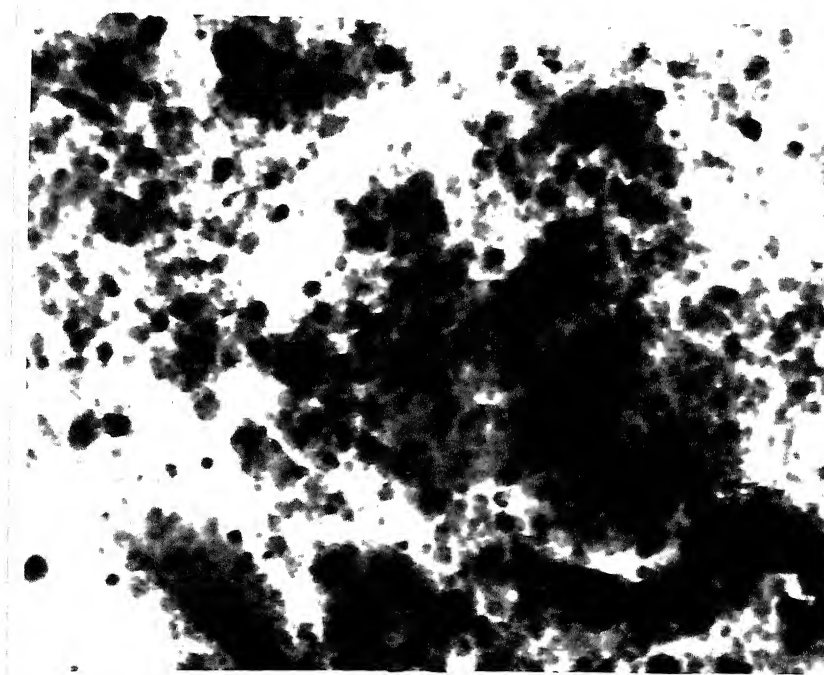
Fig.5.10 Electron micrograph of a sample of
glass no.3 reduced at 200°C for
2.0 hours
X 84,000
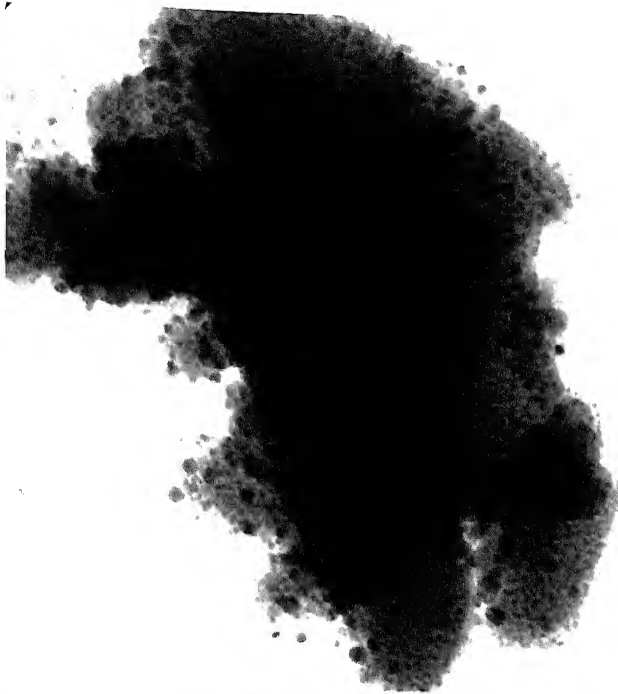
Fig.5.11 Electron micrograph of a sample of
glass no.5
X 117,000

Fig.5.12 Electron micrograph of a sample of
glass no.5 reduced at 300°C for 1 hour
X 117,000

Fig.5.13 Electron micrograph of a sample of
glass no.5 reduced at 300°C for
1.5 hours
X 117,000
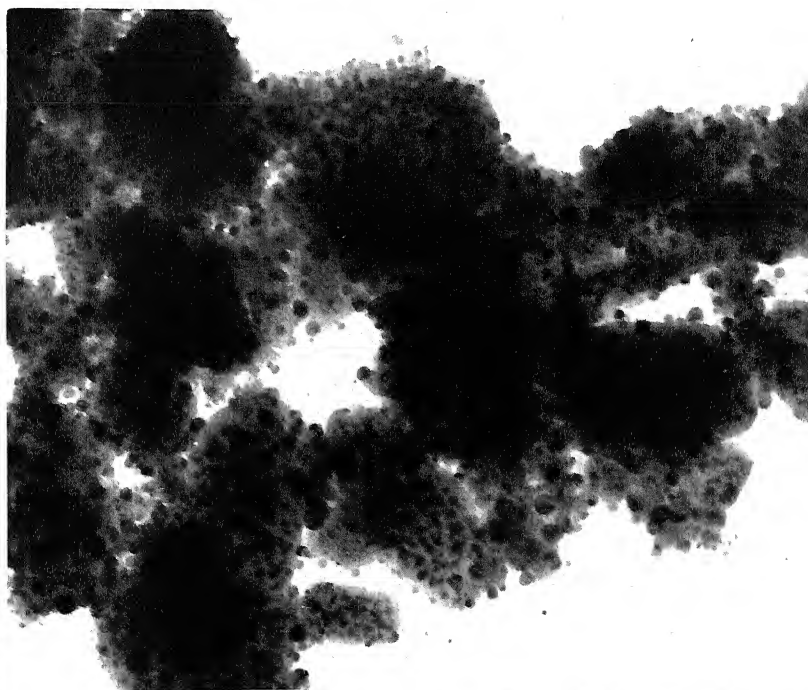
Fig.5.14 Electron micrograph of a sample of
glass no.6
X 66,000
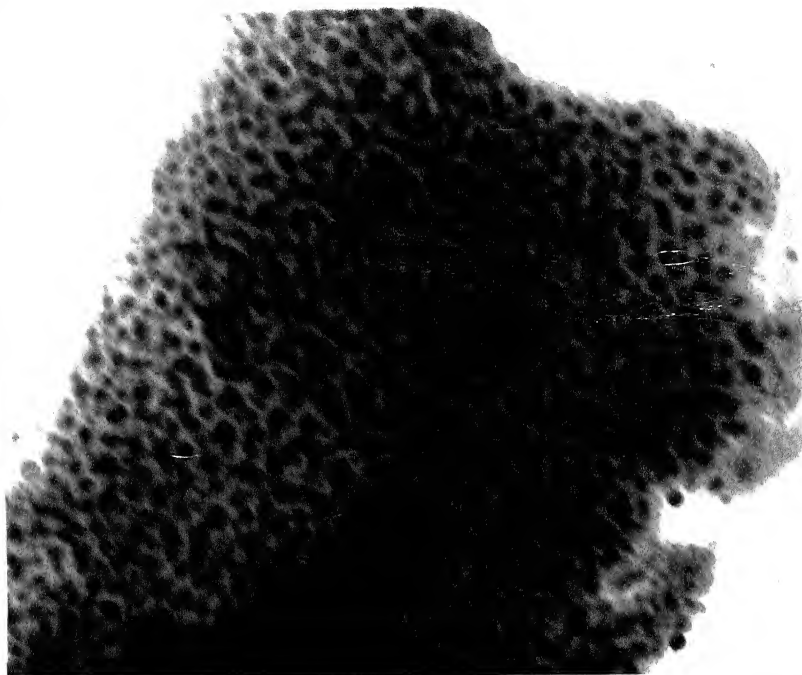
Fig.5.15 Electron micrograph of a sample of glass no.6 reduced at 300°C for 1.0 hour
X 117,000

Fig.5.16 Electron micrograph of a sample of glass no.6 reduced at 300°C for 1.5 hours
X 117,000

Table 5.2 Microstructural parameters for different glasses under various reduction treatments

Glass System	V₂O₅-P₂O₅-Bi₂O₃						SiO₂-B₂O₃-Na₂O-Bi₂O₃					
Glass No.	2		3				5			6		
Reduction T	200	200	200	200	200	200	300	300	300	300	300	300
Treatment t	1	2	1	2	1	2	1	1.5	1	1.5	1	1.5
f_c	0.4	0.47	0.49	0.25	0.50	0.40	0.35	0.44	0.47	0.50	0.50	0.56
f	0.024	0.034	0.033	0.013	0.034	0.04	0.019	0.028	0.03	0.052	0.043	0.033
$\bar{x}$	90	109	102	77	116	152	81	94	95	156	129	89
s	40	57	60	22	46	45	30	29	35	36	56	32

Note : T - Reduction temperature in degree C

    t - Reduction time in hours

for glass no.2 and 3 varies in the range 0.01 to 0.04 and
the average diameter varies in the range 75 to 155 angstroms.
For the silicate glasses f varies in the range 0.02 to 0.05
and the average particle size varies in the range of 80-160
angstroms.

Figures 5.17 and 5.18 show the SAD patterns of vanadium
phosphate system for glass no.2 and glass no.3 reduced at
200°C for 2 hours respectively. Figures 5.19 and 5.20 show the
SAD patterns for glass no.5 reduced at 300°C for 1.5 hours and
glass no.6 respectively. Tables 5.3 to 5.6 give the calculated
interplanar spacings (d_{hkl}) from figures 5.17 to 5.20 res-
pectively. Standard d_{hkl} values of metallic bismuth[108] have
been included in each table for comparison. In V_2O_5-P_2O_5
system (figures 5.5 - 5.10) globular structure is more prominent
in figures 5.8 and 5.9, while in silicate system (figures
5.11 - 5.16) globular structure is more pronounced except in
figures 5.15 and 5.16. However, in all figures certain fractions
of interconnected chains are discernible.

5.4 Discussions

Before discussing experimental results as given in the
last section we briefly describe the salient features of the
different theories available for explaining the optical behaviour
of inhomogeneous materials.
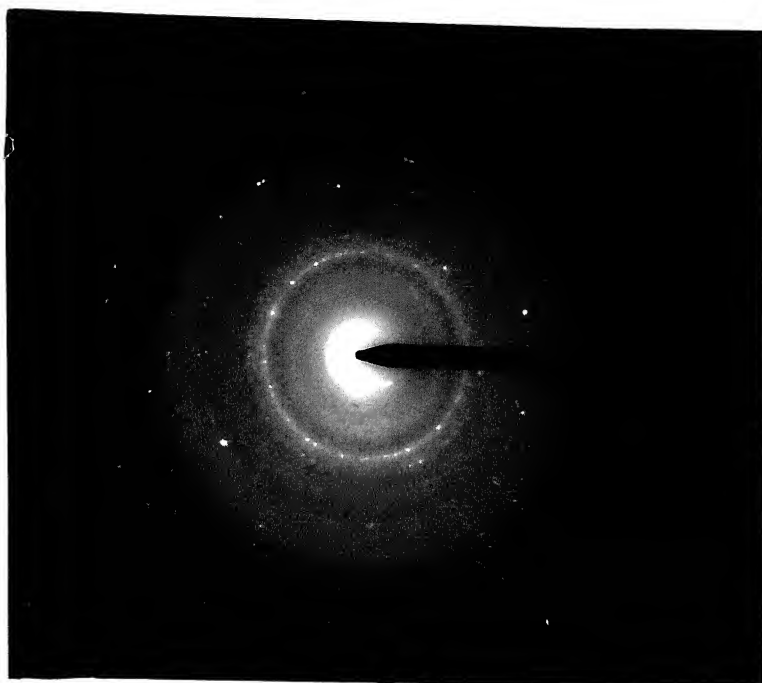
Fig.5.17 Electron diffraction pattern of a
sample of glass no.2
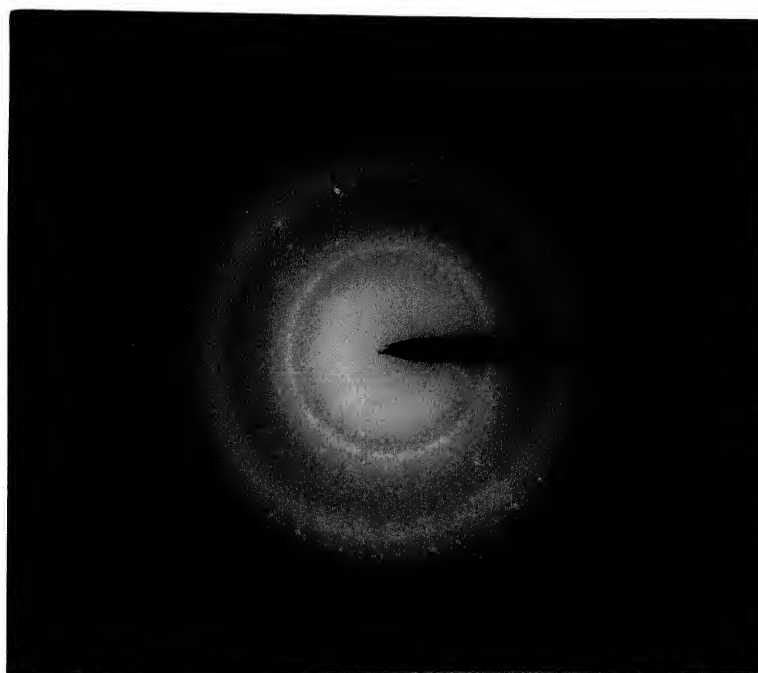
Fig.5.18 Electron diffraction pattern of a
sample of glass no.3 reduced at
200°C for 2 hours

Fig.5.19 Electron diffraction pattern of a
sample of glass no.5 reduced at
300°C for 1.5 hours
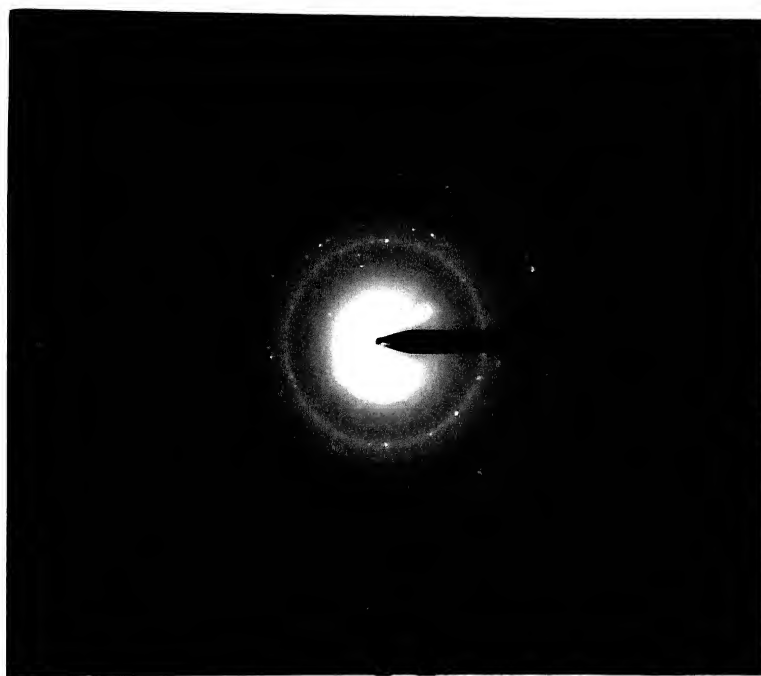
Fig.5.20 Electron diffraction pattern of a
sample of glass no.6

Table 5.3 Comparison of calculated d_{hkl} values of
glass no.2 with standard d_{hkl} values

Calculated d_{hkl} $\overset{o}{A}$	Standard d_{hkl} for bismuth[108] $\overset{o}{A}$
2.20	2.27
1.86	1.87
1.31	1.33
1.11	1.12
0.83	-

Table 5.4 Comparison of calculated d_{hkl} values of
glass no.3 reduced at $200^{o}C$ for 2.0 hours
with standard d_{hkl} values

Calculated d_{hkl} $\overset{o}{A}$	Standard d_{hkl} for bismuth[108] $\overset{o}{A}$
2.17	2.27
1.84	1.87
1.30	1.33
1.10	1.10
0.81	-

Table 5.5   Comparison of calculated d_{hkl} values of
glass no.5 reduced at $300^{\circ}C$ for 1.5 hours
with standard d_{hkl} values

Calculated d_{hkl} $\overset{\circ}{A}$	Standard d_{hkl} for bismuth[108] $\overset{\circ}{A}$
2.20	2.27
1.86	1.87
1.33	1.33
1.12	1.12

Table 5.6   Comparison of calculated d_{hkl} values of
glass no.6 with standard d_{hkl} values

Calculated d_{hkl} $\overset{\circ}{A}$	Standard d_{hkl} for bismuth[108] $\overset{\circ}{A}$
2.20	2.27
1.89	1.87
1.33	1.33
1.12	1.12

5.4.1 Mie Theory

Mie equations[137] have been derived by applying Maxwell's electromagnetic equations to small conducting particles which absorb and scatter light, the dimensions of the particles being smaller than the wavelength of the optical radiation. For identical spherical particles the solution of electromagnetic equations for each particle is given by[138]

$$Q_{scat} = \text{Real part of } \frac{8}{3} A^4 \left[\frac{m^2-1}{m^2+2}\right]^2 \tag{5.7}$$

$$Q_{abs} = \text{Imaginary part of } 4A\left(\frac{m^2-1}{m^2+2}\right) + \frac{4}{15} A^3\left[\frac{m^2-1}{m^2+2}\right]^2 \cdot$$

$$\cdot \left[\frac{m^4+27m^2+38}{2m^2+3}\right] \tag{5.8}$$

where
$$A = \frac{2\pi r N_g}{\lambda} , \tag{5.9}$$

r being the radius of particles, N_g the refractive index of glass and λ the wavelength.

$$m = \frac{N-iK}{N_g} \tag{5.10}$$

with N and K being the real and imaginary parts of optical constants of the particles. Q_{scat} and Q_{abs} are respectively defined as the proportions of light being scattered and absorbed by each particle divided by the cross-sectional area (πr^2). The optical density can be related by the following expression,

$$OD = \frac{3}{4} \frac{ML'\, Q_{ext}(2.303)}{r\rho} \qquad (5.11)$$

where $Q_{ext} = Q_{scat} + Q_{abs}$. M is the weight fraction of the metal particles per unit volume of the composite, ρ is the density of the metallic particles and L' is the sample thickness. Since Q_{scat} is related to the 4th power of radius of particle and the primary term of Q_{abs} is linearly dependent on the particle radius for sufficiently small particle radii (around 20 nm) the contribution of Q_{abs} will be dominant. In this small particle size range, as can be seen from equations (5.9) and (5.11) the optical density is independent of particle size. On the other hand the contribution from Q_{scat} becomes significant when the particle size increases. Hence for large values of particle radii the OD is dependent on the particle size. In the latter case it is likely that the particles will deviate from spherical shape. Mie theory has been modified by Gans[139,140] to take into account the effect of deviation from sphericity.

5.4.2 Effective medium theories

Effective medium theories have been used quite extensively to metal-dielectric microparticulate systems as we have discussed in Section 5.1.

The simplest effective medium theory is the one which has been developed by Maxwell-Garnett[141]. The effective permeability has been derived on the assumptions that particles are identical

spheres, they are sufficiently separated from each other to ensure independent scattering and the Lorentz correction is applicable. Under these assumptions the effective permeability ($\bar{\varepsilon}^{MG}$) is given by,

$$\frac{\bar{\varepsilon}^{MG} - \varepsilon_m}{\bar{\varepsilon}^{MG} + 2\varepsilon_m} = f \frac{\varepsilon - \varepsilon_m}{\varepsilon + 2\varepsilon_m} \qquad (5.12)$$

where ε_m is the dielectric permittivity of the matrix, f the fill factor and ε the permittivity of an individual particle.

It has been shown by Onsager[142] that only part of the field is effective in directing the dipoles in a dielectric matrix. Polder and van Santen[143] have incorporated Onsager's 'reaction field' to derive an improved effective medium permeability for particles of ellipsoidal shapes. Combining their calculations with MG approach the following effective medium permeability ($\bar{\varepsilon}^{MG-PvS}$) can be obtained[122]

$$\bar{\varepsilon}^{MG-PvS} = \varepsilon_m \frac{1 + 2/3 \; \Sigma_j f_j \delta_j}{1 - 1/3 \; \Sigma_j f_j \delta_j} \qquad (5.13)$$

where f_j is the fill factor of the particles belonging to the jth class, such that $\Sigma_j f_j = f$, where f is the fill factor. δ_j is related to the polarisability of the particles in jth interval and for ellipsoidal shape is given by[122]

$$\delta_j = \frac{1}{3} \sum_{k=1}^{3} \frac{\varepsilon_j - \bar{\varepsilon}}{\bar{\varepsilon} + L_k(\varepsilon_j - \bar{\varepsilon})} \qquad (5.14)$$

where ε_j is the size dependent dielectric permittivity of
the particle. $\bar{\varepsilon}$ is the effective permeability which can be
calculated from any effective medium theory. L_k's are the
triplet of depolarisation factors. It can be seen that for
equal-sized spheres with $L_1 = L_2 = L_3 = 1/3$, the equation
(5.13) reduces to the Maxwell-Garnett expression (5.12). Both
MG and MG-PvS theories are applicable for small values of the
fill factor.

Another effective medium theory has been put forward by
Bruggeman[144]. In this a particle is considered to be embedded
in an effective medium and its properties are determined self-
consistently. To achieve this one has to solve for local field
around the particles such that the fluctuations average out to
zero. From these requirements the effective medium permeability
($\bar{\varepsilon}^{BR}$) is given by,

$$\bar{\varepsilon}^{BR} = \varepsilon_m \frac{1 - f + \frac{1}{3} \Sigma_j f_j \delta_j}{1 - f - \frac{2}{3} \Sigma_j f_j \delta_j} \tag{5.15}$$

where δ_j is given by the expression (5.14). In principle this
theory is applicable to any fill factor, as it gives equal
weightage to the components of the inhomogeneous medium.

Hunderi[145] has derived an expression for the effective
permeability $\bar{\varepsilon}^{HU}$ from the back scattered field and it is given
by,

$$\overline{\varepsilon}^{HU} = \varepsilon_m \; (\frac{1 + \frac{1}{4} \; \Sigma_j f_j \delta_j}{1 - \frac{1}{4} \; \Sigma_j f_j \delta_j})^2 \tag{5.16}$$

δ_j being given by the expression (5.14). The theory is applicable for small fill factor.

Recently both MG and BR theories have been derived by Niklasson et al.[146] from an unified approach by specifying two types of random unit cells which represent two types of micro-structures and on the requirement that these cells when embedded in an effective medium will not be detected by an electromagnetic wave.

In the small particle size range, the grain boundary scattering should influence the mean free path of conduction electrons and hence the dielectric permeability will be particle size dependent. Secondly when the particles are not far apart the dipole-dipole interaction cannot be neglected. This interaction can be included by replacing the δ_j's in equation (5.14) by a set of equivalent depolarisation factors defined for different geometrical configurations of identical spheres[122].

5.4.3 Validity of effective medium formalism

The criterion for the validity of effective medium model as examined by Granqvist[122] is that the results predicted should be independent of experimental condition used. When a plane wave with an amplitude U_0 is incident on a thick slab

containing independently scattering particles the back scattered field has been given by Van de Hulst[147] as $i\pi U_o \rho_p S(\pi)/k^3$ where ρ_p is the particle number density, $S(\pi)$ the scattering amplitude function at an angle π and k is the wave vector. The refractive index of the medium corresponding to this field is given by[145],

$$N_R \simeq 1 - i2\pi \rho_p S(\pi)/k^3 \qquad (5.17)$$

In the transmission measurement the refractive index is given by[147],

$$N_T \simeq 1 - i2\pi \rho_p S(o)/k^3 \qquad (5.18)$$

The ratio of $S(\pi)/S(o)$ as calculated by Van de Hulst[147] from the Mie theory is given by,

$$S(\pi)/S(o) = 1 + \frac{k^2 x^2}{15} \left[\frac{(\varepsilon+4)(\varepsilon+2)}{2\varepsilon+3}\right] + O(k^4 x^4) \qquad (5.19)$$

where ε is the dielectric permittivity of the particles. In order for the effective medium approach to be valid, therefore, N_R and N_T should not differ appreciably from each other. This means that $S(\pi)/S(o)$ should be around 1. For the real and imaginary parts of the second term of equation (5.19) to be smaller than around 5 percent, the particle size will be of the order of 10 nm or less for gold[122]. The 3rd row of table 5.2 shows that the particle size is of the same order of magnitude in the present investigation. Therefore in the following

sections we have used effective medium theories to interpret
the optical absorption data as reported in Section 5.3.

5.5 Interpretation of Experimental Results

From tables 5.3 to 5.6 we see that the calculated d_{hkl}
values compare well with the standard d_{hkl} values of metallic
bismuth. The SAD data thus confirm that the particles observed
in the different glass matrices consist of metallic bismuth.

5.5.1 Computation procedure

The frequency dependent dielectric permittivity of bismuth
is of prime importance in interpreting the optical absorption
data by effective medium theories. To start with the frequency
dependent bulk dielectric permittivity of bismuth has been
calculated from the index of refraction and extinction coeffi-
cient given as a function of wavelength in reference ([148]).
The size dependent dielectric permittivity of bismuth has been
obtained from the bulk data by incorporating the size dependent
electron scattering in the Drude free electron part of the
dielectric permittivity as follows[122]

$$\varepsilon_j(\omega) = \varepsilon_{exp}(\omega) - \varepsilon_{exp}^{Drude}(\omega) + \varepsilon_j^{Drude}(\omega) \qquad (5.19a)$$

where ω is the angular frequency of radiation used. The last
two terms in the right hand side of the above equation are given
by,

$$\varepsilon_{exp}^{Drude}(\omega) = 1 - \omega_{pb}^2/\omega(\omega + i/\tau_b) \qquad (5.20)$$

$$\varepsilon_j^{Drude}(\omega) = 1 - \omega_{px_j}^2/\omega(\omega + i/\tau_j) \qquad (5.21)$$

where ω_{pb} and τ_b are the bulk plasma frequency and the mean electron life time respectively. ω_{px_j} is the apparent plasma frequency of particle of size x_j and τ_j is given by,

$$\tau_j^{-1} = \tau_b^{-1} + 2v_{Fb}/x_j \qquad (5.22)$$

where v_{Fb} is the bulk Fermi velocity of electrons and x_j the particle size of the jth class. A value of $\hbar\omega_{pb} = 16.0$ eV has been taken from reference ([149]). Values of $\tau_b/\hbar = 2.838$eV and $v_{Fb} = 1.822 \times 10^8$ cm/sec. have been calculated using free electron model[150].

Separating the real and imaginary parts of the size dependent dielectric permittivity ($\varepsilon_j = \varepsilon_j' + i\varepsilon_j''$) from equations (5.19 a)to (5.21) we get after simplification,

$$\varepsilon_j'(\omega) = \varepsilon_{exp}'(\omega) + \frac{\omega_{pb}^2}{\omega^2 + 1/\tau_b^2} - \frac{\omega_{pxj}^2}{\omega^2 + [(x_j + 2\tau_b v_{Fb})/\tau_b x_j]^2} \qquad (5.23)$$

$$\varepsilon_j''(\omega) = \varepsilon_{exp}''(\omega) + \frac{\omega_{pxj}^2[(x_j + 2\tau_b v_{Fb})/\tau_b x_j]}{\omega[\omega^2 + \{(x_j + 2\tau_b v_{Fb})/\tau_b x_j\}^2]} - \frac{\omega_{pb}^2/\tau_b\omega}{\omega^2 + (1/\tau_b^2)}$$

$$\qquad (5.24)$$

5.5.1.1 MG effective medium theory

Simplifying equation (5.12) and then separating the real and imaginary parts of $\bar{\varepsilon}^{MG}$ ($\bar{\varepsilon}^{MG} = \bar{\varepsilon}_1^{MG} + i\bar{\varepsilon}_2^{MG}$) we get,

$$\bar{\varepsilon}_1^{MG} = \frac{AC + BD}{C^2 + D^2} \qquad (5.25)$$

$$\bar{\varepsilon}_2^{MG} = \frac{BC - AD}{C^2 + D^2} \qquad (5.26)$$

where,

$$A = \varepsilon_m(1+2f)\varepsilon' + 2\varepsilon_m^2(1-f) \qquad (5.27a)$$

$$B = \varepsilon_m(1+2f)\varepsilon'' \qquad (5.27b)$$

$$C = (1-f)\varepsilon' + \varepsilon_m(2+f) \qquad (5.27c)$$

$$D = (1-f)\varepsilon'' \qquad (5.27d)$$

In equations (5.27), ε' and ε'' are given by equations (5.23) and (5.24) respectively in which x_j is replaced by the average particle size as computed by equation (5.1). The frequency dependent $\bar{\varepsilon}_1^{MG}$ and $\bar{\varepsilon}_2^{MG}$ have been computed using equations (5.25) to (5.27). For bismuth in silicate and in V_2O_5-P_2O_5 systems the dielectric permittivity of the media are taken as $2.2^{[128]}$ and $10^{[151]}$ respectively.

5.5.1.2 MG-PvS and BR theories

Equations (5.13) and (5.15) contain size dependent fill factor which can be related to f by the following equation,

$$f_j = w_j f \tag{5.28}$$

where w_j is the weight factor and is given by,

$$w_j = \frac{x_j^3 n_j}{\sum_j x_j^3 n_j} \tag{5.29}$$

where n_j is the number of particles in jth class.

From equation (5.13) separating the real and imaginary parts of the complex quantities, we get the real and imaginary parts of the effective medium permeability in the MG-PvS theory as follows :

$$\bar{\varepsilon}_1 = \varepsilon_m \frac{A_1 C_1 - B_1 D_1}{C_1^2 + D_1^2} \tag{5.30}$$

$$\bar{\varepsilon}_2 = \varepsilon_m \frac{B_1 C_1 + A_1 D_1}{C_1^2 + D_1^2} \tag{5.31}$$

where,

$$A_1 = 1 + \frac{2}{3} f \sum_j w_j \delta_j' \tag{5.32a}$$

$$B_1 = \frac{2}{3} f \sum_j w_j \delta_j'' \tag{5.32b}$$

$$C_1 = 1 - \frac{1}{3} f \sum_j w_j \delta_j' \tag{5.32c}$$

$$D_1 = \frac{1}{3} f \sum_j w_j \delta_j'' \tag{5.32d}$$

δ_j' and δ_j'' of the above equations (5.32) are given by,

$$\delta_j' = \frac{1}{3} \sum_{k=1}^{3} \frac{EG_k + FH_k}{G_k^2 + H_k^2} \tag{5.33}$$

$$\delta_j'' = \frac{1}{3} \sum_{k=1}^{3} \frac{FG_k - EH_k}{G_k^2 + H_k^2} \tag{5.34}$$

where,

$$E = \varepsilon_j' - \bar{\varepsilon}_1 \tag{5.35a}$$

$$F = \varepsilon_j'' - \bar{\varepsilon}_2 \tag{5.35b}$$

$$G_k = L_k \varepsilon_j' + (1 - L_k)\bar{\varepsilon}_1 \tag{5.35c}$$

$$H_k = L_k \varepsilon_j'' + (1 - L_k)\bar{\varepsilon}_2 \tag{5.35d}$$

In the above equations ε_j' and ε_j'' are given by expressions (5.23) and (5.24) respectively. In the Bruggeman formalism, the expressions (5.30) to (5.35) will be identical with A_1, B_1, C_1 and D_1 of equations (5.32(a) to 5.32(d)) being properly replaced by using the Bruggeman effective medium equation (5.15).

In order to compute the value of $\bar{\varepsilon}_1$ and $\bar{\varepsilon}_2$ from equations (5.30) and (5.31), we notice that the equations are of the transcendental type as they involve $\bar{\varepsilon}_1$ and $\bar{\varepsilon}_2$ on the right hand side through δ_j' and δ_j'' respectively. So $\bar{\varepsilon}_1$ and $\bar{\varepsilon}_2$ have been found iteratively as follows. First $\bar{\varepsilon}_1$ in the right hand side is assigned the value of ε_m and we set $\bar{\varepsilon}_2 = 0$. Then $\bar{\varepsilon}_1$ and $\bar{\varepsilon}_2$ are calculated from the equations (5.30) and (5.31). $\bar{\varepsilon}_1$ and $\bar{\varepsilon}_2$ of the right hand side of equations (5.30) and (5.31) are replaced by the new values as calculated in the previous iteration and $\bar{\varepsilon}_1$ and $\bar{\varepsilon}_2$ are calculated from equations (5.30)

and (5.31). This process is continued until the difference
between two successive iterations is less than a preassigned
error. In our calculation we have used an error of 0.1. L_k's,
the depolarisation factors for sphere are taken from the
reference ([122]). Once the frequency dependent $\bar{\epsilon}_1$ and $\bar{\epsilon}_2$ are
computed, the optical absorption coefficient (α) is then given
by,

$$\alpha(\omega) = (\omega/c)(\bar{\epsilon}_2/\bar{\epsilon}_1^{\frac{1}{2}}) \qquad (5.36)$$

The frequency dependent α values as computed as a function of
wavelength λ from MG, MG-PvS and BR theories for the V_2O_5-P_2O_5
and silicate systems under investigation are plotted in figures
5.21 to 5.32. In each figure is included the corresponding
experimentally determined α values for comparison. Table 5.7
contains the theoretical and experimental α values corresponding
to peak positions. It is observed that computed α values by
BR and MG-PvS theories are almost identical as are evident from
figures 5.21 to 5.32. So in table 5.7 we have only included α
values computed by MG and BR theories. The theoretically com-
puted α values for vanadium phosphate glasses containing bis-
muth show a small absorption peak at 650 nm while in the case
of silicate glasses containing bismuth the calculated α values
show a small dip. However, no peak is observed experimentally
in either of these systems around this wavelength.
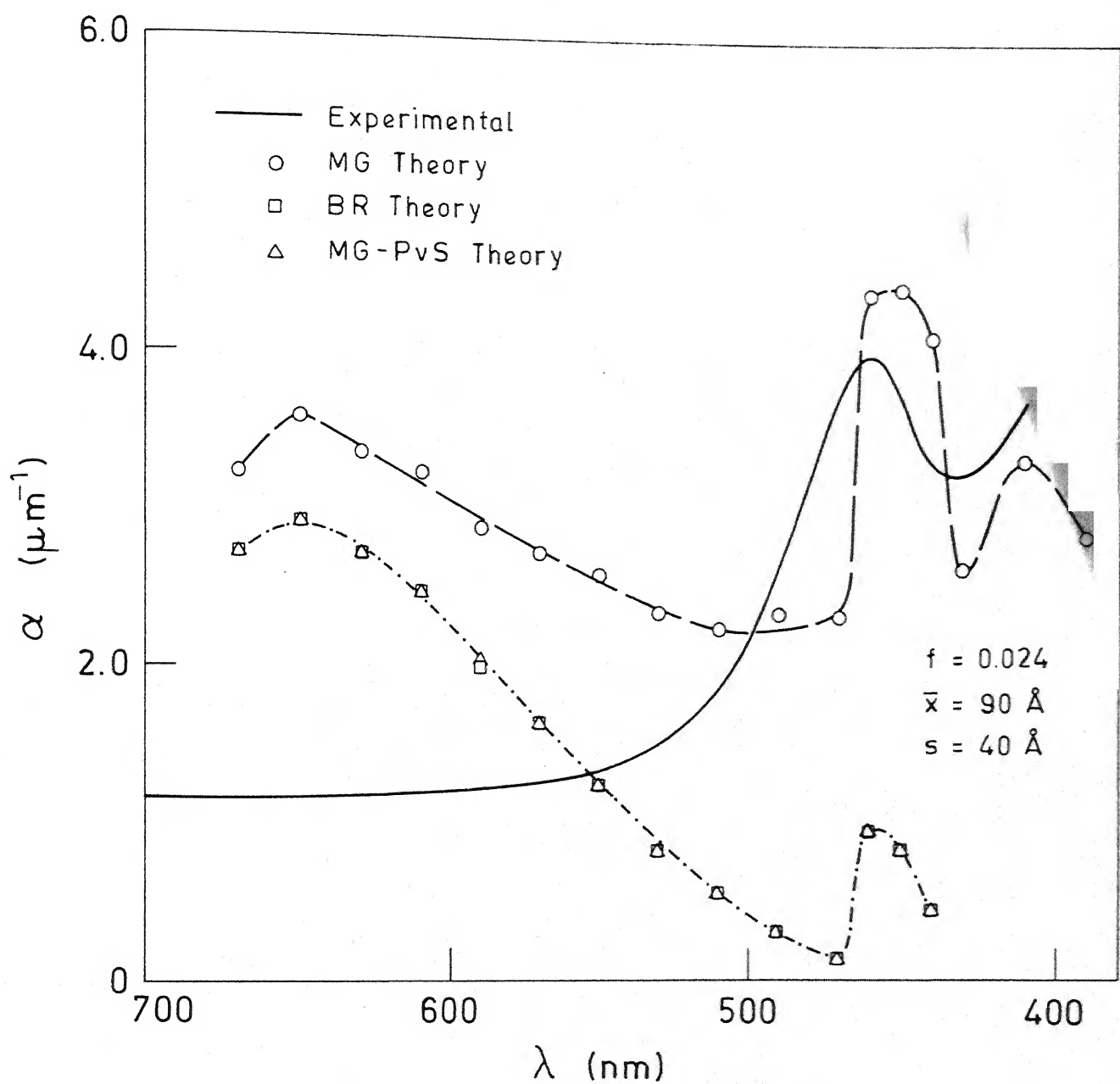
Fig. 5.21　Comparison of experimental and theoretical absorption coefficient α for glass no. 2.
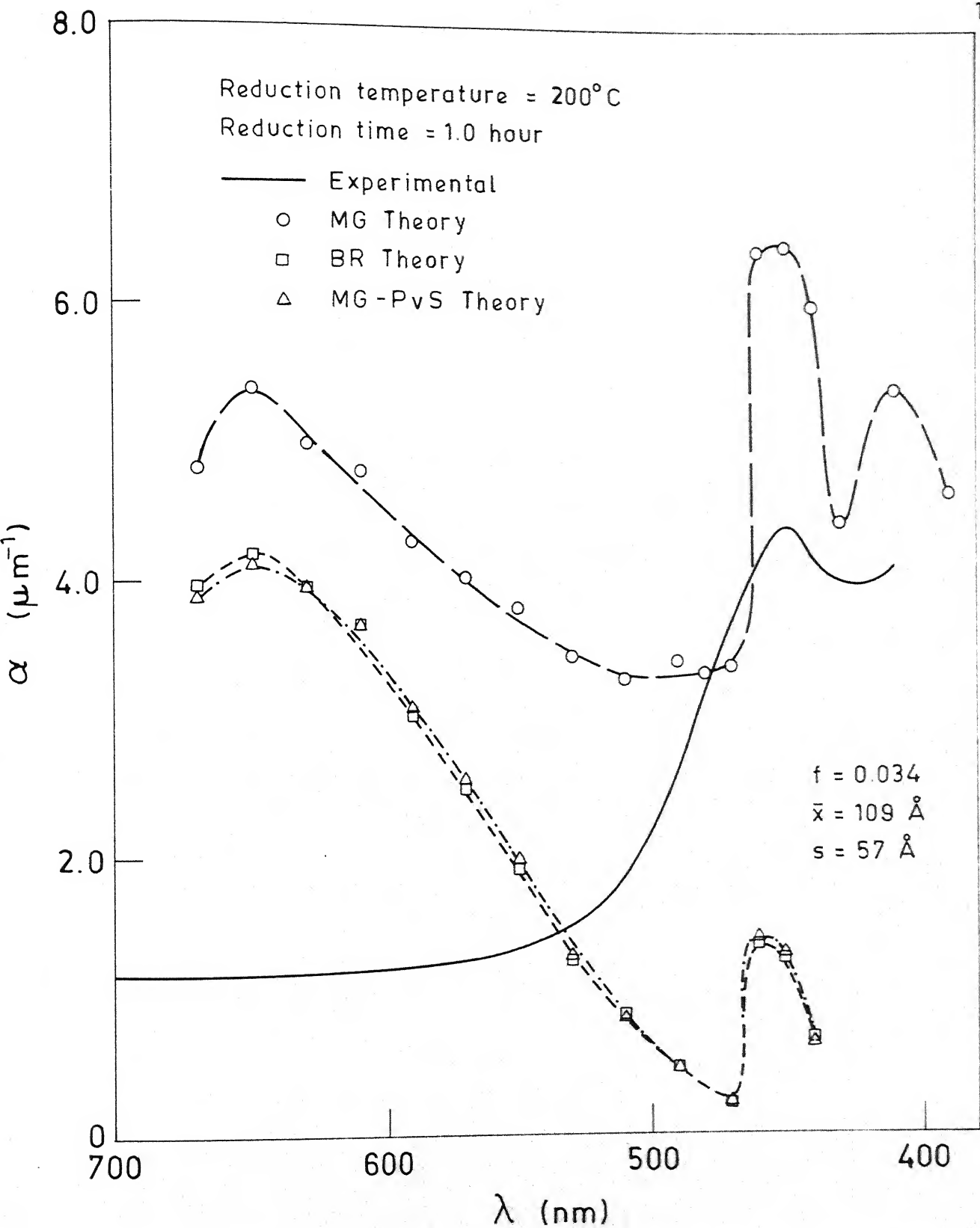
Fig. 5.22   Comparison of experimental and theoretical absorption coefficient α for glass no. 2.
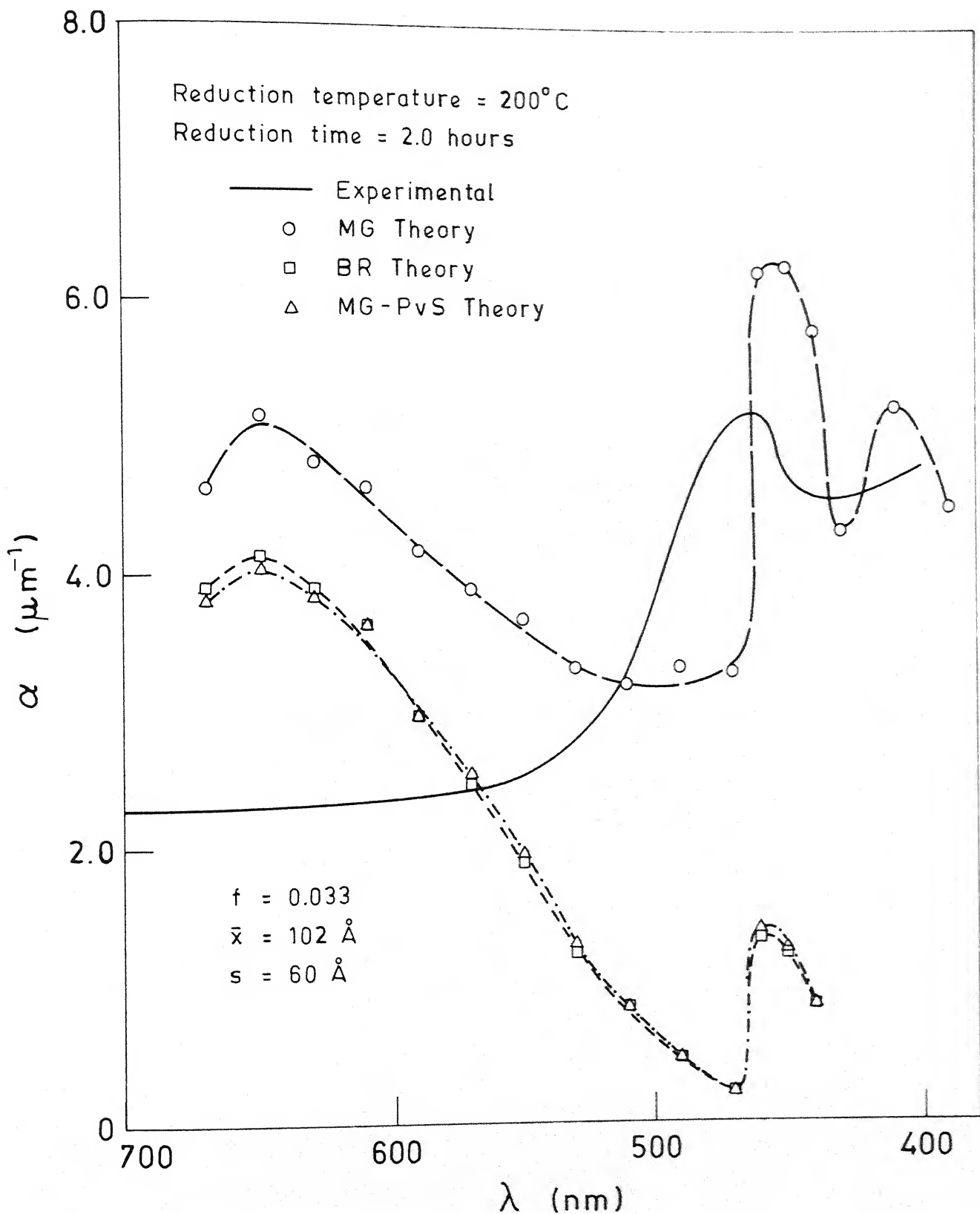
Fig. 5.23 Comparison of experimental and theoretical absorption coefficient α for glass no. 2.
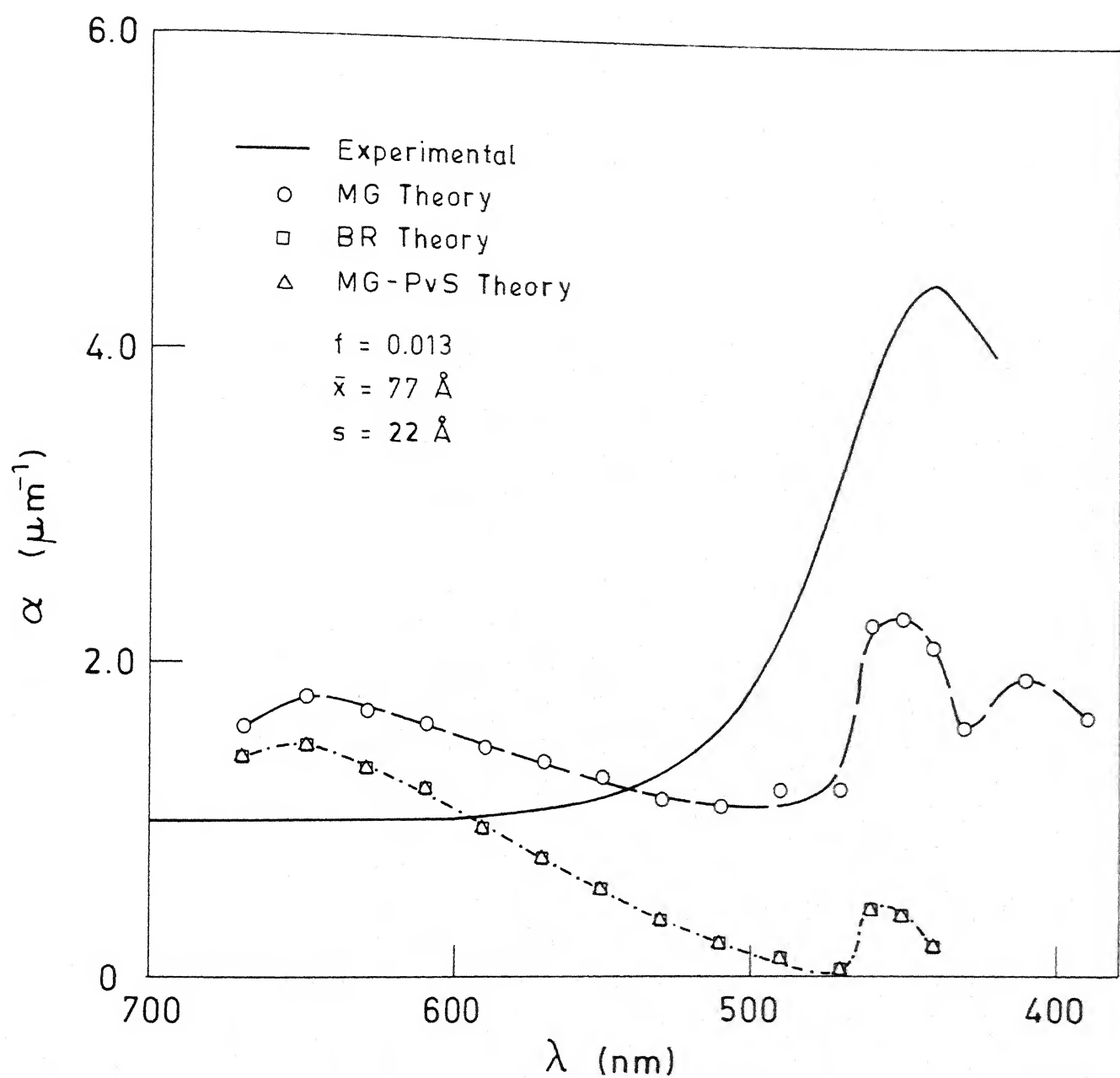
Fig. 5.24   Comparison of experimental and theoretical absorption coefficient α for glass no. 3.
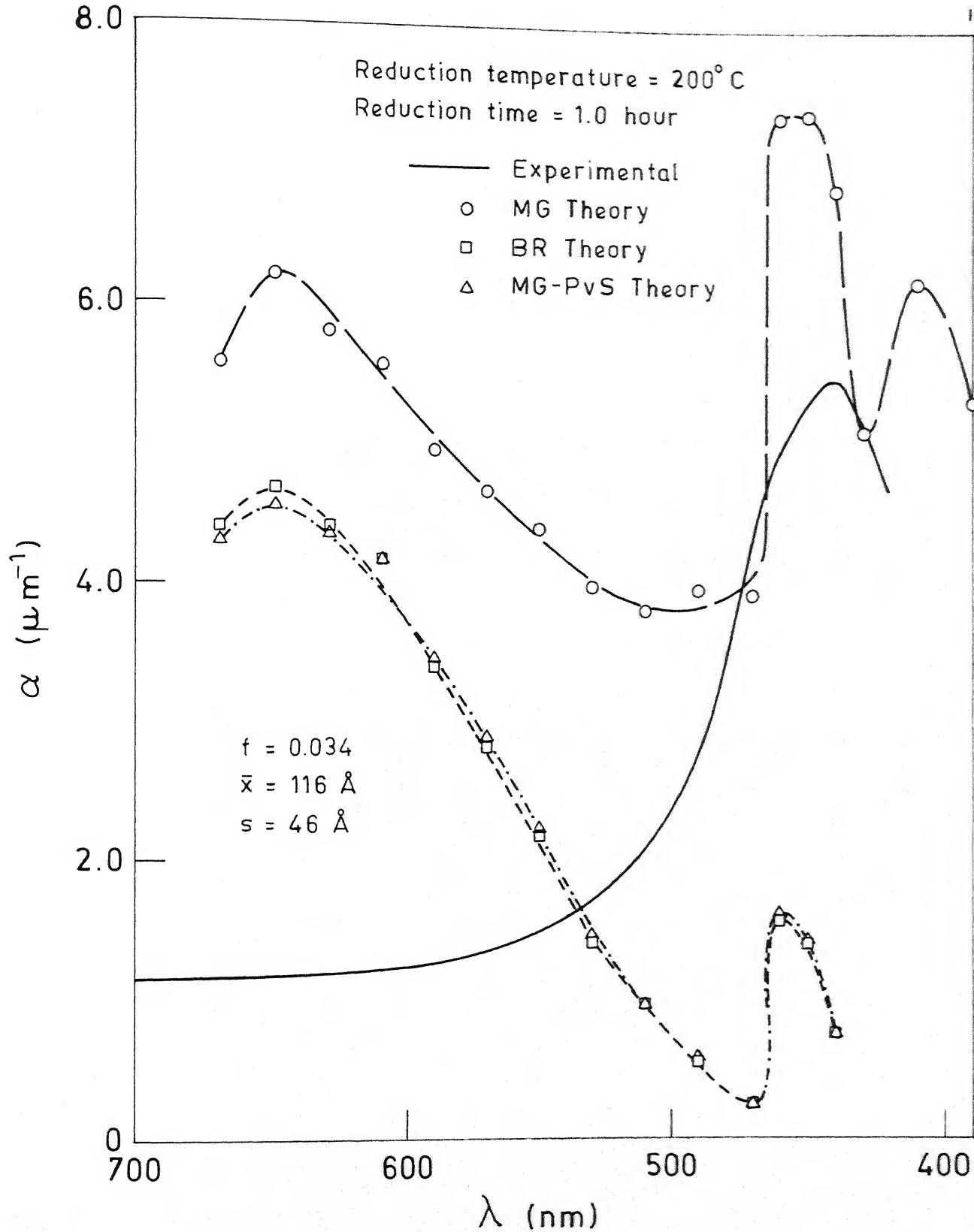
Fig. 5.25   Comparison of experimental and theoretical absorption coefficient α for glass no. 3.
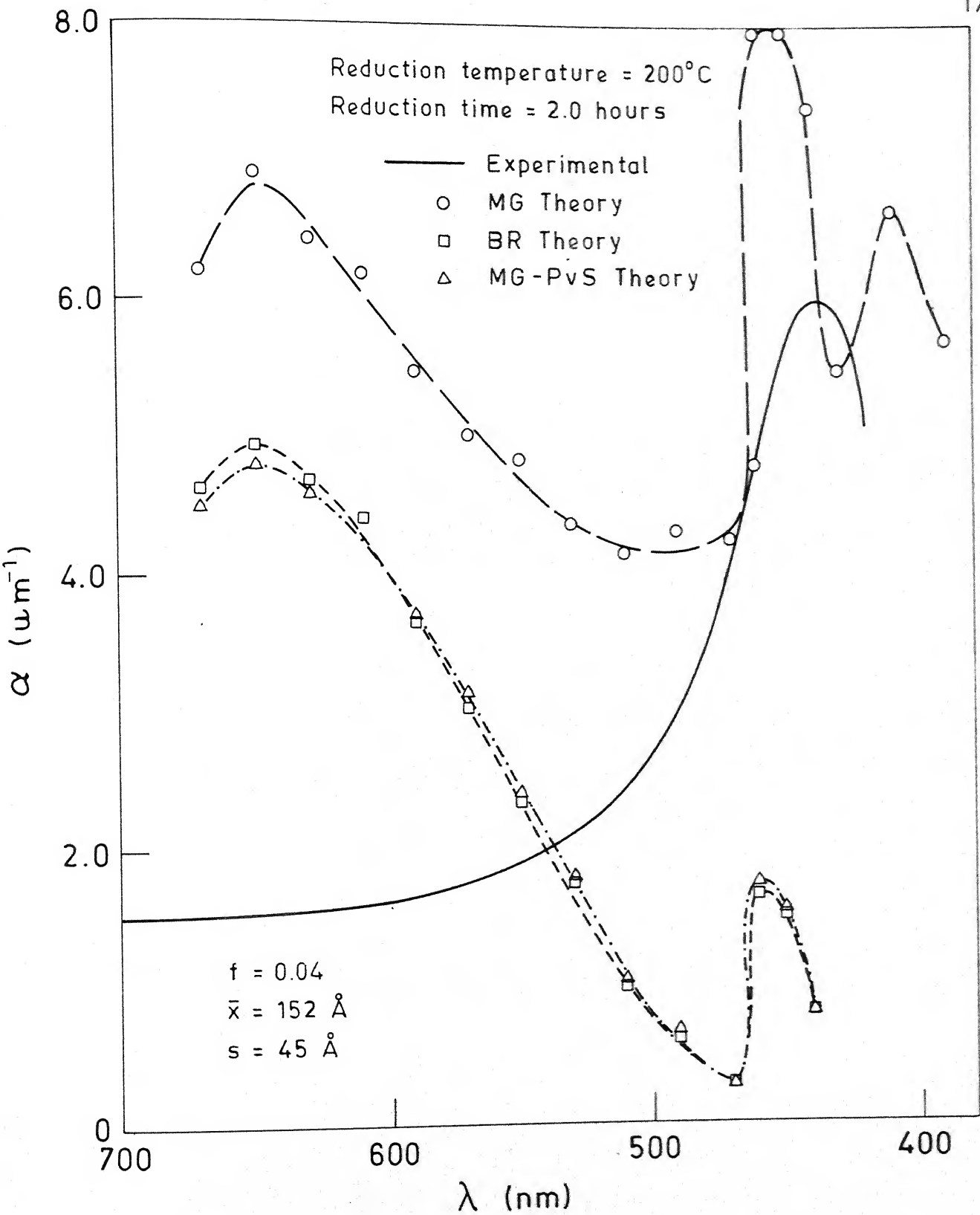
Fig. 5.26   Comparison of experimental and theoretical
             absorption coefficient α for glass no. 3.
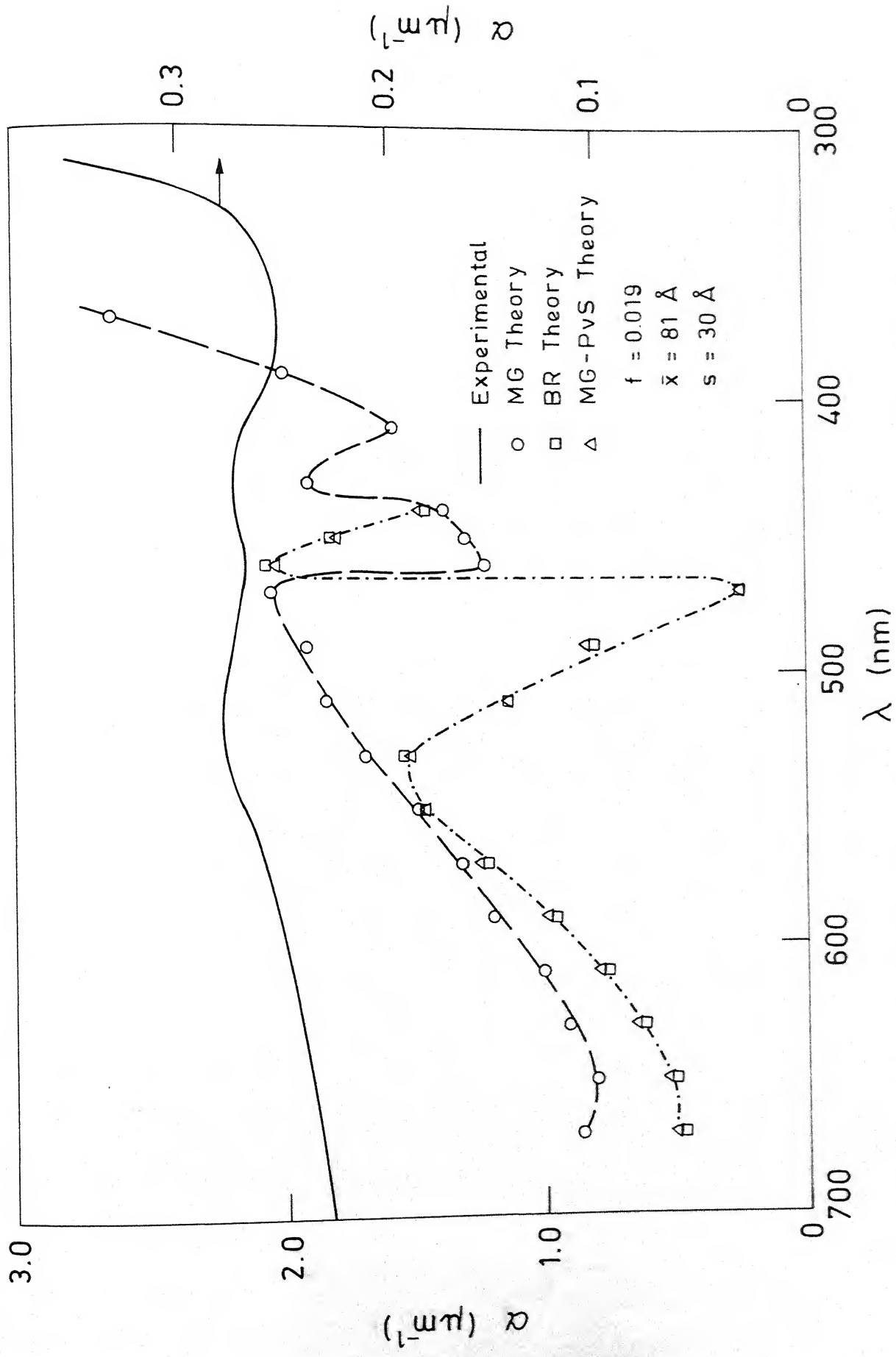
Fig. 5.27 Comparison of experimental and theoretical absorption coefficient α for glass no. 5.
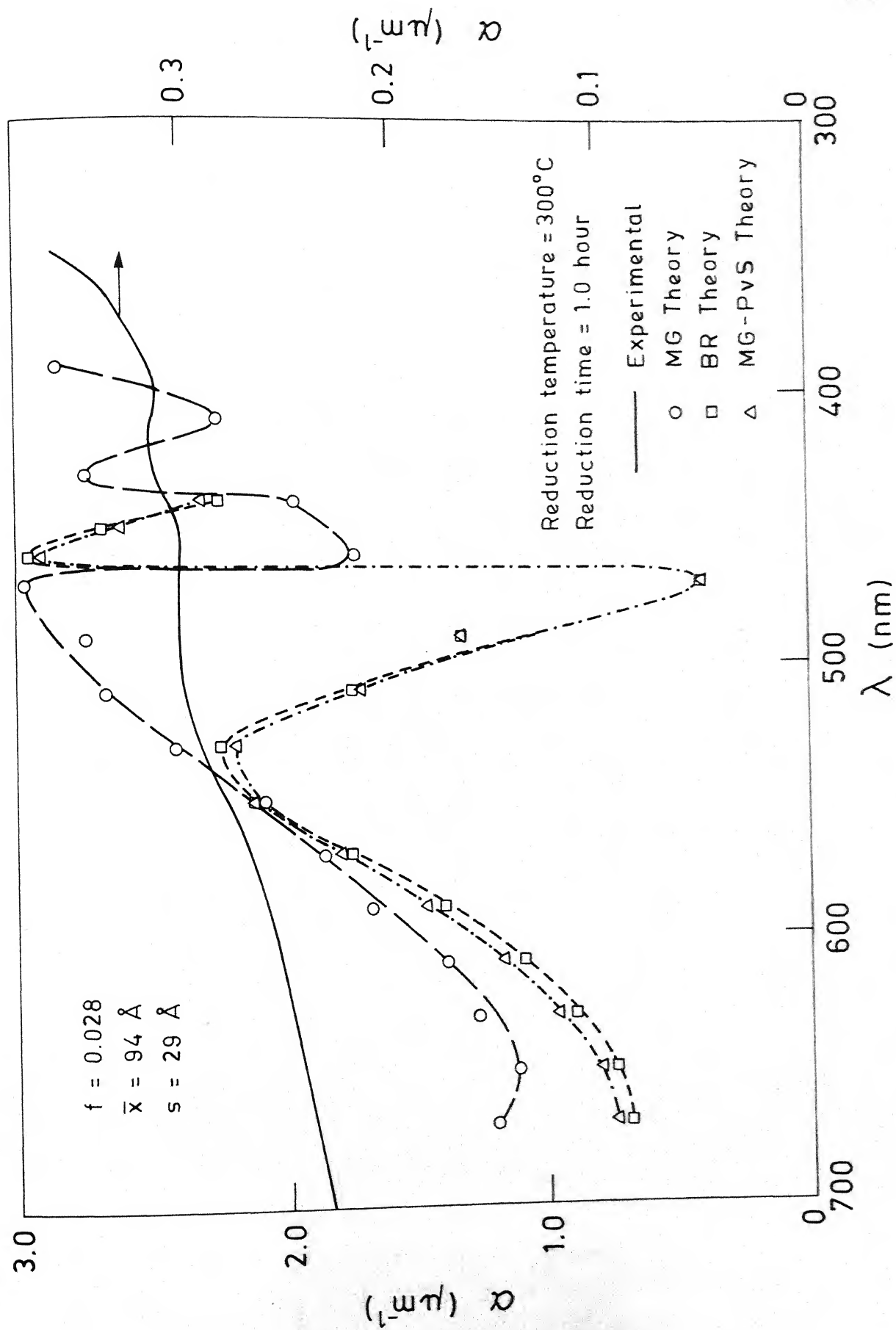
Fig. 5.28   Comparison of experimental and theoretical absorption coefficient α
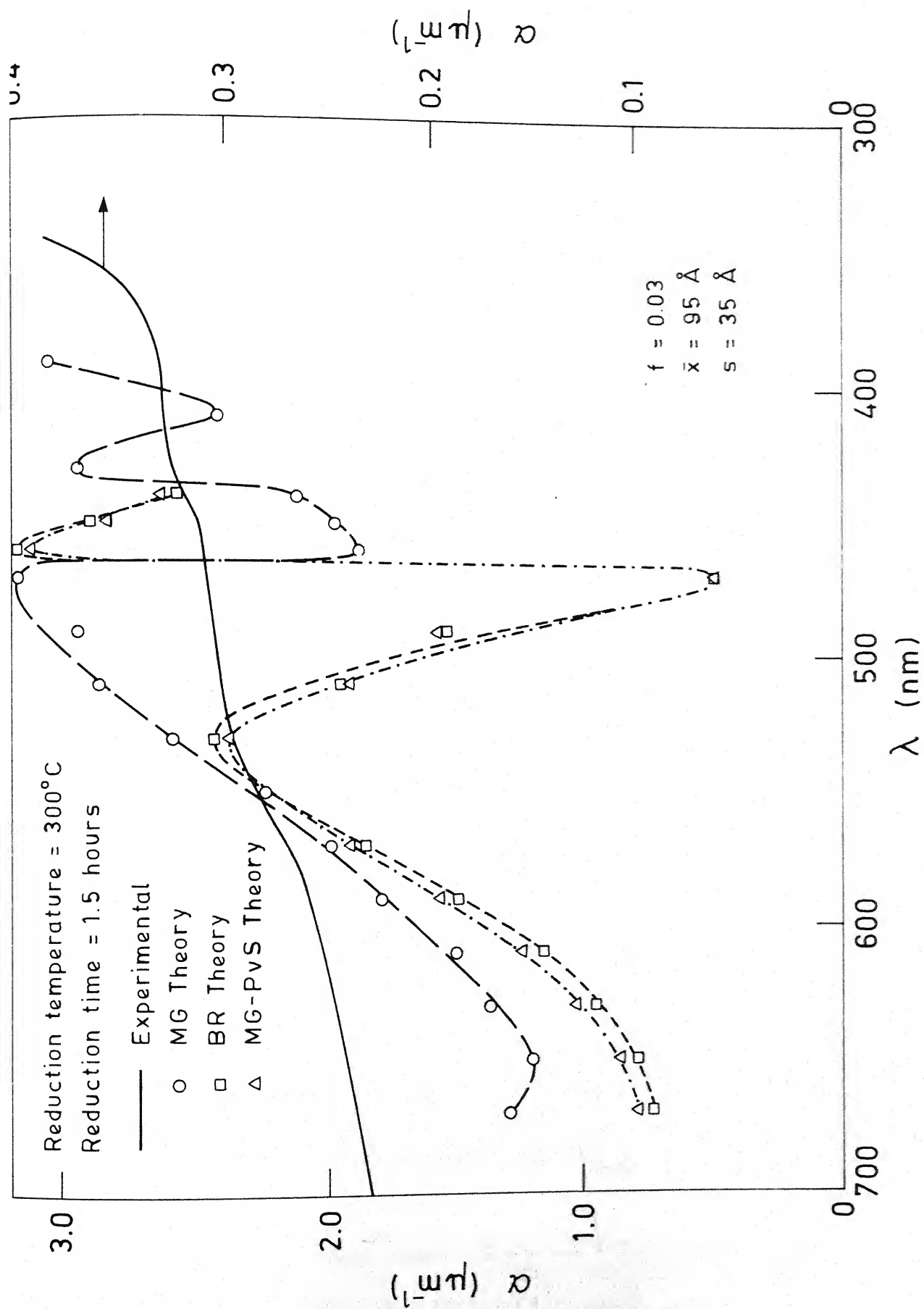
Fig. 5.29 Comparison of experimental and theoretical absorption
coefficient α for glass no. 5
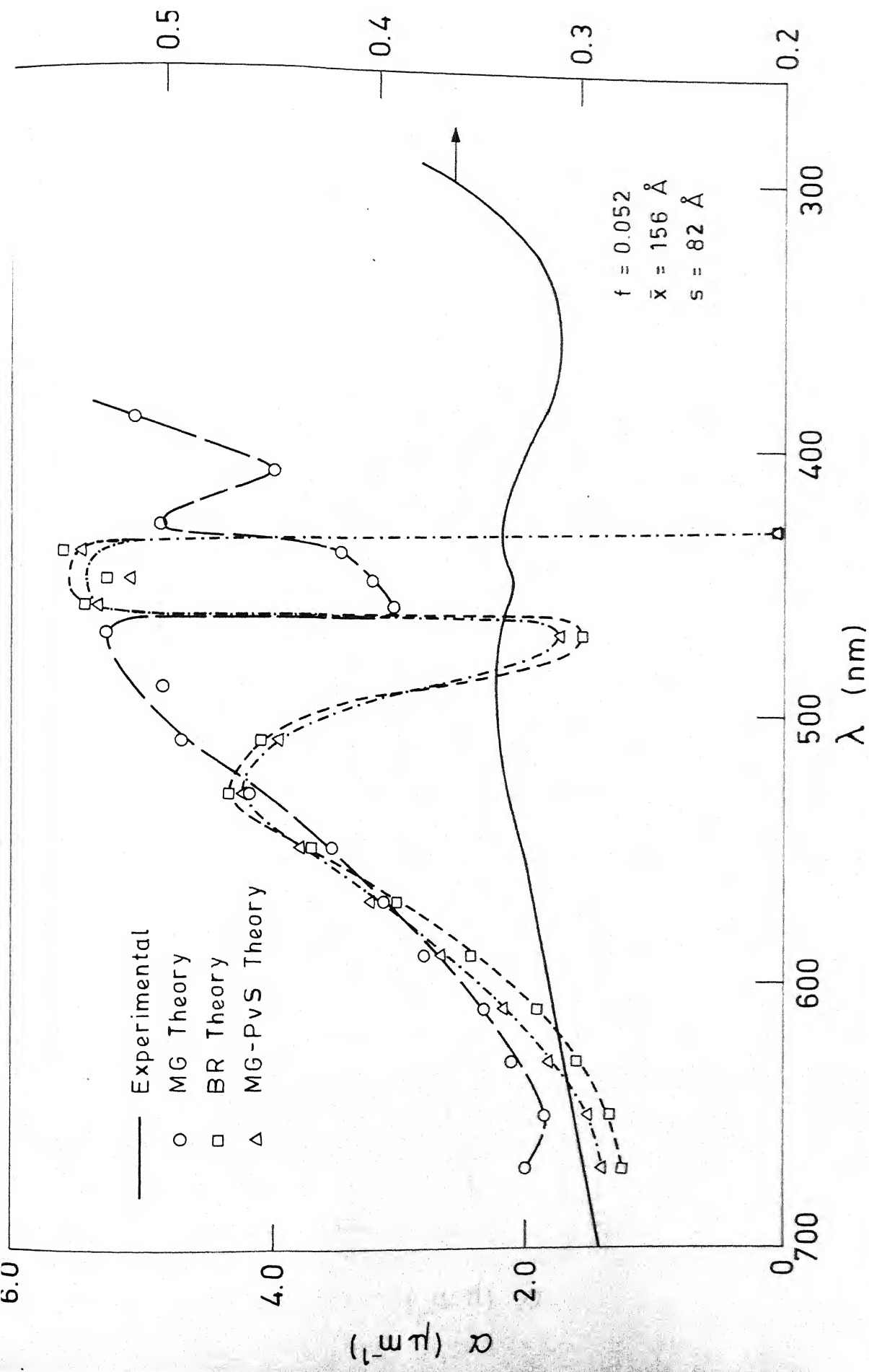
Fig. 5.30   Comparison of experimental and theoretical absorption coefficient α for glass no. 6.
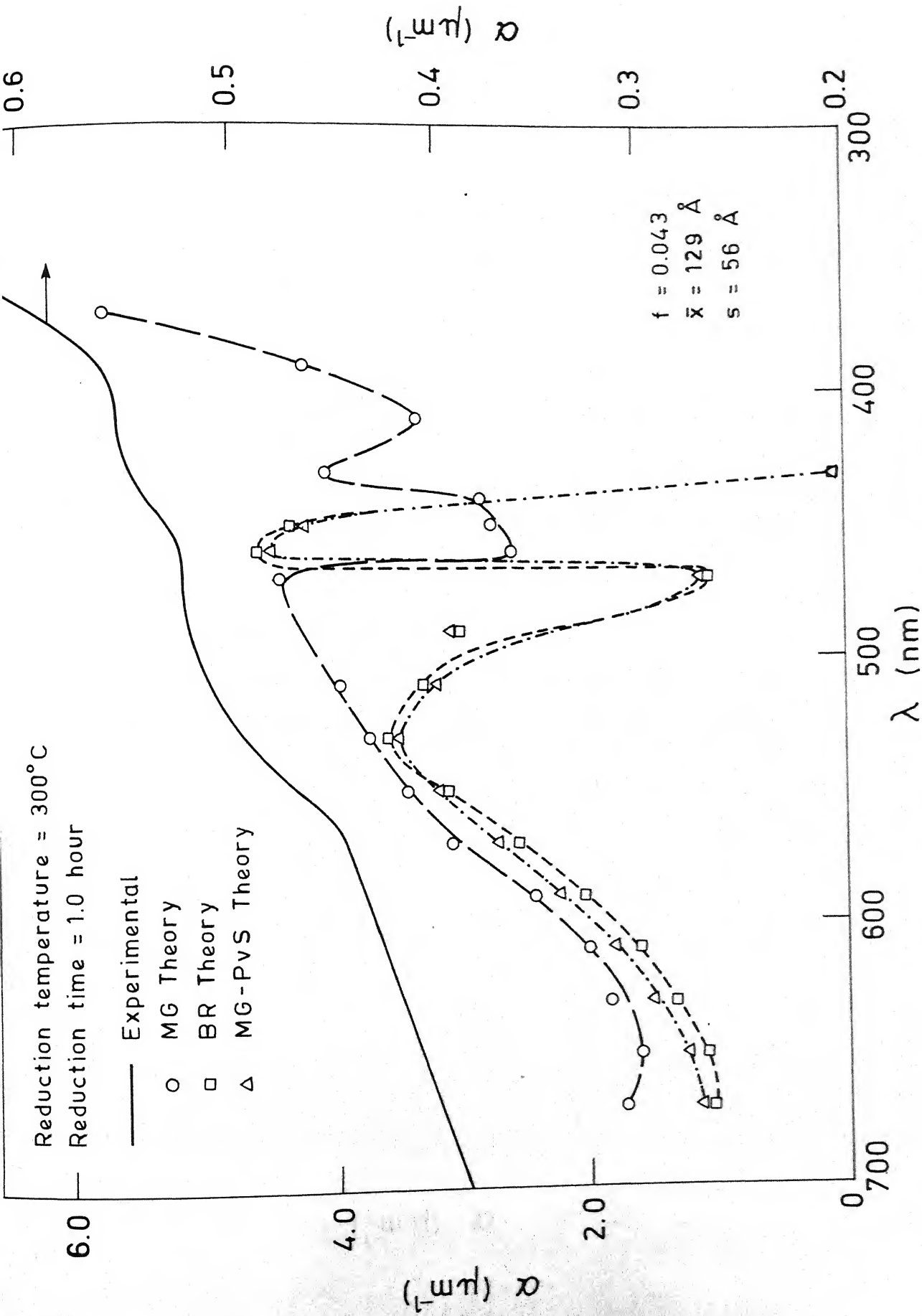
Fig. 5.31 Comparison of experimental and theoretical absorption
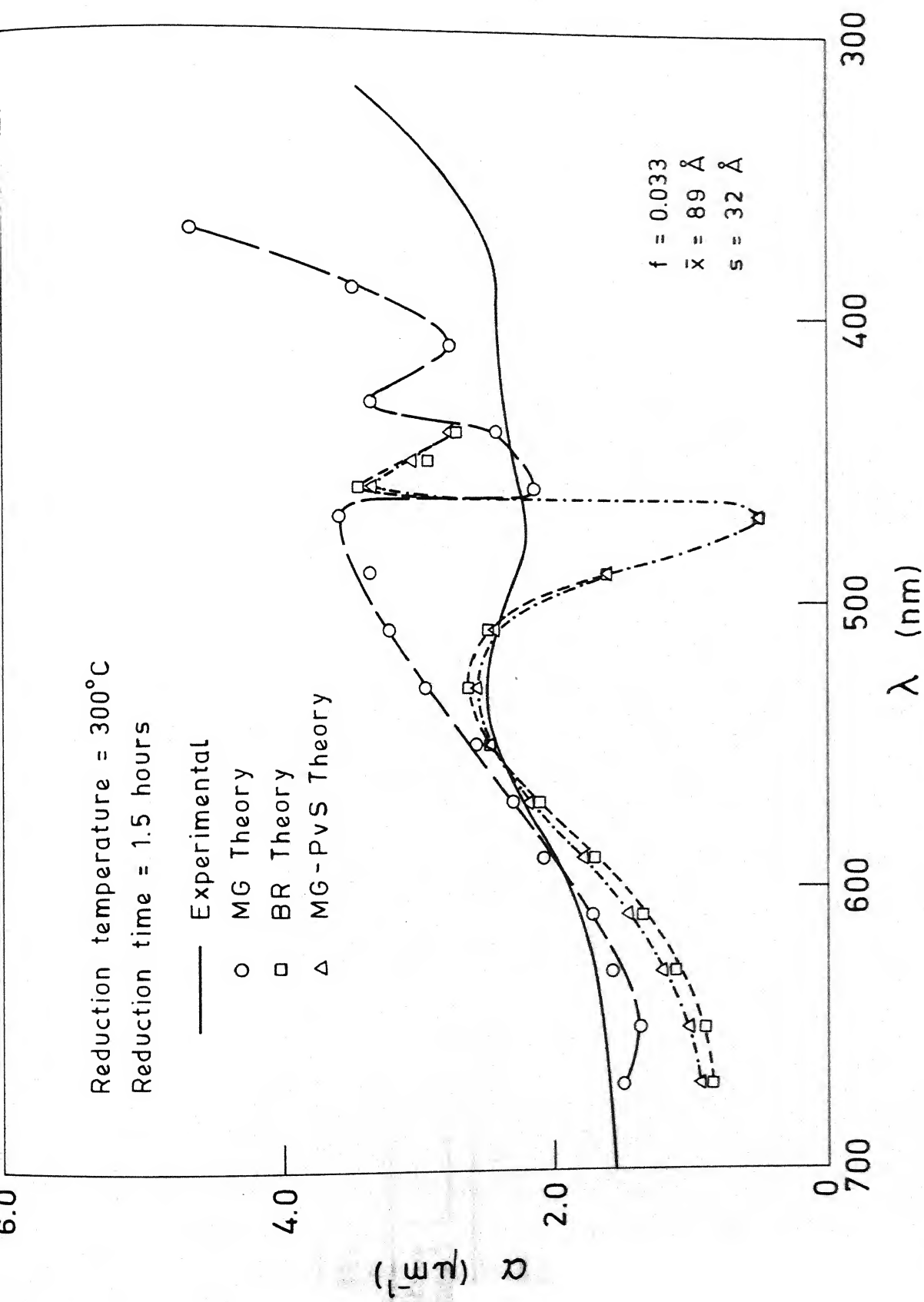
Fig. 5.32 Comparison of experimental and theoretical absorption coefficient α for glass no. 6.

Table 5.7 Comparison of experimental and theoretical α values for different glasses

	V₂O₅–P₂O₅–Bi₂O₃						SiO₂–B₂O₃–Na₂O–Bi₂O₃						
Glass No.	2	2	3	3	3	3	5	5	5	5	5	6	6
Reduction T	200	200	200	200			300	300				300	300
Treatment t	1	2	1	2			1	1.5				1	1.5
											Experimental		
Peak position nm(1)	460	450	460	440	440		520	500	510	500	500	500	530
Peak value α μm⁻¹(1)	4.0	4.4	5.2	4.48	5.6	6.0	0.28	0.30	0.303	0.34	0.34	0.515	2.48
Peak position nm(2)	–	–	–	–	–	–	430	420	420	430	420	420	430
Peak value α μm⁻¹(2)	–	–	–	–	–	–	0.275	0.313	0.325	0.34	0.34	0.55	2.36

Theoretical – M G

Peak position nm(1)	450	450	450	450	450	450	470	470	470	470	470	470
Peak value α μm⁻¹(1)	4.44	6.44	6.28	2.32	7.4	8.0	2.04	2.96	3.18	5.24	4.4	3.6
Peak position nm(2)	410	410	410	410	410	410	430	430	430	430	430	430
Peak value α μm⁻¹(2)	3.32	5.44	5.24	1.92	6.2	6.6	1.9	2.74	2.94	4.84	3.68	3.36

Peak position in LaTeX: $\alpha\ \mu m^{-1}$

Theoretical – B R

Peak position nm(1)	460	460	460	460	460	460	530	530	530	530	530	530
Peak value α μm⁻¹(1)	0.96	1.36	1.32	0.44	1.6	1.68	1.54	2.26	2.44	4.32	3.6	2.64
Peak position nm(2)	–	–	–	–	–	460	460	460	460	460	460	460
Peak value α μm⁻¹(2)	–	–	–	–	–	–	2.04	2.96	3.18	5.4	4.6	3.44

Note : T – Reduction temperature in degree C

   t – Reduction time in hours.

In V_2O_5-P_2O_5 system as the reduction time increases the experimental α values at peak positions increase (2nd row of table 5.7 and figure 5.3). This is because of the fact that with increasing reduction time the amount of precipitated bismuth becomes larger. It is evident from the second row of table 5.2 that the volume fraction (f) increases with an increase in reduction time. From the 5th and 7th rows of table 5.7 we see that α values as calculated by MG theory show two peak positions at 450 nm and 410 nm while BR theory predicts one peak at 460 nm. Beyond 440 nm the values of $\bar{\varepsilon}_1$ as calculated by BR and MG-PvS theories become negative. Experimentally we could not observe the second peak as the experimental OD could not be measured because of the full opening of the slit in Carry 17D beyond about 410 nm. Comparing the 1st and 5th rows of table 5.7 we see that the first peak position as predicted by MG theory agrees with the experimentally observed value within $\pm$ 10 nm. The peak position predicted by BR theory (9th row of table 5.7) agrees with the experimental one within an error of 20 nm. MG theory predicts results which are in better agreement with experiment than those obtained from BR and MG-PvS theories. This is evident from figures 5.21 to 5.26. It is observed that calculated α values by MG, BR and MG-PvS theories increase with increase in reduction time except for glass no.2 reduced at $200^\circ C$ for 2.0 hours. From 2nd row of table 5.2 we see that f

increases with increase in reduction time except for the one just mentioned. Except for this sample the theoretically observed trend of α values with reduction time is in agreement with experimental results.

In the silicate system we find two broad absorption peaks. This is evident from figure 5.4. From 1st and 3rd rows of tables 5.7 we see that two absorption peaks occur in the range of 500-530 nm and 420 to 430 nm respectively. The corresponding calculated peak positions by MG theory occur at 470 nm and 430 nm respectively (5th and 7th rows of table 5.7) and those computed by BR theory occur at 530 nm and 460 nm respectively (9th and 11th rows of table 5.7). Therefore, it is clear that no effective medium theory by itself can predict the peak position accurately.

From the study of table 5.7 and also from figures 5.21 to 5.32 we find that the discrepancy between the theory and the experimental data is more in silicate system than in the $V_2O_5-P_2O_5$ system. The calculated α values in the silicate system (6th, 8th, 10th and 12th rows of table 5.7) are an order of magnitude greater than those observed experimentally near the peak positions (2nd and 4th rows of table 5.7). This is believed to arise from the possibility of an over-estimation of the fill factor f as determined from the electron micrographs of the specimens concerned. The dark phase in the micrographs may consist of a metal phase and bismuth oxide rich glass

phase[152]. However, an accurate delineation of such micro-structural features is not possible by the experimental technique employed in the present investigation.

Experimentally we observe from the 2nd and 4th rows of table 5.7 that α values increase with the increase in reduction time in silicate system. However, for glass no.6 it is found that the calculated values show an opposite trend (6th, 8th, 10th and 12th rows of table 5.7). This anomalous behaviour in predicted α values, though not magnitudinally very different, for the glass no.6 and glass no.2 as mentioned earlier can be explained as follows. Figure 5.33 gives the plots of α values as calculated by MG theory for different particle sizes in the range of 80 to 160Å with a fixed fill factor of value 0.02. Figure 5.34 shows the plots of α values as calculated by MG theory for a fixed particle size with different fill factors in the vanadium phosphate as well as in silicate systems. We see from the these two figures that fill factor has a more pronounced effect on the calculated α values than the particle size. The fill factor $f \propto (\bar{x}/t_{em})$ (equation 5.4) where t_{em} is the thickness of the specimen under observation in the transmission electron microscope. A value of 1000Å has been assumed for t_{em} which is the upper limit of electron transmission. However, it is quite likely that it may be less than 1000Å. In that case the calculated f will be less than the true value and as a result there will be an underestimation of the α values.
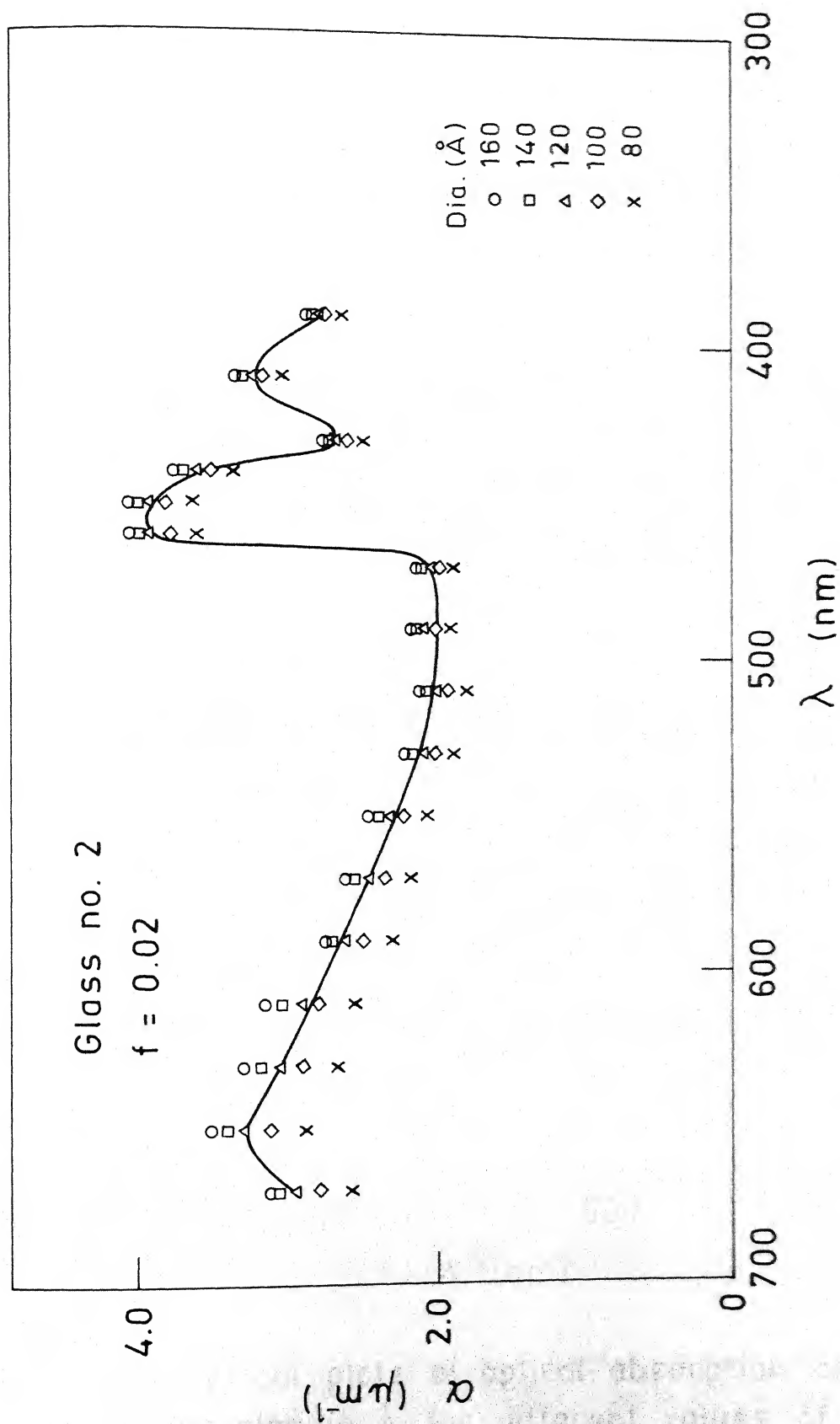
Fig. 5.33 Theoretical plots of optical absorption coefficients α vs wavelength λ for different particle diameters (calculated by MG Theory).
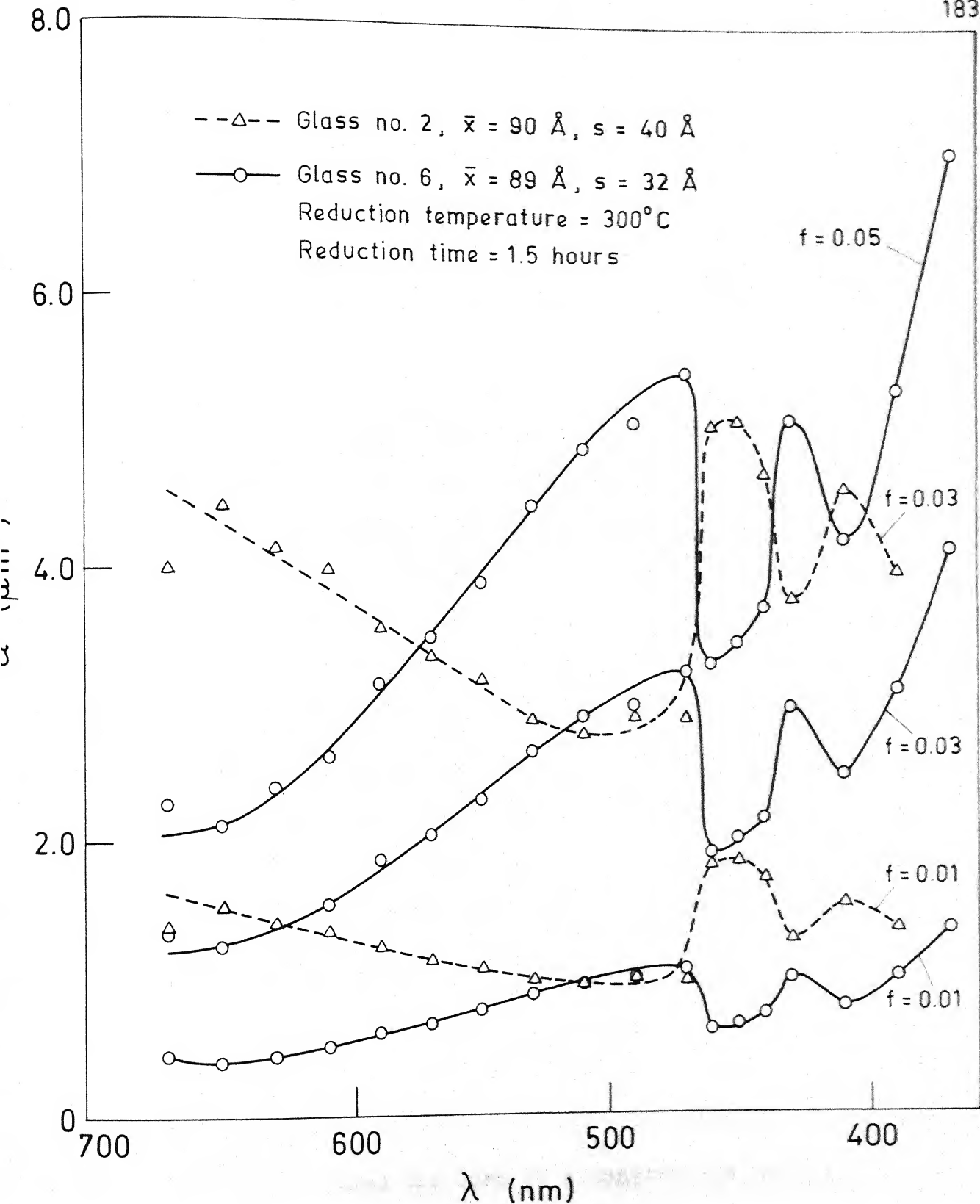
Fig. 5.34 Theoretical plots of optical absorption coefficient α vs wavelength λ for different values of fill factors. (calculated by MG Theory)

So far we have assumed that the metallic phase consists either of spherical granules of some average particle size or of a distribution of spherical particles (BR and MG-PvS theories). However, the inspection of microstructures (figures 5.5 to 5.16) suggests that elongated interconnected particles are also present. Therefore, the assumption that the metallic . bismuth phase consists of ξ fraction of spheres, ζ fraction of single strand chains and χ ($\chi = 1 - \xi - \zeta$) fraction of f.c.c. clusters is reasonable. This consideration effectively takes into account the dipole-dipole interactions between the particles as they are closely situated. This is accomplished by replacing the L_k's in equation (5.14) by effective depolarisation factors corresponding to the above mentioned geometrical configurations[122]. It has been shown by Granqvist et al.[122] that there exists an optimum combination of ξ, ζ to obtain the best agreement between experimental and calculated α values subject to the following constraints,

$$\xi \geq 0 \qquad\qquad (5.37)$$

$$\zeta \geq 0 \qquad\qquad (5.38)$$

$$\xi + \zeta \leq 1 \qquad\qquad (5.39)$$

Thus the problem takes the form of a constrained optimisation. We have chosen the MG-PvS formalism and glass no.2 reduced at 200°C for 2.0 hours for such an analysis.

5.5.2 Formulation of constrained optimisation and numerical computation

The objective function to be minimised subjected to the constraints specified in equations (5.37 - 5.39) is given by,

$$f(\vec{X}) = \sum_{\omega=1}^{n} (\alpha_{\omega}^{MG-PvS} - \alpha_{\omega}^{exp})^2 \qquad (5.40)$$

where α_{ω}^{MG-PvS} and α_{ω}^{exp} are the theoretical α values as calculated by MG-PvS theory and the experimentally observed α values respectively at an angular frequency ω and n being the number of frequencies at which the α value is calculated. $\vec{X}$ is a vector consisting of ξ, ζ - the optimisation variables. The above constrained optimisation is converted into an equivalent unconstrained optimisation by augmenting the function $f(\vec{X})$ by a penalty term within the frame work of internal penalty function method[153]. The equivalent function $\varphi(\vec{X}, r_k)$ is given by,

$$\varphi(\vec{X}, r_k) = f(\vec{X}) - r_k \sum_{j=1}^{m} \frac{1}{g_j(\vec{X})} \qquad (5.41)$$

where r_k is the penalty parameter, $g_j(\vec{X}) \le 0$ is the constraint. In our case the last term of equation (5.41) is given by,

$$\sum_{j=1}^{m} \frac{1}{g_j(\vec{X})} = [-\frac{1}{\xi} - \frac{1}{\zeta} + \frac{1}{\xi+\zeta-1}] \qquad (5.42)$$

For evaluating the α_ω^{MG-PvS} by MG-PvS theory $\bar{\epsilon}_1$ and $\bar{\epsilon}_2$ will be given by equations (5.30) and (5.31) with A_1, B_1, C_1 and D_1 of equations (5.32) replaced by the following expressions to take into account the ξ fraction of sphere, ζ fraction of single strand chain (s.c.) and X fraction of f.c.c. cluster (f.c.).

$$A_1 = 1 + \frac{2}{3} f\left[\xi \sum_j w_j \delta'_j \Big|_{sphere} + \zeta\delta' \Big|_{s.c.} + X\delta' \Big|_{f.c.} \right] \quad (5.43a)$$

$$B_1 = \frac{2}{3} f\left[\xi \sum_j w_j \delta''_j \Big|_{sphere} + \zeta\delta'' \Big|_{s.c.} + X\delta'' \Big|_{f.c.} \right] \quad (5.43b)$$

$$C_1 = 1 - \frac{1}{3} f\left[\xi \sum_j w_j \delta'_j \Big|_{sphere} + \zeta\delta' \Big|_{s.c.} + X\delta' \Big|_{f.c.} \right] \quad (5.43c)$$

$$D_1 = \frac{1}{3} f\left[\xi \sum_j w_j \delta''_j \Big|_{sphere} + \zeta\delta'' \Big|_{s.c.} + X\delta'' \Big|_{f.c.} \right] \quad (5.43d)$$

where

$\delta'_j \Big|_{sphere}$, $\delta' \Big|_{s.c.}$ and $\delta' \Big|_{f.c.}$ are respectively the real parts of the polarisability corresponding to spheres, single strand chains and f.c.c. clusters. Similarly, $\delta''_j \Big|_{sphere}$, $\delta'' \Big|_{s.c.}$ and $\delta'' \Big|_{f.c.}$ represent the imaginary parts of the polarisability corresponding to the geometrical configurations – spheres, single strand chains and the f.c.c. clusters. δ'_j and δ''_j are given by expressions (5.33) to (5.35) by introducing L_k's for sphere[122]. The effective depolarisation factors

corresponding to different geometrical configurations have been computed, as we have mentioned in Section 5.4.2, that these are made up of identical spheres[122]. Therefore, in the case of single strand chains and f.c.c. clusters an average particle size has been used to compute the values of δ' and δ''. After evaluating $\bar{\varepsilon}_1$ and $\bar{\varepsilon}_2$ numerically, the α values are computed from equation (5.36).

5.5.2.1 Numerical scheme

The following iterative scheme is used to optimise the function $\varphi(\vec{X}, r_k)$.

Step 1 : The computation is started with three initial feasible values of $\vec{X}_1, \vec{X}_2$ and $\vec{X}_3$ such that the strict inequality constraint is satisfied. An initial value of $r_1 > o$ is taken. $k = 1$ is set.

Step 2 : $\varphi(\vec{X}, r_k)$ is minimised using Simplex optimisation technique[153]. Whether the minimised $\vec{X}_k^*$ obtained corresponds to the minimum of the original problem or not ($f(\vec{X})$) is tested. If so the process is terminated. Otherwise the next step is followed.

Step 3 : New penalty parameter r_{k+1} is computed by

$$r_{k+1} = cr_k, \quad \text{where} \quad c < 1.$$

Step 4 : With the minimum value of $\vec{X}_k^*$ and setting $k = k+1$ step 2 is repeated.

The computer programme in fortran language is given in Appendix 4.

Figure 5.35 shows the plot of α values as a function of wavelength λ for an optimum combination of 26 percent spheres, 0.6 percent single strand chain and 73.4 percent f.c.c. clusters within an error of $\pm$ 4.0 percent for glass no.2 reduced at 200°C for 2 hours. In this figure are also included the computed values from MG, and MG-PvS theories and the experimental results. Figure 5.35 shows that a better agreement is obtained between theory and experiment when the microstructure is assumed to consist of a combination of spheres, single strand chains and f.c.c. clusters rather than a simple distribution of spheres. It may be mentioned that the above optimisation procedure when applied to the silicate glass system does not bring about any significant improvement in the calculated α values vis-a-vis the experimental data. This is attributed to the possibility of an overestimation of the fill factor as discussed earlier.
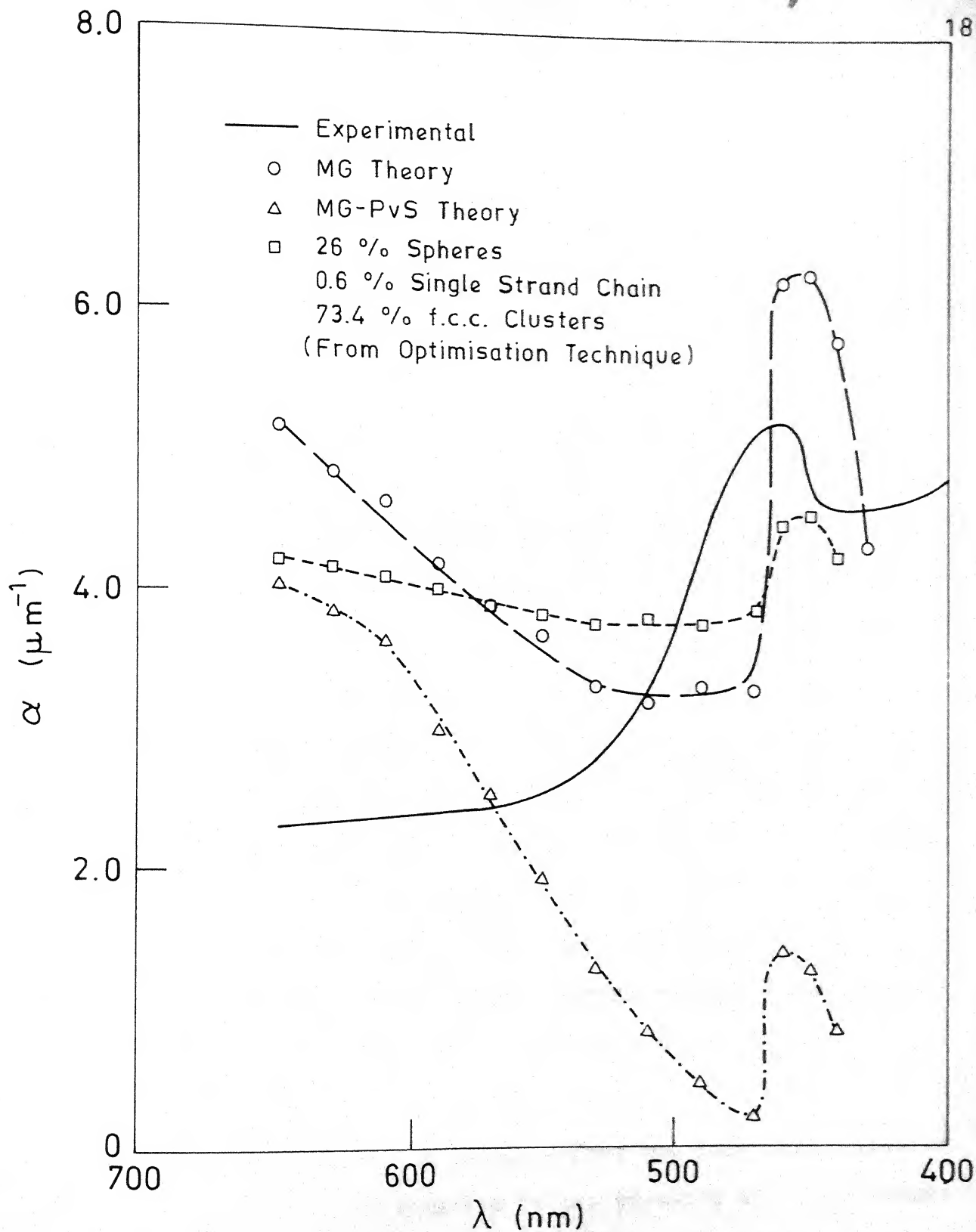
Fig. 5.35   Comparison of experimental absorption coeff-
icient α with theoretical values computed
by different models for glass no. 2 reduced
at 200°C for 2.0 hours.

CHAPTER 6

CONCLUSIONS

Based on electrical and optical studies of vanadium phosphate as well as silicate glasses containing bismuth the following conclusions are drawn.

(1) A particle stretching model in which molten metallic granules stretch under the influence of an electric field can explain semi-quantitatively most of the characteristic features of memory switching in oxide glasses containing metallic bismuth granules.

(2) Depending on the sample thickness the vanadium phosphate glasses containing bismuth can show either memory or threshold switching behaviour.

(3) The computed current-voltage characteristics especially in the negative resistance region compare reasonably well with the experimental results for vanadium phosphate glasses containing bismuth.

(4) The switching time as computed from the numerical solution of time dependent heat equation in the presence of Joule losses agrees well with experimental switching time obtained by pulse measurements.

(5)   The switching time as computed from the numerical,
solution of time dependent stretching of molten metallic bis-
muth particles in vanadium phosphate system, is found to be
very small as compared to the experimentally determined switching
time from pulse measurements. However, the fast kinetics of
stretching indicates that if the metallic bismuth particles are
in a molten state switching time of the order of nanoseconds
can be achieved.

(6)   MG, MG-PvS and BR theories predict the optical absorption
peak positions which are in fair agreement with the experimentally
observed values for both silicate and vanadium phosphate glass
systems containing bismuth granules.

(7)   MG theory predicts results with regard to the absorption
coefficient α which are in better agreement with experiment than
those obtained from MG-PvS or BR theory   in vanadium phosphate
glass-metal system.

(8)   A typical computation using constrained optimisation
technique indicates that better quantitative agreement (within
$\pm$ 4 percent) with experiment over the entire spectral range can
be achieved by assuming that the vanadium phosphate glass-metal
composites consist of certain fractions of spheres, f.c.c.
 clusters and single strand chains. The microstructural
features of most samples tend to corroborate this model.

REFERENCES

1. D. Chakravorty, Preparation and Characterization of Materials, ed., C.N.R. Rao and J.M. Honig (Academic Press, London, in press).

2. P.W. McMillan, Glass-Ceramics, 2nd Edition (Academic Press, London, 1979).

3. W.A. Weyl, Coloured glasses, Society of Glass Technology, 1951.

4. G.E. Rindone, J. Am. Ceram. Soc. 45, 7 (1962).

5. S.D. Stookey, U.S. Patent 2515275, 1950.

6. S.D. Stookey, Brit. Patent 635649, 1947.

7. S.D. Stookey, Brit. Patent 752243, 1956.

8. S.D. Stookey and R.D. Maurer, Progress in Ceramic Sciences, Vol. 2 (Pergamon Press, New York, 1962), p. 77.

9. Roger J. Araujo, Treatise on Materials Science and Technology, Vol. 12 (Academic Press, London, 1977), p. 91.

10. W.H. Armistead and S.D. Stookey, U.S. Patent 3923529, 1965.

11. J. Suzuki and M. Kume, U.S. Patent 3617316, 1971.

12. Roger J. Araujo, L.G. Sawchuk and T.P. Seward, U.S. Patent 3703388, 1972.

13. P.W. McMillan, Phys. Chem. Glasses, 17 (5), 193 (1976).

14. Y. Moriya, 10th Int. Congr. Glass, Kyoto (1974).

15. T.P. Seward, Symposium on Photochromic Glasses, Am.Ceram. Soc. Meeting, 76th Chicago, Illinois (1974).

16. S. Sakka, K. Matsusita and K.Kamiya, 10th Int. Congr. Glass, No.5, Kyoto (1974).

17. H. Besen, Proc. XIth Int. Congr. Glass, Vol.3, Prague (1977).

18. George B. Hares and Thomas P. Seward III, J. Non-cryst. Solids, 38 and 39, 205 (1980).

19. George Gliemeroth, J. Non-cryst. Solids, 38 and 39, 217(1980).

20. R.J. Araujo, R.A. Eppler and E.F. Kruse, U.S. Patent 3,328, 182 (1967).

21. E.L. Swarts and J.P. Pressau, J. Am. Ceram. Soc. 48, 333 (1965).

22. G.S. Meiling, U.S. Patent 3615, 771 (1971).

23. R.J. Araujo, G.H. Beall and L.G. Sawchuk, U.S. Patent 3923529 (1975).

24. L.G. Sawchuk and S.D. Stookey, U.S. Patent 3293052 (1966).

25. S. Sakka and J.D. MacKenzie, J. Am. Ceram. Soc. 35, 553 (1972).

26. Thomas P. Seward III, J. Appl. Phys. 46(2), 689 (1975).

27. L.J. Randall and T.P. Seward III, U.S. Patent 3208860 (1965).

28. J.J. Hammel and T. McGary, Reactivity of Solids, ed. J.W. Mitchell (Wiley, New York, (1969) p. 695.

29. T.P. Seward III, J. Non-cryst. Solids 40, 499 (1980).

30. S.D. Stookey, G.H. Beall and J.E. Pearson, J. Appl. Phys. 49, 5114 (1978).

31. N.F. Borrelli, J.B. Chodak, D.A. Nolan and T.P. Seward III, J. Opt. Soc. Am. 69, 1514 (1979).

32. John C.C. Fan and Paul M. Zavracky, Appl. Phys. Lett. 29(8), 478 (1976).

33. John C.C. Fan and Steven A. Spura, Appl. Phys. Lett. 30(10), 511 (1977).

34. H.G. Craighead and R.A. Buhrman, Appl. Phys. Lett. 31(7), 423 (1977).

35. G.A. Niklasson and C.G. Granqvist, J. Appl. Phys. 50(8), 5500 (1979).

36. H. Schulz, Glashütte, 66, 685 (1936).

37. L.J. Dykstra and E.M. Meyer, U.S. Patent 2274955 (1942).

38. T.W.H. Ward, U.S. Patent 2280135 (1942).

39. R.L. Green and B. Blodgeett, J. Am. Ceram. Soc. 31, 89 (1948).

40. K.B. Blodgeett, J. Am. Ceram. Soc. 34, 14 (1951).

41. D. Chakravorty, French Patent 31218 (1972).

42. D. Chakravorty, J. Non-cryst. Solids 15, 191 (1974).

43. G.C. Das, T.K. Reddy and D. Chakravorty, J. Mat. Sc. 13, 3211 (1978).

44. D. Chakravorty, A.R. Haranahalli and D. Kumar, Phys. Stat. Solidi (a), 51, 275 (1979).

45. D. Chakravorty, A.K. Bandopadhyay and V.K. Nagesh, J.Phys. D: Appl. Phys. 10, 2077 (1977).

46. D. Chakravorty and S. Chakrabarti, J. Non-cryst. Solids. 38 and 39, 295 (1980).

47. B. Abeles, Sheng Ping, M.D. Coutts and Y. Arie, Adv. Phys. 24, 407 (1975).

48. D. Chakravorty, B.N. Keshavram and A. Venkateswaran, J. Mat. Sc. 14, 2991 (1979).

49. D. Chakravorty and R. Bhatnagar, Proc. Int. Symp. Fibres and Composites, New Delhi, 1, 71 (1976).

50. D. Chakravorty, Appl. Phys. Lett. 24(2), 62 (1974).

51. D. Chakravorty and C.S. Murthy, J. Phys. D: Appl. Phys. 8, L162 (1975).

52. P. Hing and P.W. McMillan, J. Mat. Sc. 8, 1041 (1973).

53. B.N. Keshavram, M.Tech. Thesis, IIT Kanpur (1978).

54. A. Venkateswaran, M.Tech. Thesis, IIT Kanpur (1979).

55. S.R. Ovshinsky, Electronics, 32, 76 (1959).

56. A.D. Pearson, W.R. Northover, Jacob F. Dewald and W.F. Peck, Jr., Adv. Glass Technology (Plenum Press, New York, 1962), p. 357.

57. S.R. Ovshinsky, Phys. Rev. Lett. 21, 1450 (1968).

58. D. Adler, H.K. Henisch and N.F. Mott, Rev. Mod. Phys. 50, 209 (1978).

59. M. Kastner, D. Adler and H. Fritzsche, Phys. Rev. Lett. 37, 1504 (1976).

60. R.A. Street, Adv. Phys. 25, 397 (1976).

61. R. Grigorovici, Thin Solid Films, 9, 1(1971).

62. B.T. Kolomiets, Amorphous and Liquid Semiconductors, ed. J. Stuke and W. Brenig (Taylor and Francis, London, 1974), p. 189.

63. B.T. Kolomiets, T.N. Mamontova and A.A. Babaev, Amorphous and Liquid Semiconductors, ed. M.H. Cohen and G. Lucovosky (North Holland, Amsterdam, 1972), p. 1004.

64. J.M. Marshal, C. Main and A.E. Owen, Amorphous and Liquid Semiconductors, ed. M.H. Cohen and G. Lucovosky (North Holland, Amsterdam, 1972), p. 760.

65. C. Main and A.E. Owen, Amorphous and Liquid, Semiconductors ed. J. Stuke and W. Brening (Taylor and Francis, London, 1974) p. 783.

66. S.G. Bishop, U. Strom and P.C. Taylor, Phys. Rev. Lett. 39, 1346 (1975).

67. A.E. Owne, J.M. Robertson and C. Main, J. Non-cryst. Solids 32, 29(1979).

68. H. Fritzsche, Amorphous and Liquid Semiconductors ed. J. Tauc (Plenum Press, New York, 1974).

69. W.D. Buckley and S.H. Holmberg, Solid Stat. Electronics 18, 127 (1975).

70. A.R. Hilton, C.E. Jones and M. Brau, Phys. Chem. Glasses 7, 105 (1966).

71. J.A. Savage, J. Non-cryst. Solids 11, 121 (1972).

72. H.J. Stocker, C.A. Barlow and D.F. Weirauch, J. Non-cryst. Solids 4, 523 (1970).

73. H. Lueder and E. Epenke, Z. Tech. Phys. 16, 11(1935).

74. B.K. Ridley, Proc. Phys. Soc. 82, 954 (1963).

75. A.C. Warren, J. Non-cryst. Solids 4, 613 (1970).

76. D.C. Thomas and J.C. Male, Amorphous and Liquid Semicon-
    ductors ed. M.H. Cohen and G. Lucovsky (North Holland,
    Amsterdam, 1972) p. 522.

77. C. Popescu and H. Croitrou, Amorphous and Liquid Semicon-
    ductors ed. M.H. Cohen and G. Lucovsky (North Holland,
    Amsterdam, 1972), p. 531.

78. J.M. Robertson and A.E. Owen, J. Non-cryst. Solids 8-10,
    939 (1972).

79. J. Allison, V.R. Dawe and P.N. Robson, J. Non-cryst.
    Solids 8-10, 563 (1972).

80. D.M. Kroll and M.H. Cohen, Amorphous and liquid semicondu-
    ctors ed. M.H. Cohen and G. Lucovsky (North Holland,
    Amsterdam, 1972) p. 544.

81. A.J. Hughes, P.A. Holland and A.H. Lellington, J.Non-cryst.
    Solids 17, 89(1975).

82. P. Esquada and H.K. Henisch, J. Non-cryst. Solids 22,
    97 (1976).

83. J.K. Higgins, B.K. Temple and J.E. Lewis, J. Non-cryst.
    Solids 23, 187 (1977).

84. N.F. Mott, Contemp. Phys. 10, 125 (1969).

85. H.K. Henisch, Sci. Am. 221, 30(1969).

86. N.F. Mott and E.A. Davis, Electronic Processes in Non-
    crystalline Materials, 2nd Edition (Clarendon Press,
    Oxford, 1979), p. 509.

87. K.E. Peterson and D. Adler, J. Appl. Phys. Lett. 25, 211
    (1974).

88. K.E. Peterson and D. Adler, J. Appl. Phys. 47, 256 (1976).

89. R.W. Pryor and H.K. Henisch, J. Non-cryst. Solids 7,
    184 (1972).

90. G.F. Vendura and H.K. Henisch, J. Non-cryst. Solids 11,
    105 (1972).

91. G.C. Vezzoli, L.W. Doremus and P.J. Walsh, Amorphous and
    Liquid Semiconductors, ed. J. Stuke and W. Brenig (Taylor
    and Francis, London, 1974) p. 651.

92. P.J. Walsh and G.C. Vezzoli, Amorphous and Liquid Semiconductors ed. J. Stuke and H. Brening (Taylor and Francis, London, 1974), p.1391.

93. S.R. Ovshinsky and P.H. Klose, J. Non-cryst. Solids 8-10, 892 (1972).

94. H. Fritzsche and S.R. Ovshinsky, J. Non-cryst. Solids 2, 148 (1970).

95. E. Ahilea and A.A. Hirsch, J. Appl. Phys. 42, 5601 (1971).

96. A.W. Adamson, Physical Chemistry of Surfaces (Inter-Science, New York, 1967).

97. T. Kaplan and D. Adler, Appl Phys. Lett 19, 418(1971).

98. E. Kreyszig, Adv. Engg. Math (Wiley Eastern Ltd., New Delhi, India, 1971).

99. J.M. McCormick and M.G. Salvadori, Numerical Methods in Fortran (Prentice-Hall Inc., Englewood Cliffs, New Jersey, 1964).

100. W.D. Kingery, Introduction to Ceramics (Wiley, New York, 1967).

101. S.J. Peppiatt, Proc. Roy. Soc. 345A, 1642 (1975).

102. C.D. Hodgman, Handbook of Chemistry and Physics (Chemical Rubber Pub. Co., Cleveland, Ohio, 1962).

103. D. Turnbull, J. Chem. Phys. 18, 768 (1950).

104. J.Crank and P. Nicolson, Proc. Phil. Soc. 43, 50(1947).

105. L. Fox, Numerical Solution of Ordinary and Partial Differential Equations, ed. L. Fox (Pergamon Press, London, 1962) p. 235.

106. M.W. Davies, B. Kerrison, W.E. Cross, M.J. Robson and D.F. Wichall, J. Iron and Steel Inst. 208, 348 (1970).

107. D. Kumar, Ph.D. Thesis, IIT Kanpur (1980).

108. Selected Powder Diffraction Data for Minerals, (Published by Joint Committee on Powder Diffraction Standards, Pennsylvania, U.S.A., 1979).

109. R.R. Sutherland, J. Phys. D: Appl. Phys. $\underline{4}$, 468 (1974).

110. G. Dearnaley, D.V. Morgan and A.M. Stonehan, J. Non-cryst. Solids $\underline{4}$, 593 (1970).

111. S.W. Yuan, Foundation of Fluid Mechanics (Prentice Hall, India, Pvt.Ltd., New Delhi, 1976).

112. W.F. Ames, Numerical Methods for Partial Differential Equations (Thomas Nelson and Sons Ltd., London, 1969).

113. R.W. Doremus, J. Chem. Phys. $\underline{40}$, 2389 (1964).

114. R.W. Doremus, J. Chem. Phys. $\underline{42}$, 414 (1965).

115. H. Rawson, Phys. Chem. Glasses $\underline{6}$, 81 (1965).

116. D. Chakravorty, A. Shuttleworth and P.H. Gaskell, J. Mat. Sc. $\underline{10}$, 799 (1975).

117. P. Sarkar, M.Tech. Thesis, IIT Kanpur (1981).

118. W. Hampe, Z. Phys $\underline{152}$, 470 (1958).

119. R.W. Cohen, G.D. Cody, M.D. Coutts and B. Abeles, Phys. Rev.B $\underline{8}$, 3689 (1973).

120. P.H. Lissberger and R.G. Nelson, Thin Solid Films, $\underline{21}$, 159 (1974).

121. P.H. Lissberger and P.W. Saunders, Thin Solid Films, $\underline{34}$, 323 (1976).

122. C.G. Granqvist and O. Hunderi, Phys. Rev. B $\underline{16}$(8), 3513 (1977).

123. C.G. Granqvist and O. Hunderi, J. Appl. Phys. $\underline{51}$(3), 1751(1980).

124. C.G. Granqvist and G.A. Niklasson, J. Appl. Phys. $\underline{49}$(6), 3512(1978).

125. C.G. Granqvist, N. Calander and O. Hunderi, Solid Stat. Commun. $\underline{31}$, 249 (1979).

126. S. Norman, T. Andersson and C.G. Granqvist, Phys. Rev. B $\underline{18}$(2), 674 (1978).

127. B. Abeles and J.I. Gittleman, Appl. Opt. 15, 2328 (1976).

128. C.G. Granqvist and O. Hunderi, Phys. Rev. B 18(6), 2897 (1978).

129. C.G. Granqvist, J. Appl. Phys. 50(4), 2916 (1979).

130. J.I. Gittleman, B. Abeles, P. Zanzucchi and Y. Arie, Thin Solid Films 45, 9(1977).

131. D.R. McKenzie and R.C. McPhedran, AIP, Conf. Proc. 40, 283 (1978).

132. C.G. Granqvist and O. Hunderi, Z. Physik B 30, 47(1978).

133. C.G. Granqvist and O. Hunderi, J. Appl. Phys. 50(2), 1058 (1979).

134. L. Genzel, T.P. Martin and U. Kreibig, Z. Physik B 21, 339 (1974).

135. M.A. Smithard, Solid Stat. Commun. 13, 153 (1973).

136. R.T. DeHoff and F.N. Rhines, Quantative Microscopy (McGraw-Hill, New York, 1968).

137. G. Mie, Ann. Phys. 25, 377 (1908).

138. C.R. Bamford, Colour Generation and Control in Glasses, Glass Science and Technology 2 (Elsevier Sci. Pub. Co., Amsterdam, 1977).

139. R. Gans, Ann. Phys. 29, 277 (1909).

140. R. Gans, Ann. Phys. 37, 883 (1912).

141. J.C. Maxwell-Garnett, Phil. Trans. Roy. Soc. London 203, 385 (1904).

142. L. Onsager, J. Am. Chem. Soc. 58, 1486 (1936).

143. D. Polder and J.H. van Santen, Physica (Utrecht) 12, 257 (1946).

144. D.A.G. Bruggeman, Ann. Phys. (Leipz.) 24, 636 (1935).

145. O. Hunderi, Phys. Rev.B 7, 3419 (1973).

146. G.A. Niklasson, C.G. Granqvist and O. Hunderi, Appl. Opt. 20(1), 26 (1981).

147. H.C. Van de Hulst, Light Scattering by Small Particles
      (Wiley, New York, 1957).

148. American Institute of Physics Handbook, 3rd Edition, ed.
      Dwight E. Gray (McGraw-Hill Book Co. New York, 1972),
      p. 6-128.

149. J. Toots and L. Marton, J. Opt. Soc. Am. $\underline{59(10)}$, 1305
      (1969).

150. C. Kittle, Introduction to Solid State Physics (Wiley
      Eastern Pvt.Ltd., New Delhi, 1974).

151. A. Mansingh, R.P. Tandon and J.K. Vaid, J. Phys. C:
      Solid State Phys. $\underline{8}$, 1023 (1975).

152. D. Chakravorty, C.S. Vithlani and G.K. Mehta, J. Mat.Sc.
      $\underline{13}$, 1438 (1978).

153. S.S. Rao, Optimization, Theory and Practice (Wiley Eastern
      Ltd., New Delhi, 1979).

APPENDIX   1

```
      PROGRAMME FOR COMPUTING THE TEMPERATURE PROFILE
      TO REACH THE MELTING POINT OF BISMUTH AT THE
      CENTRE OF THE SAMPLE BY SOLVING HEAT EQUATION
      BY RUNGE-KUTTA-NYSTROM METHOD

      ************************************************************
      DA- AVERAGE PARTICLE DIA. IN METER
      CK(I)- SEPERATION TO DIA. RATIO
      TMB-MELTING TEMP OF BISMUTH

      ------------------------------------------------
      DIMENSION E(25),DA(50)
      COMMON/A1/E,THIC,K
      COMMON/A3/TPI,TMB,TI,TMX,ND
      COMMON/A5/DIFT,DIFT1,THICP,THICN,DIFTP,DIFTN
      READ12,NA,NC,ND
12    FORMAT(3I3)
      PRINT5,NA,NC,ND
5     FORMAT(50X,3I3/1X,130(1H-))
      DA(1)=700.E-10
      DO 10I=2,NA
10    DA(I)=DA(I-1)+100.E-10
      READ16,(E(K),K=1,NC)
16    FORMAT(5E7.1)
      TI=433.
      PRINT 46,TI
46    FORMAT(44X,'AMBIENT TEMP IN DEG KELVIN=',E15.8/44X,20(1H-))
      DO 40 I=1,NA
      PRINT45,DA(I)
45    FORMAT(45X,'AVERAGE PARTICLE DIA IN  METER=',E15.8)
      ------------------------------------------------
      COMPUTATION OF SIZE DEPENDENT MELTING POINT OF BISMUTH
      ------------------------------------------------
      ABI=208.87
      VA=ABI/9.67
      VB=ABI/10.
      TM=271.0+273.
      AD1=DA(I)*1.E2/2.
      DC=(VA-(VB**2)/(VB-VA))/AD1
      DB=-(2.*54.4)/(10.2*ABI*4.184E07)
      TMB=TM*EXP(DB*DC)
      PRINT 700,TMB
700   FORMAT(40X,'MELTING TEMP. OF BISMUTH  DEPENDING ON RADIUS=',F6.2)
      DO 70 K=1,NC
      PRINT75,E(K)
75    FORMAT(40X,'FIELD IN VOLT PER METER=',E15.8)
      THIC=5.E-6
      TMX=TMB+5.
      TPI=1.E2
      CALL DCT
      IF(DIFT1.LE.0.1)GO TO 70
      IF(DIFT.LT.0.)GO TO 61
62    THIC=THIC+1.E-6
      CALL DCT
      IF(DIFT1.LE.0.1)GO TO 70
      IF(DIFT.LT.0.)GO TO 63
      GO TO 62
61    THIC=THIC*.9
      CALL DCT
      IF(DIFT1.LE.0.1)GO TO 70
      IF(DIFT.GT.0.)GO TO 63
      GO TO 61
      ------------------------------------------------
      INTERPOLATION OF THICKNESS BY REGULA FALSI METHOD
      ------------------------------------------------
63    THIC=(THICP*DIFTN-THICN*DIFTP)/(DIFTN-DIFTP)
      CALL DCT
      IF(DIFT1.LE.0.1)GO TO 70
```

```
          GO TO 63
70        CONTINUE
          PRINT110
110       FORMAT(1X,130(1H*))
          PRINT130
130       FORMAT(1X,130(1HB))
40        CONTINUE
          STOP
          END

          ***********************************************************************

C         SOLUTION OF SECOND ORDER DIFF. HEAT EQ. BY 4TH ORDER RUNGE KUTTA
C         NYSTROM METHOD
C         TP(1)-FIRST DERIVATIVE OF TEMPERATURE
C         T(L)-TEMPERATURE IN DEGREE KELVIN
          SUBROUTINE DCT

C         ----------------------------------------------------------------
          DIMENSION E(25)
          COMMON/A1/E,THIC,K
          COMMON/A3/TPI,TMB,TI,TMX,ND
          COMMON/A4/DIF,DIF1,TPP,TPN,DIFP,DIFN
          COMMON/A5/DIFT,DIFT1,THICP,THICN,DIFTP,DIFTN
          CALL GOPES
          IF(DIF1.LE.0.1)GO TO 74
          IF(DIF.LT.0.)GO TO 12
15        TPI=TPI*.9
          CALL GOPES
          IF(DIF1.LE.0.1)GO TO 74
          IF(DIF.LT.0.)GO TO 16
          GO TO 15
12        TPI=TPI*1.1
          CALL GOPES
          IF(DIF1.LE.0.1)GO TO 74
          IF(DIF.GT.0.)GO TO 16
          GO TO 12
C         ----------------------------------------------------------------
C         INTERPOLATION OF FIRST ORDER DERIVATIVE OF TEMPERATURE
C         BY REGULA FALSI METHOD
C         ----------------------------------------------------------------
16        TPI=(TPP*DIFN-TPN*DIFP)/(DIFN-DIFP)
          CALL GOPES
          IF(DIF1.LE.0.1)GO TO 74
          GO TO 16
74        IF(DIFT.GT.0.) TPI=TPI*.9
          RETURN
          END

          ***********************************************************************

C         SUBROUTINE GOPES

C         ----------------------------------------------------------------
          DIMENSION E(25),TP(200),T(200)
          COMMON/A1/E,THIC,K
          COMMON/A2/TT,FUN
          COMMON/A3/TPI,TMB,TI,TMX,ND
          COMMON/A4/DIF,DIF1,TPP,TPN,DIFP,DIFN
          COMMON/A5/DIFT,DIFT1,THICP,THICN,DIFTN,DIFTN
          BND=ND
          H=1./BND
          NN=ND+1
30        TP(1)=TPI
          T(1)=TI
          DO 60 L=2,NN
          TT=T(L-1)
          IF(TT.LT.50.)TPI=TPI+1.E2
```

```
             GO TO 63
70           CONTINUE
             PRINT110
110          FORMAT(1X,130(1H*))
             PRINT130
130          FORMAT(1X,130(1HB))
40           CONTINUE
             STOP
             END

      ************************************************************

C     SOLUTION OF SECOND ORDER DIFF. HEAT EQ. BY 4TH ORDER RUNGE
C     NYSTROM METHOD
C     TP(1)-FIRST DERIVATIVE OF TEMPERATURE
C     T(L)-TEMPERATURE IN DEGREE KELVIN
C          SUBROUTINE DCT
C
C     ----------------------------------------------------------------
C
             DIMENSION E(25)
             COMMON/A1/E,THIC,K
             COMMON/A3/TPI,TMB,TI,TMX,ND
             COMMON/A4/DIF,DIF1,TPP,TPN,DIFP,DIFN
             COMMON/A5/DIFT,DIFT1,THICP,THICN,DIFTP,DIFTN
             CALL GOPES
             IF(DIF1.LE.0.1)GO TO 74
             IF(DIF.LT.0.)GO TO 12
15           TPI=TPI*.9
             CALL GOPES
             IF(DIF1.LE.0.1)GO TO 74
             IF(DIF.LT.0.)GO TO 16
             GO TO 15
12           TPI=TPI*1.1
             CALL GOPES
             IF(DIF1.LE.0.1)GO TO 74
             IF(DIF.GT.0.)GO TO 16
             GO TO 12
C     ----------------------------------------------------------------
C     INTERPOLATION OF FIRST ORDER DERIVATIVE OF TEMPERATURE
C     BY REGULA FALSI METHOD
C     ----------------------------------------------------------------
16           TPI=(TPP*DIFN-TPN*DIFP)/(DIFN-DIFP)
             CALL GOPES
             IF(DIF1.LE.0.1)GO TO 74
             GO TO 16
74           IF(DIFT.GT.0.) TPI=TPI*.9
             RETURN
             END

C     ************************************************************

C          SUBROUTINE GOPES
C
C     ----------------------------------------------------------------
C
             DIMENSION E(25),TP(200),T(200)
             COMMON/A1/E,THIC,K
             COMMON/A2/TT,FUN
             COMMON/A3/TPI,TMB,TI,TMX,ND
             COMMON/A4/DIF,DIF1,TPP,TPN,DIFP,DIFN
             COMMON/A5/DIFT,DIFT1,THICP,THICN,DIFTP,DIFTN
             BND=ND
             H=1./BND
             NN=ND+1
30           TP(1)=TPI
             T(1)=TI
             DO 60 L=2,NN
             TT=T(L-1)
             IF(TT.LT.50.)TPI=TPI+1.E2
```

```
      IF(IT.LT.50.)GO TO 30
      CALL ROSE
      AA=(H/2.)*FUN
      BITA=(H/2.)*(TP(L-1)+AA/2.)
      TI=T(L-1)+BITA
      IF(TT.LT.50.)TPI=TPI+1.E2
      IF(TT.LT.50.)GO TO 30
      CALL ROSE
      BB1=(H/2.)*FUN
      DEL=H*(TP(L-1)+BB1)
      TT=T(L-1)+DEL
      IF(TT.LT.50.)TPI=TPI+1.E2
      IF(TT.LT.50.) GO TO 30
      CALL ROSE
      DD=(H/2.)*FUN
      AK=1./3.*(AA+2.*BB1)
      AKS=1./3.*(AA+4.*BB1+DD)
      T(L)=T(L-1)+H*(TP(L-1)+AK)
      TP(L)=TP(L-1)+AKS
60    CONTINUE
      DIF=T(NN)-T(1)
      DIF1=ABS(DIF)
      IF(DIF.GT.0.)GO TO 20
      TPN=TP(1)
      DIFN=DIF
      GO TO 25
20    TPP=TP(1)
      DIFP=DIF
25    IF(DIF1.GT.0.1)GO TO 73
      NN1=(NN+1)/2
      DIFT=TMB-T(NN1)
      DIFT1=ABS(DIFT)
      IF(DIFT.GT.0.)GO TO 40
      THICN=THIC
      DIFTN=DIFT
      GO TO 45
40    THICP=THIC
      DIFTP=DIFT
45    IF(DIFT1.GT.0.1)GO TO 73
      PRINT135,THIC
135   FORMAT(48X,'THICKNESS IN METER=',E15.8/48X,18(1H-))
      PRINT700,(T(L),L=1,NN)
700   FORMAT(1X,8E15.8)
      PRINT105
105   FORMAT(2X,128(1H-))
73    RETURN
      END

      ****************************************************************

      SUBROUTINE ROSE

      --------------------------
      DIMENSION E(25)
      COMMON/A1/E,THIC,K
      COMMON/A2/TT,FUN
      SIG=-(2.3*1.25*1000./TT)
      SIG1=(100./1.334)*EXP(SIG)
      FUN=-(THIC**2/1.6744)*SIG1*E(K)**2
      RETURN
      END
```

APPENDIX   2

```
C     PROGRAMME FOR COMPUTING THE I-V CHARACTERISTICS OF
C     VANADIUM PHOSPHATE GLASS CONTAINING BISMUTH AND DETERMINATION
C     OF TEMPERATURE PROFILE BY SOLVING TIME DEPENDENT HEAT EQUATION
C     ***********************************************************
C     DA(I) AVERAGE PARTICLE DIAMETER IN METER
C     CK(J) SEPERATION TO DIA RATIO
C     TMB-MELTING TEMP OF BISMUTH
C     ------------------------------------------------------------
      DIMENSION TI1(100),TI2(100)
      DIMENSION DA(50),CK(50),VAP(100),CUR(100)
      COMMON/A1/THIC,BD,DM,ICOND,ROHM
      COMMON/A2/DIF,DIF1,TKN,TKP,TIME,TK,TI1,E,H,TI2,M,TMB
      COMMON/A3/TT,SIGT
      DATA NA,NB,ND/1,6,10/
      PRINT5,NA
5     FORMAT(50X,I3/1X,130(1H-))
      DA(1)=800.E-10
      DO 10 I=2,NA
10    DA(I)=DA(I-1)+100.E-10
      CK(1)=0.02
      DO 20 J=2,NB
      CK(J)=CK(J-1)+0.01
20    CONTINUE
      TI=309.
      TK=0.1
      THIC=45.E-6
      RS=100.
      RSO=30.
      AREA=16.E-6
      PRINT 900,AREA
900   FORMAT(50X,'AREA=',E12.4)
      ROHM=(RSO*AREA)/THIC
      TIMX=(THIC**2*(2.87E03*0.16*4.184E03))/TK
      PRINT 2,THIC,TIMX
2     FORMAT(20X,'THICKNESS IN METER=',E12.4,5X,'MAX. TIME    =',E12.4
      H=0.1
      PRINT 46,TI
46    FORMAT(44X,'AMBIENT TEMP IN DEG KELVIN=',E15.8/44X,20(1H-))
      ICOND=1
      TT=TI
      CALL ROSE
      REST=(1./SIGT)*(THIC/AREA)
      PRINT 47,REST
47    FORMAT(40X,'RESISTANCE AT ROOM TEMP.=',F8.2)
      DO 40 I=1,NA
      PRINT45,DA(I)
45    FORMAT(45X,'AVERAGE PARTICLE DIA IN  METER=',E15.8)
C     ----------------------------------------------------------
C     COMPUTATION OF SIZE DEPENDENT MELTING POINT OF BISMUTH
C     ----------------------------------------------------------
      ABI=208.98
      VA=ABI/9.67
      VB=ABI/10.
      TM=271.+273.
      AD1=DA(I)*1.E2/2.
      DC=(VA-(VB**2)/(VB-VA))/AD1
      DB=-(2.*54.4)/(10.2*ABT*4.184E07)
      TMB=TM*EXP(DB*DC)
      PRINT 700,TMB
700   FORMAT(40X,'MELTING TEMP. OF BISMUTH DEPENDING ON RADIUS=',F6.2)
      DO50 J=1,NB
      PRINT55,CK(J)
55    FORMAT(50X,'RATIO OF PARTICLE SEPERATION TO DIA=',F9.3)
      M=6
      TIME=7.E-5
      TI2(1)=TI
      DO 11 K1=2,11
      TI2(K1)=TI2(K1-1)
```

```
11          CONTINUE
            BD=THIC
            DM=0.
            ND1=ND+1
            M4=0
C           ------------------------------------------------
C           COMPUTATION OF CRITICAL FIELD V/METRE
C           ------------------------------------------------
            P=1.+CK(J)
            C=4.*0.0544/(0.885418E-11*30.*(DA(I)/2.))
            E=SQRT(C*(P-SQRT(P)))
            VAPP=(THIC*E)/(1.+1./CK(J))
            VAP(1)=VAPP/10.
            DO 86 L=2,10
            VAP(L)=VAP(L-1)+VAPP/10.
86          CONTINUE
            DO 85 L=1,10
            CUR(L)=VAP(L)/REST
85          CONTINUE
            PRINT*,(VAP(L),CUR(L),L=1,10)
            GO TO 72
42          M4=M4+1
            IF(M4.EQ.1)GO TO 780
            GO TO 770
780         SUM=0.
            M2=M
            DO 781 K8=1,M2
            K9=0
            T4=TI2(K8)
782         K9=K9+1
            T5=T4+(TI2(K8+1)-TI2(K8))*0.1
            TT=(T4+T5)/2.
            ICOND=1
            CALL ROSE
            T4=T5
            SUM=SUM+(1./SIGI)*0.01*THIC
            IF(K9.LE.9)GO TO 782
781         CONTINUE
            RD=SUM*2./AREA
            SI=VAPP/(RD+RS)
            SV=VAPP
            PRINT*,RD,TIME
            PRINT 783,SI,SV
783         FORMAT(15X,'OFF STATE CURRENT AMP.=',E15.8,15X,'POT. DROP
           1ACROSS SAMPLE VOLT=',E15.8)
            PRINT110
            GO TO 72
770         M2=M
            XL=M
            BD=XL*0.1*THIC*2.
            DM=THIC-BD
            RM=(ROHM*DM)/AREA
            SUM=0.
            DO 90 K8=1,M2
            K9=0
            T4=TI2(K8)
91          K9=K9+1
            T5=T4+(TI2(K8+1)-TI2(K8))*0.1
            TT=(T4+T5)/2.
            ICOND=1
            CALL ROSE
            T4=T5
            SUM=SUM+(1./SIGI)*0.01*THIC
            IF(K9.LE.9)GO TO 91
90          CONTINUE
            RD=SUM*2./AREA
            ED=(VAPP*(1.+1./CK(J))*RD)/(BD*(RM+RS+RD))
            EM=(VAPP*ROHM)/(AREA*(RM+RS+RD))
```

```
          E=(BD*ED+DM*EM)/THIC
          PRINT972,BD,RD,ED,DM,RM,EM,TIME
972       FORMAT(10X,7E16.7)
          SI=VAPP/(RD+RM+RS)
          SV=SI*(RD+RM)
          PRINT 94,ST,SV
94        FORMAT(20X,'CURRENT AMP.=',E15.8,20X,'POT. DROP ACROSS
         1SAMPLE VOLTS=',E15.8)
          PRINT110
72        PRINT75,E
75        FORMAT(40X,'FIELD IN VOLT PER METER=',E15.8)
          IF(M.EQ.1)GO TO 80
          DO 12 K1=1,11
          TI1(K1)=TI2(K1)
12        CONTINUE
          IF(TIME.GT.TIMX)GO TO 50
          CALL TEMEV
          IF(DIF1.LE.1.0)GO TO 41
          IF(DIF.LE.0.)GO TO 500
506       TIME=TIME-0.1*TIME
          IF(TIME.GT.TIMX)GO TO 50
          CALL TEMEV
          IF(DIF1.LE.1.0)GO TO 41
          IF(DIF.LT.0.)GO TO 505
          GO TO 506
500       TIME=TIME+0.1*TIME
          IF(TIME.GT.TIMX)GO TO 50
          CALL TEMEV
          IF(DIF1.LE.1.0)GO TO 41
          IF(DIF.GT.0.)GO TO 505
          GO TO 500
C         -----------------------
C         METHOD OF BISECTION
C         -----------------------
505       TIME=(TKN+TKP)/2.
          IF(TIME.GT.TIMX)GO TO 50
          CALL TEMEV
          IF(DIF1.LE.1.0)GO TO 41
          GO TO 505
41        M=M-1
          IF(M.GE.2)GO TO 42
          IF(M.EQ.1)GO TO 770
80        RM=(ROHM*THIC)/AREA
          SI=VAPP/(RM+RS)
          SV=SI*RM
          PRINT*,RM,TIME
          PRINT 761,SI,SV
761       FORMAT(15X,'ON STATE CURRENT AMP.=',E15.8,15X,'POT. DROP
         1ACROSS SAMPLE VOLT=',E15.8)
50        CONTINUE
          PRINT110
100       FORMAT(IX,130(1H(*))
40        CONTINUE
          STOP
          END
C         *********************
          SUBROUTINE TEMEV
C         GAUSS ITERATION
C         -----------------------
          DIMENSION TI1(100),T1(100),T2(100),BN(100),TI2(100)
          COMMON/A1/THIC,BD,DM,ICOND,ROHM
          COMMON/A2/DIF,DIF1,TKN,TKP,TIME,TK,TI1,E,H,TI2,M,TMB
          COMMON/A3/TT,SIGI
          RHOC=2.87E03*0.16*4.184E03
          D2=(THIC**2*RHOC)/(TIME*TK)
          K5=0
125       K5=K5+1
          T1(1)=TI1(1)
```

```
          T1(11)=TI1(11)
          D4=1.6744/(H**2)
          D5=D4/2.
          K9=0
105       K9=K9+1
          DO 85 K3=3,9
          TT=TI1(K3)
          IF(K9.GE.2)TT=(TI1(K3)+T1(K3))/2.
          TCOND=2
          CALL ROSE
          D6=D5*(TI1(K3-1)+TI1(K3+1))+(D2-D4)*TI1(K3)
          BN(K3)=D6+(THIC*E)**2*SIGI
          BN(K3)=BN(K3)/(D2+D4)
85        CONTINUE
          TT=TI1(2)
          IF(K9.GE.2)TT=(TI1(2)+T1(2))/2.
          CALL ROSE
          BN(2)=D4*TI1(1)+(D2-D4)*TI1(2)+D5*TI1(3)+(THIC*E)**2*SIGT
          BN(2)=BN(2)/(D2+D4)
          TT=TI1(10)
          IF(K9.GE.2)TT=(TI1(10)+T1(10))/2.
          CALL ROSE
          BN(10)=D5*TI1(9)+(D2-D4)*TI1(10)+D4*TI1(11)+(THIC*E)**2*SIGI
          BN(10)=BN(10)/(D2+D4)
          R1=D5/(D2+D4)
          IF(K9.GE.2)GO TO 205
          T1(2)=BN(2)
          DO 80 K2=3,10
          T1(K2)=BN(K2)+R1*T1(K2-1)
80        CONTINUE
          K8=0
205       K8=K8+1
          DO 95 K4=2,10
          IF(K4.GE.10)GO TO 800
          IF(K4.LE.2)GO TO 805
          T2(K4)=BN(K4)+R1*(T1(K4-1)+T1(K4+1))
          GO TO 95
805       T2(K4)=BN(K4)+R1*T1(K4+1)
          GO TO 95
800       T2(K4)=BN(K4)+R1*T1(K4-1)
95        CONTINUE
          T2(1)=T1(1)
          T2(11)=T1(11)
          DO 109 K4=2,10
          TCHE=ABS(T2(K4)-T1(K4))
          IF(TCHE.GT.0.1)GO TO 108
109       CONTINUE
          GO TO 119
108       DO 111 K4=1,11
          T1(K4)=T2(K4)
111       CONTINUE
          GO TO 105
119       DO 120 K4=1,11
          TI1(K4)=T2(K4)
120       CONTINUE
          IF(K5.LE.9)GO TO 125
          DIF=T1(M)-TMB
          DIF1=ABS(DIF)
          IF(DIF1.LE.1.0)GO TO 406
          IF(DIF.LT.0.)GO TO 400
          TKP=TIME
          GO TO 405
400       TKN=TIME
405       DO 12 I=1,11
          TI1(I)=TI2(I)
12        CONTINUE
          GO TO 407
406       DO 14 I=1,11
```

```
         TI2(I)=T2(I)
14       CONTINUE
         PRINT 115,(T2(K4),K4=1,11)
115      FORMAT(2X,11F10.2)
407      RETURN
         END
C        *****************
         SUBROUTINE ROSE
C        COMPUTATION OF ELECTRICAL CONDUCTIVITY
C        ----------------------------------------
         COMMON/A1/THIC,BD,DM,ICOND,ROHM
         COMMON/A3/TT,SIGI
         SIG=-(2.3*1.25*1000./TT)
         SIGI=(100./1.334)*EXP(SIG)
         IF(ICOND.EQ.1)GO TO 72
         SIGI=THIC/(BD/SIGI+DM/(1./ROHM))
72       RETURN
         END
```

APPENDIX 3

```fortran
C      COMPUTATION OF  SWITCHING TIME FOR TWO PROXIMATE
C      GRAINS TO JOIN IN MOLTEN CONDITION UNDER THE ACTION
C      OF AN ELECTRIC FIELD
C      ************************************************************
C      A=SEMI MAJOR AXIS,B=SEMI MINOR AXIS
C      ------------------------------------------------
       DIMENSION RAD(15),CK(15)
       COMMON/A4/TIME,RAD,CK,KK,LL,SMAJ,SMIN,TKN,TKP,ADIF1,ADIF
       TIME=1.E-9;N1=9;N2=7
       RAD(1)=100.E-10
       DO 15 KK=2,N1
       RAD(KK)=RAD(KK-1)+50.E-10
15     CONTINUE
       CK(1)=0.01
       DO 20 LL=2,N2
       CK(LL)=CK(LL-1)+0.01
20     CONTINUE
       DO 30 KK=1,N1
       PRINT 120,RAD(KK)
120    FORMAT(25X,'RADIUS IN METER',E15.8)
       DO 40 LL=1,N2
       PRINT 130,CK(LL)
130    FORMAT(20X,'SEP. TO DIA. RATIO=',F5.2)
       GO TO 90
80     TIME=TIME*0.1
90     CONTINUE
       CALL SWDYN
       IF(SMIN.LT.0.)GO TO 80
       IF(ADIF1.LT.0.1)GO TO 45
       IF(ADIF.LT.0.0)GO TO 50
70     TIME=TIME-0.1*TIME
       CALL SWDYN
       IF(SMIN.LT.0.0)GO TO 80
       IF(ADIF1.LT.0.1)GO TO 45
       IF(ADIF.LT.0.0)GO TO 60
       GO TO 70
50     TIME=TIME+0.1*TIME
       CALL SWDYN
       IF(SMIN.LT.0.0)GO TO 80
       IF(ADIF1.LT.0.1)GO TO 45
       IF(ADIF.GT.0.0)GO TO 60
       GO TO 50
C      METHOD OF BISECTION
60     TIME=(TKN+TKP)/2.
       CALL SWDYN
       IF(ADIF1.LT.0.1)GO TO 45
       GO TO 60
45     CONTINUE
       PRINT 100,(TIME,SMAJ,SMIN)
100    FORMAT(5X,'SWITCHING TIME=',E15.8,5X,'A=',F6.2,5X,'B=',
      1E15.8/2X,127(1H-))
40     CONTINUE
30     CONTINUE
       STOP
       END

C      ************************************************************

       SUBROUTINE SWDYN
C      SOLUTION OF DYNAMICS OF SWITCHING

C      ------------------------------------------------
       DIMENSION RAD(15),CK(15)
       DIMENSION PHIBX(-1:15),PHIBXT(-1:15),PHIBY(-1:15),PHIBYT(-1:15
       DIMENSION VX(-1:15),UY(-1:15),VY(-1:15),XX(-1:15),ALX(-1:15)
       DIMENSION PHII(-1:12,-1:12),PHIF(-1:12,-1:12),U(-1:12,-1:12)
       DIMENSION UX(-1:15),ALY(-1:15),V(-1:12,-1:12)
       COMMON/A1/CO1,CO2,PHII,A1,B1,FUN
```

```
      COMMON/A3/I,J,PHIBYT,PHIBXT,N4,N6,DX,DY
      COMMON/A2/A,H,AK,B,PHIF,SUM1,SUM2
      COMMON/A4/TIME,RAD,CK,KK,LL,SMAJ,SMIN,TKN,TKP,ADIF1,ADIF
      I=0.1;AK=0.1
      EP=30.;EPU=0.885418E-11;DENS=10.E3
      A=RAD(KK);B=RAD(KK);SUTEN=0.0544
      P=1.+CK(LL)
      C=4.*SUTEN/(EP*EPO*RAD(KK))
      E=SQRT(C*(P-SQRT(P)))
      SO1=(1.+CK(LL))*RAD(KK)*1.E10
      PHIBX(0)=0.;PHIBY(0)=0.
      UX(0)=0.;VX(0)=0.;UY(0)=0.;VY(0)=0.;XX(0)=0.
      DO 10 I=1,10
      XX(I)=XX(I-1)+0.1
      PHIBX(I)=PHIBX(I-1)
      PHIBY(I)=PHIBY(I-1)
      UX(I)=UX(I-1);VX(I)=VX(I-1)
      UY(I)=UY(I-1);VY(I)=VY(I-1)
10    CONTINUE
      L=0
300   L=L+1
      RAD1=RAD(KK)*1.E08
      A3=A*1.E08
      B3=B*1.E08
      ALX(0)=1.0
      I=0;X=0.
      SO=CK(LL)*2.*RAD1
      S=SO-2.*(A3-RAD1)
      F=E*(SO/S)
      C1=(0.75*EP*EPO*E**2)/DENS
      C2=SUTEN/DENS
30    C3=2.303*C1*ALOG10(3./(3.-X**2))
      C4=(A3/B3)**2*(1.-X**2)
      C5=(A3/B3)*(C4+1.+X**2)
      C6=(C4+X**2)**1.5
      C7=(C5/C6)*(1./B3)
      C8=(C2*1.E08)*(C7-2./RAD1)
      C9=.5*(UX(I)**2+VX(I)**2)
      C10=C3-C8-C9
      PHIBXT(I)=PHIBX(I)+0.1*TIME*C10
      Y=SQRT(1.-XX(I)**2)
      IF(I.EQ.0)GO TO 35
      DO 36 J=0,10
      IF(Y.GT.XX(J))GO TO 36
      II=J-1
      GO TO 37
36    CONTINUE
37    ALX(I)=(Y-XX(II))/H
35    CONTINUE
      I=I+1
      X=X+0.1
      IF(I.LE.10)GO TO 30
      DO 20 I=0,10
      DO 25 J=0,10
      PHII(I,J)=PHIBXT(5)
25    CONTINUE
20    CONTINUE
      ALY(0)=1.0
      I=0;Y=0.
40    X=SQRT(1.-Y**2)
      C3=2.303*C1*ALOG10(3./(3.-X**2))
      C4=(A3/B3)**2*(1.-X**2)
      C5=(A3/B3)*(C4+1.+X**2)
      C6=(C4+X**2)**1.5
      C7=(C5/C6)*(1./B3)
      C8=(C2*1.E08)*(C7-2./RAD1)
      C9=.5*(UY(I)**2+VY(I)**2)
      C10=C3-C8-C9
```

```
        PHIBYT(I)=PHIBY(I)+0.1*TIME*C10
        IF(I.EQ.0)GO TO 46
        DO 45 J=0,10
        IF(X.GT.XX(J)) GO TO 45
        II=J-1
        GO TO 47
45      CONTINUE
47      ALY(I)=(X-XX(II))/AK
46      CONTINUE
        I=I+1
        Y=Y+0.1
        IF(I.LE.10)GO TO 40
C------------------------------------------------------------------
C       EVALUATION OF LAPLACE EQUATION BY GAUSS ITERATION
C------------------------------------------------------------------
        A1=((A/B)*H)**2
        B1=AK**2
        CO1=(1./A1)/(2.*(1./A1+1./B1))
        CO2=(1./B1)/(2.*(1./A1+1./B1))
        L1=0
140     N4=9;N6=4;K=0
        L1=L1+1
        DO 50 J=0,9
        K=K+1
        IF(K.GT.5)GO TO 55
        DY=ALY(J);DX=1.
        IF(J.EQ.N6)DX=ALX(N4)
        DO 60 I=0,N4
        CALL FUNEAV
        PHIF(I,J)=FUN
60      CONTINUE
        GO TO 50
55      N4=8;N6=5
        IF(K.GT.6)GO TO 65
        DY=ALY(J);DX=ALX(N4)
        DO 70 I=0,N4
        CALL FUNEAV
        PHIF(I,J)=FUN
70      CONTINUE
        GO TO 50
65      N4=7;N6=7
        IF(K.GT.8)GO TO 75
        DY=ALY(J);DX=1.0
        IF(J.EQ.N6)DX=ALX(N4)
        DO 80 I=0,N4
        CALL FUNEAV
        PHIF(I,J)=FUN
80      CONTINUE
        GO TO 50
75      N4=5;N6=8
        IF(K.GT.9)GO TO 92
        DY=ALY(J);DX=ALX(N4)
        DO 85 I=0,N4
        CALL FUNEAV
        PHIF(I,J)=FUN
85      CONTINUE
        GO TO 50
92      N4=4;N6=9
        DO 90 I=0,N4
        DX=ALX(I);DY=1.
        IF(I.EQ.N4)DY=ALY(N6)
        CALL FUNEAV
        PHIF(I,J)=FUN
90      CONTINUE
50      CONTINUE
        DO 95 J=0,9
        N4=4
        IF(J.LE.4)N4=9;IF(J.EQ.5)N4=8;IF(J.EQ.6.OR.J.EQ.7)N4=7
```

```
        IF(J.EQ.8)N4=5
        DO 100 I=0,N4
        DIF=(PHIF(I,J)-PHII(I,J))/PHII(I,J)
        DIF=ABS(DIF)
        IF(DIF.GT.0.01)GO TO 105
100     CONTINUE
95      CONTINUE
        GO TO 130
105     CONTINUE
        DO 110 J=0,9
        N4=4
        IF(J.LE.4)N4=9;IF(J.EQ.5)N4=8;IF(J.EQ.6.OR.J.EQ.7)N4=7
        IF(J.EQ.8)N4=5
        DO 120 I=0,N4
        PHII(I,J)=PHIF(I,J)
120     CONTINUE
110     CONTINUE
        GO TO 140
130     CONTINUE
        DO 600 J=0,9
        N4=4
        IF(J.LE.4)N4=9;IF(J.EQ.5)N4=8;IF(J.EQ.6.OR.J.EQ.7)N4=7
        IF(J.EQ.8)N4=5
        DO 610 I=0,N4
        PHII(I,J)=PHIF(I,J)
610     CONTINUE
        GO TO 600
        PRINT 620,(PHII(I,J),I=0,N4)
620     FORMAT(10E12.5)
600     CONTINUE
C       -----------------------------------
C       COMPUTATION OF VELOCITY COMPONENTS
C       -----------------------------------
        N4=9;N6=4;K=0
        DO 160 J=1,9
        K=K+1
        IF(K.GT.N6)GO TO 165
        DY=ALY(J);DX=1.0
        IF(J.EQ.N6)DX=ALX(N4)
        DO 170 I=1,N4
        CALL VELEAV
        U(I,J)=SUM1
        V(I,J)=SUM2
170     CONTINUE
        GO TO 160
165     N4=8;N6=5
        IF(K.GT.N6)GO TO 175
        DY=ALY(J);DX=ALX(N4)
        DO 180 I=1,N4
        CALL VELEAV
        U(I,J)=SUM1
        V(I,J)=SUM2
180     CONTINUE
        GO TO 160
175     N4=7;N6=7
        IF(K.GT.N6)GO TO 185
        DY=ALY(J);DX=1.0
        IF(J.EQ.N6)DX=ALX(N4)
        DO 190 I=1,N4
        CALL VELEAV
        U(I,J)=SUM1
        V(I,J)=SUM2
190     CONTINUE
        GO TO 160
185     N4=5;N6=8
        IF(K.GT.N6)GO TO 195
        DY=ALY(J);DX=ALX(N4)
        DO 200 I=1,N4
```

```
            CALL VELEAV
            U(I,J)=SUM1
            V(I,J)=SUM2
200         CONTINUE
            GO TO 160
195         N4=4;N6=9
            DO 210 I=1,N4
            DX=ALX(I);DY=1.
            IF(I.EQ.N4)DY=ALY(N6)
            CALL VELEAV
            U(I,J)=SUM1
            V(I,J)=SUM2
210         CONTINUE
160         CONTINUE
            DO 710 J=1,9
            N4=4
            GO TO 710
            IF(J.LE.4)N4=9;IF(J.EQ.5)N4=8;IF(J.EQ.6.OR.J.EQ.7)N4=7
            IF(J.EQ.8)N4=5
710         CONTINUE
C
C       ----------------------------------------
C       EXTRAPOLATE TO FIND U,V ON BOUNDARY
        ----------------------------------------
            A2=A*H
            B2=B*AK
            UY(0)=(PHIBYT(0)-PHIF(9,0))/A2;VY(0)=0.
            VY(10)=(PHIBYT(10)-PHIF(0,9))/B2;UY(10)=0.
            DO 220 J=1,9
            IF(J.EQ.6.OR.J.EQ.8)GO TO 230
            IF(J.GT.4)GO TO 400
            DIS1=SQRT(1.-(FLOAT(J-1)*.1)**2)-SQRT(1.-(FLOAT(J)*0.1)**2)
            DIS2=(ALY(J-1)*H-DIS1)
            IF(J.GT.0.0.AND.J.LE.4)N4=9
            PHI=(DIS1/(ALY(J-1)*H))*PHIF(N4,J-1)+PHIBYT(J-1)*DIS2/(ALY(J-
           1)*H)
            UY(J)=(PHIBYT(J)-PHIF(N4,J))/(A2*ALY(J))
            VY(J)=(PHIBYT(J)-PHI)/B2
            GO TO 220
230         CONTINUE
            IF(J.EQ.6)GO TO 240
            VY(J)=(PHIBYT(J)-PHIF(J-2,J-1))/B2
            UY(J)=(PHIBYT(J)-PHIF(J-3,J))/A2
            GO TO 220
240         VY(J)=(PHIBYT(J)-PHIF(J+2,J-1))/B2
            UY(J)=(PHIBYT(J)-PHIF(J+1,J))/A2
            GO TO 220
400         CONTINUE
            IF(J.EQ.7)N4=7;IF(J.EQ.9)N4=4;IF(J.EQ.5)N4=8
            DIS1=FLOAT(N4+1)*H-SQRT(1.-(FLOAT(J)*AK)**2)
            DIS2=H-DIS1
            PHI=(DIS1/H)*PHIF(N4,J-1)+(DIS2/H)*PHIF(N4+1,J-1)
            UY(J)=(PHIBYT(J)-PHIF(N4,J))/A2
            VY(J)=(PHIBYT(J)-PHI)/B2
220         CONTINUE
            VX(0)=(PHIBXT(0)-PHIF(0,9))/B2;UX(0)=0.
            UX(10)=(PHIBXT(10)-PHIF(9,0))/A2;VX(10)=0.
            DO 250 I=1,9
            IF(I.EQ.6.OR.I.EQ.8)GO TO 260
            IF(I.GT.4)GO TO 430
            DIS1=SQRT(1.-(FLOAT(I-1)*0.1)**2)-SQRT(1.-(FLOAT(I)*0.1)**2)
            DIS2=ALX(I-1)*AK-DIS1
            IF(I.GT.0.0.AND.I.LE.4)N4=9
            PHI=(DIS1/(ALX(I-1)*AK))*PHIF(I-1,N4)+(DIS2/(ALX(I-1)*AK))*
           1PHIBXT(I-1)
            UX(I)=(PHIBXT(I)-PHI)/A2
            VX(I)=(PHIBXT(I)-PHIF(I,N4))/(ALX(I)*B2)
            GO TO 250
260         CONTINUE
```

```
        IF(I.EQ.8)GO TO 270
        UX(I)=(PHIBXT(I)-PHIF(I-1,I+2))/A2
        VX(I)=(PHIBXT(I)-PHIF(I,I+1))/B2
        G) TO 250
270     UX(I)=(PHIBXT(I)-PHIF(I-1,I-2))/A2
        VX(I)=(PHIBXT(I)-PHIF(I,I-3))/B2
        GO TO 250
430     CONTINUE
        IF(I.EQ.7)N4=7;IF(I.EQ.9)N4=4;IF(I.EQ.5)N4=8
        DIS1=FLOAT(N4+1)*AK-SQRT(1.-(FLOAT(I)*H)**2)
        DIS2=AK-DIS1
        PHI=(DIS1/AK)*PHIF(I-1,N4)+(DIS2/AK)*PHIF(I-1,N4+1)
        UX(I)=(PHIBXT(I)-PHI)/A2
        VX(I)=(PHIBXT(I)-PHIF(I,N4))/B2
250     CONTINUE
C
C----------------------------------------------------
C
C       COMPUTATION OF NEW BOUNDARY
C----------------------------------------------------
        BF=B+AK*TIME*VX(0)
        A=RAD(KK)*(RAD(KK)/BF)**2
        B=BF
        DO 800 I=0,10
        PHIBX(I)=PHIBXT(I)
        PHIBY(I)=PHIBYT(I)
800     CONTINUE
        SMAJ=A*1.E10;SMIN=B*1.E10
        IF(B.LT.0.0)GO TO 350
        IF(L.LT.10)GO TO 300
        ADIF=SMAJ-S01
        ADIF1=ABS(ADIF)
        IF(ADIF1.LT.0.1)GO TO 350
        IF(ADIF.LT.0.0)GO TO 900
        TKP=TIME
        GO TO 350
900     TKN=TIME
350     RETURN
        END
C
C      ***********************************************************
C
        SUBROUTINE FUNEAV
C       EVALUATION OF PHI FUNCTIONS
C
C----------------------------------------------------
        DIMENSION PHII(-1:12,-1:12),PHIBYT(-1:15),PHIBXT(-1:15)
        COMMON/A1/C01,C02,PHII,A1,B1,FUN
        COMMON/A3/I,J,PHIBYT,PHIBXT,N4,N6,DX,DY
        IF((J-1).LT.0)PHII(I,J-1)=PHII(I,J+1)
        IF((I-1).LT.0)PHII(I-1,J)=PHII(I+1,J)
        IF(J.EQ.9)GO TO 15
        IF(I.EQ.N4)GO TO 15
        FUN=C01*(PHII(I-1,J)+PHII(I+1,J))+C02*(PHII(I,J-1)+PHII(I,J+1)
        GO TO 10
15      D=2.*(1./(A1*DY)+1./(B1*DX))
        CX1=(2./(A1*(DY+1.)))/D
        CX2=(2./(A1*DY*(DY+1.)))/D
        CY1=(2./(B1*(DX+1.)))/D
        CY2=(2./(B1*DX*(DX+1.)))/D
        IF(J.EQ.9)GO TO 20
        GO TO 30
20      PHII(I,J+1)=PHIBXT(I)
        IF(I.EQ.N4)PHII(I+1,J)=PHIBYT(J)
        GO TO 25
30      PHII(N4+1,J)=PHIBYT(J)
        IF(J.EQ.N6)PHII(N4,J+1)=PHIBXT(N4)
25      FUN=CX1*PHII(I-1,J)+PHII(I+1,J)*CX2+PHII(I,J-1)*CY1+PHII(I,
        1J+1)*CY2
10      RETURN
```

END

```
****************************************************************

      SUBROUTINE VELEAV
      EVALUATION OF VELOCITY COMPONENTS U,V

      -----------------------------------------
      DIMENSION PHIF(-1:12,-1:12),PHIBYT(-1:15),PHIBXT(-1:15)
      COMMON/A3/I,J,PHIBYT,PHIBXT,N4,N6,DX,DY
      COMMON/A2/A,H,AK,B,PHIF,SUM1,SUM2
      CF1=1./(2.*A*H)
      CF2=1./(2.*AK*B)
      IF(J.EQ.9)GO TO 15
      IF(I.EQ.N4)GO TO 15
      SUM1=CF1*(PHIF(I+1,J)-PHIF(I-1,J))
      SUM2=CF2*(PHIF(I,J+1)-PHIF(I,J-1))
      GO TO10
15    CX1=1./(A*H*DY*(DY+1.))
      CX2=DY/(A*H*(DY+1.))
      CX3=(1.-DY)/(A*H*DY)
      CY1=1./(B*AK*DX*(DX+1.))
      CY2=DX/(B*AK*(DX+1.))
      CY3=(1.-DX)/(B*AK*DX)
      IF(J.EQ.9)GO TO 20
      GO TO 30
20    PHIF(I,J+1)=PHIBXT(I)
      IF(I.EQ.N4)PHIF(I+1,J)=PHIBYT(J)
      GO TO 25
30    PHIF(N4+1,J)=PHIBYT(J)
      IF(J.EQ.N6)PHIF(N4,J+1)=PHIBXT(N4)
25    SUM1=CX1*PHIF(I+1,J)-CX2*PHIF(I-1,J)-CX3*PHIF(I,J)
      SUM2=CY1*PHIF(I,J+1)-CY2*PHIF(I,J-1)-CY3*PHIF(I,J)
10    RETURN
      END
```

APPENDIX   4

```
C      CONSTRAINED OPTIMISATION PROGRAMME TO FIND THE OPTIMUM
C      COMBINATION OF FRACTIONS OF SPHERES,SINGLE STRAND CHAINS
C      AND F.C.C CLUSTERS USING SIMPLEX TECHNIQUE AND MG-PVS THEORY
C      ******************************************************************
C      DEP(M,1)=DEPOLARISATION TRIPLET FOR SINGLE STRAND CHAIN
C      DEP(M,2)=DEPOLARISATION TRIPLET FOR F.C.C CLUSTER
C      ZI=X(1,1)=FRACTION OF SPHERE
C      SI X(1,2)=FRACTION OF SINGLE STRAND CHAIN
C      DPL(M)=DEPOLARISATION TRIPLET FOR SPHERE
C      EPMED=DIELECTRIC PERMITTIVITY OF GLASS MATRIX
C      ------------------------------------------------------------------
       DIMENSION X(10,10),XH(10),XL(10),X0(10),XR(10),XE(10),XC(10)
       DIMENSION F(10),Y(10,10),ABCOEF(100),DEP(5,5),EXALP(100)
       DIMENSION XX(300),ALMD(100),EPB1(100),EPB2(100),ABCOE(100)
       DIMENSION CSUM(10),CPEFUN(10)
       COMMON N3,N4,XX,ALMD,EPB1,EPB2,DEP,EXALP,X,I,ALPHA,SUM1,PEFU
       COMMON RK,ABCOE,ABCOEF,ICOND,WPB,TB,VFB,WPX,FIF,AVD,EPMED
       N=2
       N1=N+1
       N2=N+2
       WPB=(16.0*1.602E-12)/1.054E-27
       TB=1.054E-27/(2.8381*1.602E-12)
       VFB=1.822E08
       WPX=WPB
       FIF=.043
       DATA A,B,C/1.0,0.5,2.0/
       N4=13;N3=189
       READ*,(ALMD(JJ),EPB1(JJ),EPB2(JJ),JJ=1,N4)
       PRINT*,(ALMD(JJ),EPB1(JJ),EPB2(JJ),JJ=1,N4)
       READ*,(XX(II),II=1,N3)
       READ*,((DEP(M,M1),M=1,3),M1=1,2)
       PRINT*,((DEP(M,M1),M=1,3),M1=1,2)
       READ*,((Y(J,I),J=1,N),I=1,N1)
       READ*,(EXALP(JJ),JJ=1,N4)
       DO 650 JJ=1,N4
       ZAPP=EPB1(JJ)
       EPB1(JJ)=EPB1(JJ)**2-EPB2(JJ)**2
       EPB2(JJ)=2.*EPB2(JJ)*ZAPP
650    CONTINUE
       PRINT*,(XX(II),II=1,N3)
       DO 5 I=1,N1
       DO 6 J=1,N
       X(I,J)=Y(J,I)
       PRINT*,X(I,J)
6      CONTINUE
5      CONTINUE
C      ------------------------------------------------------
C              SIMPLEX OPTIMISATION TECHNIQUE
C      ------------------------------------------------------
       K=0;ICOND=0
       I=1;RK=.1
       CALL FUNEAV
       RK=0.3*SUM1/(-1.*PEFUN)
       ICOND=ICOND+1
       DO 15 I=1,N1
       CALL FUNEAV
       F(I)=ALPHA
       CSUM(I)=SUM1
       CPEFUN(I)=PEFUN
15     CONTINUE
170    K=K+1
       K9=0
110    IH=1
       K9=K9+1
       FMAX=F(1)
       DO 20 I=2,N1
       IF(FMAX.GT.F(I))GO TO 20
       FMAX=F(I)
```

```
            IH=1
20          CONTINUE
            DO 22 J=1,N
            XH(J)=X(IH,J)
22          CONTINUE
            FMIN=F(1)
            IL=1
            DO 25 I=2,N1
            IF(FMIN.LT.F(I))GO TO 25
            FMIN=F(I)
            IL=I
25          CONTINUE
            DO 26 J=1,N
26          XL(J)=X(IL,J)
            AN=N
            DO 30 J=1,N
            SUM=0.
            DO 40 I=1,N1
            IF(I.EQ.IH)GO TO 40
            SUM=SUM+X(I,J)
40          CONTINUE
            SUM=SUM/AN
            X0(J)=SUM
30          CONTINUE
            DO 35 J=1,N
35          X(N2,J)=X0(J)
            I=N2
            CALL FUNEAV
            FX0=ALPHA
            SUM0=SUM1
            DO 45 J=1,N
            XR(J)=(1.+A)*X0(J)-A*XH(J)
            X(N2,J)=XR(J)
45          CONTINUE
            I=N2
            CALL FUNEAV
            FXR=ALPHA
            IF(FXR.LT.FMIN)GO TO 50
            DO 60 I=1,N1
            IF(I.EQ.IH)GO TO 60
            IF(FXR.LE.F(I))GO TO 65
60          CONTINUE
            GO TO 85
50          CONTINUE
            DO 55 J=1,N
            XE(J)=C*XR(J)+(1.-C)*X0(J)
55          X(N2,J)=XE(J)
            I=N2
            CALL FUNEAV
            FXE=ALPHA
            IF(FXE.LT.FMIN)GO TO 70
65          CONTINUE
            DO 75 J=1,N
            XH(J)=XR(J)
75          X(IH,J)=XH(J)
            GO TO 80
70          CONTINUE
            DO 90 J=1,N
            XH(J)=XE(J)
90          X(IH,J)=XH(J)
80          CONTINUE
            DO 95 I=1,N1
            IF(I.EQ.IH)GO TO 410
            GO TO 95
410         CALL FUNEAV
            CSUM(I)=SUM1
            CPEFUN(I)=PEFUN
            F(I)=ALPHA
```

```
95          CONTINUE
145         SUM=0.
            DO 100 I=1,N1
100         SUM=SUM+(F(I)-FX0)**2
            CONV=SQRT(SUM/N1)
            IF(CONV.LT.0.01)GO TO 105
            DO 700 I=1,N1
            DO 800 J=1,N
            Y(J,I)=X(I,J)
800         CONTINUE
700         CONTINUE
            IF(K9.GT.150)GO TO 500
            GO TO 110
85          CONTINUE
            IF(FXR.GT.FMAX)GO TO 115
            DO 120 J=1,N
120         XH(J)=XR(J)
115         CONTINUE
            DO 125 J=1,N
            XC(J)=B*XH(J)+(1.-B)*X0(J)
125         X(N2,J)=XC(J)
            I=N2
            CALL FUNEAV
            FXC=ALPHA
            IF(FXC.GT.FMAX)GO TO 130
            DO 135 J=1,N
            XH(J)=XC(J)
135         X(IH,J)=XH(J)
            DO 140 I=1,N1
            IF(I.EQ.IH)GO TO 400
            GO TO 140
400         CALL FUNEAV
            CSUM(I)=SUM1
            CPEFUN(I)=PEFUN
            F(I)=ALPHA
140         CONTINUE
            GO TO 145
130         CONTINUE
            DO 150 I=1,N1
            DO 155 J=1,N
            X(I,J)=(X(I,J)+XL(J))/2.
155         CONTINUE
150         CONTINUE
            DO 750 I=1,N1
            CALL FUNEAV
            F(I)=ALPHA
            CSUM(I)=SUM1
            CPEFUN(I)=PEFUN
750         CONTINUE
            GO TO 145
105         CONTINUE
            IF(K.EQ.1)GO TO 180
            FUN2=SUM0
            GO TO 190
180         FUN1=SUM0
            RK=0.2*RK
            DO 430 I=1,N1
            F(I)=CSUM(I)-RK*CPEFUN(I)
430         CONTINUE
            GO TO 170
190         DEV=ABS((FUN2-FUN1)/FUN2)
            PRINT*,DEV,RK
            PRINT*,(X0(J),J=1,N)
            IF(DEV.LT.0.005)GO TO 200
            PRINT 900,(ALMD(JJ),ABCOEF(JJ),EXALP(JJ),ABCOE(JJ),JJ=1,N4)
900         FORMAT(2X,4(4X,F10.5))
            RK=RK*0.2
            PRINT 950
```

```
950       FORMAT(3X,127(1H-))
          FUN1=FUN2
          DO 440 I=1,N1
          F(I)=CSUM(I)-RK*CPEFUN(I)
440       CONTINUE
          GO TO 170
200       PRINT 600,FIF,AVD
600       FORMAT(25X,'FILL FACTOR=',F6.4,25X,'PARTICLE SIZE=',F6.1)
          PRINT*,(XO(J),J=1,N)
          PRINT 250,(ALMD(JJ),ABCOEF(JJ),EXALP(JJ),ABCOE(JJ),JJ=1,N4)
250       FORMAT(2X,4(4X,F10.5))
500       STOP
          END
C         *******************************************************
          SUBROUTINE FUNEAV
C         EVALUATION OF OPTICAL ABSORPTION COEFFICIENT BY MG-PVS THEO
C         -------------------------------------------------------
          DIMENSION XX(300),ALMD(100),EPB1(100),EPB2(100),X1(100)
          DIMENSION NF1(100),F1(100),W(100),EPS1(100),EPS2(100)
          DIMENSION PEPS1(100),PEPS2(100)
          DIMENSION DEP(5,5),DPL(5),ALPH1(5),ALPH2(5)
          DIMENSION EPME1(100),EPME2(100),ABCOE(100),ABCOEF(100)
          DIMENSION X(10,10),EXALP(100),A3(100)
          COMMON N3,N4,XX,ALMD,EPB1,EPB2,DEP,EXALP,X,I,ALPHA,SUM1,PEF
          COMMON RK,ABCOE,ABCOFF,ICOND,WPB,TB,VFB,WPX,FIF,AVD,EPMED
          ZI=X(I,1)
          SI=X(I,2)
          AKI=(1.-(ZI+SI))
          IF(ICOND.EQ.1)GO TO 80
          EPMED=10.0
          EPM1=EPMED;EPM2=0.
          DPL(1)=1./3.
          DO 5 M=2,3
5         DPL(M)=DPL(M-1)
          AVA=0.
          SUM=0.
          BMAX=XX(1)
          DO 10 II=2,N3
          IF(XX(II).GT.BMAX)BMAX=XX(II)
10        CONTINUE
          K=0
          A=30.
15        B=A+5.
          K=K+1
          NF=0
          DO 20 II=1,N3
          IF(XX(II).GT.A.AND.XX(II).LE.B)GO TO 30
          GO TO 20
30        NF=NF+1
20        CONTINUE
          X1(K)=(A+B)/2.*1.E-8
          NF1(K)=NF;ANF=NF
          F1(K)=NF1(K)
          AVA=AVA+FLOAT(NF1(K))*(A+B)/2.
          SUM=SUM+X1(K)**3*FLOAT(NF1(K))
          A=B
          IF(A.GT.BMAX)GO TO 35
          GO TO 15
35        AVA=(AVA/FLOAT(N3))*1.E-8
          AVD=AVA*1.E08
          DO 40 J=1,N4
          W(J)=(2.*(22./7.)*3.E10)/(ALMD(J)*1.E-4)
          G1=((AVA+2.*TB*VFB)/(TB*AVA))**2+W(J)**2
          H1=W(J)**2+1./TB**2
          Q1=G1-W(J)**2
          EPS1(J)=EPB1(J)+(WPB/H1)*WPB-(WPX/G1)*WPX
          EPS2(J)=EPB2(J)+(WPX/W(J))*(WPX*SQRT(Q1)/G1)-(WPB/(TB*W(J))
         1*(WPB/H1)
```

```
40        CONTINUE
80        CONTINUE
          DO 85 J=1,N4
          K1=0
65        A1=0.
          B1=0.
          K1=K1+1
          DO 45 L=1,K
          IF(K1.GE.2)GO TO 48
          G1=((X1(L)+2.*TB*VFB)/(TB*X1(L)))**2+W(J)**2
          O1=G1-W(J)**2
          PEPS1(L)=EPB1(J)+(WPB/H1)*WPB-(WPX/G1)*WPX
          PEPS2(L)=EPB2(J)+(WPX/W(J))*(WPX*SQRT(O1)/G1)-(WPB/(TB*W(J)
         1*(WPB/H1)
          A3(L)=(X1(L)**3*F1(L))/SUM
48        ALP1=0.
          ALP2=0.
          AP=PEPS1(L)-EPM1
          BP=PEPS2(L)-EPM2
          DO 50 M=1,3
          CP=EPM1*(1.-DPL(M))+PEPS1(L)*DPL(M)
          DP=EPM2*(1.-DPL(M))+PEPS2(L)*DPL(M)
          A2=CP**2+DP**2
          ALP1=ALP1+(1./3.)*(AP*CP+BP*DP)/A2
          ALP2=ALP2+(1./3.)*(BP*CP-AP*DP)/A2
50        CONTINUE
          A1=A1+A3(L)*ALP1
          B1=B1+A3(L)*ALP2
45        CONTINUE
          AI=EPS1(J)-EPM1
          BI=EPS2(J)-EPM2
          DO 55 M1=1,2
          ALPH1(M1)=0.
          ALPH2(M1)=0.
          DO 60 M=1,3
          CI=EPM1*(1.-DEP(M,M1))+EPS1(J)*DEP(M,M1)
          DI=EPM2*(1.-DEP(M,M1))+EPS2(J)*DEP(M,M1)
          A4=CI**2+DI**2
          ALPH1(M1)=ALPH1(M1)+(1./3.)*(AI*CI+BI*DI)/A4
          ALPH2(M1)=ALPH2(M1)+(BI*CI-AI*DI)/A4
60        CONTINUE
55        CONTINUE
          R1=ZI*AI+SI*ALPH1(1)+AKI*ALPH1(2)
          R2=ZI*BI+SI*ALPH2(1)+AKI*ALPH2(2)
          A=1.+(2./3.)*FIF*R1
          B=(2./3.)*FIF*R2
          C=1.-(1./3.)*FIF*R1
          D=(1./3.)*FIF*R2
          EPME1(J)=EPMED*((A*C-B*D)/(C**2+D**2))
          EPME2(J)=EPMED*((B*C+A*D)/(C**2+D**2))
          DEV1=ABS(EPM1-EPME1(J))
          DEV2=ABS(EPM2-EPME2(J))
          IF(DEV1.LT.0.01.AND.DEV2.LT.0.01)GO TO 70
          EPM1=EPME1(J)
          EPM2=EPME2(J)
          GO TO 65
70        ABCOE(J)=(W(J)/3.E10)*(EPME2(J)/SQRT(EPME1(J)))*1.E-4
          ABCOEF(J)=ABCOE(J)
          ABCOE(J)=ALOG10(ABCOE(J))
          IF(EPME1(J).LT.0.)PRINT*,ALMD(J),EPME1(J)
85        CONTINUE
          SUM1=0.
          DO 75 J=1,N4
          SUM1=SUM1+(EXALP(J)-ABCOEF(J))**2
75        CONTINUE
C         ********************************************************
C         FORMULATION OF INTERNAL PENALTY FUNCTION -PEFUN
          PEFUN=-1./X(I,1)-1./X(I,2)+1./(X(I,1)+X(I,2)-1.)
```

```
ALPHA=SUM1-RK*PEFUN
RETURN
END
```

Addendum to section 2.2.4, chapter 2.

In section 2.2.4, it is true that we did not explicitly discuss the justification of the boundary conditions. Only we have referred to T. Kaplan and D. Adler's paper [Ref. 97, page 197] where similar boundary condition has been used for chalcogenide glassy material sandwiched between two metallic elec ... . The justification of this boundary condition is based on the assumption that the metallic electrodes have much higher thermal conductivity compared to glassy material so that the metallic electrodes can be treated as infinite heat sinks which fix the end temperatures at the surfaces of the sample to the experimental temperature. It has been stated in the same reference that for molybdenum metal and a typical chalcogenide glass the ratio of thermal conductivity of metal to that of glass is approximately 500 and this fact makes the infinite heat sink assumption an excellent one. Our glass sample is also sandwiched between two metallic electrodes of noble metal gold. For gold [Ref. R. C. Weast, ed., CRC Handbook of Chemistry and Physics, 61st edition (CRC Press, Inc., Boca Raton, Florida, 1980-'81)] and soda-lime-silica glasses [Ref. W. D. Kingery, Introduction to Ceramics (Wiley, New York, 1967)] the ratio of thermal conductivity of metallic gold to soda-lime-silica glass is approximately 190. This, therefore, justifies the boundary condition in section 2.2.4.

electric field (E) produces same voltage drop $\Delta V = Ew$ between
neighbouring layers of neighbouring grains. Here $w = s_o + d$ is the
average separation between layers and s_o and d are average interpar-
ticle separation and diameter of particles respectively. Moreover
has been assumed that the layers are roughly perpendicular to the
macroscopic field. Therefore, if t be the thickness, V be the
applied voltage and n be the number of layers,

$$E = \frac{V}{t} = \frac{V}{n(s_o+d)} = \frac{(V/n)}{s_o+d} = \frac{\Delta V}{s_o+d}$$

Therefore applied electric field is uniform throughout the matrix
and is perpendicular to electrodes. This is one of the assumptions
(assumption 1, page 25) based on which the formulation has been mad
Further it should be stated that the computed electric field (E_m)
between the neighbouring metallic particles is assumed to be
related to the bulk electric field (E_m^b) calculated on the basis of
thickness by the expression (2.39a), page 38. This assumption is
justified because of the large value of $\rho_{glass}/\rho_{metal}$ ratio
[Ref. 47, page 194], ρ being the electrical resistivity.

Addendum to section 2.2.1, chapter 2.

It is true that when a metallic body is placed in a previously
uniform field between two plates of a large parallel plate capacitor,
the field around the metallic particle is distorted. The surface
remains at constant potential, the field is perpendicular to equipo-
tential surface and the force is proportional to surface charge den-
sity. But the system which has been investigated is very complicated
because of the fact that a large number of metallic particles is
distributed in the glassy phase. Therefore, applying these electro-
static principles to an individual particle and then extending to the
large number of particles present in the system under investigation
will be an intractable problem to solve. We have therefore followed
an alternative approximate approach which is accepted in literature.
/ Ref. B. Abeles, Sheng Ping, M. D. Coutts and Y. Arie, Adv. Phys.
24, 407 (1975) /. It has been stated in literature by Abeles et al
that when an electric field is applied to a granular metal (metal-
dielectric composite) it is reasonable to assume that the equipo-
tential surfaces are approximately perpendicular to the applied
macroscopic field and every metallic particle lies on one of the equi-
potential surfaces. These surfaces divide the whole granular metal samp
into a large number of layers so that each particle lying on one of the
layers is approximately at the same potential. Significant potential
drop occurs between neighbouring grains only when they are in different